UNIVERSITY OF OKLAHOMA

GRADUATE COLLEGE

EXPLORING THE GENERATION AND PRESERVATION OF DUST DURING THE QUATERNARY AND NEOPROTEROZOIC

A DISSERTATION

SUBMITTED TO THE GRADUATE FACULTY

In partial fulfillment of the requirements for the

Degree of

DOCTOR OF PHILOSOPHY

BY

Alicia L. Bonar
Norman, Oklahoma
2023

Downloaded from SHAREOK. Persistent Handle URL: https://hdl.handle.net/11244/337556

EXPLORING THE GENERATION AND PRESERVATION OF DUST DURING THE QUATERNARY AND NEOPROTEROZOIC

A DISSERTATION APPROVED FOR THE
SCHOOL OF GEOSCIENCES

BY THE COMMITTEE CONSISTING OF

Dr. Gerilyn Soreghan, Chair

Dr. Michael Soreghan

Dr. Megan Elwood Madden

Dr. Andrew Elwood Madden

Dr. Kelly Feille

© Copyright by Alicia L. Bonar, 2023
All rights reserved.

TABLE OF CONTENTS

Introduction

Acknowledgements v

Dissertation Abstract vi

Chapter I. Assessing silt generation and origins in granitoid-hosted soils: implications for loess formation

Main Text 1

Figures and Tables 14

References Cited 24

Chapter II. Maximum depositional ages and provenance analysis of the Neoproterozoic Manyovu redbeds, Tanzania: implications for Pan African Orogenesis

Main Text 32

Figures and Tables 47

References Cited 58

Chapter III. Loess and paleosols recorded in the Neoproterozoic Manyovu redbeds of western Tanzania

Main Text 65

Figures and Tables 78

References Cited 86

Supplemental Materials

Chapter I Supplemental Material 93

Chapter II Supplemental Material 103

Chapter III Supplemental Material 129

ACKNOWLEDGEMENTS

I would first like to thank my advisor, Dr. Lynn Soreghan, for offering support throughout my PhD journey and providing me with a multitude of experiences and opportunities that essentially created the professional scientist I am today. Second, I would like to thank Dr. Mike Soreghan, who guided me through a once-in-a-lifetime trip to Tanzania and helped develop and supported the research reported in chapters II and III of this dissertation. Thank you to Dr. Megan Elwood Madden for reviews and edits for chapter I of this dissertation. A big thank you to all of my committee members: Drs. Lynn Soreghan, Mike Soreghan, Megan Elwood Madden, Andy Elwood Madden, and Kelly Feille for guiding me through all the major steps that resulted in the successful defense and passing of this dissertation. I would also like to thank Dr. Michael Msabi for his thorough reviews and assistance with the writing and science reported in chapters II and III.

Next, I would like to thank my masters advisor, Dr. Brian Hampton, for continuing to support and encourage me throughout my academic career. I need to thank all the friends I made during my time at the University of Oklahoma, especially Lily Pfeifer-Johnson, Steve Adams, and Katie Welch; I wouldn't have made it through without you. Thank you to all my amazing friends and family for their continued encouragement over the years. A very special thank you to my husband, Cole – I would not have completed this stage of my life without you by my side; you encouraged, supported, and believed in me every step of the way, and I am forever grateful to have you as my husband. Thank you to Declan Martin and Bren Cable, who assisted with data collection for this dissertation. Additionally, a big shout out to Mupape Mukuli for being the best field assistant in all of Tanzania; I hope we get to meet again someday. A huge thank you to the OU Geosciences Staff: Ashley Tullius, Ginger Leivas, Rebecca Fay, and Leah Moser for keeping this department running and always being available to help with all things school-related.

This research was supported by the National Science Foundation (NSF) under NSF-EAR-1424907 (Awarded to M. Soreghan), NSF-OISE-1658614 (Awarded to M. Soreghan and G. Soreghan), and NSF-1543344 (Awarded to G. Soreghan and M. Elwood Madden). Thank you to the Tanzanian Fisheries Research Institute (TAFIRI) and the Tanzanian Mining Commission for research and logistics support. Research related to chapters II and III was completed under Tanzania Commission for Science and Technology Research Permit # 2021-445-NA-2018-169. Additional funding support for this research included the Robberson Research Grant (OU) and the OU School of Geosciences Eberly Chair. I am very thankful for additional financial support I received, including Mewbourne Family support, the O H "Ike" Hill Endowed Scholarship, the Kelvin Cates Endowment, the West Texas Geological Society Women in Geosciences (WinGS) Scholarship, the James A Gibbs Scholarship, and the Frank Gouin Geology Scholarship.

And finally, this dissertation is dedicated to my first child. Thank you for reminding me of my strength and perseverance, as well as being my motivation these last few months. Mom and dad can't wait to meet you and already love you endlessly.

ABSTRACT

Global sediment movement and production are important to understand when reconstructing Earth's past geography and climate. Loess—terrestrial sedimentary deposits composed of predominantly eolian-transported silt—record the most complete records of climate in the nonmarine realm and some of the largest concentrations of dust in Earth's geologic record. The goals of this dissertation are to 1) test hypotheses related to the on-going debate surrounding the generation of abundant fine-grained material that accumulates as loess deposits, and 2) identify and characterize the sediment transport mechanisms and depositional environments of a massive and structureless sedimentary sequence in Tanzania, which is herein interpreted as a record of Neoproterozoic loess. This abstract aims to illustrate the connections and relationships between the three chapters submitted as part of this dissertation. Each chapter is formatted for publication in various peer-reviewed scientific journals, including the Journal of Geophysical Research (American Geophysical Union) and the Journal of African Earth Sciences (Elsevier).

Many processes have been proposed to be efficacious mechanisms in the production of silt. These include glacial grinding, eolian saltation, fluvial comminution, and many types of weathering such as insolation-, salt-, frost- and pedogenic weathering. While processes such as glacial grinding and eolian saltation have been extensively studied to illustrate their efficacy for generating silt, pedogenic weathering has not been tested rigorously, either by experimental or empirical studies. **Chapter I** aims to test this hypothesized mechanism for silt generation by comparing granulometric data and major, trace, and rare earth element geochemistry of two modern soils from varying climates (hot-arid and hot-humid), in order to discern whether the silt fraction formed *in situ* (autochthonous) or was sourced from eolian processes (allochthonous). Granulometric results indicate that the hot-humid soil (located in southeastern Puerto Rico) contains abundant (>70%) silt- and clay-sized grains (average mode ~15 μm), while the hot-dry soil (located in southern California) contains very minimal silt-sized material (<6%; average mode ~40μm); additionally, geochemical results indicate the Puerto Rico silt- and clay-fraction is at least partially derived from eolian inputs (e.g., African dust, Lesser Antilles volcanic ash) and the Anza Borrego silt-fraction is indistinguishable from local and regional dust sources (e.g., Greater Mojave Desert dust). Therefore, the results from **Chapter I** suggest pedogenic weathering is not a significant factor in silt production for geologically significant loess deposits, as the Puerto Rico soil contains significant silt in a grain-size fraction finer than typical loess, and the Anza Borrego soils contains essentially no *in situ* silt.

Chapters II and **III** of this dissertation concentrate on describing, analyzing, and interpreting the provenance, sediment transport mechanisms, and depositional environment of the Neoproterozoic Manyovu redbeds in western Tanzania, which we interpret as a partial record of loess. The Manyovu redbeds are a unique, and understudied, sedimentary deposit that records extreme tectonic and climatic shifts in Earth history, such as supercontinent assembly as well as major climatic shifts including the enigmatic Snowball Earth events. First, we utilized U-Pb detrital zircon geochronology and modal composition trends to better constrain

the age and source of sediment preserved in the Manyovu strata **(Chapter II)**. U-Pb detrital zircon ages indicate maximum depositional ages (MDAs) as young as 613.6 ± 1.2 Ma, which is almost 200 Ma younger than the previously dated, underlying lavas. Additionally, detrital zircon age spectra and modal compositions indicate the sediment for the Manyovu redbeds was both locally and regionally sourced, and the mid-Manyovu strata likely record the initiation of Pan-African Orogenesis in the Mozambique Belt of Eastern Africa.

After determining the new age constraints and provenance for the Manyovu redbeds, we utilized field observations, particle-size analysis, and supplementary geochemical data to better constrain the depositional environment **(Chapter III)**. Previous work had described the Manyovu redbeds as thick, massive, monotonous, red sandstone, and interpreted the deposits as shallow marine rocks. We logged a 285-m section, where we found no evidence for water-laid deposition of these units. The strata lacked sedimentary structures, channelization, and erosive contacts; instead, a significant fraction of the Manyovu redbeds studied is internally massive, fine-grained (silt – fine sand), and exhibits blocky fracture patterns, concretion horizons, and microfabrics indicative of pedogenesis. Based on these observations, we reinterpret the Manyovu redbeds as recording deposition in a continental, eolian-dominated setting. Together, **Chapters II** and **III** redefine the Manyovu redbeds as at least late Cryogenian to Ediacaran in age, consisting of mostly loess and pedogenically altered loess that may record periglacial deposition, yielding broad implications for Neoproterozoic paleoclimate and Pan-African Orogenesis in East Africa.

CHAPTER I

ASSESSING SILT GENERATION AND ORIGINS IN GRANITOID-HOSTED SOILS: IMPLICATIONS FOR LOESS FORMATION

ASSESSING SILT GENERATION AND ORIGINS IN GRANITOID-HOSTED SOILS: IMPLICATIONS FOR LOESS FORMATION

ABSTRACT

The origin and production of silt are key factors in the formation of loess deposits. Although many processes can potentially lead to silt generation, few are known to produce silt in the volumes and particle-size modes required to form geologically significant loess deposits. Here we investigate the hypothesis that pedogenic weathering in tropical and Mediterranean climates can generate abundant *in situ* silt, and therefore contribute significantly to loess formation throughout geologic time. We utilize granulometric and geochemical data from soils formed in Puerto Rico (hot-humid) and Southern California (hot-arid) to discern whether the mud fraction (<62.5 μm) is generated from bedrock (autochthonous) or sourced from eolian contributions (allochthonous). Our study demonstrates that the Puerto Rico soil contains abundant (up to 72%) silt- and clay-sized grains compared to the Anza Borrego soil (<6%). However, the silt fraction of the Puerto Rico soil is at least partially derived from eolian inputs, and the silt fraction of the Anza Borrego soil is geochemically indistinguishable from allochthonous dust sources. Furthermore, while intense chemical weathering in a tropical climate can produce abundant fines, the majority are significantly finer (average mode ~15 μm) than the modes of most "typical" loess deposits (modes more than 20 – 30 μm). In contrast, weathering in Mediterranean climates produces volumetrically sparse silt. Hence, pedogenic weathering in hot climates appears to be ineffectual for producing the volume and size distributions of silt-sized material needed to generate significant loess deposits.

PLAIN LANGUAGE SUMMARY

Global sediment movement is important to understand when reconstructing Earth's past geography and climate. Windblown silt deposits, known as loess, are particularly useful for recording paleoclimatic conditions, but the origin of the silt that forms large loess accumulations remains controversial. In this study, we aim to better understand processes that can generate silt in large quantities by investigating whether significant silt is form in place during soil formation from underlying bedrock, or if the silt observed in soils was delivered from elsewhere. We compare silt in two different soils, one from a hot-dry climate and one from a hot-wet climate, which provides additional information about how weathering processes can influence the results. Our findings demonstrate that soil forming in the hot-wet climate can create abundant silt, but with a grain size smaller than most loess deposits, whereas soil from hot-dry climates produces minimal silt. Additionally, both soils show evidence for silt inputs from local and regional dust sources. Our results suggest that soil formation is not a major process for silt production that contributes to loess deposits.

INTRODUCTION

Loess is a significant component of the terrestrial rock record in the Quaternary (e.g., Catt, 1988; Smalley, 1995; Assallay et al., 1998; Muhs and Bettis, 2003; Muhs, 2013; Li et al., 2020) and covers approximately 6% of Earth's surface today (Li et al., 2020). The largest deposits are spatially

linked to former ice margins and typically found in mid – high latitude regions (Catt, 1988; Smalley, 1995). Hence, glacial grinding is known to be an especially efficacious way to generate large quantities of silt (Pye, 1995; Smalley, 1995; Assallay et al., 1998; Soreghan et al., 2008) in typical loess grain size modes (~20 – 40 μm; e.g., Smalley and Krinsley, 1978; Tsoar and Pye, 1987; Assallay et al., 1998; Anderson, 2007). However, smaller accumulations of loess and loess-like deposits also occur in lower-latitude hot climates— for example, the Negev loess in Israel— indicating that silt that forms loess deposits can be produced by processes unrelated to glaciation (e.g., Pye and Tsoar, 1987; Crouvi et al., 2008). Therefore, eolian saltation and abrasion in desert environments have also been suggested as processes for silt generation (Smalley and Vita-Finzi, 1968; Tsoar and Pye, 1987; Smith et al., 2002; Crouvi et al., 2008; Enzel et al., 2010), although experiments using realistic wind velocities and starting material indicate that saltation abrasion produces insufficient silt to form loess (e.g., Kuenen, 1960; Swet et al., 2019; Adams and Soreghan, 2020). Furthermore, fluvial comminution (Wright and Smith, 1993), as well as insolation-, salt-, and frost-weathering (e.g., Pye and Sperling, 1983; Wright et al., 1998; Wright, 2001) have also been suggested to generate silt, but no systematic data exist that illustrate the efficacy of producing large volumes of silt by these means.

Pedogenic weathering has also been widely suggested as a potential means for silt production in warm climates (e.g., equatorial, tropical, and Mediterranean) originally by Nahon and Trompette (1982), and subsequently reiterated by others (e.g., Wright, 2001, 2007). Nahon and Trompette (1982) argued that chemical weathering in soils can form abundant silt-sized quartz and feldspar grains and predicted that mature soil profiles that develop on even coarse-grained, granitoid bedrock can contain between 50 – 75% silt-sized grains. They suggested that the primary mechanism for creating this silt is the breakdown of crystals in intense combinations of chemical and physical weathering, resulting in fragmentation due to dissolution along subplanar microfractures now known as Moss defects (Moss, 1966; Moss and Green, 1975). Wright (2007) supported this claim that pedogenic weathering can be a key contributor to silt production through their review of the efficacy of weathering processes to generate fine-grained material on a variety of parent rocks, as well as analysis of grain-size characteristics in weathering profiles.

Nahon and Trompette (1982) based their hypothesis on examination of thin sections illustrating the presence of many fine grains (both quartz and feldspar) with uniform extinction that appear to have been components of a pre-existing single crystal, indicating the *in situ* breakdown of larger crystals. They also cited an increasing abundance of silt- and clay-sized quartz grains at the tops of weathering profiles, which they attributed to the progressive dissolution of quartz from the bedrock up-profile (Nahon and Trompette, 1982; Wright, 2001). Additionally, mature weathering profiles can exceed 10 m in thickness, especially in humid climates, and tropical, equatorial, and Mediterranean soils typically contain ferruginous or carbonate matrices, which can readily disaggregate to ultimately release the entrained silt. However, the efficacy of pedogenic weathering for silt production has not been tested rigorously – experimentally or empirically.

Here, we test the hypothesis of abundant pedogenic generation of silt in warm-climate soils by assessing the grain size and geochemistry of silt recovered in a hot-wet (tropical) weathering

profile from southeastern Puerto Rico and a hot-dry (Mediterranean) profile from the Anza Borrego Desert, southwestern United States (U.S.). Our results highlight significant differences in the potential for *in situ* silt generation in soils from these varying climates, both in terms of the volume and particle size modes of produced silt. These results contribute to our understanding of the formation of loess deposits through Earth history, and their possible paleoclimatic significance.

GEOLOGIC SETTING

We focused on two localities, each characterized by granitoid bedrock and hot climates, but contrasting precipitation: arid-hot Anza Borrego Desert in southern California (southwestern U.S.) and wet-tropical southeastern Puerto Rico (Caribbean Islands; Fig. 1). Refer to Table 1 for details regarding climate classification and soil formation variables including bedrock geology and dust influences. Both study regions are hosted primarily on crystalline granitoid bedrock characterized by a relatively coarse grain-size (Fig. 2, 3). In addition to potential *in situ* formation of silt in the soil profiles, both locations receive either local dust or long range traveled (LRT) dust (Table 1; references within). We sampled surficial profiles characterized as "modern," that likely record time-averaged dynamic climatic conditions of the late Pleistocene. For example, southern California experienced a wetter climate during interglacials of the Quaternary (e.g., Reheis et al., 2012), and Puerto Rico was influenced by glacial and interglacial cycles through changing sea levels which likely affected vegetation and biodiversity (e.g., Weigelt et al., 2016).

In southern California, the study area encompasses Indian Gorge within the southern part of the Anza Borrego Desert (Fig. 1A), where the bedrock geology consists of the Middle Cretaceous La Posta tonalite (Fig. 2) overlain by first-cycle Quaternary alluvial sediment (of late Pleistocene or younger age; Fletcher et al., 2011; Blisniuk et al., 2012). Both the bedrock and derived alluvial sediment contain majority plagioclase, quartz, biotite, and potassium feldspar (Clinkenbeard and Walawender, 1989; Joo et al., 2016). Allochthonous eolian material is likely delivered to the Anza Borrego Desert by seasonal Santa Ana wind events from the Greater Mojave Desert region (Muhs, 1983; Reheis et al., 1995, 2002; Muhs et al., 2007a; Fig. 1A). Previous studies documented the grain size distribution of Mojave Desert dust as mostly silt (up to 70%) with some clay-sized material (20 – 45%; Reheis et al., 1995)

The Puerto Rico study area lies within the Rio Guayanés watershed of southeastern Puerto Rico (Fig. 1B). The Rio Guayanés watershed is underlain predominantly by the Late Cretaceous San Lorenzo granodiorite, as well as first-cycle alluvium (Rogers et al., 1977), both of which contain plagioclase, quartz, potassium feldspar, hornblende, and chlorite with minor accessory minerals (Fig. 2; Joo et al., 2018). Dust deposition on the Caribbean Islands is well established from previous studies (Table 1), with two major sources identified: Saharan and Sahel desert dust from North Africa, and volcanic ash from the Lesser Antilles volcanic arc in the eastern Caribbean Sea. More than 60 million tons of Saharan dust is deposited annually (Prospero and Lamb, 2003; Lau and Kim, 2007). African dust from the Saharan and Sahel deserts contains mostly fine-silt sized quartz (4 – 20 μm) and clay-sized (<4 μm) mica; 30 – 50% of the dust is <2.5 μm (e.g., Prospero et al.,1970; Glaccum and Prospero, 1980). Volcanoes within the Lesser Antilles have been active

since the Pleistocene (e.g., Frey et al., 2018), with multiple explosive eruptions recorded in marine sediments west of the arc (e.g., Carey and Sigurdsson, 1978; Sigurdsson and Carey, 1980; Le Friant et al., 2008). Many of the tephra units contain plagioclase, augite, hornblende, rhyolite glass, and some quartz, with the largest phenocrysts ranging in size from 0.5 – 2 mm (e.g., Carey and Sigurdsson, 1980). There is also considerable silt-sized crystals and glass within the ashfalls, with glass content increasing with decreasing grain size (Carey and Sigurdsson, 1980).

METHODS

Sample Collection

Soil, bedrock, and dust samples were collected from the Anza Borrego Desert in southern California in December 2013. Soil, bedrock, and Pleistocene carbonate beach rock (a proxy dust trap) samples were collected from the Rio Guayanés watershed in southeastern Puerto Rico in 2014 (Fig. 1, 2, 3). Anza Borrego soil samples (N=7, ~20 cm spacing) were collected along the Indian Gorge in the Tierra Blanca Mountains from a 1.5-m profile formed on first-cycle proximal alluvial fan sediment atop tonalite bedrock (N=3). Dust traps (a total of 12, patterned after designs in Reheis and Kihl,1995 and Reheis, 2003; Fig. 2A) were deployed throughout the area, but only one trap was salvageable (N=1). Due to the low volume of dust collected, we obtained two dust trap samples from Marith Reheis (dust traps T57 and T59; Reheis and Kihl, 1995) to supplement our dataset. Puerto Rico soil samples (N=6, ~50 cm intervals) were collected from a 2.5-m profile formed on granodiorite bedrock (N=2). Dust traps were deployed in the Puerto Rico study area (total of 5, using the same model as the Anza Borrego locality) but did not survive the deployment. Instead, we collected samples of Pleistocene carbonates with karst-filling mudstones from the southern coast near Guánica as a proxy dust sample (N=1; Fig. 1B).

Sample pre-treatment and analysis

Representative subsamples of the soil profile were first wet-sieved to assess proportions of gravel (> 2 mm), sand (63 μm – 2 mm), and mud (< 63 μm). A subsample of the muds from all samples were treated with buffered acetic acid for 24 hours to remove carbonates and 30% hydrogen peroxide (up to 2 weeks) to remove organic matter. Owing to the high carbonate content of the Pleistocene beach rock, this sample was processed with 2N HCl for 24 hours to fully disaggregate the sample prior to hydrogen peroxide treatment. Processed subsamples were used for laser particle size analysis (LPSA) and whole rock, trace element, rare earth element, and base metal geochemical analyses. Samples analyzed by the LPSA were run in triplicate to ensure reproducibility of histograms and reported modes. The small volume recovered from our Anza Borrego trap precluded LPSA analysis, as all material was used for geochemical analysis; however, dust traps T57 and T59 (Reheis and Kihl, 1995) were used for LPSA. We further wet sieved the Puerto Rico mud samples to compare the chemistry of the < 20 μm mud fraction, the 20 – 63 μm fraction, and the total < 63 μm fraction. We note that all 3 fractions produced comparable geochemical compositions (refer to supplemental data); therefore, we elected to only present data from the total < 63 μm fraction for direct comparison with the other sediment samples.

We used the Wentworth Scale size classification customarily used by sedimentologists (Wentworth, 1922) to describe grain sizes since we apply our interpretations to the deep-time rock record; accordingly, we consider the < 4 μm fraction as clay, and the 4 – 63 μm fraction as silt. LPSA was completed at the University of Oklahoma using a Malvern Mastersizer 3000, where soil and dust samples were combined with distilled water and a few drops of dispersant (sodium hexametaphosphate) and sonicated for 1 minute prior to addition to the LPSA. Crystal size determinations for the bedrock samples were completed by tracing > 100 random crystals from thin sections of each sample and importing the traces into the ImageJ software using the particle size analysis function. Data were reported in area (μm^2), which was used to calculate the 2D diameter (μm) then converted to a 3D measurement using methods described in Johnson (1994). Geochemical analyses were completed by ALS Global using ICP-AES for whole rock analyses; fuse bead, acid digestion and ICP-MS for trace element and rare earth element analysis; and separate four acid digestion for base metal analysis.

RESULTS

Granulometric data

Anza Borrego

The Anza Borrego soil profile is predominantly gravel (18.2 – 33.1%) and sand (62.1 – 78.8%) with minor (1.2 – 5.6%) mud (Fig. 4; Table 2). Overall, the mud fraction and gravel fractions both increase toward the top of the profile, with the top 0.5 m containing 4.7 – 5.6% mud and 27.5 – 33.1% gravel. The mud fractions exhibit coarse-silt modes of 36 – 42 μm (average ~40 μm) that are invariant throughout the profile, with fine-skewed, relatively unimodal distributions (Fig. 4). The mud fraction is predominantly coarse silt (32.8 – 38.2%) with lesser amounts of medium (25.3 – 30.1%) and fine silt (14.9 – 18.4%), and minor very fine silt (6.9 – 8.6%) and clay (6.2 – 8.3% ; Table 2). The average silt content in bulk samples from the Anza Borrego profile is <5% with only a trace volume of clay-sized material (<0.5%). Dust samples from T57 and T59 report different modes, but similar silt-fraction distributions (Table 2). Dust trap T57 yielded a mode of 83.3 μm (very fine sand), and T59 yielded a mode of 32.1 μm (coarse silt; Table 2, Fig. 4). Note, however, that T57 contains abundant biotite, which produces unreliable laser diffractometry results owing to the platy cleavage.

Puerto Rico

Grain size data in the Puerto Rico soil contrast significantly with those observed in the Anza Borrego samples, containing minor gravel (0 – 1.5%), with significant sand (28.4 – 55.9%) and mud (42.6 – 71.6%; Fig. 4, Table 2). Unlike Anza Borrego, where the average grain size within the mud fraction remains consistent at each depth, the mud fraction of the Puerto Rico soil samples exhibits modes between 6 – 18 μm that decrease towards the surface of the profile. LPSA histograms from the Puerto Rico soil profile exhibit relatively unimodal peaks in the

deeper profile, but display finer, bimodal peaks in the uppermost samples (Fig. 4). At 0.1 m, 0.5 m, and 1 m depths, the Puerto Rico soil samples show distinct modes at both ~5 μm and ~18 μm (Fig. 4). The dust proxy sample (siliciclastic fraction of the carbonate rock) is dominated by clay-sized particles (> 60%), with 14% very fine silt, 13.7% fine silt, and approximately 11% coarse and medium-silt combined (Table 2). Histograms of the Puerto Rico dust proxy exhibit bimodal peaks at < 1 μm and ~5 μm, with an average reported mode of 4.9 μm (Fig. 4).

Among the Puerto Rico soil samples and dust proxy (beach rock), the soil samples exhibit the highest fraction of fine silt (25.0 – 29.2%) and clay (21.3 – 31.2%; Table 2) and the dust proxy contains the highest percentage of clay-sized particles (60.9%; Table 2). The soil samples contain only minor amounts of coarse silt (4.6 – 8.6%) and moderate medium silt (16.7 – 21.6%). The soil samples exhibit a silt distribution similar to that of the modern dust analog, but have significantly less clay-sized particles (up to 40%). When compared to total soil contents (gravel, sand, and mud fractions), the silt fraction of the Puerto Rico soil ranges from 31 – 50% (Table 2).

Bedrock Crystals

Crystal sizes from the Anza Borrego (n=137) and Puerto Rico bedrock (n=204) range from fine to very coarse crystals (Table 3). Data are reported for calculated crystal area (μm^2), 2D diameter (μm), and converted 3D diameter (μm; Table 3). The diameters are calculated based on the simplification of a spherical shape, and the converted 3D measurements are thus larger than the 2D diameters. Accordingly, these data are a semi-quantitative estimate of bedrock crystal size, but nevertheless demonstrate that both granitoids are coarse-grained; however, the Anza Borrego bedrock crystals are, on average, 2-times larger than the Puerto Rico bedrock (Table 3). The average crystal diameter in the Anza Borrego tonalite is 982 μm, while the average crystal diameter in the Puerto Rico granodiorite is 653 μm (Table 3).

Geochemical Data

Major element geochemistry

Major element geochemistry from the soils, bedrock, and dust samples reflects weathering intensity at the Anza Borrego and Puerto Rico localities (refer to supplementary files for raw data). Major element concentrations were plotted in A-CN-K space using the molar ratios of Al_2O_3-CaO+Na_2O-K_2O following Nesbitt and Young (1984, 1989) to assess weathering trends (Fig. 5). Since all samples were processed to remove carbonate, compositional values of CaO are interpreted to represent values of the silicate fractions. However, after geochemical analysis, an elevated LOI value for the Pleistocene beach rock indicated remnant carbonate bound CaO. The CaO value used for CIA analysis for the Puerto Rico dust proxy is corrected following methods of Taylor and McClennan (1985). CIA values were calculated to understand weathering intensity between each soil compared to potential sources (bedrock and dust) with the

following equation using molecular values (Nesbitt and Young, 1982): [Al_2O_3/(Al_2O_3 + CaO + Na_2O + K_2O)] x 100. We note that these values are used only to understand weathering intensity of each soil compared to bedrock, not as a comparison of weathering between each location. As traditionally interpreted, CIA values of 50 – 65 indicate minimal chemical weathering, values of 65 – 85 reflect intermediate chemical weathering, and values >85 indicate extreme chemical weathering (e.g., Nesbitt and Young, 1982, 1984, 1989); however, these values are also affected by the composition of the source material.

In general, the soil samples from Anza Borrego are slightly more Al-rich than the associated bedrock but plot close to bedrock on the A-CN-K ternary diagram. Anza Borrego bedrock samples have CIA values around 50 and the soil samples exhibit CIA values between ~54 – 56, consistent with incipient leaching through chemical weathering relative to the host bedrock. The Anza Borrego dust trap material exhibits the lowest CIA value at 48, indicating that the dust delivered to the Anza Borrego desert was likely derived from more mafic sources.

All Puerto Rico samples plot closer to the CN apex compared to the K apex, attributable to a high fraction of plagioclase in the bedrock (e.g., Joo et al., 2018). Puerto Rico soils are significantly shifted towards the A apex from the host bedrock in A-CN-K space (Fig. 5). Puerto Rico bedrock samples also plot within a similar region as both the Anza Borrego bedrock and soil samples. This indicates that the Puerto Rico soils have experienced significant Ca, Na, and K leaching via chemical weathering. The Puerto Rico bedrock samples exhibit CIA values around 45, consistent with both the Ca-rich bedrock chemistry and minimal chemical weathering of the granitoid bedrock. Puerto Rico soil samples exhibit CIA values of ~85 – 98 indicating uniformly intense chemical weathering compared to the very low values in the bedrock. The Puerto Rico dust proxy has a CIA of ~95 likely reflecting intense chemical weathering and/or abundant detrital clay minerals, as indicated by high clay-sized particle content.

Element-Depth Profiles

Elements considered to be relatively immobile in low-temperature and near-surface environments are commonly utilized in dust and sedimentary rock provenance studies (Cullers et al., 1979; Bhatia and Crook, 1986; McLennan, 1989; Olivarez et al., 1991; Nakai et al., 1993; Sun, 2002; Muhs et al., 2007a, 2007b; Reheis et al., 2009). We applied a Tau calculation (Eq. 1; Brimhall and Dietrich, 1987; Chadwick et al., 1990; Anderson et al., 2002) normalized to Ti and plotted results on element-depth plots to determine whether immobile elements are enriched or depleted in soil samples compared to weathered bedrock and fresh bedrock.

$$\tau_{i,j} = \frac{C_{j,w}}{C_{j,p}} \frac{C_{i,p}}{C_{i,w}} - 1 \qquad \text{Eq. 1}$$

In equation 1, C represents the concentration (ppm) of immobile (i) and mobile (j) elements in the weathered (w) and parent (p) material. Weathered material is considered all samples other than fresh bedrock. We use Ti as the immobile element because 1) it is minimally

mobile in many environments (Bern et al., 2015) and 2) the concentrations of Ti in the soil samples from both Anza Borrego and Puerto Rico do not indicate signs of illuviation or leaching. When $\tau = 0$, the calculated elemental concentration in the soil matches that of the bedrock; however, if $\tau > 0$, the weathered material is enriched in that element compared to the bedrock and when $\tau < 0$, the weathered material is depleted in that element compared to bedrock. For example, a τ of -1 indicates 100% loss of the element. We plotted the elements Nb and Zr (immobile and common elements used to indicate allochthonous material), Ta and Th (commonly used in soil provenance, e.g., Muhs et al., 2007a, 2007b) and Fe and Al (typically highlight redistribution or illuviation; e.g., Chadwick et al., 1990) normalized to Ti in both Anza Borrego and Puerto Rico localities (Fig. 6).

The element-depth plot for the Anza Borrego soil shows enriched values for Th, Ta, and Nb, and a slight enrichment of Zr in the soil profile samples compared to the fresh and weathered bedrock, all of which are indicative of allochthonous additions to the profile (Fig. 6; e.g., Brantley et al., 2007). The elemental enrichment values for Th and Ta are on the order of 10-20 times that of the parent material, indicating abundant accumulation of material from external sources for the mud fraction. Conversely, the Anza Borrego profile is depleted in Fe and Al compared to the bedrock samples (Fig. 6). Al is minimally depleted in the soil profile with τ-values between -0.1 – -0.2, while Fe is substantially depleted in the soil samples (τ-values = ~ -0.5) indicating almost 50% loss of Fe compared to the bedrock chemical composition. Th has the largest range of values within the soil profile with no consistent pattern between the lower and higher values. Ta, Nb, Fe, Al, and Zr values are consistent between depths within the profile. Refer to supplemental files for detailed τ-values.

Similar to the Anza Borrego profile, the Puerto Rico element-depth plot shows enriched values for Th, Ta, Nb, and Al, while Fe has an immobile pattern and Zr is almost completely depleted from the soil samples compared to the bedrock (Fig. 6). Although Zr is typically considered an immobile element, several studies have shown that the intense chemical weathering in eastern Puerto Rico causes even Zr to be mobilized (e.g., McKlintock et al., 2015; Buss et al., 2008, White, 2002) and thus depleted relative to unweathered bedrock. For this reason, we normalize to Ti for all element-depth plots in this study. In the Puerto Rico profile Fe τ-values in the upper-most samples are slightly enriched and deeper samples contain values that are slightly depleted; Zr is depleted from the uppermost portion of the profile and becomes slightly enriched in the deeper samples (Fig. 6). Notably, the highest enrichment values for all the elements occur at depths of 1.5 m and 2.5 m (Fig. 6).

Rare Earth Element Signatures

Rare earth element (REE; La through Lu) compositional distributions and abundances can also be used to determine provenance (e.g., Taylor and McLennan, 1995). REEs were normalized to chondritic meteorite compositions using values from Taylor and McLennan

(1985). Chondrite REE patterns are expected to form smooth REE distributions; therefore, positive (enriched) and/or negative (depleted) anomalies of Ce and Eu as well as relative enrichments or depletions in the heavy REEs (HREE; Gd through Lu) and the light REEs (LREE; La through Sm) can be compared to the crystalline parent rock and dust samples to determine likely sources. The majority of REEs are contained in the clay and silt fractions, and sedimentary processes (especially granite weathering) can result in positive Ce anomalies due to the formation of Ce^{4+} and cerium hydroxides (Nesbitt, 1979; Banfield and Eggleton, 1989; Taylor and McLennon, 1995) and negative Eu anomalies via plagioclase weathering (Condie et al., 1995; Compton et al., 2003; Babechuk et al., 2014).

At the Anza Borrego locality, we plotted REE signatures for bedrock samples, dust trap sediment, and the soil profile (Fig. 7). The Anza Borrego bedrock samples have moderately low REE abundances with slightly higher LREE abundances than HREE. All three samples show slight negative Ce anomalies, and two samples show positive Eu anomalies. The Anza Borrego dust trap sediment has elevated LREE abundance, a negative Eu anomaly, and a flat distribution of HREE, but total REE abundances are higher than the bedrock samples. The soil samples all produce a consistent REE pattern that is similar to the dust trap sample, in both REE abundance and distribution.

At the Puerto Rico locality, we plotted REE signatures for bedrock samples, the dust proxy sample, and the soil profile (Fig. 7). The Puerto Rico bedrock samples have relatively flat REE patterns, with similar abundances between the LREE and HREE. Both samples exhibit negative Eu anomalies and low total REE values. However, the Puerto Rico soil samples exhibit variable REE patterns. In general, samples from the deeper intervals contain higher abundances of both LREE and HREE compared to the upper-most samples; all depths have negative Eu anomalies and positive Ce anomalies. Deeper samples also resemble patterns similar to the Puerto Rico dust proxy, however with lower total abundances of REE. Near-surface samples exhibit strong positive Ce anomalies, which are not observed in either the bedrock or dust proxy samples.

DISCUSSION

Intensity of Chemical Weathering

Chemical weathering and associated alteration of host material were evaluated using changes in concentrations of major elements and associated CIA values, ranges of element mobility represented in the element-depth plots, and REE patterns of the soil and bedrock samples from both localities. Unsurprisingly, all data indicate that chemical weathering is most intense in the Puerto Rico soil (Fig. 5, 6, 7). In contrast, the Anza Borrego soil shows minimal chemical weathering, consistent with low CIA values that are only slightly elevated relative to the bedrock (Fig. 5). Plagioclase weathering plays an important role at both localities, especially in initial bedrock weathering, indicated by the complete loss of the positive Eu anomaly in soil

samples in Anza Borrego, despite its presence in the bedrock samples, and an increase in the intensity of the negative Eu anomaly between bedrock and soil samples in Puerto Rico (Fig. 7; Condie et al., 1995; White et al., 1998; Compton et al., 2003; Buss et al., 2008; Babechuk et al., 2014; Joo et al., 2016, 2018). The REE observations and patterns from the mud fractions of the Anza Borrego soil samples show enrichments in the LREE, negative Eu anomalies, and overall higher abundances of REE compared to the bedrock samples. In Puerto Rico, the REE observations and patterns from the mud fractions of the soil samples include overall depleted REE abundance (both LREE and HREE), positive Ce anomalies, and more intense negative Eu anomalies (Fig. 6). Positive Ce anomalies in the soils, compared to none to slightly negative Ce anomalies in the Puerto Rico bedrock, are documented in other granitoid soils forming in humid and tropical climates (e.g., Ghani et al., 2019). The enrichment of Ce in the soil samples is likely due to the change from Ce^{3+} to Ce^{4+} attributable to oxidizing conditions, which is more stable and can be retained by clay minerals which are likely abundant in the Puerto Rico soils indicated by the grain size and Al-enrichment (Ghani et al., 2019).

Figure 6 shows the variations in depletion and enrichment of typically immobile elements representing chemical and biological processes at play at each locality. In Anza Borrego, both Al and Fe are slightly to moderately depleted, which is commonly associated with mineral weathering by organic (fluvic and humic) acids and/or microbial degradation (e.g., Lundström et al., 2000). Depletion of Al and Fe is a typical observation in podzols, which exhibit leaching of Fe and Al in the upper soil profile; however, podzols form in cool, humid climates with abundant vegetation (McKeague et al., 1983)— the opposite of the modern climate in the Anza Borrego Desert. The Anza Borrego profile exhibits minimal chemical weathering and minimal clay mineral content, which we would expect to result in an immobile pattern and not a depletion for these elements. Instead, we posit that this pattern likely records the influence of wetter climates of the late Pleistocene in this region (e.g., Reheis et al., 2012).

In contrast, the element-depth plots for Puerto Rico indicate leaching and associated illuviation of nearly all the plotted elements, reiterated by the low total REE abundances in the soil samples, especially in the shallow depths of the profile, all indicating mobilization of elements (Fig. 6, 7). The highest enrichment values of relatively immobile elements occur at depths of 1.5 m and 2.5 m signaling illuviation horizons, even though all depths show enrichment values for Th, Ta, Nb, and Al. Additionally, Al exhibits higher enrichment values at 0.1 m and 0.5 m depths compared to 1.0 m, which does not occur with other elements, and likely reflects dust input near the surface of the profile (Fig. 6). Fe appears to represent an immobile element in this profile, with no clear addition or depletion patterns, which could indicate bioturbation, or biogeochemical cycling (e.g., White and Buss, 2014).

The variability in chemical weathering and subsequent element mobility between the two localities is expected given the order-of-magnitude larger mean-annual precipitation and higher mean-annual temperature in Puerto Rico compared to Anza Borrego. This difference likely

impacts the resulting silt generation in each profile, which partly explains the extremely low volumes of silt and clay in Anza Borrego and abundance of silt and clay in the Puerto Rico soil. Additionally, the finer initial crystal size of the Puerto Rico bedrock likely contributes to the efficacy of chemical (and physical) weathering in creating the abundant mud fraction observed in these samples. In contrast, it seems unlikely that the silt in Anza Borrego formed from bedrock weathering— either chemically or physically— as explored further below.

Evidence for Dust Additions

The role of soil as a trap for dust is well recognized (e.g., Yaalon and Ganor, 1973; review by Muhs, 2013); indeed, dust can deliver significant macro- and micronutrients to soil ecosystems. Dust can contribute significant volumes of fine-grained material to soils depending on their geographic proximity to potential dust sources, and many studies have documented additions of long-range-traveled (LRT) dust to soils (e.g., Birkeland, 1999; Kurtz et al., 2001; Muhs et al., 2021) including in the Caribbean Islands (e.g., Muhs et al., 2007b; Pett-Ridge, 2009; Pett-Ridge et al., 2009; McClintock et al., 2015, 2019) and southern California (Muhs et al., 2007a, 2008; Reheis et al., 2009). Ultimately, soils developed on coarse-grained host rocks can produce some autochthonous silt via pedogenic weathering but can also contain allochthonous silt attributable to local dust inputs. These processes are potentially distinguishable by comparing particle size and geochemical attributes of the soils relative to parent rock and dust sources.

Both study profiles follow expected grain-size distribution patterns: the Anza Borrego soil is predominately sand, representing a more arenaceous profile common in temperate climates (e.g., Hall, 1985; 1987), and the Puerto Rico profile is predominately mud, especially very fine silt and clay, representing an argillaceous profile more expected in humid climates (Fig. 4, Table 2). The distribution of grain sizes in each profile largely reflects the significant contrast in intensity of chemical weathering, as well as differences in eolian inputs. In addition to the A-CN-K diagram and element-depth plots, we plot elements with low expected mobility, Nd-Cr-Ta and Th-La-Sc (Taylor and McLennon, 1985; Olivarez et al., 1991; Muhs et al., 2007b, 2021) on ternary diagrams to further investigate the provenance of the mud fraction (cf., Muhs and Budahn, 2009; Muhs et al., 2007b, 2010, 2021; Reheis et al., 2009). Figure 8 compares data from this study and potential dust source fields from previous works by Muhs et al. (2007b) and Reheis (2003).

The Anza Borrego dust trap sediment exhibits bulk geochemistry which likely reflects a mafic source. The addition of dust to the Anza Borrego profile could influence the geochemical signature of the soils, potentially shifting to lower CIA values, for example (Fig. 5, 7; discussion above). The REE signatures of the soil samples from Anza Borrego and the dust trap samples are comparable and plot similarly to other Greater Mojave Desert dust samples within the region (Fig. 7; e.g., Reheis et al., 2002). The dust trap sample we analyzed from Reheis and Kihl (1995) (T59; that was not influenced by mica) reported a mode of 32 μm which aligns with the data

observed in the soil profile and is consistent with other studies. Emery (1960) reported dust from Santa Ana wind events collected in Los Angeles as having grain-size modes between 30 – 40 μm, comparable to the modes of the mud fraction in the Anza Borrego soil (Fig. 9). Additionally, Reynolds et al., (2006) reported silt contents from dust traps around the Greater Mojave Desert region as predominantly coarse silt (up to 55%), also aligning with the granulometric results from the Anza Borrego soil profile. Figure 8 illustrates that the geochemical signatures from the mud fractions of the soil samples and the dust trap data plot within the Greater Mojave Desert dust provenance fields reported by Reheis (2003) and Reheis et al. (2002). Within Nd-Cr-Ta space, the soil samples cluster near the Nd apex along with the dust trap sample, all of which fall within the Greater Mojave Desert dust field; similarly, in Th-La-Sc space the soil samples and dust trap sediment create a distinct cluster near the La apex within the Greater Mojave Desert dust field. Additionally, the bedrock samples plot in separate clusters closer to the Cr apex in Nd-Cr-Ta space and towards the Sc apex in Th-La-Sc space. Figure 6 also shows evidence for allochthonous additions to the Anza Borrego profile with enrichment values upwards of 15 for Th and well above 1 for Ta and Nb. These data reinforce the interpretation of a predominantly allochthonous, eolian origin for the mud fraction of the Anza Borrego soil, rather than an *in situ* origin by pedogenic weathering of the parent material.

The Puerto Rico dust proxy is predominantly clay with a very fine mode of 5 μm, which is also consistent with LRT dust likely from the North African Saharan or Sahel deserts or the Lesser Antilles volcanic arc system (Fig. 4). Although the only soil depth that aligns granulometrically with the dust proxy occurs at 0.5 m, the top two meters of the Puerto Rico profile display bimodal histograms with both ~5 and 18 μm modes (Fig. 4). This bimodal distribution is consistent with the possibility of multiple sources for the fines in this profile – e.g. autochthonous production of clays by weathering, and allochthonous input of LRT dust. Since the lower depths are more consistently coarse, we posit that the majority of the coarser mode of 18 μm represents the autochthonous silt fraction produced via pedogenic weathering, while the 5 μm mode likely represents (at least partially) the LRT dust fraction, as typical grain-sizes of African dust particles are 2.5 – 5 μm (Fig. 9; Li-Jones and Prospero, 1998). Examples from distal ash falls from Dominica range in grain size from coarse silt (45 μm) to fine silt (14 μm); however more proximal ashfall would be coarser (Carey and Sigurdsson, 1980). Grain size decreases with distance from an eruption, so we assume that any dust that reached Puerto Rico would be in the coarse silt range (Carey and Sigurdsson; 1980), consistent with the proximity of the arc.

Similar to Anza Borrego, Puerto Rico soil samples also exhibit enriched values for multiple immobile elements including Nb, Ta, Th, and Al indicating external sources for the mud fraction (Fig. 6). Additions of volcanic and clay minerals from dust sources likely contribute to the high CIA values in the dust proxy as well as the enrichment of Al in the element-depth plots. However, unlike the comparable attributes observed between the Anza Borrego dust sediment and soils, the Puerto Rico dust proxy does not align entirely with the soil samples in Puerto Rico,

as shown in Figure 8. Interestingly, the dust proxy plots in between the values for the provenance of African dust, Dominica and St. Lucia volcanics (Muhs et al., 2007b) on the Th-La-Sc ternary plot, but plots closer to the St. Vincent volcanics provenance field in the Nd-Cr-Ta ternary plot. In the Th-La-Sc plot, the soil samples fall near a mixing line between the bedrock samples and the dust proxy data point, plotting near the volcanic provenance fields, but not overlapping. In the Nd-Cr-Sc plot, the bedrock and dust proxy samples do not align with the soil samples, but a few of the soil samples overlap with St. Vincent volcanics and African dust. Overall, the soil samples produce irregular signatures with regards to dust data fields, but the Th-La-Sc plot indicates a strong African dust influence, while the Nd-Cr-Ta plot indicates a mix of potential sources.

In summary, geochemical evidence from both localities are consistent with the influence of allochthonous dust to the soil profiles, despite the lack of eolian mantles apparent in the A horizons (the uppermost part of the profile, e.g., Yaalon and Ganor, 1973). The data support an almost entirely dust-derived silt fraction in Anza Borrego, and a completely homogenized silt fraction mixed with both parent rock and dust inputs in Puerto Rico, regardless of sample depth.

Implications for Loess Formation

To examine the efficacy of pedogenic weathering (by physical, chemical, and biological processes) as a major mechanism for silt generation, we evaluate the results from both profiles within the context of critical attributes of geologically significant loess deposits. At the broadest scale, these factors include 1) the grain-size mode of the silt fraction in each soil profile compared to typical loess modes and 2) the amount of silt contained in the soil compared to the volume of silt in a loess deposit. Note that we focus not only on the mode and volume of silt-sized quartz, but on all the silt-sized mineral constituents within the mud fraction of each soil. Although loess is commonly dominated by quartz silt, most loess deposits contain varying amounts of quartz, plagioclase, K-feldspar, carbonate minerals, mica, and phyllosilicate clay minerals including chlorite, illite, kaolinite, and smectite (e.g., Tsoar and Pye, 1987; Muhs, 2013). The profiles in Puerto Rico and Anza Borrego were evaluated holistically in order to achieve a broader understanding of the attributes of the extant silt.

Soil particle size distribution hinges to a large degree on grain- or crystal-size within the parent material. For example, a soil profile forming on loess, or on a siltstone, phyllite, or tuff is likely silt rich due to the abundant silt available in the host. In contrast, particle size trends within granitoid-hosted weathering profiles exhibit a predominance of sand with minimal silt and clay (e.g., Hoskin and Sundeen, 1985; Dixon and Young, 1981; Wang et al., 1981; Taboada and Garcia, 1999; Wright, 2002a, 2002b), indicating that typical weathering profiles formed from coarse-grained parent material do not contain significant amounts of autochthonous silt. The weathering profiles from Anza Borrego and Puerto Rico both formed from granitoid bedrock,

enabling assessment of the efficacy of pedogenic weathering in creating silt from grains typically coarser than 0.5 mm diameter (Fig. 2; Table 3).

Loess deposits are reported to have "typical" grain size modes of 20 – 40 μm (e.g., Tsoar and Pye, 1987; Assallay et al., 1998; Anderson, 2007), although some authors report modes of up to 50 μm (e.g., Smalley and Krinsley, 1978). Modes vary owing to distance from sources and predominant wind velocities, among other factors. For example, Chinese loess exhibits a typical mode of ~25 μm (e.g., Assalley et al., 1998; Lu et al., 2001) although more proximal deposits are coarser than the distal loess (e.g., Ding et al., 2001), the Peoria loess (midwest U.S.) has an average mode of ~40 μm (Wang et al., 2006), and the Negev loess (Israel) is bimodal, with a coarse (50 – 60 μm) and fine (<10 μm) mode (Crouvi et al., 2008). Regardless, it's widely agreed that typical modes fall within the medium and coarse silt range, with very few studies reporting geologically significant loess or loess-like deposits with modes in the fine silt range (e.g., Pfeifer et al., 2020).

Medium (16 – 31 μm) and coarse (31 – 62.5 μm) silt accounts for about 20% of the Puerto Rico soil, and <3% of the Anza Borrego soil (Table 2; Fig. 9). Ultimately, neither the Anza Borrego nor Puerto Rico soils contain a significant volume of silt in the typical loess ranges discussed above; the Anza Borrego mud-fraction mode (40 μm) is relatively coarse, but constitutes a negligible amount by volume, and the Puerto Rico mud-fraction is skewed finer (5 – 18 μm) relative to the typical grain size modes observed in loess deposits (Fig. 9). For comparison, Nahon and Trompette (1982) reported quartz and feldspar fragments between 1 and 20 μm diameter in the soils from their original study when proposing that abundant silt was produced by pedogenic weathering. These diameters are smaller than the typical loess size modes (typically > 20μm; references above), but similar to the results of the tropical soil profile from Puerto Rico where the majority of the soil was clay to fine silt.

If soil weathering is an efficacious mechanism to generate the silt that forms loess, it must produce silt in modes similar to (or larger than) those of typical loess in sufficient volumes to produce a loess deposit. We can evaluate the efficiency of silt production by considering the maximum silt contents in each soil profile (e.g., Anza Borrego: 5%; Puerto Rico: 50% of total soil) assuming development of a mature, 10-m profile thickness, and assess the area needed to source a small (e.g. Negev) or large (e.g. Chinese) loess deposit. The Negev loess, a relatively small accumulation, covers ~5,500 km^2 with an average thickness of ~10 m (Crouvi et al., 2008; Ben-Israel et al., 2015). The Chinese Loess Plateau (CLP) is the largest loess accumulation on Earth today, at 640,000 km^2 with an average mean thickness of ~100 m (e.g., Zhu et al., 2018).

$$(\boldsymbol{area\ of\ soil\ km^2} \times \boldsymbol{thickness\ of\ soil\ km}) \times \%\ \boldsymbol{silt\ in\ soil} = \boldsymbol{volume\ of\ loess\ km^3} \quad \text{Eq. 2}$$

Using equation 2, in order to generate sufficient silt to form the Negev loess, a soil comparable to Puerto Rico would need to cover an area about twice the size of the loess deposit (~11,000 km^2) and a soil comparable to Anza Borrego would need to cover 20-times the area of

the loess (~110,000 km^2). To supply the likes of the Chinese Loess Plateau, a soil with silt contents similar to Puerto Rico would need to cover 20-times the area of the CLP (about 12.8 million km^2; about 2-times the land area of Russia) and a soil similar to the Anza Borrego profile would need to cover an area 200-times that of the loess plateau (128 million km^2; approximately 25% of the Earth's total land area). These are conservative estimates, since 1) we assume use of the entire silt fraction and not just the fractions of the typical loess modes and 2) a soil profile formed in a climate like the Anza Borrego Desert is unlikely to reach a thickness of 10 m. Additionally, these profiles would need to be reworked to release all of their silt, then undergo additional transport and sedimentation processes to isolate the silt-size grains, eventually to be deposited at an accumulation site. For comparison, experimental studies have shown that sand saltation as a means for silt generation for desert loess would require a primary dune field 85-times larger than the accumulated loess deposit (Adams and Soreghan, 2020).

The Anza Borrego profile contains insignificant volumes of silt. Thus, the Anza Borrego profile cannot be a major source of silt for loess generation, particularly given that geochemical results indicate that the little silt observed in this soil is likely completely derived from eolian transport. Conversely, the Puerto Rico soil contains significant silt, enough to be reworked and deposited to form a major loess deposit. However, the largest mode (18 μm) is finer than the lower end of the typical loess mode range proposed in literature (Smalley and Krinsley, 1978; Tsoar and Pye, 1987; Assallay et al., 1998; Anderson, 2007).

CONCLUSIONS

Pedogenic weathering in hot (tropical and Mediterranean) climates has been long cited as an effective means for silt generation to source loess, but this hypothesis has not been tested rigorously. The efficacy of pedogenic weathering in the production of silt is important for constraining potential climatic and environmental interpretations of loess deposits, especially in deep time. Granulometric and geochemical data from soils in tropical hot-humid (Puerto Rico) and Mediterranean hot-arid (Anza Borrego) localities contrast greatly, despite formation on similar granitoid-derived bedrock. The soil profile from Anza Borrego contains insufficient silt to form a geologically significant loess deposit, and much of the silt that is present was likely delivered via eolian processes and was not formed in-situ. The Puerto Rico soil generates autochthonous silt *in situ*, and also incorporates allochthonous silt and clay from eolian additions, but the modes tend to be finer than typical loess modes. Intense pedogenic weathering in wet and hot climates could account for portions of silt distributions throughout geologic time, and merits further study to quantitatively decipher the source of the silt, as well as the mineralogy of the silt, and the volume of silt produced within a typical weathering profile. However, in general, unrealistically large volumes of soil would be needed to generate significant loess deposits. Future studies must consider the mechanisms needed to release and

rework the grains within these weathering profiles and the geographic locations of modern and ancient loess in relation to tropically weathered soil profiles.

ACKNOWLEDGMENTS

This research was supported by the U.S. National Science Foundation (NSF) grant # 1543344, with supplemental support from the Eberly Family Chair in Geosciences at the University of Oklahoma. Thank you to N. Webb and Y.J. Joo for sample collection and assistance with data collection. Thank you to M. Reheis for discussion related to this work and her generosity in sharing her Anza Borrego Desert dust samples for additional analyses. We thank C. Floyd and C. Hodges for additional discussions regarding data and research-related questions.

FIGURES AND TABLES

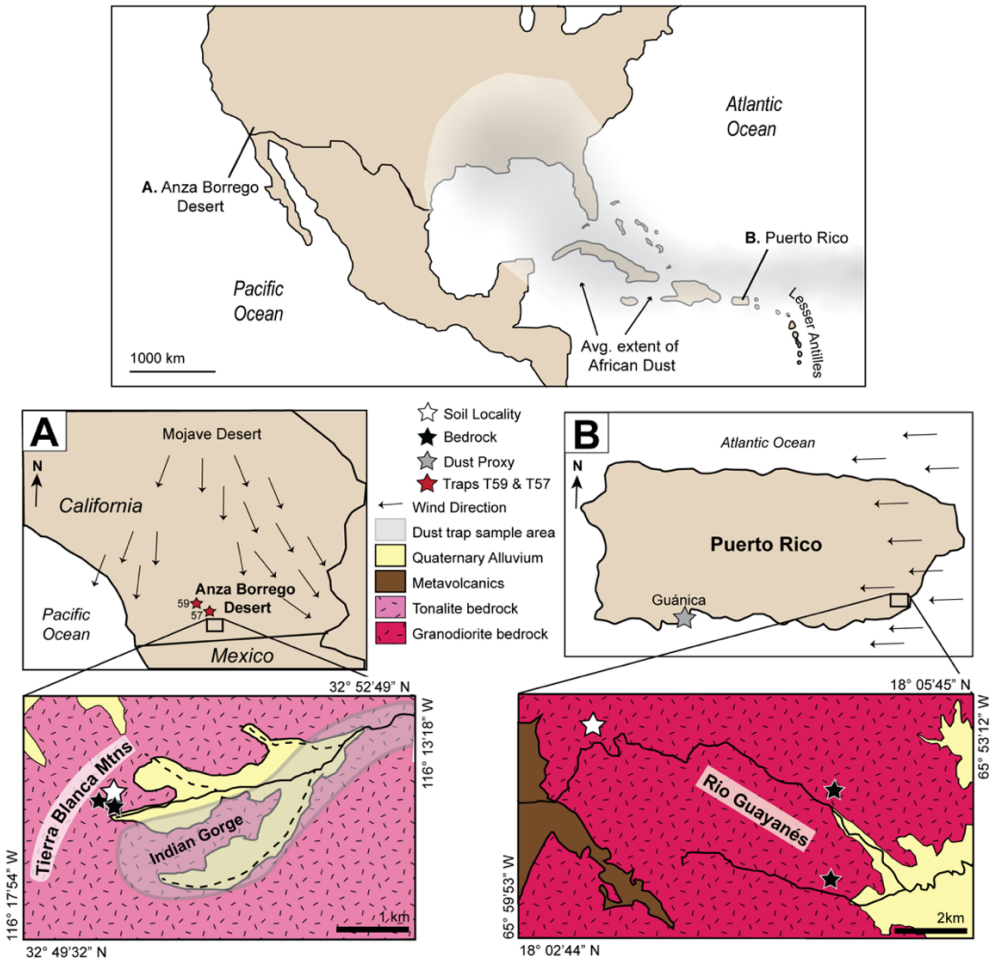


Figure 1. Regional geographic map showing both study localities within southern North America, the average extent of African dust during summer, and the location of the Lesser Antilles volcanic arc. Zoomed-in study areas are shown in A and B with representative wind directions, soil (white star), bedrock (black star), and dust trap (red star)/proxy (grey star) locations. A) Anza Borrego Desert in Southern California and relative directions for Santa Ana wind events from the north/northeast (modified from Muhs et al., 2007b). Locations for dust traps T57 and T59 are outside the zoomed-in study area (from Reheis and Kihl, 1995). The Indian Gorge ephemeral-stream system (black and black dashed lines) is covered in Quaternary alluvium while the surrounding area and Tierra Blanca Mountains expose Cretaceous tonalite bedrock. Dust trap sample area is highlighted in light gray (modified from Joo et al., 2016). B) Rio Guayanés watershed (black lines) in southeastern Puerto Rico and relative direction of Lesser Antilles Arc and African dust movement from the east, and location of the dust proxy (gray star) in southern Puerto Rico. The eastern extent of the watershed is covered by Quaternary alluvium and the majority of the study area is exposed granodiorite bedrock (modified from Joo et al., 2018).

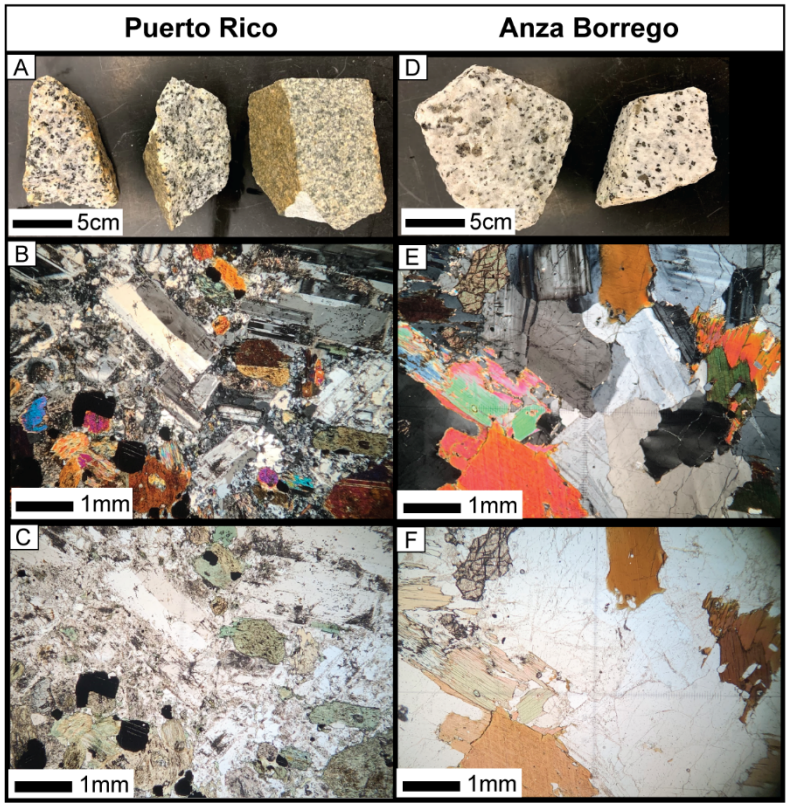


Figure 2. Hand sample photographs (A, D) and thin section photomicrographs (B, C, E, F). for the Anza Borrego and Puerto Rico bedrock samples. B) representative photomicrograph depicting typical crystal size, weathering, and mineralogy of the San Lorenzo granodiorite from Puerto Rico (XPL); C) photomicrograph from B in PPL E); representative photomicrograph

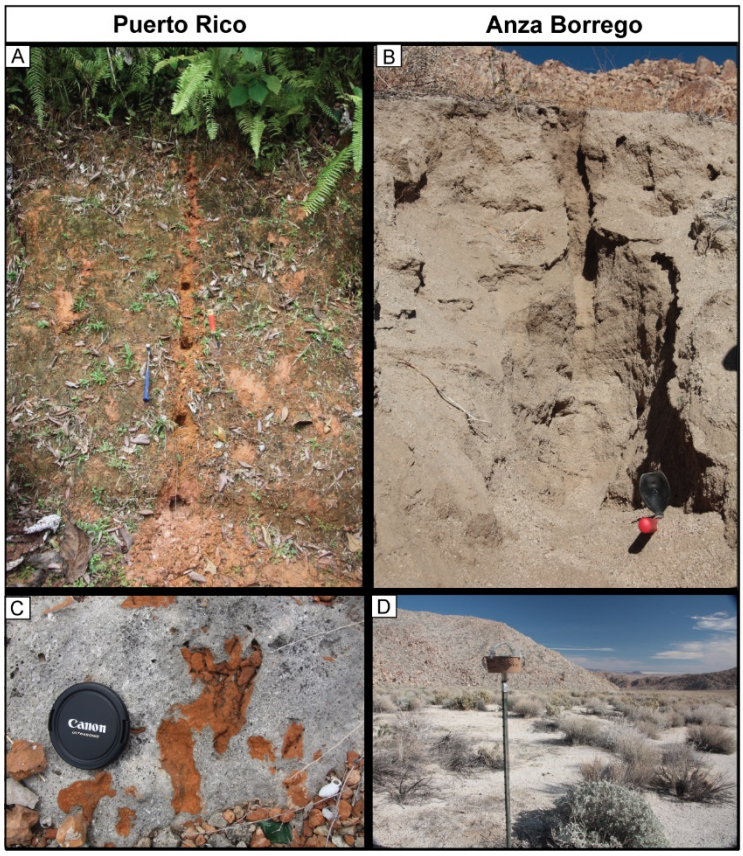


Figure 3. Field photos of soil profiles and dust samples for each study locality. A) Puerto Rico soil and sub-sample locations; hammer for scale. B) Anza Borrego soil; minimal soil integrity prevented sub-sample location preservation; trowel for scale. C) Pleistocene beach rock from the shoreline in Guánica used as a dust proxy for Puerto Rico. The orange, dust-derived sediment filled in karst-openings in the carbonate; camera lens-cap for scale. D) Example of dust trap apparatus (~ 1.75 m tall) deployed in the Anza Borrego Desert.

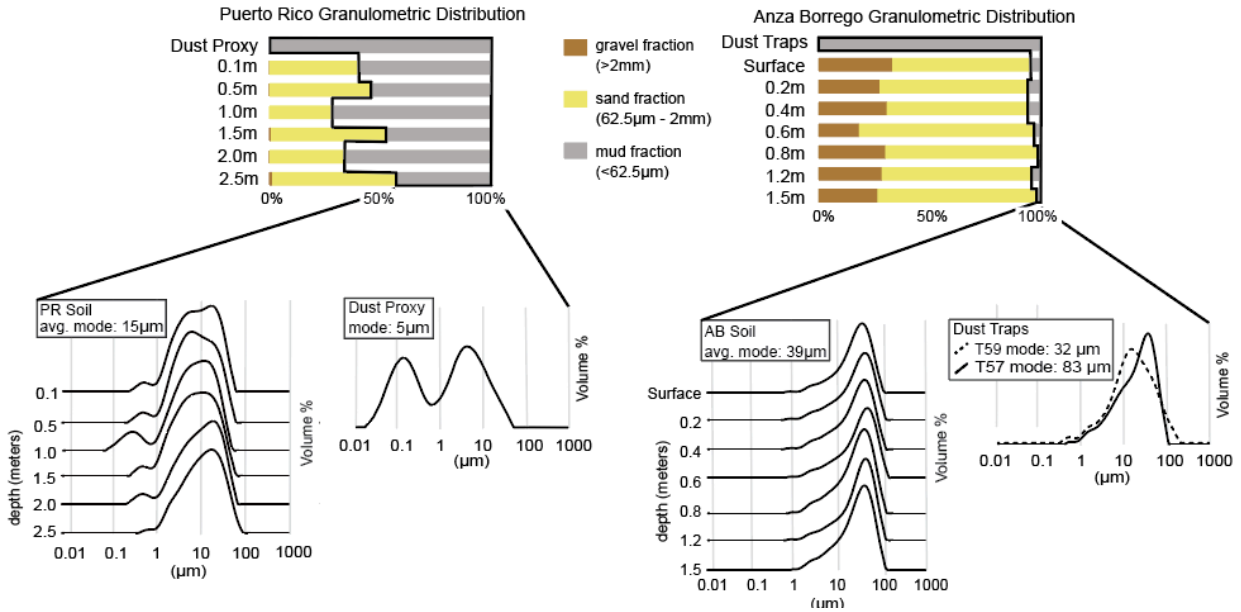


Figure 4. Puerto Rico and Anza Borrego soil and dust granulometric distributions. Gravel (brown), sand (yellow), and mud (gray) fractions are represented as bar graphs for each respective soil profile depth out of 100% total soil sample weight. LPSA histograms and average reported modes of the mud fraction are shown for soil and dust samples.

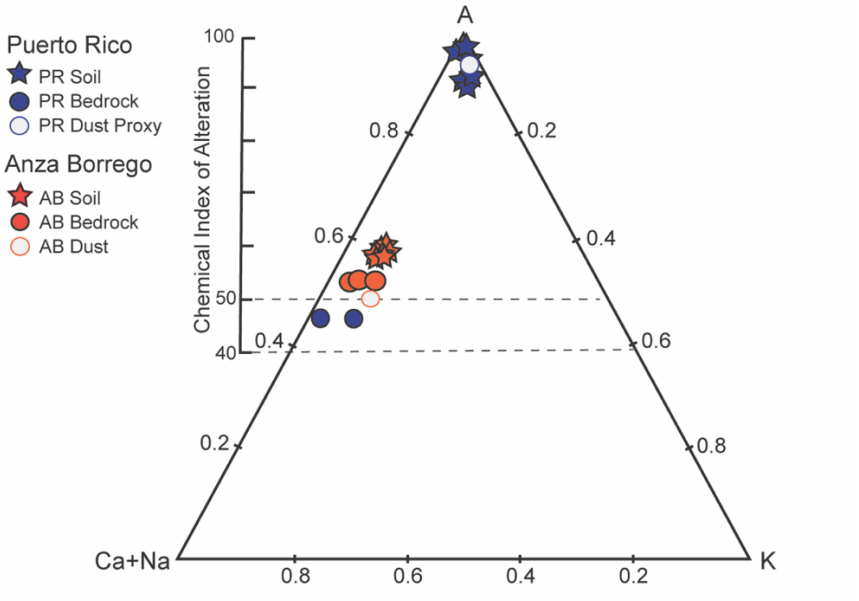


Figure 5. Ternary plot of Puerto Rico (PR) and Anza Borrego (AB) soil, bedrock, and dust sample geochemistry in A-CN-K space with Chemical Index of Alteration (CIA) values labeled on the left. See supplemental files for data references.

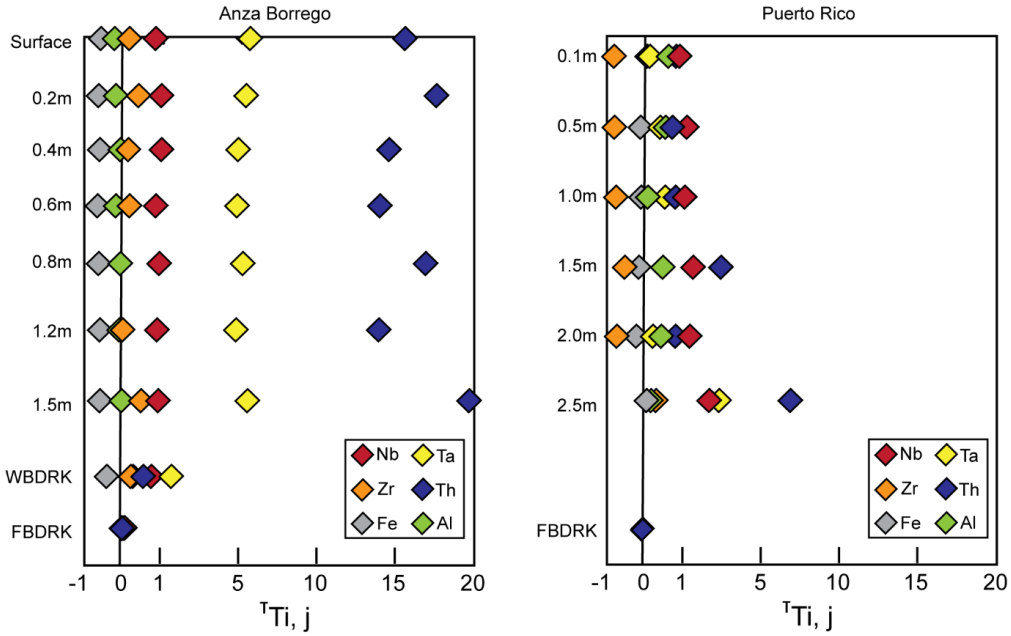


Figure 6. Tau plots showing elemental enrichment and/or depletion with depth. All elements are normalized to Ti for both Anza Borrego and Puerto Rico. Sample depth is labeled on the y-axis and depletion and enrichment values are labeled on the x-axis.

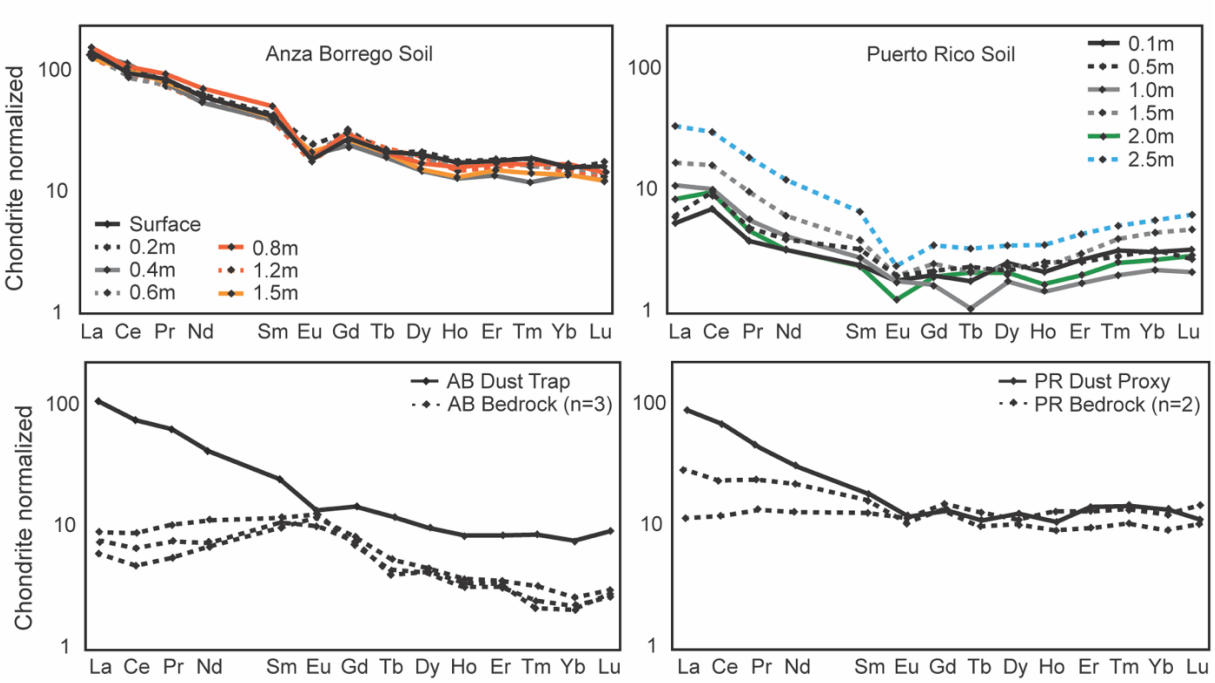


Figure 7 Chondrite-normalized REE composition and patterns of Anza Borrego (AB) and Puerto Rico (PR) soil, bedrock, dust sediment and dust proxy.

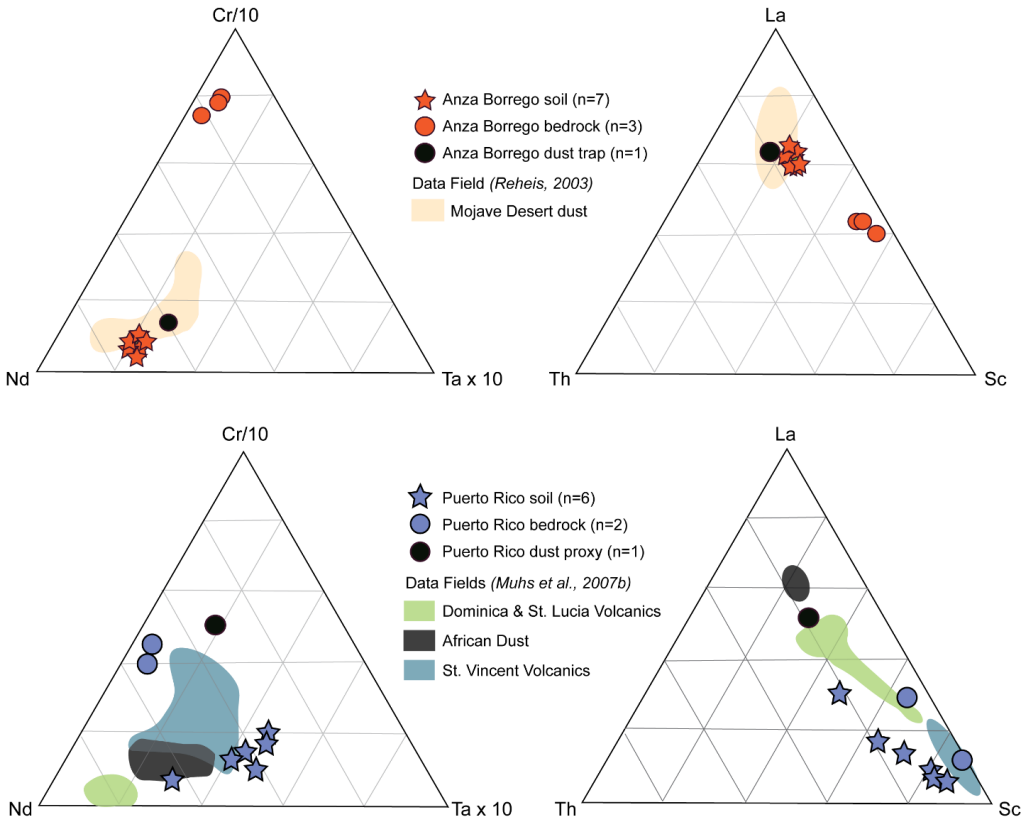


Figure 8. Cr/10 - Nd - Tax10 and La - Th - Sc ternary diagrams of Anza Borrego and Puerto Rico samples compared to previously published data of Mojave Desert dust (Reheis, 2003), Lesser Antilles volcanic system (Turner et al., 1996; Heath et al., 1998; Muhs et al., 2007b), and African dust (Muhs et al., 2007b). These diagrams show that the mud-fraction from the Anza Borrego soil is geochemically indistinguishable from dust sources and the Puerto Rico soil is largely affected by chemical weathering, making it fall between potential sources.

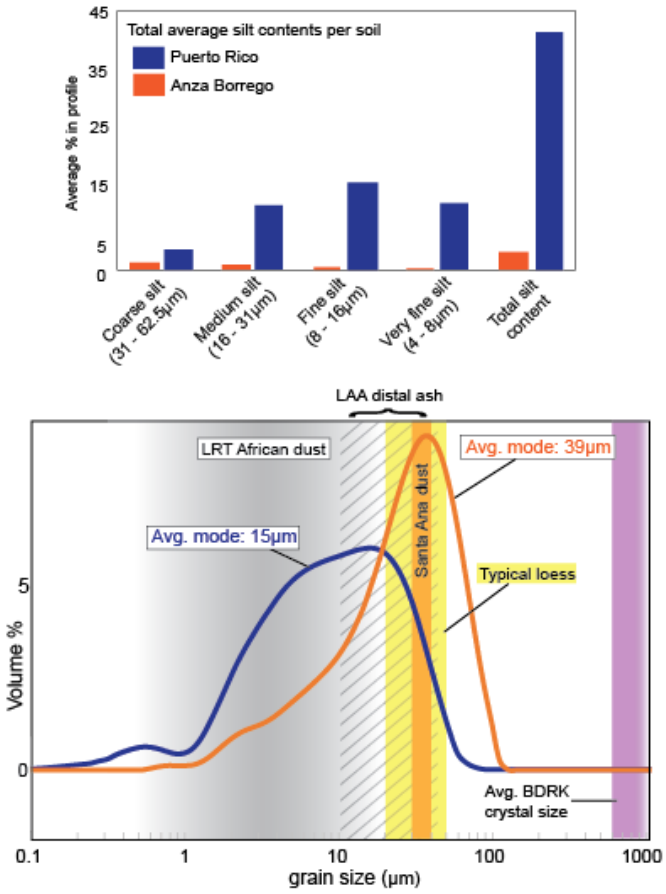


Figure 9. Average total silt contents in each soil profile (above) and grain size distributions compared to potential dust sources (below) for the two localities. The annotated histogram-plot of grain size distributions for the average soil (Puerto Rico in blue, Anza Borrego in orange) compared to typical loess modes (yellow), typical grain size collected in Santa Ana dust (orange), reported Lesser Antilles Arc (LAA, gray diagonal lines) grain sizes for distal ash, and reported LRT African dust (gray) grain sizes. The representative average bedrock crystal size from thin section observations is shown in purple. The range of typical loess grain size falls directly between the soil modes, and the bedrock-host crystals are substantially coarser than both the soil and a typical loess deposit. However, there is a strong overlap in grain size between Santa Ana dust and the Anza Borrego soil. Similarly, the Puerto Rico soil overlaps with LRT African dust and LAA distal ash.

Field Locality Variable	Anza Borrego Desert	Southeastern Puerto Rico
Climate Classification [1]	Csa - hot-dry summer Meditteranean	Af - tropical rainforest
Mean Annual Temperature [2, 3]	23˚C	27˚C
Mean Annual Precipitation [2, 3]	132 mm	1382 mm
Bedrock type [4]	tonalite and first-cycle alluvial sediment	granodiorite
Potential dust influence [5]	Greater Mojave Desert, local Anza Borrego Desert	Africa (Saharan and Sahel Deserts), Lesser Antillies volcanism

[1] *Beck et al. (2020)*

[2] *NOAA Climate Normals, 1991-2020, Station Borrego Desert Park*

[3] *NOAA Climate Normals, 1991-2020, Station Guayama 2E*

[4] *Rogers et al. (1977); Clinkenbeard and Walawender (1989); Joo et al. (2016, 2018)*

[5] *Muhs (1983); Muhs et al. (2007a, 2007b); Reheis et al. (1995, 2002)*

Table 1. Summary of climate classifications and soil formation variables for the Anza Borrego Desert and southeastern Puerto Rico field localities.

	Sample Descriptions and Depths	LPSA Results (%)									Mud distribution in total soil (%)					
		Gravel %	Sand %	Mud %	C Silt	M Silt	F Silt	VF Silt	Clay	Avg. Mode (μm)	C Silt	M Silt	F Silt	VF Silt	Clay	Total Silt %
Anza Borrego	Dust Trap T57				26.5	15.2	11.3	7.9	5.8	83.3						
	Dust Trap T59				22.9	20.3	14.1	8.7	7.9	32.1						
	Surface	33.1	62.1	4.7	32.8	30.1	18.4	7.5	7.0	35.5	1.5	1.4	0.9	0.4	0.3	**4.1**
	0.2 m	27.5	66.9	5.5	33.6	28.1	17.5	8.1	7.8	39.2	1.9	1.6	1.0	0.4	0.4	**4.8**
	0.4 m	30.7	63.7	5.6	33.0	27.4	17.6	8.6	8.3	37.7	1.9	1.5	1.0	0.5	0.5	**4.9**
	0.6 m	18.2	78.8	3.0	37.4	25.3	15.0	7.3	6.6	42.3	1.1	0.8	0.4	0.2	0.2	**2.5**
	0.8 m	30.0	68.6	1.4	32.2	27.9	18.4	8.6	7.9	36.6	0.5	0.4	0.3	0.1	0.1	**1.2**
	1.2 m	26.5	69.6	3.9	38.2	27.2	14.9	6.9	6.2	41.1	1.5	1.1	0.6	0.3	0.2	**3.4**
	1.5 m	28.4	70.4	1.2	33.8	27.1	17.6	8.3	7.1	39.5	0.4	0.3	0.2	0.1	0.1	**1.0**
Puerto Rico	Dust Proxy				3.6	7.5	13.7	14	60.9	4.98						
	0.1 m	0.2	40.0	59.9	5.9	19.4	26.1	20.8	27.8	17.5	3.5	11.6	15.6	12.5	16.6	**43.2**
	0.5 m	0.0	45.8	54.1	4.6	16.7	25.0	22.4	31.2	6.3	2.5	9.0	13.5	12.1	16.9	**37.2**
	1 m	0.0	28.4	71.6	5.7	18.1	25.7	19.6	30.9	13.9	4.1	13.0	18.4	14.0	22.1	**49.5**
	1.5 m	1.0	51.6	47.4	7.6	18.6	26.1	20.5	27.2	14.1	3.6	8.8	12.4	9.7	12.9	**34.5**
	2 m	0.0	34.1	65.9	6.2	21.1	27.8	19.5	25.4	18.1	4.1	13.9	18.3	12.8	16.7	**49.1**
	2.5 m	1.5	55.8	42.6	8.6	21.6	29.2	19.4	21.3	18.3	3.7	9.2	12.5	8.3	9.1	**33.6**

Table 2. Summary of granulometric analytical results and total silt content percentages for Anza Borrego and Puerto Rico localities. Abbreviations: Coarse (C), medium (M), fine (F), very-fine (VF). Dust samples were not analyzed for gravel, sand, mud distributions.

	Area ($\mu m^2 \times 10^3$)		Diameter (μm)*			
			2D		3D Corrected**	
	AB	**PR**	**AB**	**PR**	**AB**	**PR**
Min	18	18	152	151	158	156
Max	19,020	12,177	4,921	3,938	5,095	4,077
Mean	1,044	459	949	630	982	653
Median	480	224	782	534	809	553

*Diameters are calculated with the assumption of spherical crystals
**Conversion from Johnson (1994)

Table 3. Calculated bedrock crystal sizes from the San Lorenzo granodiorite in Puerto Rico (PR) and the La Posta tonalite in Anza Borrego (AB).

REFERENCES CITED

Adams, S. M., & Soreghan, G. S. (2020). A test of the efficacy of sand saltation for silt production: Implications for the interpretation of loess. *Geology*, *48*(11), 1105–1109. https://doi.org/10.1130/G47282.1

Anderson, S. P. (2007). Biogeochemistry of glacial landscape systems. *Annual Review of Earth and Planetary Sciences*, *35*(1), 375-399.

Anderson, S. P., Dietrich, W. E., & Brimhall Jr, G. H. (2002). Weathering profiles, mass-balance analysis, and rates of solute loss: Linkages between weathering and erosion in a small, steep catchment. *Geological Society of America Bulletin*, *114*(9), 1143-1158.

Assallay, A. M., Rogers, C. D. F., Smalley, I. J., & Jefferson, I. F. (1998). Silt: 2-62 μm, 9-4φ. *Earth Science Reviews*, *45*(1–2), 61–88. https://doi.org/10.1016/S0012-8252(98)00035-X

Babechuk, M. G., Widdowson, M., & Kamber, B. S. (2014). Quantifying chemical weathering intensity and trace element release from two contrasting basalt profiles, Deccan Traps, India. *Chemical Geology*, *363*, 56-75.

Banfield, J. F., & Eggleton, R. A. (1989). Apatite replacement and rare earth mobilization, fractionation, and fixation during weathering. *Clays and Clay Minerals*, *37*(2), 113-127.

Beck, H. E., Zimmermann, N. E., McVicar, T. R., Vergopolan, N., Berg, A., & Wood, E. F. (2018). Present and future köppen-geiger climate classification maps at 1-km resolution. *Scientific Data*, *5*, 1–12. https://doi.org/10.1038/sdata.2018.214

Ben-Israel, M., Enzel, Y., Amit, R., & Erel, Y. (2015). Provenance of the various grain-size fractions in the Negev loess and potential changes in major dust sources to the Eastern Mediterranean. *Quaternary Research*, *83*(1), 105-115.

Bern, C. R., Thompson, A., & Chadwick, O. A. (2015). Quantification of colloidal and aqueous element transfer in soils: The dual-phase mass balance model. *Geochimica et Cosmochimica Acta*, *151*, 1-18.

Bhatia, M. R., & Crook, K. A. (1986). Trace element characteristics of graywackes and tectonic setting discrimination of sedimentary basins. *Contributions to mineralogy and petrology*, *92*(2), 181-193.

Birkeland, P. W. (1984). *Soils and geomorphology*. Oxford university press.

Blisniuk, K., Oskin, M., Fletcher, K., Rockwell, T. & Sharp, W. (2012). Assessing the reliability of U-series and 10 Be dating techniques on alluvial fans in the Anza Borrego Desert, California. *Quaternary Geochronology, 13*, 26–41.

Brantley, S. L., Goldhaber, M. B., & Vala Ragnarsdottir, K. (2007). Crossing disciplines and scales to understand the critical zone. *Elements*, *3*(5), 307–314. https://doi.org/10.2113/gselements.3.5.307

Braun, J. J., Viers, J., Dupré, B., Polve, M., Ndam, J., & Muller, J. P. (1998). Solid/liquid REE fractionation in the lateritic system of Goyoum, East Cameroon: the implication for the present dynamics of the soil covers of the humid tropical regions. *Geochimica et Cosmochimica Acta*, *62*(2), 273-299.

Brimhall, G. H., & Dietrich, W. E. (1987). Constitutive mass balance relations between chemical composition, volume, density, porosity, and strain in metasomatic hydrochemical systems: results on weathering and pedogenesis. *Geochimica et Cosmochimica Acta*, *51*(3), 567-587.

Buss, H. L., Sak, P. B., Webb, S. M., & Brantley, S. L. (2008). Weathering of the Rio Blanco quartz diorite, Luquillo Mountains, Puerto Rico: Coupling oxidation, dissolution, and

fracturing. *Geochimica et Cosmochimica Acta*, *72*(18), 4488–4507. https://doi.org/10.1016/j.gca.2008.06.020

Carey, S. N., & Sigurdsson, H. (1978). Deep-sea evidence for distribution of tephra from the mixed magma eruption of the Soufrière on St. Vincent, 1902: Ash turbidites and air fall. *Geology*, *6*(5), 271–274.

Carey, S. N., & Sigurdsson, H. (1980). The Roseau ash: Deep-sea tephra deposits from a major eruption on Dominica, Lesser Antilles arc. *Journal of Volcanology and Geothermal Research*, *7*(1–2), 67–86. https://doi.org/10.1016/0377-0273(80)90020-7

Catt, J. A. (1988). Loess—its formation, transport and economic significance. In *Physical and chemical weathering in geochemical cycles* (pp. 113-142). Springer, Dordrecht.

Chadwick, O. A., Brimhall, G. H., & Hendricks, D. M. (1990). From a black to a gray box - a mass balance interpretation of pedogenesis. *Geomorphology*, *3*(3–4), 369–390. https://doi.org/10.1016/0169-555X(90)90012-F

Clinkenbeard, J. P., & Walawender, M. J. (1989). Mineralogy of the La Posta pluton: Implications for the origin of zoned plutons in the eastern Peninsular Ranges batholith, southern and Baja California. *American Mineralogist, 74*(11-12), 1258-1269.

Compton, J. S., White, R. A., & Smith, M. (2003). Rare earth element behavior in soils and salt pan sediments of a semi-arid granitic terrain in the Western Cape, South Africa. *Chemical Geology*, *201*(3-4), 239-255.

Condie, K. C., Dengate, J., & Cullers, R. L. (1995). Behavior of rare earth elements in a paleoweathering profile on granodiorite in the Front Range, Colorado, USA. *Geochimica et Cosmochimica Acta*, *59*(2), 279-294.

Crouvi, O., Amit, R., Enzel, Y., Porat, N., & Sandler, A. (2008). Sand dunes as a major proximal dust source for late Pleistocene loess in the Negev Desert, Israel. *Quaternary Research*, *70*(2), 275–282. https://doi.org/10.1016/j.yqres.2008.04.011

Cullers, R., Chaudhuri, S., Kilbane, N., & Koch, R. (1979). Rare-earths in size fractions and sedimentary rocks of Pennsylvanian-Permian age from the mid-continent of the USA. *Geochimica et Cosmochimica Acta*, *43*(8), 1285-1301.

Dixon, J. C., & Young, R. W. (1981). Character and origin of deep arenaceous weathering mantles on the Bega Batholith, southeastern Australia. *Catena*, *8*(1), 97-109.

Emery, K. O. (1960). *The sea off southern California, a modern habitat of petroleum*. John Wiley and Sons, Inc.

Enzel, Y., Amit, R., Crouvi, O., & Porat, N. (2010). Abrasion-derived sediments under intensified winds at the latest Pleistocene leading edge of the advancing Sinai-Negev erg. *Quaternary Research, 74,* 121–131, https://doi .org/10.1016/j.yqres.2010.04.002

Fletcher, K. E., Rockwell, T. K., & Sharp, W. D. (2011). Late Quaternary slip rate of the southern Elsinore fault, Southern California: Dating offset alluvial fans via 230Th/U on pedogenic carbonate. *Journal of Geophysical Research: Earth Surface, 116*(F2). doi:10.1029/2010JF001701

Frey, H., Schmidt, A., Joseph, E., & Waters, L. (2018). Hazards in the Caribbean: the History of Magma Chambers, Eruptions, Landslides, Streams, and Fumeroles in Dominica. *Short Contributions KECK Geology Consortium*, *31*, 1–12.

Ghani, A. A., Muzammil, S., Ng, T. F., Noer, E. H. I., Mohamad, T. M. Z., Nur, I., et al. (2019). Ce Anomaly in I–Type Granitic Soil from Kuantan, Peninsular Malaysia: Retention of Zircon in the Weathering Product. *Sains Malaysiana*, *48*(2), 309-315.

Glaccum, R. A., & Prospero, J. M. (1980). Saharan aerosols over the tropical North Atlantic—Mineralogy. *Marine geology, 37*(3-4), 295-321.
Hall, A. M. (1985). Cenozoic weathering covers in Buchan, Scotland and their significance. *Nature*, *315*(6018), 392-395.
Hall, A. M. (1987). Deep weathering patterns in north-east Scotland and their geomorphological significance. *Zeitschrift für Geomorphologie*, 407-422.
Heath, E., Macdonald, R., Belkin, H., Hawkesworth, C., & Sigurdsson, H. (1998). Magmagenesis at Soufriere Volcano, St Vincent, Lesser Antilles Arc. *Journal of Petrology*, *39*(10), 1721-1764.
Hoskin, C. M., & Sundeen, D. A. (1985). Grain size of granite and derived grus, Enchanted Rock pluton, Texas. *Sedimentary geology*, *42*(1-2), 25-40.
Johnson, M. R., (1994). Thin section grain size analysis revisited. *Sedimentology, 41,* 985–999. https://doi.org/10.1111/j.1365-3091.1994.tb01436.x
Joo, Y. J., Madden, M. E. E., & Soreghan, G. S. (2016). Chemical and physical weathering in a hot-arid, tectonically active alluvial system of Anza Borrego desert, California. *Sedimentology*, *63*(5), 1065–1083. https://doi.org/10.1111/sed.12249
Joo, Y. J., Madden, M. E. E. E., & Soreghan, G. S. (2018). Anomalously low chemical weathering in fluvial sediment of a tropical watershed (Puerto Rico). *Geology*, *46*(8), 691–694. https://doi.org/10.1130/G40315.1
Kuenen, P.H. (1960). Experimental abrasion 4: Eolian action*: The Journal of Geology, 68,* 427–449.
Kurtz, A. C., Derry, L. A., & Chadwick, O. A. (2001). Accretion of Asian dust to Hawaiian soils: isotopic, elemental, and mineral mass balances. *Geochimica et Cosmochimica acta*, *65*(12), 1971-1983.
Lau, K. M., & Kim, K. M. (2007). Cooling of the Atlantic by Saharan dust. *Geophysical Research Letters*, *34*(23), 8–11. https://doi.org/10.1029/2007GL031538
Le Friant, A., Lock, E. J., Hart, M. B., Boudon, G., Sparks, R. S. J., Leng, M. J., et al. (2008). Late Pleistocene tephrochronology of marine sediments adjacent to Montserrat, Lesser Antilles volcanic arc. *Journal of the Geological Society*, *165*(1), 279–289. https://doi.org/10.1144/0016-76492007-019
Li, Y., Shi, W., Aydin, A., Beroya-Eitner, M. A., & Gao, G. (2020). Loess genesis and worldwide distribution. *Earth-Science Reviews*, *201*, 102947. https://doi.org/10.1016/j.earscirev.2019.102947
Li-Jones, X., & Prospero, J. M. (1998). Variations in the size distribution of non-sea-salt sulfate aerosol in the marine boundary layer at Barbados: Impact of African dust. *Journal of Geophysical Research: Atmospheres*, *103*(D13), 16073-16084.
Lu, H., Vandenberghe, J., & An, Z. (2001). Aeolian origin and palaeoclimatic implications of the 'red clay' (north China) as evidenced by grain-size distribution. *Journal of Quaternary Science: Published for the Quaternary Research Association*, *16*(1), 89-97.
Lundström, U. S., Van Breemen, N., & Bain, D. (2000). The podzolization process. A review. *Geoderma*, *94*(2-4), 91-107.
McClintock, M. A., Brocard, G., Willenbring, J., Tamayo, C., Porder, S., & Pett-Ridge, J. C. (2015). Spatial variability of African dust in soils in a montane tropical landscape in Puerto Rico. *Chemical Geology*, *412*, 69-81.

McClintock, M. A., McDowell, W. H., González, G., Schulz, M., & Pett-Ridge, J. C. (2019). African dust deposition in Puerto Rico: Analysis of a 20-year rainfall chemistry record and comparison with models. *Atmospheric Environment*, *216*, 116907.

McKeague, J. A., De Connick, F., & Franzmeier, D. P. (1983). Spodsols. In: Wilding, L. P., Smeck, Ž. N. E., Hall, G. F. (Eds.), *Pedogenesis and Soil Taxonomy*. (217–252). Elsevier, New York.

McLennan, S. M. (1989). Rare earth elements in sedimentary rocks: Influence of provenance and sedimentary processes. *Mineralogical Society of America Reviews in Mineralogy, 21*, 169-200.

Moss, A. J. (1966). Origin, shaping and significance of quartz sand grains. *Journal of the Geological Society of Australia*, *13*(1), https://doi.org/10.1080/00167616608728607

Moss, A. J., & Green, P. (1975). Sand and silt grains: Predetermination of their formation and properties by microfractures in quartz. *Journal of the Geological Society of Australia*, *22*(4), 485–495. https://doi.org/10.1080/00167617508728913

Muhs, D. R. (1983). Airborne dust fall on the California Channel Islands, U.S.A (Mojave Desert). *Journal of Arid Environments*, *6*(3), 223–238. https://doi.org/10.1016/s0140-1963(18)31507-6

Muhs, D. R. (2013). The geologic records of dust in the Quaternary. *Aeolian Research*, *9*, 3–48.

Muhs, D. R., & Bettis, E. A. (2003). Quaternary loess-paleosol sequences as examples of climate-driven sedimentary extremes. *Special Paper of the Geological Society of America*, *370*(303), 53–74. https://doi.org/10.1130/0-8137-2370-1.53

Muhs, D. R., & Budahn, J. R. (2009). Geochemical evidence for African dust and volcanic ash inputs to terra rossa soils on carbonate reef terraces, northern Jamaica, West Indies. *Quaternary International*, *196*(1–2), 13–35. https://doi.org/10.1016/j.quaint.2007.10.026

Muhs, D. R., Budahn, J., Reheis, M., Beann, J., Skipp, G., & Fisher, E. (2007a). Airborne dust transport to the eastern Pacific Ocean off southern California: Evidence from San Clemente Island. *Journal of Geophysical Research Atmospheres*, *112*(13), 1–17. https://doi.org/10.1029/2006JD007577

Muhs, D. R., Budahn, J. R., Prospero, J. M., & Carey, S. N. (2007b). Geochemical evidence for African dust inputs to soils of western Atlantic islands: Barbados, the Bahamas, and Florida. *Journal of Geophysical Research: Earth Surface*, *112*(2), 1–26. https://doi.org/10.1029/2005JF000445

Muhs, D. R., Budahn, J. R., Johnson, D. L., Reheis, M., Beann, J., Skipp, G., et al. (2008). Geochemical evidence for airborne dust additions to soils in Channel Islands National Park, California. *Bulletin of the Geological Society of America*, *120*(1–2), 106–126. https://doi.org/10.1130/B26218.1

Muhs, D. R., Cattle, S. R., Crouvi, O., Rousseau, D. D., Sun, J., & Zárate, M. A. (2014). Loess records. In *Mineral Dust* (411-441). Springer, Dordrecht.

Muhs, D. R., Meco, J., Budahn, J. R., Skipp, G. L., Simmons, K. R., Baddock, M. C., et al. (2021). Long-term African dust delivery to the eastern Atlantic Ocean from the Sahara and Sahel regions: Evidence from Quaternary paleosols on the Canary Islands, Spain. *Quaternary Science Reviews*, *265*, 107024. https://doi.org/10.1016/j.quascirev.2021.107024

Nahon, D., & Trompette, R. (1982). Origin of siltstones: glacial grinding versus weathering. *Sedimentology*, *29*(1), 25–35. https://doi.org/10.1111/j.1365-3091.1982.tb01706.x

Nakai, S. I., Halliday, A. N., & Rea, D. K. (1993). Provenance of dust in the Pacific Ocean. *Earth and Planetary Science Letters*, *119*(1-2), 143-157.

Nesbitt, H. W. (1979). Mobility and fractionation of rare earth elements during weathering of a granodiorite. *Nature*, *279*(5710), 206-210.
Nesbitt, H., & Young, G. M. (1982). Early Proterozoic climates and plate motions inferred from major element chemistry of lutites. *Nature*, *299*(5885), 715-717.
Nesbitt, H. W., & Young, G. M. (1984). Prediction of some weathering trends of plutonic and volcanic rocks based on thermodynamic and kinetic considerations. *Geochimica et Cosmochimica Acta*, *48*(7), 1523–1534. https://doi.org/10.1016/0016-7037(84)90408-3
Nesbitt, H. W., & Young, G. M. (1989). Formation and diagenesis of weathering profiles. *The Journal of Geology*, *97*(2), 129-147.
NOAA Climate Normals. (2021). Latest 30 year period 1991-2020, National Centers for Environmental Information. U.S. Climate Normals Quick Access Station Borrego Desert Park. NOAA NCEI U.S. Climate Normals Quick Access
NOAA Climate Normals. (2021). Latest 30 year period 1991-2020, National Centers for Environmental Information. U.S. Climate Normals Quick Access Station Guayama 2E. NOAA NCEI U.S. Climate Normals Quick Access
Olivarez, A. M., Owen, R. M., & Rea, D. K. (1991). Geochemistry of eolian dust in Pacific pelagic sediments: Implications for paleoclimatic interpretations. *Geochimica et Cosmochimica Acta*, *55*(8), 2147-2158.
Pfeifer, L. S., Soreghan, G. S., Pochat, S., & Van Den Driessche, J. (2021). Loess in eastern equatorial Pangea archives a dusty atmosphere and possible upland glaciation. *GSA Bulletin*, *133*(1-2), 379-392.
Prospero, J. M., Bonatti, E., Schubert, C., & Carlson, T. N. (1970). Dust in the Caribbean atmosphere traced to an African dust storm. *Earth and Planetary Science Letters*, *9*(3), 287–293. https://doi.org/10.1016/0012-821X(70)90039-7
Prospero, J. M., & Lamb, P. J. (2003). African Droughts and Dust Transport to the Caribbean: Climate Change Implications. *Science*, *302*(5647), 1024–1027. https://doi.org/10.1126/science.1089915
Pye, K. (1995). The nature, origin and accumulation of loess. *Quaternary Science Reviews*, *14*(7–8), 653–667. https://doi.org/10.1016/0277-3791(95)00047-X
Pye, K., & Sperling, C. H. B. (1983). Experimental investigation of silt formation by static breakage processes: the effect of temperature, moisture and salt on quartz dune sand and granitic regolith. *Sedimentology*, *30*(1), 49–62. https://doi.org/10.1111/j.1365-3091.1983.tb00649.x
Pett-Ridge, J. C. (2009). Contributions of dust to phosphorus cycling in tropical forests of the Luquillo Mountains, Puerto Rico. *Biogeochemistry*, *94*(1), 63–80. https://doi.org/10.1007/s10533-009-9308-x
Pett-Ridge, J. C., Derry, L. A., & Kurtz, A. C. (2009). Sr isotopes as a tracer of weathering processes and dust inputs in a tropical granitoid watershed, Luquillo Mountains, Puerto Rico. *Geochimica et Cosmochimica Acta*, *73*(1), 25–43. https://doi.org/10.1016/j.gca.2008.09.032
Reheis, M.C. (2003). Dust deposition in Nevada, California, and Utah, 1984–2002. *US Geological Survey Open-File Report 03-138.*
Reheis, M. C., & Kihl, R. (1995). Dust deposition in southern Nevada and California, USA 1984-1989: relations to climate, source area and source lithology. *Journal of Geophysical Research, 100*, 8893–8918. DOI: 10.1029/94JD03245

Reheis, M. C., Goodmacher, J. C., Hardem, J. W., McFadden, L. D., Rockwell, T. K., Shroba, R. R., et al. (1995). Quaternary soils and dust deposition in southern Nevada and California. *Geological Society of America Bulletin*, *107*(9), 1003–1022. https://doi.org/10.1130/0016-7606(1995)107<1003:QSADDI>2.3.CO;2

Reheis, M.C., Budahn, J.R., & Lamothe, P.J. (2002). Geochemical evidence for diversity of dust sources in the southwestern United States. *Geochimica et Cosmochimica Acta, 66,* 1569–1587. doi: 10.1016/S0016- 7037(01)00864-X

Reheis, M. C., Budahn, J. R., Lamothe, P. J., & Reynolds, R. L. (2009). Compositions of modern dust and surface sediments in the Desert Southwest, United States. *Journal of Geophysical Research: Earth Surface*, *114*(1), 1–20. https://doi.org/10.1029/2008JF001009

Reheis, M. C., Bright, J., Lund, S. P., Miller, D. M., Skipp, G., & Fleck, R. J. (2012). A half-million-year record of paleoclimate from the Lake Manix Core, Mojave Desert, California. *Palaeogeography, Palaeoclimatology, Palaeoecology, 365*, 11-37.

Reynolds, R. L., Reheis, M., Yount, J., & Lamothe, P. (2006). Composition of aeolian dust in natural traps on isolated surfaces of the central Mojave Desert - Insights to mixing, sources, and nutrient inputs. *Journal of Arid Environments*, *66*(1), 42–61. https://doi.org/10.1016/j.jaridenv.2005.06.031

Rogers, C. L., Cram, C. M., Pease, M. H., & Tischler, M. S. (1977). *Geologic Map of the Yabucoa and Punta Tuna Quadrangles, Puerto Rico* (No. 77-651). US Geological Survey.

Smalley, I. (1995). Making the material: The formation of silt sized primary mineral particles for loess deposits. *Quaternary Science Reviews*, *14*(7–8), 645–651. https://doi.org/10.1016/0277-3791(95)00046-1

Smalley, I. J., & Vita-Finzi, C. (1968). The formation of fine particles in sandy deserts and the nature of "desert' loess. *Journal of Sedimentary Research, 38*(3), 766-774.

Smalley, I. J., & Krinsley, D. H. (1978). Loess deposits associated with deserts. *Catena, 5*(1), 53–66. https://doi.org/10.1016/S0341-8162(78)80006-X.

Smith, B. J., Wright, J. S., & Whalley, W. B. (2002). Sources of non-glacial, loess-size quartz silt and the origins of "desert loess". *Earth-Science Reviews, 59*(1-4), 1-26.

Soreghan, L. S., Soreghan, M. J., & Hamilton, M. A. (2008). Origin and significance of loess in late Paleozoic western Pangaea: A record of tropical cold*? Palaeogeography, Palaeoclimatology, Palaeoecology, 268*(3-4), 234–259. https://doi.org/10.1016/j.palaeo.2008.03.050

Soreghan, G. S., Joo, Y. J., Elwood Madden, M. E., & Van Deventer, S. C. (2016). Silt production as a function of climate and lithology under simulated comminution. *Quaternary International*, *399*, 218–227. https://doi.org/10.1016/j.quaint.2015.05.010

Sun, J. (2002). Provenance of loess material and formation of loess deposits on the Chinese Loess Plateau. *Earth and planetary science letters*, *203*(3-4), 845-859.

Swet, N., Elperin, T., Kok, J. F., Martin, R. L., Yizhaq, H., & Katra, I. (2019). Can active sands generate dust particles by wind-induced processes?. *Earth and Planetary Science Letters, 506,* 371-380.

Taboada, T., & Garcia, C. (1999). Smectite formation produced by weathering in a coarse granite saprolite in Galicia (NW Spain). *Catena*, *35*(2-4), 281-290.

Taylor, S. R., & McLennan, S. M. (1985). *The continental crust: its composition and evolution.* Blackwell Scientific.

Taylor, S. R., & Mclennan, S. M. (1995). The geochemical evolution of the continental crust. *Reviews in Mineralogy and Geochemistry*, *33*(2), 241–265.

Teruggi, M. E. (1957). The nature and origin of Argentine loess. *Journal of Sedimentary Research*, *27*(3), 322-332.
Tsoar, H., & Pye, K. (1987). Dust transport and the question of desert loess formation. *Sedimentology, 34*(1), 139–153. https://doi.org/10.1111/j.1365-3091.1987. tb00566.x.
Turner, S., Hawkesworth, C., Van Calsteren, P., Heath, E., Macdonald, R., & Black, S. (1996). U-series isotopes and destructive plate margin magma genesis in the Lesser Antilles. *Earth and Planetary Science Letters*, *142*(1-2), 191-207.
Wang, C., Ross, G. J., & Rees, H. W. (1981). Characteristics of residual and colluvial soils developed on granite and of the associated pre-Wisconsin landforms in north-central New Brunswick. *Canadian Journal of Earth Sciences*, *18*(3), 487-494.
Wang, H., Mason, J. A., & Balsam, W. L. (2006). The importance of both geological and pedological processes in control of grain size and sedimentation rates in Peoria Loess. *Geoderma*, *136*(1-2), 388-400.
Weigelt, P., Steinbauer, M. J., Cabral, J. S., & Kreft, H. (2016). Late quaternary climate change shapes island biodiversity. *Nature*, *532*(7597), 99–102. https://doi.org/10.1038/nature17443
Wentworth, C. K. (1922). A scale of grade and class terms for clastic sediments. *The journal of geology, 30*(5), 377-392.
White, A. F. (2002). Determining mineral weathering rates based on solid and solute weathering gradients and velocities: Application to biotite weathering in saprolites. *Chemical Geology*, *190*(1–4), 69–89. https://doi.org/10.1016/S0009-2541(02)00111-0
White, A.F., Blum, A.E., Schultz, M.S., Vivit, D.V., Stonestrom, D.A., Larsen, M., Murphy, S.F., and Eberl, D. (1998,). Chemical weathering in a tropical watershed, Luquillo Mountains, Puerto Rico: I. Long-term versus short-term weathering fluxes: *Geochimica et Cosmochimica*, *62*, 209–226. https:// doi .org /10 .1016 /S0016 -7037 (97)00335 -9.
White, A. F., & Buss, H. L. (2014). 7.4-Natural weathering rates of silicate minerals. *Treatise on Geochemistry, Second Edition. Elsevier, Oxford*, 115-155.
Wright, J. (2001). Making loess-sized quartz silt: Data from laboratory simulations and implications for sediment transport pathways and the formation of "desert" loess deposits associated with the Sahara. *Quaternary International*, *76–77*, 7–19. https://doi.org/10.1016/S1040-6182(00)00085-9
Wright, J. S. (2002a). Particle size characteristics and quartz microfracture patterns in I-and S-type granitoid weathering profiles: some preliminary observations from Eastern Australia. *Transactions of the Japanese Geomorphological Union*, *23*, 309-334.
Wright, J. S. (2002b). Granitoid weathering profiles as a source of loessic silt. *Transactions of the Japanese Geomorphological Union*, *23*(5), 769-793.
Wright, J. S. (2007). An overview of the role of weathering in the production of quartz silt. *Sedimentary Geology*, *202*(3), 337–351. https://doi.org/10.1016/j.sedgeo.2007.03.024
Wright, J., & Smith, B. (1993). Fluvial Comminution and the Production of Loess-Sized Quartz Silt: A Simulation Study. *Geografiska Annaler. Series A, Physical Geography*, *75*(1/2), 25–34.
Wright, J., Smith, B., & Whalley, B. (1998). Mechanisms of loess-sized quartz silt production and their relative effectiveness: Laboratory simulations. *Geomorphology*, *23*(1), 15–34. https://doi.org/10.1016/S0169-555X(97)00084-6
Yaalon, D. H., & Ganor, E. (1973). The influence of dust on soils during the Quaternary. *Soil Science*, *116*(3), 146-155.

Zárate, M., & Blasi, A. (1993). Late Pleistocene-Holocene eolian deposits of the southern Buenos Aires Province, Argentina: a preliminary model. *Quaternary International*, *17*, 15-20.

Zhu, Y., Jia, X., & Shao, M. (2018). Loess Thickness Variations Across the Loess Plateau of China. *Surveys in Geophysics*, *39*(4), 715–727. https://doi.org/10.1007/s10712-018-9462-6

CHAPTER II

MAXIMUM DEPOSITIONAL AGES AND PROVENANCE ANALYSIS OF THE NEOPROTEROZOIC MANYOVU REDBEDS, TANZANIA: IMPLICATIONS FOR PAN AFRICAN OROGENESIS

MAXIMUM DEPOSITIONAL AGES AND PROVENANCE ANALYSIS OF THE NEOPROTEROZOIC MANYOVU REDBEDS, TANZANIA: IMPLICATIONS FOR PAN AFRICAN OROGENESIS

ABSTRACT

The Manyovu redbeds are an up to ~400–600 m succession of fine-grained siliciclastic strata in northwestern Tanzania and are part of the Neoproterozoic Bukoban Supergroup. Previous authors estimated the age of the Manyovu redbeds to be Neoproterozoic or older based on K-Ar dates of underlying volcanic rocks (~800 Ma); however, no other age-constraints exist for these Neoproterozoic units. U-Pb detrital zircon results from six stratigraphic intervals, including both sandstone and siltstone samples, of the Manyovu units indicate maximum depositional ages as young as 613.6 ± 1.2 Ma, almost 200 Ma younger than the underlying volcanics, with major detrital contributions from Pan-African Orogenesis, indicating these units are syn-tectonic accumulations associated with the assembly of Greater Gondwana/Pannotia. Detrital zircon spectra and modal compositions reveal that the sediments that formed these strata were sourced from a range of terranes, including continental blocks (i.e., Tanzania Craton), magmatic arcs (i.e., Mozambique Belt and Arabian-Nubian Shield), and recycled orogens (e.g., Ubendian-Usagaran Belts). Together, these data indicate that the Manyovu redbeds may have formed following the Marinoan Snowball Earth event (~635Ma) and record the initiation of collision along the Mozambique Belt during the formation of Greater Gondwana and Pan-African orogenesis.

INTRODUCTION

The Neoproterozoic (1000 – 541 Ma) was an extraordinary time in Earth history, well known as an era of supercontinent deconstruction and assembly (e.g., Frimmel et al., 2002; Stern et al., 2008), extreme climatic shifts and the enigmatic Snowball Earth events (Hoffman et al., 1998; Hoffman and Schrag, 2002; Hoffman et al., 2017), as well as the lead-up to the evolutionary explosion of the Phanerozoic biosphere (Knoll, 2003; Tziperman et al., 2011; Kennedy, 2013). Despite its seemingly otherworldly extremes, disentangling the interconnections among climatic, tectonic, and biospheric events during this time shed light on the workings of the Earth System writ large. But we need to access the record, and only ~16% of Earth's continental area is known to be Neoproterozoic in age (Goodwin, 1991; Stern et al., 2008). Additionally, sedimentary successions provide critical data for deciphering Earth's paleoclimatic and tectonic histories, but many Neoproterozoic exposures are either volcanically sourced, or metamorphosed. A global dearth of well-dated sedimentary successions for the Neoproterozoic impedes efforts to develop a better understanding of this intriguing interval.

Africa has the largest area of Neoproterozoic rock exposed at the surface (50% of the continent; Goodwin, 1991; Stern et al., 2008), including volcanic and sedimentary successions within paleo-orogenic belts and associated basins. Many of these rock units have undergone

relatively recent uplift and exposure associated with the East African Rift (EAR) during the Cenozoic. The EAR system began in the Early Miocene (22 – 25 Ma; e.g., Roberts et al., 2012; Macgregor, 2015) and comprises half-graben basins with normal-fault blocks exposing Neoproterozoic volcanic and sedimentary rocks throughout eastern Africa, some of which remain minimally metamorphosed. Lake Tanganyika is an EAR lake that borders western Tanzania and eastern Democratic Republic of the Congo (DRC) in East Africa (Fig. 1A), and exposures of the Bukoban Supergroup occur along the lake's eastern margin (Fig. 1B, Fig. 2).

The Neoproterozoic Manyovu redbeds (Fig. 2, 3), part of the Bukoban Supergroup, crop out in one of the uplifted fault blocks and have been described previously as a monotonous succession of red, micaceous, fine-grained sandstone, shale, and conglomerate, and interpreted as shallow marine deposits (Halligan, 1962; Piper, 1972). However, these units lack accurate age constraints, with previous dating reliant primarily on poorly resolved K-Ar dates of underlying volcanic rocks of the Gagwe Amygdaloidal Lavas (~800 – 830 Ma, Fig. 3; Cahen and Snelling, 1974; Deblond et al., 2001) and paleomagnetic studies of the Bukoban Supergroup (Piper, 1972), but no previous studies focus on these strata.

Here we present new U-Pb detrital zircon ages, sandstone modal compositions, and grain size analyses from the Manyovu redbeds along northeastern Lake Tanganyika. We report the first maximum depositional ages for the Manyovu redbeds and utilize U-Pb detrital zircon ages from both sandstone and siltstone units to explore temporal provenance shifts. This study provides a means for broadening our understanding of the Neoproterozoic world by making initial connections between the climate and tectonics of this time period.

GEOLOGIC BACKGROUND

Paleogeography and Paleoclimate

The Bukoban System (here referred to as deposited in the Bukoban Basin) is part of a series of Neoproterozoic basins that evolved during both the break-up of the supercontinent Rodinia (~830 Ma) as continental rift-related and extensional basins, and during the assembly of Pannotia (Greater Gondwana; ~630 Ma) as collision-related peripheral foreland basins (e.g., Frimmel et al., 2002; Stern et al., 2008). These basins commonly occur along the margins of Archean cratons throughout central and southern Africa as well as the eastern coast of South America (Frimmel, 2000; Hanson, 2003). Most basins contain both sedimentary and volcanic deposits, which record episodes of active uplift, subsidence, and volcanism.

During Cryogenian – Ediacaran time, the major tectonic events are lumped into the Pan-African Orogens. Two main types of orogenic belts make up the Pan-African system as identified by Kröner and Stern (2005). The first is juvenile (mantle-derived) Neoproterozoic supracrustal and magmatic assemblages including the Arabian-Nubian Shield, Lufilian Arc, West Congo Belt, and most orogenic belts of west Africa from this time. These belts likely represent the closing of the newly created oceanic margins formed after the break-up of Rodinia

(e.g., the Mozambique Ocean). The second type of orogenic belt is more enigmatic and contains high-grade metamorphic complexes of unspecified origin(s), but mostly older Proterozoic and Archean continental crust. Examples include the Mozambique Belt in East Africa and Madagascar, as well as the Zambezi Belt in southeastern Africa.

During the break-up of Rodinia (beginning of the Cryogenian), much of the global volcanism consisted of continental flood basalts and subaerial rift-related igneous activity. Most new arcs were subaqueous during this time. In contrast, arc-related volcanism predominated toward the end of the Cryogenian, especially in the Arabian-Nubian Shield and East African Orogen (e.g., Stern et al., 2006, 2008). U-Pb dates from early Paleozoic strata within East Africa show a predominance of ages between 600 – 650 Ma (Avigad et al. 2003; Kolodner et al. 2006), supporting likely active volcanism across the Cryogenian – Ediacaran boundary in this area. Large amounts of arc- and collision-related (e.g., newly formed subduction zones) volcanism accompanied the assembly of Pannotia around the end of Cryogenian, commonly on continental crust, promoting explosive volcanic eruptions (Stern et al., 2008).

Climate shifts and extremes accompanied both intervals of major continent reconstruction. The Tonian coincided with multiple glacial events including the Bitter Springs (~800 – 815 Ma; still poorly constrained and debated, e.g., Maloof et al., 2006; Stern et al., 2008), Mahd (780 – 800 Ma; Stern et al., 2011; Swanson-Hysell et al., 2015), and Kaigas (~750 Ma; Hoffmann et al., 2006) events. The Bitter Springs is hypothesized as a glacial event owing solely to a seemingly global negative carbon isotope excursion (e.g., Halverson et al., 2010), whereas dated tillites support a glacial interpretation for both the Mahd (Stern et al., 2011) and Kaigas event deposits (~740 Ma; Frimmel et al., 1996); however, neither episode has been defined globally. The oldest hypothesized Snowball Earth event is the Sturtian (~710 Ma, e.g., Hoffman and Li, 2009), but glacial deposits thought to record the Sturtian Snowball Earth exhibit ages ranging throughout the Cryogenian from 645 – 724 Ma (e.g., Lund et al. 2003; Kendall et al. 2006; Hoffman and Li, 2009; Rooney et al., 2015). Accordingly, the nature of the Sturtian as either a single or multiple glacial event(s) remains debated (e.g., Hoffman and Li, 2009). Finally, marking the end of the Cryogenian and beginning of the Ediacaran, the Marinoan event is the oldest and only documented Snowball Earth event that has withstood multiple tests over the years. Marinoan glacial deposits are the most widespread, with global correlations of syn-glacial cap carbonates and well-constrained ages that overlap within error of ~635 Ma (e.g., Schmidt and Williams, 1995; Kennedy et al., 1998; Hoffman et al., 1998; Hoffmann et al., 2004), making this extreme climatic event coeval with the apex of Greater Gondwana (Pannotia) assembly.

Uha Group Stratigraphy

Early Proterozoic metamorphic rocks, and the Neoproterozoic Bukoban Supergroup (Fig. 1B, 2) form the Tanzanian border of Lake Tanganyika. The Bukoban Supergroup spans much of the Neoproterozoic and comprises volcanics as well as carbonate and siliciclastic deposits, some affected by low-grade metamorphism. These units likely accumulated in a subsiding basin

created by extension during Rodinia rifting, but the region remained a topographic low into the Pan-African orogenic events of Greater Gondwanan amalgamation. The Uha Group (estimated to span the Cryogenian – Ediacaran) consists of the (oldest to youngest) Gagwe Amygdaloidal Lavas, Ilagala Dolomitic Limestone, and the Manyovu redbeds, with disconformities separating each unit (Fig. 2; Halligan, 1962). The Gagwe Amygdaloidal Lavas form 600 m of tholeiitic flood basalts encompassing an indistinguishable number of eruptions (e.g., Halligan, 1962; Piper, 1972), dated to 822 ± 30 Ma using (recalculated) K-Ar methods (Briden et al., 1971; Deblond et al., 2001). Accordingly, these likely record magmatism associated with the break-up of Rodinia. The Illagala Dolomitic Limestones comprise ~150 m of dolomitic limestone with chert, a basal conglomerate, and calcareous sand sheets (Halligan, 1962).

Minimal previous work exists on the Manyovu redbeds. Halligan (1959) and Henderson (1961) studied the southern-most extent of the Manyovu exposures along the Karurumpeta Ridge south of Kigoma, Tanzania. Halligan (1962) provided the most detailed description of the Manyovu, noting that the best exposures occur in both the south (Karurumpeta Ridge) and north of Kigoma into Burundi. Halligan (1962) described the southern exposure of the Manyovu as having a thin, laterally discontinuous basal conglomerate. A basal conglomerate persists in most localities, but thins northward. In areas with no conglomerate, a fine-grained orthoquartzite or light-colored sandstone marks the base of the unit. In both the north and south, the rest of the unit consists of 400 – 600 m of monotonous, fine-grained, micaceous, red sandstone and siltstone (Halligan, 1962; Piper, 1972), although Halligan (1962) noted flaggy bedding and hackly fracturing predominantly in the northern exposures.

In the study area, a white to pink, well-sorted, fine-grained and massive sandstone marks the base of the Manyovu unit (Fig. 3B). Tabular, 30 – 40 cm thick beds occur locally throughout this basal facies. Much of the section consists of a massive siltstone/mudstone (locally up to 50 m of unbedded, continuous section), displaying an irregular fracture pattern (here defined as “blocky”) also described by Halligan (1962) (Fig. 3C, 3D). Commonly this facies intercalates with thin (~10 – 50 cm), tabular, relatively resistant sand sheets (Fig. 3F, 3G). No ripple cross-lamination, cross-stratification, or erosive contacts occur throughout the unit; however, small-scale horizontal laminations are rarely observed, as well as horizons with large (~15 cm diameter) clusters of concretions (Bonar et al., in review).

METHODS

We identified ~300 m of continuous section of the Manyovu redbeds west of Mkalinzi, Tanzania (Fig. 1), exposed along an uplifted fault block associated with the EARS ~30 km north of Kigoma (Fig. 2, 3A). We logged the section (Fig. 2) and collected samples for U-Pb detrital zircon geochronology to constrain maximum depositional ages and provenance (N=6), thin section analysis (N=29) and subsequent point counting for supplemental provenance interpretations (N=13). Each detrital zircon sample was also prepped for particle-size analysis (N=6).

Detrital zircon geochronology

We analyzed six stratigraphic intervals from the Manyovu redbeds for detrital zircon geochronology, including both very fine to fine sandstone (N=3; Fig. 3B, 3F, 3G) and siltstone samples (N=3; Fig. 3C, 3D, 3E). Samples were processed to isolate zircon grains following methods described by Gehrels (2011). Prior to zircon analysis, grains were polished and imaged using a Hitachi 3400N scanning electron microscope (SEM) and a Gatan cathodoluminescence (CL2) detector system for backscatter electron (BSE) images to select zircons and conduct grain morphology analysis. U-Pb geochronology was conducted using laser-ablation multicollector inductively coupled mass spectrometry (LA-MC-ICPMS) at the Arizona LaserChron Center (Gehrels et al., 2006; Gehrels and Pecha, 2014). The analyses involve ablation of zircon with a Photon Machines Analyte G2 excimer laser using a spot with a diameter of 30 μm and ablation depth of ~15 μm. For detailed methods for U-Pb detrital zircon geochronologic methods and processing, refer to Gehrels et al. (2006) and Gehrels (2011).

Upon completion of data processing, we imported the data into detritalPy (Sharman et al., 2018), a python-based coding program, to aid in interpretation and visualization of detrital zircon data. To represent the relative probability distributions of data for provenance analysis, we use kernel density estimations (KDE), where a selected bandwidth (manually set at 15 Myr) captures the standard deviation of each Gaussian (Vermeesch, 2012). For calculating maximum depositional ages (MDA), detritalPy uses three metrics from Dickinson and Gehrels (2009): the youngest single grain (YSG), the youngest cluster of 2 or more ages with overlapping 1σ uncertainties (YC1σ(2+)), and the youngest cluster of 3 or more ages with overlapping 2σ uncertainties (YC2σ(3+)). We report all three MDA calculations for reference and discussion. For more details on MDA calculations, refer to Sharman et al. (2018).

Point counting and thin section analysis

A total of 29 samples were prepared for petrographic analysis and subsequent point counting to determine sandstone modal compositions. Thin sections were stained for both plagioclase (P) and potassium feldspar (K). All thin sections were analyzed for general grain size, shape, and sorting, grain textures, and micro-sedimentary structures, as well as mineral composition to aid in depositional and sediment transport interpretations. Photomicrographs were taken to illustrate modal frameworks, changes in grain size and sorting, and microfabrics.

Out of the 29 thin sections, only 13 were used for point counting owing to grain size limitations. For each thin section used for modal compositional trends, a total of 400 grains were counted using the Gazzi-Dickinson method (e.g., Dickinson et al., 1983; Ingersoll et al., 1984). Table 1 lists parameters for point counting. Recalculated modal percentages of point-count data were then plotted as ternary plots (Q-F-L and Qm-F-Lt). Ternary plots were created using TRI-PLOT in excel (Graham and Midgley, 2000).

Particle-size Analysis

We conducted particle-size analysis (N=6) on each of the intervals used for detrital zircon geochronology to quantify overall grain size. Most intervals are remarkably friable and easily disaggregated manually. For more lithified samples, a ceramic mortar and pestle were used to crush samples to pea-sized granules to increase surface area for chemical treatment; the granules were then rinsed with distilled water to remove any artificially generated particles <250 μm. Samples were then submerged in 2N HCl for 24 hours for carbonate removal and combusted at 500 ºC for ~15 hours to remove organic matter. Finally, samples were treated with citrate-bicarbonate-dithionite (CBD; Sur et al., 2010; Rea and Janecek, 1981) to remove iron oxides. Fully disaggregated samples were measured using a Malvern Mastersizer 3000 Laser Particle Size Analyzer (LPSA), after the addition of a few drops of sodium hexametaphosphate as a liquid dispersant, and sonication for ~two minutes.

RESULTS

Detrital Zircon Age Spectra

U-Pb detrital zircon ages from the Manyovu redbeds consisted of 1537 concordant to slightly discordant Archean – Neoproterozoic age zircons (see Supp. Files). Overall, strata yield U-Pb age distributions dominated by Neoproterozoic grains (28 – 54%) and Paleoproterozoic grains (19 – 37%), with moderate occurrences of Mesoproterozoic grains (15 – 27%), and minor Archean-age grains (1 – 13%) (Fig. 4). Age populations within the Neoproterozoic Era are predominantly Tonian (16 – 35%) and Cryogenian (11 – 27%) with minor amounts of grains with Ediacaran ages (0 – 8%) which are the youngest grains in the units. The general trend is an increasing abundance of Neoproterozoic grains up-section (Fig. 4); however, the middle of the section has the most Ediacaran-age grains.

Maximum Depositional Ages

The youngest age populations within a detrital zircon spectrum provide an estimate of the depositional age of a sample, known as the maximum depositional age (MDA; Fedo et al., 2003; Dickinson and Gehreals, 2009). MDAs are reported as YSG, YC1σ(2+), and YC2σ(3+). YSG will always report the least conservative MDA estimate, while YC2σ(3+) will always report the most conservative MDA estimate (Fig. 5). The two detrital zircon samples from the bottom of the section report the oldest YC2σ(3+) ages, with MDAs of 657.6 ± 1.7 Ma and 663.8 ± 2.0 Ma, followed by (in stratigraphic order) 613.6 ± 1.2 Ma, 616.9 ± 2.1 Ma, 640.7 ± 1.4 Ma, and 621.2 ± 3.1 Ma (Fig. 5). These ages fall within both the Cryogenian and Ediacaran periods. However, not all of the MDA calculations fall in chronological order stratigraphically, as the youngest reported MDAs (for all three calculations) fall within the middle of the Manyovu redbeds section (MANY-7 and MANY-8). Additionally, the youngest YSG-ages reported occur in the finest-grained samples: MANY-1silt (mode: 36.5 μm), MANY-7 (mode: 52.8 μm), and MANY-8 (mode: 47.6 μm), and the youngest YSG occurs in MANY-1silt (559.4 ± 4.2 Ma), even though the conservative MDA estimate for this sample is the oldest at 663.8 ± 2.0 Ma (Table 2).

Sandstone Modal Compositions

Compositional data were obtained from 13 sandstone and siltstone thin sections (5,200 grain counts) collected from throughout the studied section of the Manyovu redbeds (Fig. 6). Overall, the modal composition of the Manyovu units comprises predominantly quartz (47 – 85%), with variable feldspar (10 – 39%) consisting of mostly plagioclase (6 – 31%) with minor potassium feldspar (1 – 13%), and lithic fragments (6 – 19%) (See Supp. Files for raw data). Lithic fragments (out of 100%) are predominantly lithic volcanic (63 - 97%) with variable lithic metamorphic (0 – 17%) or sedimentary fragments (0 – 30%). Mica makes up the majority of accessory phases (up to 14%). Up-section trends include an overall decrease in Q abundance and corresponding increase in F abundance.

Using Q-F-L percentages, most samples plot in the lithic arkose field of Folk (1968), but others plot as arkose, feldspathic litharenite, or subarkose (Fig. 7). Using the ternary provenance provinces from Dickinson et al. (1983), Q-F-L percentages plot in the recycled orogen field, except one sample that barely plots in transitional continental (Fig. 7). Plots using the Qm-F-Lt percentages are more scattered, with most samples plotting around the transitional continental, mixed, and quartzose recycled provenance fields (Fig. 7).

Particle size analysis

Disaggregated samples from the six intervals of Manyovu redbeds contain grain-size modes of coarse silt (N=3), very-fine sand (N=2), and fine sand (N=1; Wentworth, 1922). The basal sand exhibits the coarsest mode (210 μm), and its silty counterpart exhibits the finest mode (36.5 μm; Table 2). The samples with the finest grain-size modes (MANY-1silt, MANY-7, and MANY-8) also report the youngest YSG ages for MDA (Fig. 5).

DISCUSSION

Provenance Interpretation

The detrital zircon and sandstone modal composition data reported here provide the first constraints on provenance for the Manyovu redbeds. Overall, KDEs of the detrital zircon ages display primary peaks within the Late Neoproterozoic (637 – 701 Ma) and the Paleoproterozoic (~1880 Ma and 1980 Ma) (Fig. 8). Secondary age peaks occur mostly within the Mesoproterozoic around ~990 Ma and ~1050 Ma, with other secondary peaks at ~780 Ma, and within the Archean (2626 – 2709 Ma). Modal compositions of the Manyovu are variable, and fall within all three major tectonic provinces defined by Dickinson and Suczek (1979): continental block, recycled orogen, and magmatic arc. Fine sand samples tend to exhibit the largest variability for modal compositions, while coarse silt trends toward continental block fields, and the very-fine sand trends towards magmatic arc fields with the most lithic fragments (grain sizes based on thin section analysis; Fig 6).

Archean cratons (>2500 Ma)

Southern and Central Africa contain multiple Archean cratons including the Congo, Tanzania, Zimbabwe, and Angola-Kasai cratons (Fig. 8). Zircons >2500 Ma make up between 5 – 16% of the interpreted detrital zircon spectra, with MANY-1 (both the sand-sized sample and silt-sized sample) containing the most grains within this age-range (Fig. 9). The Tanzania craton is likely a source for Archean-age zircons in the Manyovu redbeds, considering its proximal location and variety of reported ages between ~2645 – 2850 Ma (Borg and Krogh, 1999; Kabete et al., 2012). While the peaks in the reported detrital zircon spectra are slightly younger than this range (e.g., 2626 Ma and 2634 Ma), particularly at the bottom of the section, they are within error for these reported ages. Additionally, modal composition results indicate at least partial derivation of sediments from continental block sources (transitional continental and basement uplift; Fig. 7) with a few samples falling along the provenance field line between cratonic and recycled orogen sources.

2050 – 1800 Ma orogens

The Ubendian and Usagaran belts surround the Tanzania craton on the southern and western margins, and typically contain rock assemblages with ages between 1800 – 2050 Ma (Fig. 8). Detrital zircons between 1800 – 2050 Ma contribute between 15 – 28% of the grains analyzed from the Manyovu (Fig. 9). Peaks within this age range are usually around 1880 and 1980 Ma in all samples, however the older peak (1980 Ma) becomes more predominant up-section (Fig. 9). The Ubendian and Usagaran belts were part of a series of Paleoproterozoic accretionary events and contain supracrustal assemblages that record sedimentary and volcanic successions that have undergone greenschist, amphibolite, and granulite metamorphic conditions (Priem et al., 1979; Gabert, 1984; Mruma, 1989; Hanson, 2003; Boniface and Tsujimori, 2021). Nd-isotope signatures support both juvenile mantle and Archean crustal sources for intruding granitoid plutons (Maboko and Nakamura, 1996). Therefore, modal compositions of sediment from the Ubendian and Usagaran belts would likely plot in the transitional continental and recycled orogen provenance fields, which are the most-represented compositions of the Manyovu redbeds regardless of estimated sample grain size (Fig. 7).

Throughout the Usagaran Belt, age dates from the supracrustal rock assemblages range from *c.* 1890 – 1920 Ma (Maboko and Nakamura, 1996) and granitoids yield ages between ~1750 – 2000 Ma (e.g., Wendt et al., 1972; Priem et al., 1979). The eastern extent of the Usagaran belt was reworked during Pan African Orogenesis, specifically during the assembly of the Mozambique Belt. The Ubendian Belt is the western extent of the orogen (Priem et al., 1979; Gabert, 1984; Boniface and Tsujimori, 2021 and references within), and is most proximal to the Bukoban Basin (Fig. 8). Late – post-orogenic calc-alkaline granites and granodiorites are located between the Ubendian Belt and Tanzanian Craton, and these intrusive granites are widespread and have Rb-Sr whole-rock dates of 1869 ± 20 Ma to 1816 ± 11 Ma (e.g., Brewer et al. 1979; Schandelmeier, 1983). Additional ages of various granitoids exposed along the eastern margin of Lake Tanganyika range in age from 1864 ± 32 Ma to 1723 ± 41 Ma (Lenoir et al., 1994). In

summary, many of the rocks incorporated in the formation of the Ubendian and Usagaran Belts overlap with the Paleoproterozoic ages observed in the Manyovu samples.

1350 – 900 Ma orogens

Mesoproterozoic magmatism and orogenesis (formation of Rodinia) are represented by the Kibaran and Irumide belts both north and south of the study area (Fig. 8). These belts include metamorphic assemblages and granitic plutons with ages ranging from 900 – 1350 Ma (Hanson, 2003 and references within). Detrital zircons within the 900 – 1350 Ma age-range contribute 26 – 40% of the observed ages in the spectra (Fig. 9). The bottom of the section exhibits unimodal peaks in this age range (~995 Ma), but samples in the middle of the section change to a bimodal distribution in this range with both ~980 and ~1045 Ma peaks; however, the top of the section becomes again unimodal with a 978 Ma peak (Fig. 9). Modal compositions from detritus sourced from these terranes would likely fall in both continental block and recycled orogen fields.

The Kibaran Belt, just northwest of the Bukoban Supergroup deposits, contains predominantly bimodal intrusions with ages of both *c.* 1380 Ma and *c.* 1370 Ma (Tack et al., 2010), which are not ages represented in the detrital zircon spectra. However, minor emplacements of A-type granitoids of ~1250 – 1275 Ma occur throughout the orogen, and leucogranites that occur along the entire belt are dated to ~960 – 1006 Ma (Cahen & Ledent 1979; Ikingura et al., 1992; Tack et al., 2010) which are ages that occur in the detrital zircon results throughout the section. The Irumide belt is separated from the Kibaran Belt to the north and is less well-dated than its counterpart. Pre- and syn-tectonic plutons are dated as ~1350 – 1420 Ma (Cahen et al., 1984; Daly, 1986), and some A-type granites yield ages ranging from ~1080 – 1130 Ma (Ring et al., 1999). Additionally, post-tectonic plutons yield dates between ~900 – 1020 Ma (Daly, 1986; De Waele et al., 2006, 2009). Overall, the Kibaran and Irumide belts record active tectonism between ~1350 – 1200 Ma, but also contain post-orogenic plutons with younger ages (~1050 – 900 Ma).

Given the predominance of ~1350 – 1200 Ma ages within the Irumide and Kibaran belts, and the lack of these age ranges in the detrital zircon spectra in the Manyovu, we interpret these terranes as a minor contributor to the Manyovu redbeds. While the Mesoproterozoic orogenic belts contain some post-tectonic plutons in the 900 – 1000 Ma age range (well-represented in the detrital zircon spectra), these populations would likely be accompanied by a 1200 – 1350 Ma peak if the Irumide and Kibaran Belts provided a primary source of detritus. Only one sample—MANY-1silt— contains a small population of grains with a peak at 1243 Ma (Fig. 9).

850 – 500 Ma orogenic belts

The Neoproterozoic terranes of eastern and southcentral Africa are known as the Pan-African terranes, which formed between ~ 870 – 500 Ma (e.g., Kröner and Stern, 2004 and references within). Three major segments of the Pan-African orogen occur: 1) East African Orogen (EAO; Stern, 1994; Kusky et al., 2003), which comprises the Mozambique Belt and

Arabian-Nubian Shield, 2) the Damara Belt, Lufilian Arc, and Zambezi Belt known as the transcontinental orogen, and 3) the western-most margin along west Africa consisting of the West Congo, Kaoko, Gariep, and Saldania Belts (e.g., Trompette, 1994). Given the distal location of the third segment, we focus on the first two for provenance interpretations of the Manyovu (Fig. 8; Hanson, 2003 and references within). Detrital zircon within the Pan-African orogenic timeframe compose 17 – 41% of the spectra in the Manyovu redbeds section (Fig. 9). In the 500 – 850 Ma age-range, peaks predominantly occur around ~680 – 700 Ma, with secondary peaks between 747 – 780 Ma (Fig. 9).

Within the transcontinental orogen, the Lufilian Arc mostly comprises the Katanga Supergroup, which is a thick, sedimentary (clastic and carbonate strata, including evaporites) and volcanic sequence that was deposited in the early Neoproterozoic (Jackson et al., 2003; Master et al., 2005; Cailteux and De Putter, 2019). The Katanga Supergroup contains volcanic successions with ages ranging from 765 – 735 Ma (e.g., Kampunzu et al., 1998); however metamorphic assemblages are dated to ~500 – 650 Ma (e.g., Richards et al. 1988). Detrital zircon results from the Katanga strata support a predominant provenance signature from Ubendian-Usagaran terranes with Paleoproterozoic ages (~1830 – 2080 Ma; Master et al., 2005). Sediment sourced from the Lufilian Arc would likely have a predominantly recycled orogen modal composition, which is strongly represented in the Manyovu samples (Fig. 7). Differentiating between primary sourcing of the Ubendian-Usaragan Belts and secondary recycling of the Lufilian Arc strata remains unclear; however, both likely contribute to the Paleoproterozoic grains in the Manyovu. The Zambezi Belt contains mostly amphibolite- and gneiss-facies with ages between 850 – 870 Ma (Hansen, 2003; Kröner and Stern, 2004). There are also additional granitoids with ages of ~1100 Ma, and other metamorphic assemblages ~520 – 540 Ma (e.g., Vinyu et al., 1999; Goscombe et al., 2000), which were likely deformed post-Manyovu deposition based on current MDAs. Ages within the Zambezi Belt are not well-represented in the Manyovu detrital zircon spectra.

The Arabian-Nubian Shield contains some of the oldest Neoproterozoic ages within the EAO that range from ~870 – 667 Ma (Johnson and Woldehaimanot, 2003; Kröner and Stern, 2004), and comprises mostly juvenile, Neoproterozoic crust. On the other hand, in the EAO to the south, the Mozambique Belt contains a broad range of rock-types and ages, mostly due to its reworking of older Paleoproterozoic and Mesoproterozoic crust (e.g., the eastern extent of the Usagaran Belt and the Irumide Belt) and the presence of accreted terranes (Grantham et al., 2003; Kröner and Stern, 2004). A range of ages occur within this older crust, including ~1000 – 1100 Ma intrusive, granitoid gneisses along Tanzania and Malawi, (Costa et al., 1994; Kröner et al., 1997, 2001) and slightly younger ages between 930 – 950 Ma (Barr et al., 1978; Kokonyangi et al., 2001). Within the northern section of the Mozambique Belt, there are no reported ages for terrane older than ~1100 Ma (e.g., Grantham et al., 2003). The Mozambique Belt also contains minor amounts of juvenile crust with younger ages, including mafic, intrusive igneous complexes age-dated *c.* 609 – 841 Ma (Coolen et al., 1982; Möller et al., 2000; Kröner et al.,

2001; Muhongo et al., 2001). Meert (2003) reported radiometric ages for the Mozambique Belt with a dominant occurrence of ages between ~600 – 650 Ma.

Additionally, both the Arabian-Nubian Shield and Mozambique Belt record evidence for syn-orogenic magmatism. The Arabian-Nubian Shield experienced long-lived volcanism recorded by granitoid plutons and sedimentary-volcanic successions in associated basins. Volcanic rocks in the northern segment have been dated between 630 – 590 Ma (e.g., Be'eri-Shlevin et al., 2011). Other phases of magmatism and volcanism have been dated ~605 – 690 Ma (e.g., Johnson et al., 2011). The Mozambique Belt also consists of many magmatic arcs and island arcs associated with accreted terranes (e.g., Grantham et al., 2003; Stern et al., 2008); therefore, detritus sourced from these provinces would likely produce modal compositions that would verge between recycled orogens and magmatic arcs. In the Qm-F-Lt ternary diagram, four samples fall along the boundaries of both mixed and dissected arc provenance fields (Fig. 7), and lithic volcanic fragments make up between 62 – 98% of counted lithics in point count results (Supp Files).

Based on these age constraints and the various provenance types preserved in the Pan-African orogens, the EAO and transcontinental orogen were likely predominant sediment sources for the Manyovu redbeds. Intermittent Lufilian Arc and Arabian-Nubian Shield magmatism could be the sources for the 700 – 800 Ma peaks observed throughout the section. Additionally, given the abundant reworking of older terranes in the Mozambique Belt, this terrane likely contributed to the ~950 – 1050 Ma peaks as well as the younger, 600 – 700 Ma peaks in the spectra (Fig. 9). Overall, the most parsimonious interpretation for the provenance of the Manyovu redbeds calls upon local sourcing. No differences in provenance exist between the finer-grained, siltstone samples relative to the coarser-grained, sandstone samples, and the detrital zircon spectra do not record an unroofing record of older Neoproterozoic deposits of the Bukoban Supergroup or equivalent strata. However, the middle of the section gains an additional source represented by the bimodal peak in the 1350 – 900 Ma terrane age range, accompanied by a ~750 – 780 Ma peak (Fig. 9). In the lower-most two samples and the upper-most sample, there is a ~990 Ma age peak, but the middle three samples also have a prominent ~1050 Ma age peak (Fig. 9), indicating the possible initiation of orogenesis along the Mozambique Belt in the Late Neoproterozoic, explored in the next section.

Age Constraints for the Manyovu redbeds

MDAs represent the maximum age of a sedimentary unit; however, depending on the depositional setting, these ages can be used as a proxy for the true depositional age (TDA) as long as data are interpreted in ways that are stratigraphically coherent and tectonically relevent. Additionally, most MDAs used as TDA estimates are supplimented with other age constraints, such as biostratigrahic studies or volcanic ash geochronology, which are not available for the Manyovu redbeds. In order for the youngest grains in a detrital zircon spectra to be used to interpret MDA or TDA, these grains should be 1) contemporaneous or near-contomporeaneous

with deposition, 2) sufficiently abundant, 3) within acceptable age concordance definitions (e.g., Sharman and Malkowski, 2020). Based on the above discussion on provenance interpretations for the Manoyvu redbeds, the detrital zircon spectra clearly display evidence for contemporaneous deposition of sediment during Manyovu deposition represented by the sediment additions from the EAO and Mozambique Belt during the late Neoproterozoic. Pan African Orogeneis began around 650 Ma, and continued throughout Africa leading up to the Cambrian (e.g., Master et al., 2005; Zhou et al., 2019; Nelson et al., 2020). Therefore, it is likely that there would be syn-depositional contributions of volcanically-sourced zircons during Manyovu deposition. Additionally, in almost all samples, the youngest ages generate the primary peak within the detrital zircon spectra, indicating primary contributions and abundant sediment supply from contemporaneous sources during deposition. Finally, all ages are analyzed and processed for adequate concordance (Supp. Files).

Therefore, it is likely that the MDAs reported for the Manyovu are potentail proxies for a TDA. However, there are a few inconsistencies within the detrital zircon data. First, MDAs reported in the Manoyvu do not follow stratigraphic order (Fig. 5); therefore, we interpret all units stratigraphically above MANY-7 (MDA of 613.6 ± 1.2 Ma) to be at least 614 Ma or younger, even though some reported MDAs are as old as 640.7 ± 1.4 Ma. Second, two units include YSGs with ages almost 50 My younger than other reported MDAs: 559.4 ± 4.2 Ma in MANY-1silt and 598.5 ± 2.7 Ma in MANY-7. Considering the persistence of volcaism in the time interval of interest, we would expect abundant grains in these age ranges if they were truly representative of a depositional age for the Manyovu. While both of these ages are concordant, these ages are not statistically relevant, and likely represent either sample contamination, measurement error, or concealed lead loss (e.g., Anderson et al., 2019; Sharman and Malkowski, 2020). For these reasons we do not utilize YSG analyses as estimations for TDA in the Manyovu units, and interpret a most conservative MDA estimate for the Manyovu as approximately 614 Ma; however a TDA for the Manyovu is likely slightly younger.

Implications for orogenesis and sediment transport

Sedimentary successions associated with mountain building record evidence for orogenesis, and exhumation, and thus provide insight to sedimentation rates and patterns. Owing to the predominance of Neoproterozoic ages in the Manyovu detrital zircon spectra, these units likley accumulated during active magmatism associated with the EAO. The youngest Neoproterozoic peaks range between 637 – 698 Ma, which overlaps with initial closing of the Mozambique ocean and assembly of Greater Gondwana (e.g., Grantham et al., 2003). The MDAs fall on the younger side of these peaks, but overlap with Pan-African orogenesis. While no clear unroofing sequence occurs in the detrital zircon signatures for the Manyovu study section, there is evidence for 1) contributions from the Lufilian Arc and its sedimentary cover, and 2) synorogenic sediment contributions from the Mozambique Belt.

Our analysis hinges on the interpretation that zircons that produce MDAs derive from active volcanic sources, but note that the youngest MDAs occur within the middle—rather than top—of the section. The Manyovu interval contains increasing numbers of lithic fragments (mostly volcanic; up to 19% of total counts) and feldspar grains (up to 39%) and fewer quartz grains progressively up section, indicating more detrital contributions from magmatic arc sources throughout deposition. The young zircons recovered from the middle of the Manyovu section correlate to the appearance of peaks in the Mesoproterozoic age range (~1050 Ma; Fig. 9). As noted above, the Mozambique Belt contains multiple reworked terranes, and rocks with ages between ~1009 – 1094 Ma are common (Costa et al., 1994; Kröner et al.,1997, 2001). These ages are similar to those in the Irumide Belt, which implies that the Mozambique Belt reworked terranes of the Irumide orogen during orogenesis, and that during the middle of Manyovu deposition the Mozambique Belt was likely active and exhuming rocks of the Irumide Belt into the basin. This timing also correlates with the youngest maximum depositional ages in the succession (613.6 ± 1.2 Ma and 616.9 ± 2.1 Ma), coeval with the initiation of orogenesis of the Mozambique Belt in Mozambique and Malawi. In Mozambique, metamorphic facies and thrusting yield dates of ~615 – 586 Ma (e.g., Kröner et al., 1997) and plutonism in Malawi exhibits a broad age range from ~711 – 555 Ma (Hanson, 2003 and references within). Therefore, the youngest MDAs likely reflect initiation of orogenesis, exhumation, and active volcanism within the Mozambique belt mid-Manyovu deposition.

The *c.* 1975 Ma peak observed in the Manyovu data is ambiguous. Considering the persistence (including apparent increasing abundance) throughout the section and relatively consistent age, it appears to record exhumation of an older terrane during Pan-African orogenesis. This could reflect reworking of the Usagaran Belt by the Mozambique Belt in the Cryogenian – Ediacaran. High grade gneisses, granitoids, and metasediments of the Usagaran along the Mozambique Belt have been dated to ~2020 – 1820 Ma (e.g., Fritz et al., 2013; Boniface and Tsujimori, 2021). However, few assemblages exposed today within the Mozambique Belt contain this age-range. Alternatively, the ~1975 Ma peak could record second-order recycling of the Katanga Supergroup within the Lufilian Arc, as these reportedly contain zircon ages of ~1800 – 2050 Ma (Master et al., 2005). A recycling explanation, however would require associated uplift and exhumation of the Lufilian Arc sedimentary strata during this time, which is unclear with current data. Additionally, questions remain regarding the sediment transport mechanisms for the Manyovu and interpreting the possibility of sources from both modern-day southwest and eastern Africa.

During the Neoproterozoic, Lake Tanganyika and Tanzania were ~15° south of the equator (Fig. 10), situating the study area within the southeasterly trade winds, assuming zonal circulation. These winds would cross directly over the mountains associated with the Mozambique Belt, Arabian-Nubian Shield, and the Lufilian Arc (Fig. 9, 11) and—depending on elevations, likely produce an orographic effect resulting in dry winds (similar to modern-day Chinook winds of the North American cordillera). Interestingly, most of the interpreted source

areas are located east/southeast (in modern coordinates) of the Bukoban Supergroup basin (e.g., Tanzania craton, Usagaran Belt, and Pan-African orogens). This orientation would also explain the sparsity of provenance signatures from local source terranes to the modern-day north of Tanzania (e.g., Kibaran Belt). Given the combination of paleoclimate and paleogeography of this time, there is potential for abundant production of fine-grained material along the EAO which is the predominant interpreted source for the Manyovu units.

CONCLUSIONS

This study provides the first isotopic age constraints for the Manyovu redbeds of Tanzania and indicates that these units likely accumulated in the latest Cryogenian and/or early Ediacaran of the late Neoproterozoic—nearly 200 My younger than previously estimated. Maximum depositional ages indicate syn-tectonic deposition of these strata associated with Pan-African orogenic events that formed the Arabian-Nubian Shield, Mozambique Belt, and Lufilian Arc. Furthermore, the exceptional preservation and unmetamorphosed state of these sedimentary units implies that they archive relatively pristine paleoenvironmental data for this fascinating interval of Earth history.

ACKNOWLEDGEMENTS

We would like to thank our field assistants, Bren Cable and Mupape Mukuli for help with sample collection and field work. Also, the Tanzanian Fisheries Research Institute (TAFIRI) and the Tanzanian Mining Commission for research and logistics support. Thank you to Declan Martin for assistance with collected LPSA data. This work was completed under Tanzania Commission for Science and Technology Research Permit # 2021-445-NA-2018-169. This work was completed with funding support from the Robberson Research Grant (OU), NSF-EAR-1424907 (Awarded to M. Soreghan), NSF-OISE-1658614 (Awarded to M. Soreghan and G. Soreghan), and the OU School of Geosciences Eberly Chair. Thank you to the University of Arizona Laserchron Center for assistance with U-Pb geochronology (NSF-EAR-2050246).

FIGURES AND TABLES

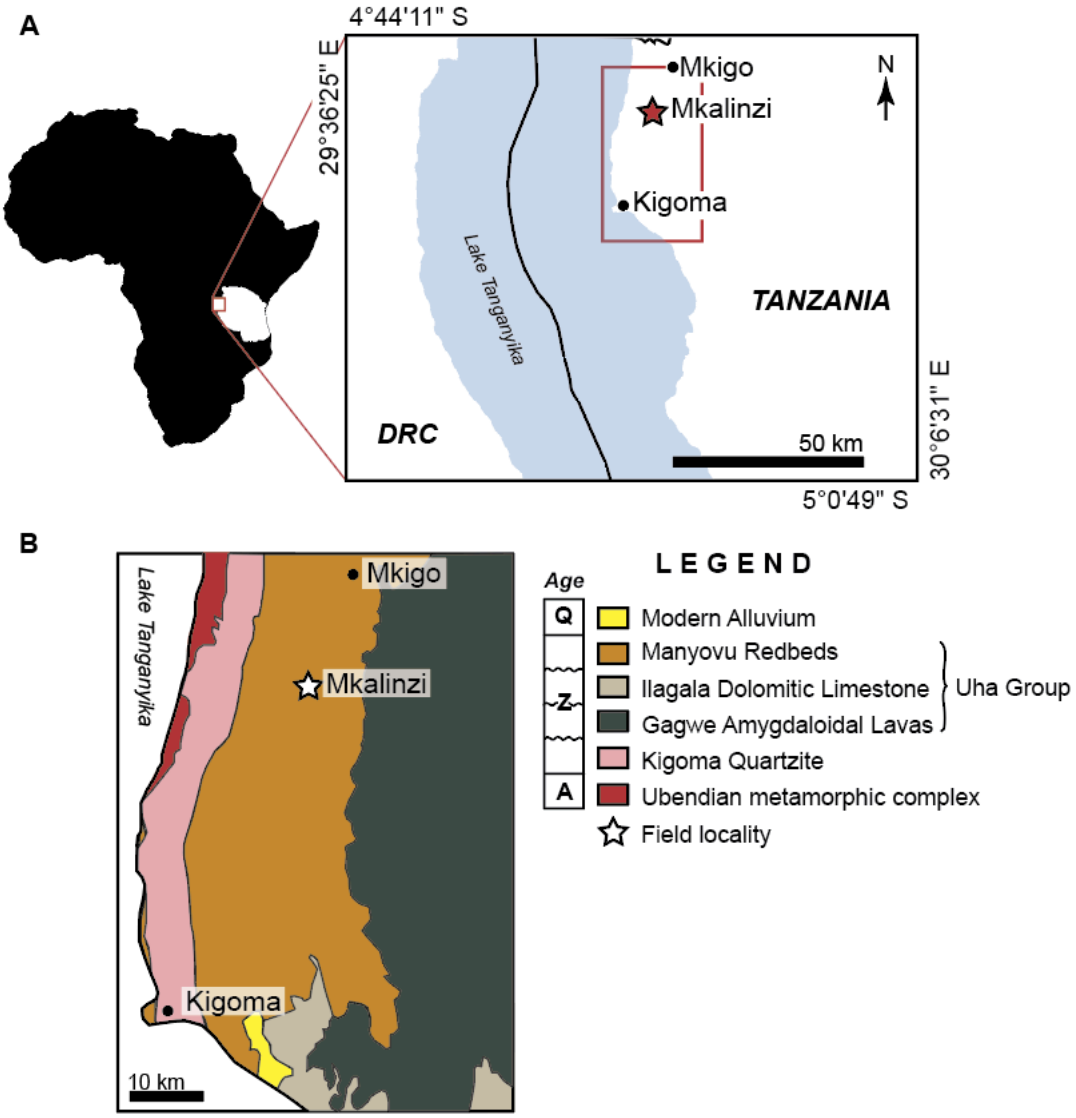


Figure 1. Regional geographic and geologic maps of the study area. A) General geographic map showing the location of Tanzania in Africa enlarged to illustrate the northeastern shore of Lake Tanganyika. Kigoma and Mkigo are labeled as reference points, and the red star marks the study area. Red box highlights area represented in B. B) Geologic map of the local area around the study site (white star). Most units are bounded by unconformities and the area is mostly Archean – Neoproterozoic rocks with modern alluvium and lake deposits southeast of Kigoma. Geologic map is modified from Kasanzu and Manya (2020).

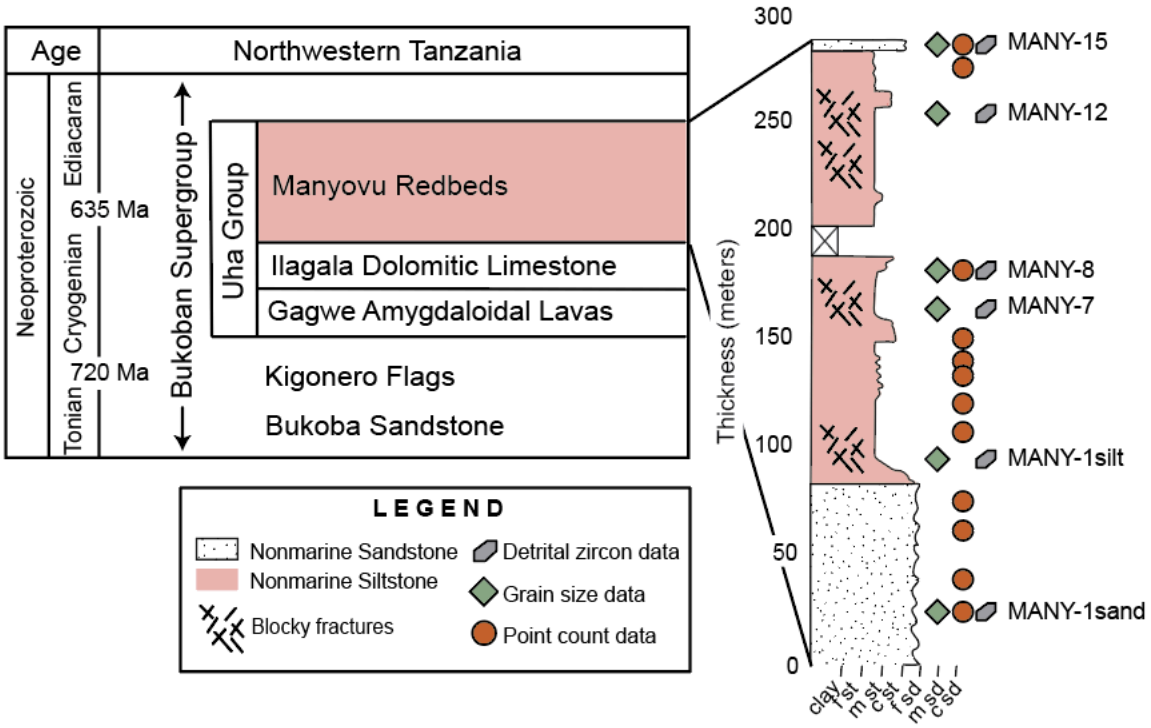


Figure 2. Stratigraphic column showing the Uha Group within the Neoproterozoic Bukoban Supergroup modified from Halligan (1962), Cahen and Snelling (1974), and Deblond et al. (2001). The pink color indicates the interval of interest expanded to show a generalized measured section for the study area including sample locations and facies thicknesses and variations. Labeled sample names correspond to detrital zircon samples.

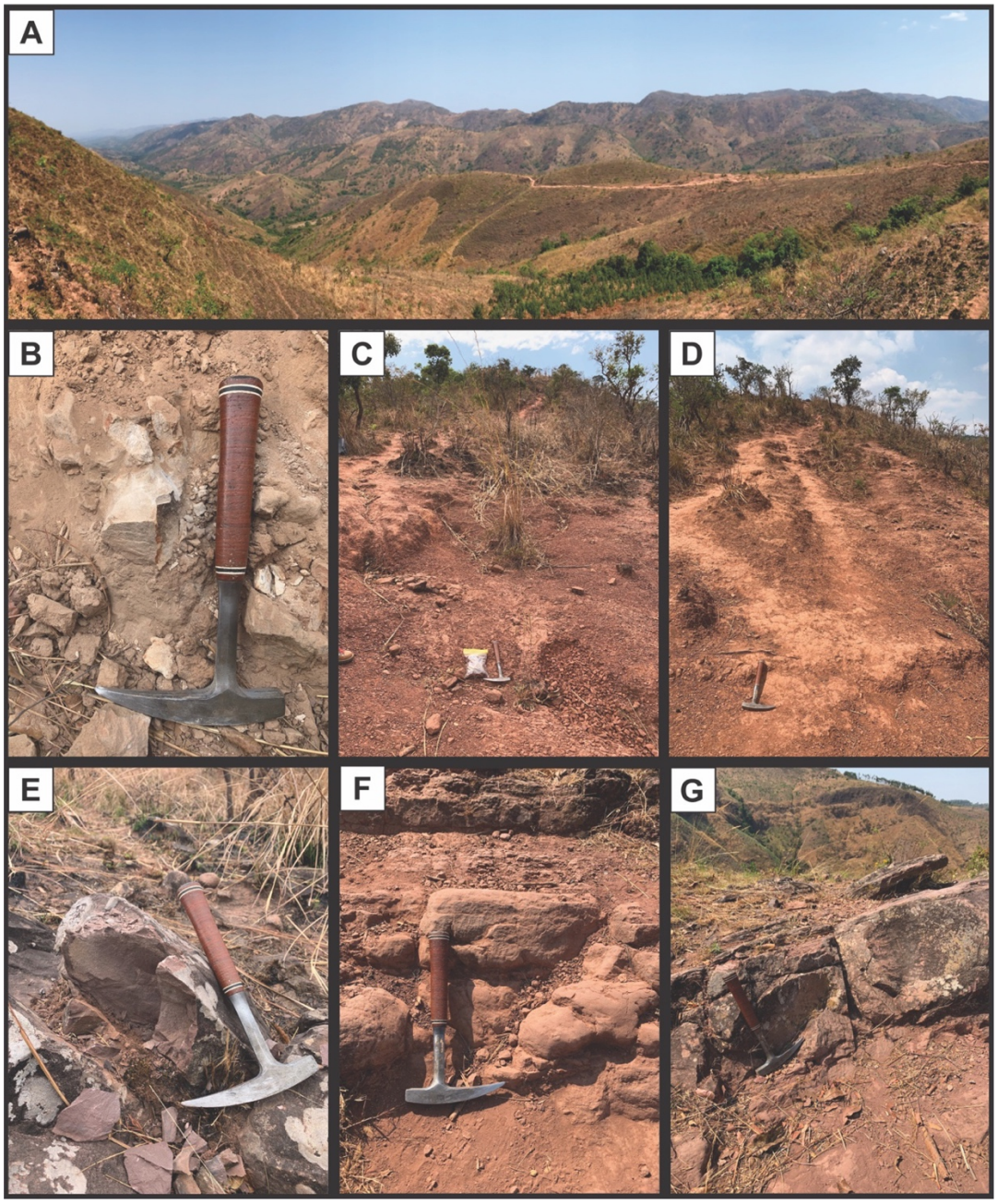


Figure 3. Field photos of the Manyovu redbeds from study area west of Mkalinzi, Tanzania. A) Overview of the study area where the section was logged. We followed the visible trail down the side of the exposed fault block. B) Representative photo of the basal sandstone facies and DZ sample MANY-1sand. C & D) Representative photos of the siltstone/mudstone facies with blocky fracture patterns (C) and DZ samples MANY-1silt (C) and MANY-7 (D). E) Field photo of DZ sample MANY-8. F) Field photo of DZ sample MANY-12 and example of a more resistant bed of silt-size grains without the blocky fracture pattern. G) Field photo of DZ sample MANY-15 and an example of a thicker sand sheet within the section. Hammer for scale in all photos.

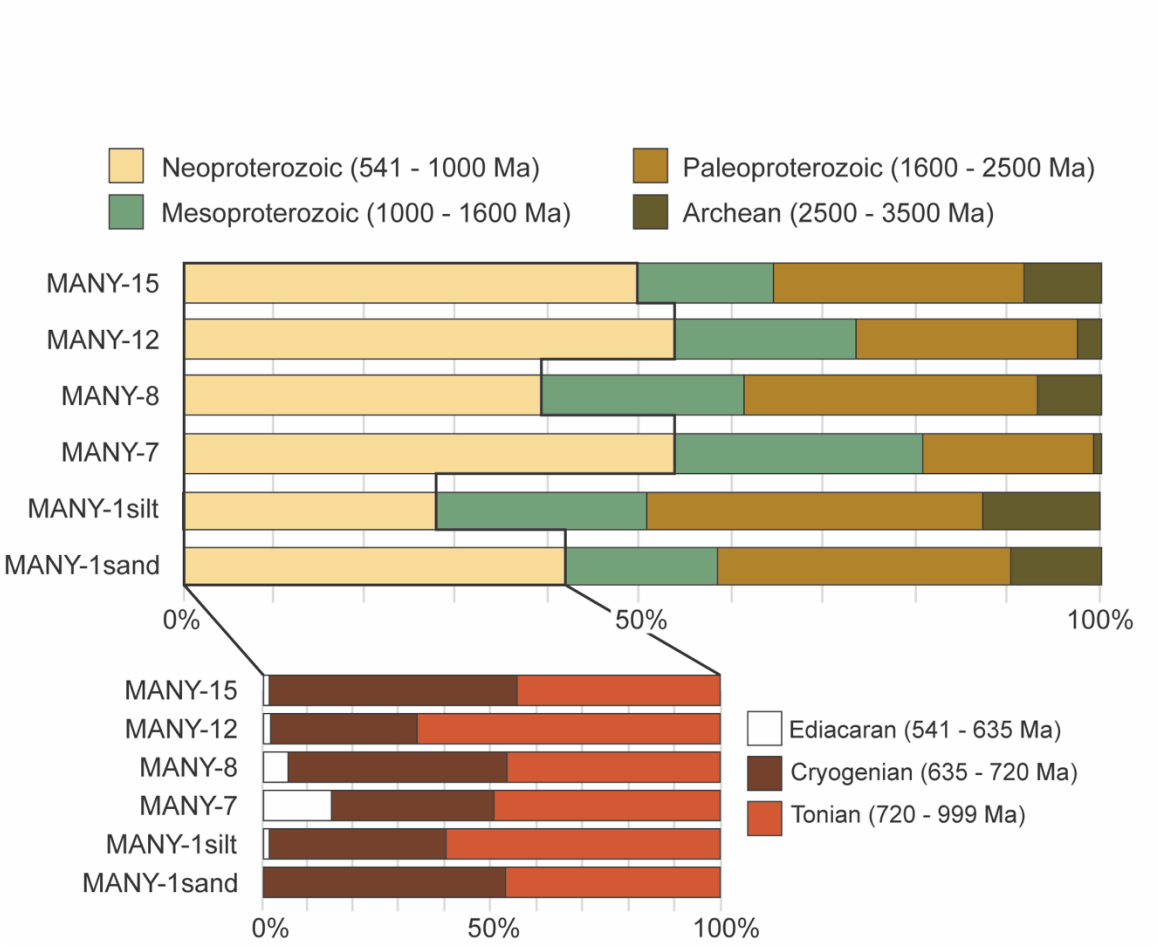


Figure 4. Bar graphs showing the distribution (out of 100% of each sample) of ages in each detrital zircon spectrum. Overall, Neoproterozoic grains increase in abundance up-section, with the most abundant Ediacaran (youngest time-period observed) grains in the middle of the section (MANY-7).

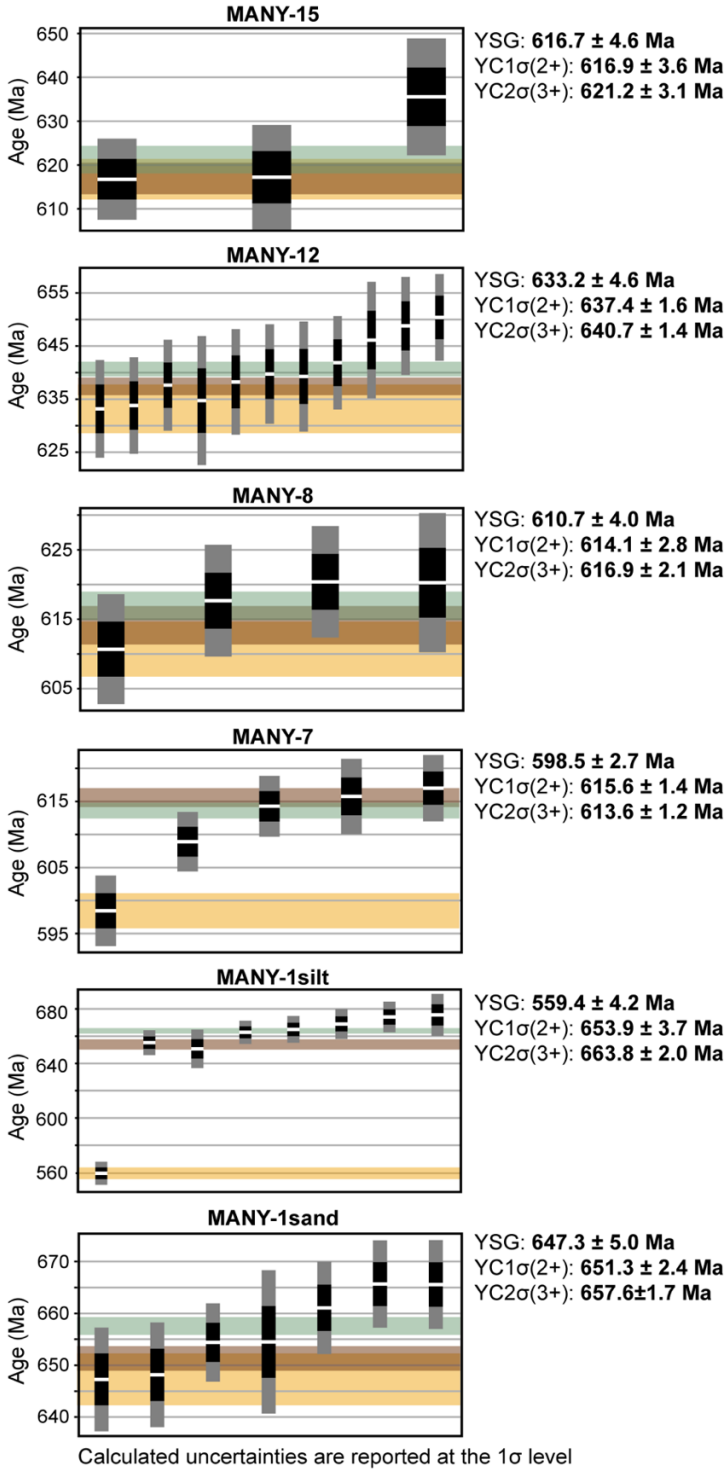


Figure 5. Maximum depositional ages reported for each sample as YSG, YC1σ(2+), and YC2σ(3+); see methods text for explanations. Age (Ma) is on the y-axis and x-axis is number of grains represented. Color bars highlight age and associated uncertainties (1-sigma) for each group of calculations (yellow = YSG, brown = YC1σ(2+), green = YC2σ(3+)). The vertical bars represent the reported age for each grain (white line), with 1-sigma uncertainty (black bar) and 2-sigma uncertainty (gray bar). Plot generated in detritalPy (Sharman et al., 2018).

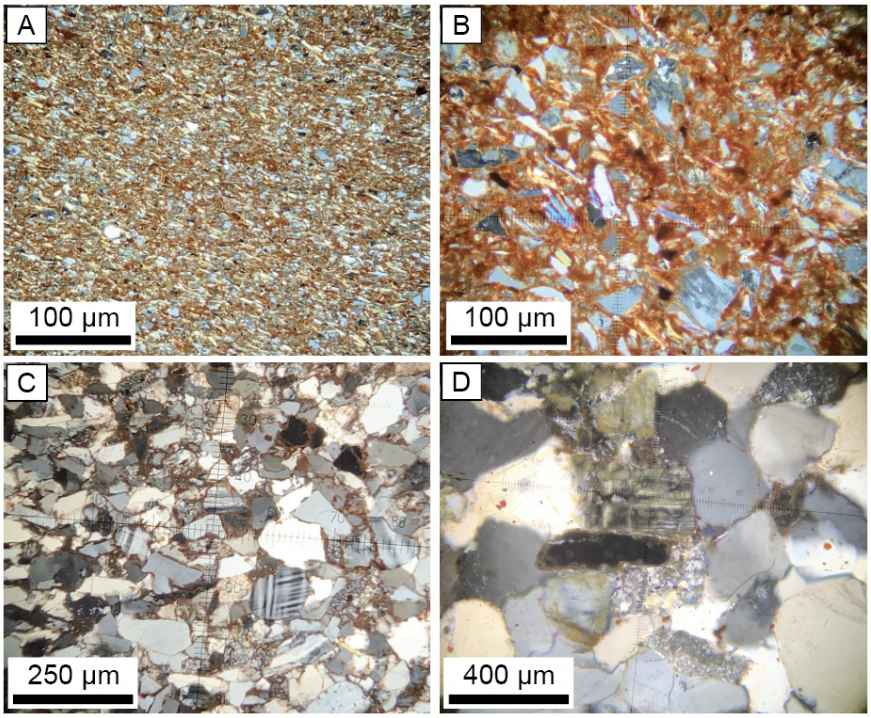


Figure 6. Photomicrographs (XPL) illustrating the grain composition, shape, and sorting within the Manyovu section. A) Mudstone with clay and silt-sized grains; B) Silt – sand sized grains floating in a clay, iron-oxide matrix. Grains are mostly quartz, feldspar, mica, and some lithic fragments; all are angular to sub-angular. C) very fine sand-sized, rounded – sub-rounded and moderately sorted quartz, pristine feldspars (k-spar, plagioclase), and lithics. D) Fine sand-sized quartz and k-feldspar with lithic volcanics. Sample was stained for potassium feldspar.

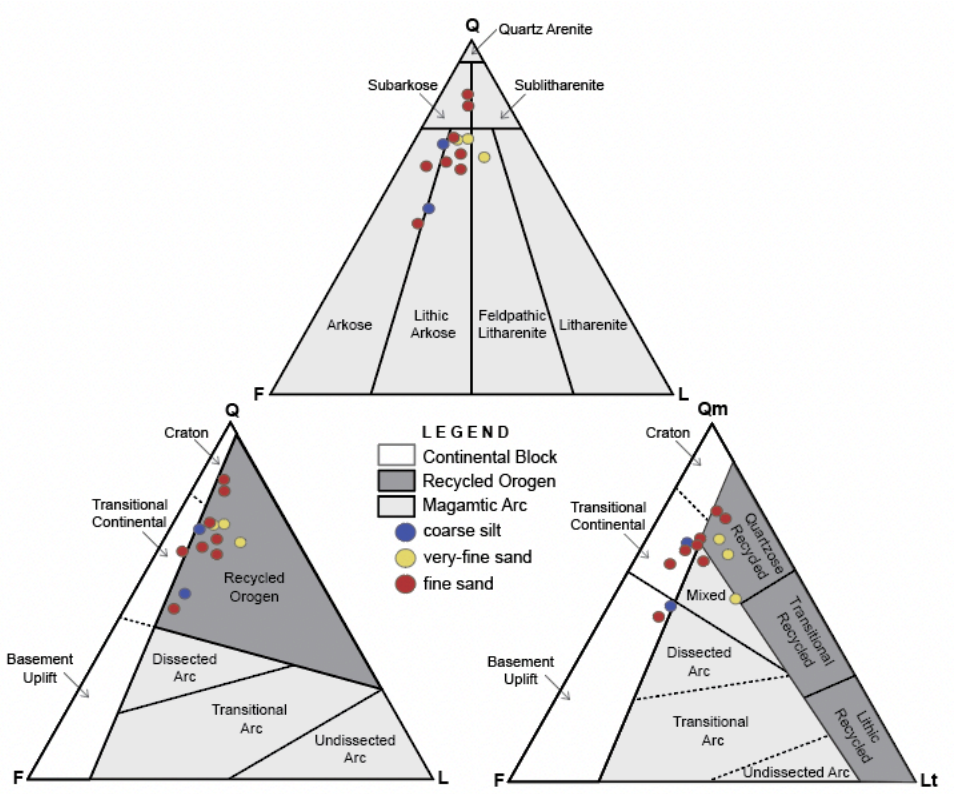


Figure 7. Ternary diagrams showing modal compositions and interpreted source provinces (from Dickinson et al., 1983 and Ingersoll et al., 1984). Point count samples are represented by their grain-size to determine possible correlations. The fine-sand samples have the broadest compositions and possible source provinces, while the coarse silt samples trend between continental block and magmatic arc, and very-fine sand samples represent mostly recycled orogens.

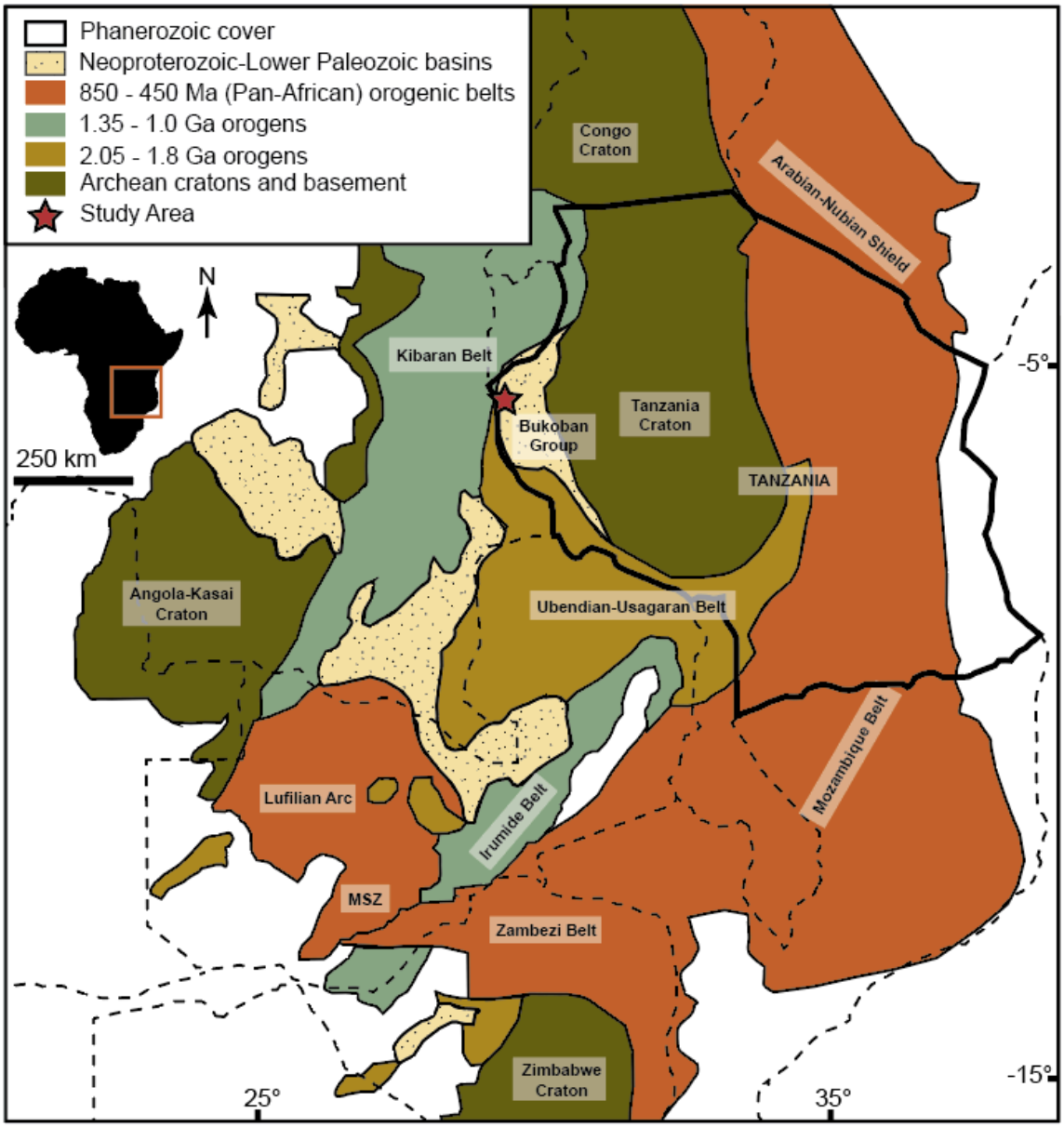


Figure 8. Map of Precambrian source terranes and basement provinces in Tanzania and surrounding areas in south-central and east Africa. The country border of Tanzania is indicated with a heavier line weight; dashed lines denote other country boundaries. The red star designates the study area in the Bukoban Group basin. Colors are representative of generalized ages for each terrane; refer to discussion text for details. Map modified and created using data and maps from Hanson (2003), Fritz et al. (2013), and de Wit et al. (2015). Colors coordinate with source age-ranges in Figure 10.

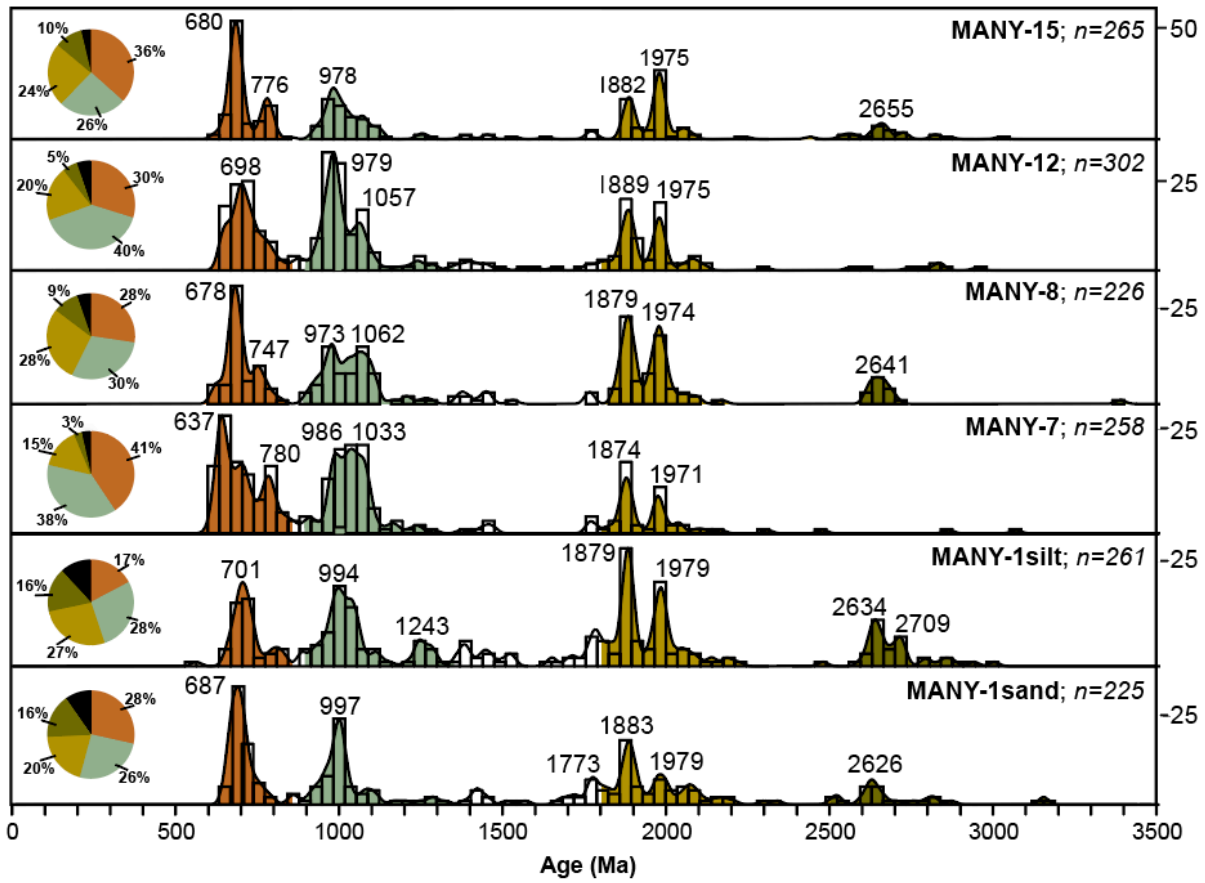


Figure 9. Interpreted detrital zircon spectra with normalized kernel density estimates (KDEs) and grain count histograms. Age (Ma) is on the x-axis and the y-axis represents the number of grains represented in the histogram plots. Significant peaks in the KDEs are labeled for each sample. Pie graphs are a visual representation of the distributions (out of 100%) of each generalized terrane age-range, colors from Fig. 9; black is unrepresented ages in source terranes. Pan-African (orange) orogenic belts represent most primary peaks, while 1.35 – 1.0 Ga (light teal) and 2.05 – 1.8 Ga orogens (tan) represent secondary peaks. Colors correlate to Figure 9. Plot made in detritalPy (Sharman et al (2018).

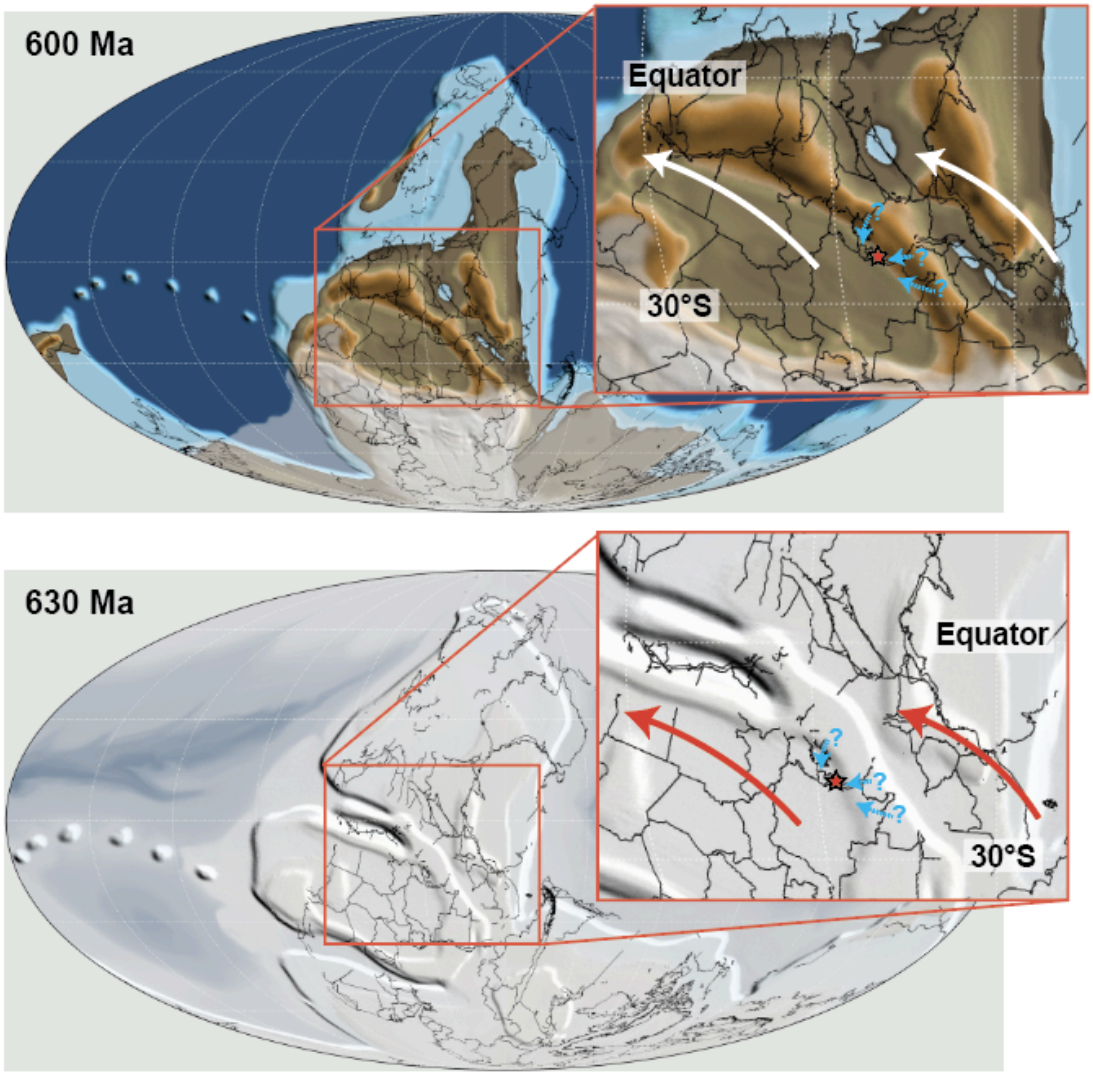


Figure 10. Paleogeographic maps from time-slices 630 Ma (early Ediacaran) and 600 Ma (Mid-Ediacaran) with hypothesized sediment transport mechanisms for the Manyovu redbeds. Maps are Mollweide projections from Scotese (2021). Each map zooms in to the regional study area (red star). Red and white arrows represent interpreted zonal Tradewinds that likely carried sediment from the active highs of the Pan-African orogenies into an intracratonic foreland of modern-day Africa. Blue dashed arrows represent potential highland-streams or rivers that possibly carried sediment to be deflated and redeposited in the basin.

Point Count Parameters
Quartz (Q) = Qm + Qp + chert
- Monocrystalline quartz (Qm)
- Polycrystalline quartz (Qp)
- Chert (C)
Feldspar (F) = P + K
- Plagioclase (P)
- Potassium feldspar (K)
Lithic fragments (L) = Ls + Lm + Lv
- Lithic sedimentary (Ls)
- Lithic metamorphic (Lm)
- Lithic volcanic (Lv)
Lt = Ls + Lm + Lv + Qp + chert
Accessory Minerals* (A)

*Accessory minerals include mica and dense minerals

Table 1. Point count parameters for determining modal compositional trends. From Dickinson et al. (1983).

Sample	Section location (m)	Grain-size mode (μm; LPSA)	Grain-size category	MDA (Ma) YC2σ(3+)
MANY-15	285	105	very-fine sand	621.2 ± 3.1
MANY-12	254	113	very-fine sand	640.7 ± 1.4
MANY-8	184	47.6	coarse silt	616.9 ± 2.1
MANY-7	167	52.8	coarse silt	613.6 ± 1.2
MANY-1silt	100	36.5	coarse silt	663.8 ± 2.0
MANY-1sand	23	210	fine sand	657.6 ± 1.7

Table 2. Summary table with each DZ sample and location in the logged section, reported grain-size mode and associated grain size category (Wentworth, 1922), and most conservative MDA estimate. MDAs fall within the Cryogenian-Ediacaran boundary, both do not decrease with younger samples or correlate to various grain-size modes.

REFERENCES CITED

Avigad, D., Kolodner, K., McWilliams, M., Persing, H., Weissbrod, T., 2003, Origin of northern Gondwana Cambrian sandstone revealed by detrital zircon SHRIMP dating: Geology, v. 31, p. 227–230.

Batumike, M.J., Cailteux, J.L.H., and Kampunzu, A.B., 2007, Lithostratigraphy, basin development, base metal deposits, and regional correlations of the Neoproterozoic Nguba and Kundelungu rock successions, central African Copperbelt: Gondwana Research, v. 11, p. 432–447, doi:10.1016/j.gr.2006.04.012.

Be'eri–Shlevin, Y., Samuel, M.D., Azer, M.K., Rämö, O.T., Whitehouse, M.J. and Moussa, H.E., 2011, The Ediacaran Ferani and Rutig volcano–sedimentary successions of the northernmost Arabian–Nubian Shield (ANS): new insights from zircon U–Pb geochronology, geochemistry and O–Nd isotope ratios: Precambrian Research, v. 188 (1–4), p. 21 – 44.

Brewer, M.S., Haslam, H.W., Darbyshire, D.P.F. and Davis, A,E., 1979, Rb–Sr age determination in the Bangweulu Block, Luapula Province, Zambia: Republic Institute Geological Sciences, 11 p.

Briden, J. C., Piper, J. D. A., Henthorn, D. I. & Rex, D. C., 1971, New palaeomagnetic results from Africa and related potassium–argon age determinations, University of Leeds, p. 46 – 50.

Boniface, N. and Tsujimori, T., 2021, New tectonic model and division of the Ubendian–Usagaran Belt, Tanzania: A review and in–situ dating of eclogites, in Wakabayashi, J., and Dilek, Y., eds., Plate Tectonics, Ophiolites, and Societal Significance of Geology: A Celebration of the Career of Eldridge Moores: Geological Society of America Special Paper 552, p. 133–175, https://doi.org/10.1130/2021.2552(08).

Borg, G. and Krogh, T., 1999, Isotopic age data of single zircons from the Archaæan Sukumaland Greenstone Belt, Tanzania: Journal of African Earth Sciences, v. 29(2), p. 301–312.

Cahen, L. and Snelling, N.J., 1974, Potassium–argon ages & additions to the stratigraphy of the Malagarasian (Bukoban system of Tanzania) of SE Burundi: Journal of the Geological Society, v. 130, p. 461–470, doi:10.1144/gsjgs.130.5.0461.

Cahen, L. and Ledent, D., 1979, Précisions sur l'age, la pétrogénèse et la position stratigraphique des granites à étain de l'est de l'Afrique Centrale. Bull. Soc. Belg. Géol, v. 88, p. 33–49.

Cahen, L., Snelling, N.J., Delhal, J., Vail, J.R., Bonhomme, M. and Ledent, D., 1984, The geochronology and evolution of Africa: London, Oxford, 512 p.

Cailteux, J.L. and De Putter, T., 2019, The Neoproterozoic Katanga Supergroup (DR Congo): State–of–the–art and revisions of the lithostratigraphy, sedimentary basin and geodynamic evolution: Journal of African Earth Sciences, v. 150, p. 522 – 531.

Coolen, J.M., Priem, H.N.A., Verdurmen, E.T. and Verschure, R.H., 1982, Possible zircon U–Pb evidence for Pan–African granulite–facies metamorphism in the Mozambique belt of southern Tanzania: Precambrian Research, v. 17(1), p. 31 – 40.

Costa, M., Cadoppi, P., Sacchi, R., Fanning, C.M., 1994, U–Pb "SHRIMP" dating of zircons from Mozambique gneiss: Bollettino Societa Geoleologica Italiana, v. 113, p. 173 – 178.

Daly, M.C., 1986, The intracratonic Irumide belt of Zambia and its bearing on collision orogeny during the Proterozoic of Africa: Geological Society, London, Special Publications, v. 19(1), p. 321 – 328.

Deblond, A., Punzalan, L.E., Boven, A., and Tack, L., 2001, The Malagarazi supergroup of Southeast Burundi and its correlative Bukoba supergroup of Northwest Tanzania: Neo– and Mesoproterozoic chronostratigraphic constraints from Ar–Ar ages on mafic intrusive rocks: Journal of African Earth Sciences, v. 32, p. 435–449, doi:10.1016/s0899–5362(01)90107–1.

De Waele, B., Kampunzu, A.B., Mapani, B.S.E. and Tembo, F., 2006, The Mesoproterozoic Irumide belt of Zambia: Journal of African Earth Sciences, v. 46(1–2), p. 36 – 70.

De Waele, B.F., Wingate, M.T.D., Tembo, F., Mapani, B.S.E., and Belousova, E.A., 2009, The geochronological framework of the Irumide Belt: a prolonged crustal history along the margin of the Bangweulu Craton: American Journal of Science, v. 309, p. 132–187, https://doi.org/10.2475/02.2009.03.

Dickinson, W.R., Beard, L.S., Brakenridge, G.R., Erjavec, J.L., Ferguson, R.C., Inman, K.F., Knepp, R.A., Lindberg, F.A., and Ryberg, P.T., 1983, Provenance of North American Phanerozoic sandstones in relation to tectonic setting: GSA Bulletin, v. 94, p. 222–235, doi:10.1130/0016–7606(1983)94.

Dickinson, W. R., & Gehrels, G. E., 2009, Use of U-Pb ages of detrital zircons to infer maximum depositional ages of strata: A test against a Colorado Plateau Mesozoic database: Earth and Planetary Science Letters, v. 288, p. 115–125.

Frimmel, H.E., Klötzli, U.S. and Siegfried, P.R., 1996, New Pb–Pb single zircon age constraints on the timing of Neoproterozoic glaciation and continental break–up in Namibia: The Journal of Geology, v. 104(4), p. 459–469.

Frimmel, H.E., 2000, New U–Pb zircon ages for the Kuboos pluton in the Pan–African Gariep belt, South Africa: Cambrian mantle plume or far field collision effect?: South African Journal of Geology, v. 103(3–4), p. 207 – 214.

Frimmel, H.E., Fölling, P.G., and Eriksson, P.G., 2002, Neoproterozoic tectonic and climatic evolution recorded in the Gariep belt, Namibia and South Africa: Basin Research, v. 14, p. 55–67, doi:10.1046/j.1365–2117.2002.00166.x.

Fritz, H., Abdelsalam, M., Ali, K.A., Bingen, B., Collins, A.S., Fowler, A.R., Ghebreab, W., Hauzenberger, C.A., Johnson, P.R., Kusky, T.M. and Macey, P., 2013, Orogen styles in the East African Orogen: a review of the Neoproterozoic to Cambrian tectonic evolution: Journal of African Earth Sciences, v. 86, p. 65 – 106.

Gabert, G., 1984, Structural–lithologic units of Proterozoic rocks in East Africa, their base, cover and mineralization: Géologie Africaine, p. 11–22.

Gehrels, G., 2011, Detrital zircon U-Pb geochronology: Current methods and new opportunities. Tectonics of sedimentary basins: Recent advances, p. 45–62.

Gehrels, G., Valencia, V. and Pullen, A., 2006, Detrital zircon geochronology by laser–ablation multicollector ICPMS at the Arizona LaserChron Center: The Paleontological Society Papers, v. 12, p. 67–76.

Gehrels, G. and Pecha, M., 2014, Detrital zircon U–Pb geochronology and Hf isotope geochemistry of Paleozoic and Triassic passive margin strata of western North America: Geosphere, v. 10(1), p. 49–65.

Goodwin, A.M., 1991, Precambrian geology: the dynamic evolution of the continental crust: Academic Press, London, 666 p.

Goscombe, B., Armstrong, R., and Barton, J.M., 2000, Geology of the Chewore Inliers, Zimbabwe: constraining the Mesoproterozoic to Paleozoic evolution of the Zambezi Belt: Journal of African Earth Sciences, 3v. 0(3), p. 589–627.

Graham, D.J. and Midgley, N.G., 2000, Graphical representation of particle shape using triangular diagrams: an Excel spreadsheet method: Earth Surface Processes and Landforms, v. 25(13), p. 1473–1477.
Grantham, G.H., Maboko, M. and Eglington, B.M., 2003, A review of the evolution of the Mozambique Belt and implications for the amalgamation and dispersal of Rodinia and Gondwana: Geological Society, London, Special Publications, v. 206(1), p. 401–425.
Halligan, R., 1959, South Kigoma and North–West Mpanda Districts: Quarter Degree Sheet 35 SE and NE and 36 SW: Rec. Geologic Survey Tanganyika, v. VII, p. 14–20.
Halligan, R., 1962, The Proterozoic rocks of Tanganyika: Geological Survey of Tanzania, 22 p.
Halverson, G.P., Hoffman, P.F., Schrag, D.P., Maloof, A.C., and Rice, A.H.N., 2005, Toward a Neoproterozoic composite carbon–isotope record: Geological Society of America Bulletin, v. 117, p. 1181–1207, doi: 10 .1130 /B25630.1.
Halverson, G.P., Wade, B.P., Hurtgen, M.T. and Barovich, K.M., 2010, Neoproterozoic chemostratigraphy: Precambrian Research, v. 182(4), p. 337–350.
Hanson, R.E., 2003, Proterozoic geochronology and tectonic evolution of southern Africa: Geological Society Special Publication, v. 206, p. 427–463, doi:10.1144/gsl.sp.2003.206.01.20.
Henderson, G. 1961, The geology of the Bukoban–type rocks of the Kigoma and Mpanda Districts, Western Province, Tanganyika: Geological Society of South Africa, v. LXIII, p. 12 – 19.
Hoffman, P.F., Kaufman, A.J., Halverson, G.P., and Schrag, D.P., 1998, A Neoproterozoic Snowball Earth: Science, v. 281, p. 1342–1346, doi:10.1126/science.281.5381.1342.
Hoffman, P.F. and Schrag, D.P., 2002, The snowball Earth hypothesis: testing the limits of global change: Terra Nova, v. 14, p. 129–155.
Hoffman, P.F. and Li, Z.X., 2009, A paleogeographic context for Neoproterozoic glaciation: Palaeogeography, Palaeoclimatology, Palaeoecology, v. 277(3–4), p. 158–172.
Hoffmann, K.H., Condon, D.J., Bowring, S.A. and Crowley, J.L., 2004, U–Pb zircon date from the Neoproterozoic Ghaub Formation, Namibia: constraints on Marinoan glaciation: Geology, v. 32(9), p. 817–820.
Hoffmann, K.H., Condon, D.J., Bowring, S.A., Prave, A.R., Fallick, A., 2006, Lithostratigraphic, carbon isotope and U–Pb zircon age constraints on early Neoproterozoic (ca. 755 Ma) glaciation on the Gariep Belt, Southern Namibia, in: Snowball Earth Conference, Ascona, Switzerland.
Hoffman, P.F., Lamothe, K.G., LoBianco, S.J.C., Hodgskiss, M.S.W., Bellefroid, E.J., Johnson, B.W., Hodgin, E.B., and Halverson, G.P., 2017, Sedimentary depocenters on Snowball Earth: Case studies from the Sturtian Chuos formation in Northern Namibia: Geosphere, v. 13, p. 811–837, doi:10.1130/ges01457.1.
Ikingura, J.R., Reynolds, P.H., Watkinson, D.H. and Bell, K., 1992, $^{40}Ar/^{39}Ar$ dating of micas from granites of NE Kibaran Belt (Karagwe–Ankolean), NW Tanzania: Journal of African Earth Sciences (and the Middle East), v. 15(3–4), p. 501–511.
Ingersoll, R.V., Bullard, T.F., Ford, R.L., Grimm, J.P., Pickle, J.D. and Sares, S.W., 1984, The effect of grain size on detrital modes: a test of the Gazzi–Dickinson point–counting method: Journal of Sedimentary Research, v. 54(1), p. 103–116.
Jackson, M.P.A., Warin, O.N., Woad, G.M. and Hudec, M.R., 2003, Neoproterozoic allochthonous salt tectonics during the Lufilian orogeny in the Katangan Copperbelt, central Africa: Geological Society of America Bulletin, v. 115(3), p. 314–330.

Johnson, P.R. and Woldehaimanot, B., 2003, Development of the Arabian–Nubian Shield: perspectives on accretion and deformation in the northern East African Orogen and the assembly of Gondwana: Geological Society, London, Special Publications, v. 206(1), p. 289–325.

Johnson, P.R., Andresen, A., Collins, A.S., Fowler, A.R., Fritz, H., Ghebreab, W., Kusky, T. and Stern, R.J., 2011, Late Cryogenian–Ediacaran history of the Arabian–Nubian Shield: a review of depositional, plutonic, structural, and tectonic events in the closing stages of the northern East African Orogen: Journal of African Earth Sciences, v. 61(3), p.167–232.

Kabete, J.M., Groves, D.I., McNaughton, N.J. and Mruma, A.H., 2012, A new tectonic and temporal framework for the Tanzanian Shield: implications for gold metallogeny and undiscovered endowment: Ore Geology Reviews, v. 48, p. 88–124.

Kampunzu, A.B., Bonhomme, M.G. and Kanika, M., 1998, Geochronology of volcanic rocks and evolution of the Cenozoic Western Branch of the East African Rift System: Journal of African Earth Sciences, v. 26(3), p. 441–461.

Kasanzu, C.H., and Manya, S., 2020, Evidence for a Record of Possible Paleo-Tsunami or Storm Deposits in the Fluviatile Neoproterozoic Malagarasi Supergroup of North-Western Tanzania: Tanzania Journal of Science, v. 2, p. 460–474.

Kendall, B., Creaser, R.A., and Selby, D., 2006, Re–Os geochronology of postglacial black shales in Australia: Constraints on the timing of "Sturtian" glaciation: Geology, v. 34, p. 729–732, doi:10.1130/G22775.1.

Kennedy, M.J., Runnegar, B., Prave, A.R., Hoffmann, K.H. and Arthur, M.A., 1998, Two or four Neoproterozoic glaciations?: Geology, v. 26(12), p. 1059–1063.

Kennedy, M., 2013, The nonlinear effects of evolutionary innovation biospheric feedbacks on qualitative environmental change: From the microbial to metazoan world: The American Naturalist, v. 181(S1), p. 100–111.

Knoll, A.H., 2003, The geological consequences of evolution: Geobiology, v.1, p. 3–14, https://doi.org/10.1046/j.1472–4669.2003.00002.x

Kolodner, K., Avigad, D., McWilliams, M., Wooden, J.L., Weissbrod, T. and Feinstein, S., 2006, Provenance of north Gondwana Cambrian–Ordovician sandstone: U–Pb SHRIMP dating of detrital zircons from Israel and Jordan: Geological Magazine, v. 143(3), p. 367–391.

Kröner, A., and Rankama, K., 1972, Late Precambrian glaciogenic sedimentary rocks in southern Africa: A compilation with definitions and correlations: University of Cape Town Precambrian Research Unit Bulletin , v. 11, 37 p.

Kröner, A., Sacchi, R., Jaeckel, P.T. and Costa, M., 1997, Kibaran magmatism and Pan–African granulite metamorphism in northern Mozambique: single zircon ages and regional implications: Journal of African Earth Sciences, v. 25(3), p. 467–484.

Kröner, A., Willner, A.P., Hegner, E., Jaeckel, P. and Nemchin, A., 2001, Single zircon ages, PT evolution and Nd isotopic systematics of high–grade gneisses in southern Malawi and their bearing on the evolution of the Mozambique belt in southeastern Africa: Precambrian Research, v. 109(3–4), p. 257–291.

Kröner, A., Stern, R.J., 2004, Pan–African orogeny, in: Encyclopedia of Geology, v. 1, p. 1–12.

Kusky, T.M., Abdel Salam, M.G., Stern, R.J. and Tucker, R.D., 2003, Evolution of the East African and related orogens, and the assembly of Gondwana: Precambrian Research, v. 123, n. 2, p. 81 – 85.

Lenoir, J.L., Liégois, J.P., Theunissen, K., and Klerkx, J., 1994, The Palaeoproterozoic Ubendian shear belt in Tanzania: geochronology and structure: Journal of African Earth Sciences, v. 19, n. 3, p. 169–184, https://doi .org/10.1016/0899–5362(94)90059–0.

Lund, K., Aleinikoff, J.N., Evans, K.V. and Fanning, C.M., 2003, SHRIMP U–Pb geochronology of Neoproterozoic Windermere Supergroup, central Idaho: Implications for rifting of western Laurentia and synchroneity of Sturtian glacial deposits: Geological Society of America Bulletin, v. 115(3), p. 349–372.

Maboko, M.A. and Nakamura, E., 1996, Nd and Sr isotopic mapping of the Archaean–Proterozoic boundary in southeastern Tanzania using granites as probes for crustal growth: Precambrian Research, v. 77(1–2), p. 105–115.

Macgregor, D., 2015, History of the development of the East African Rift System: A series of interpreted maps through time: Journal of African Earth Sciences, v. 101, p. 232–252.

MacLennan, S.A., Eddy, M.P., Merschat, A.J., Mehra, A.K., Crockford, P.W., Maloof, A.C., Southworth, C.S., and Schoene, B., 2020, Geologic evidence for an icehouse Earth before the Sturtian global glaciation: Science Advances, v. 6, p. 1–6, doi:10.1126/sciadv.aay6647.

Maloof, A.C., Halverson, G.P., Kirschvink, J.L., Schrag, D.P., Weiss, B.P. and Hoffman, P.F., 2006, Combined paleomagnetic, isotopic, and stratigraphic evidence for true polar wander from the Neoproterozoic Akademikerbreen Group, Svalbard, Norway: Geological Society of America Bulletin, v. 118(9), p. 1099–1124.

Master, S., Rainaud, C., Armstrong, R.A., Phillips, D., and Robb, L.J., 2005, Provenance ages of the Neoproterozoic Katanga Supergroup (Central African Copperbelt), with implications for basin evolution: Journal of African Earth Sciences, v. 42, p. 41–60, doi:10.1016/j.jafrearsci.2005.08.005.

Meert, J.G., and Voo, R. van der, 1994, The Neoproterozoic (1000–540 Ma) glacial intervals: No more snowball earth? Earth and Planetary Science Letters, v. 123, p. 1–13, doi:10.1016/0012–821x(94)90253–4.

Meert, J.G., 2003, A synopsis of events related to the assembly of eastern Gondwana: Tectonophysics, v. 362(1–4), p. 1–40.

Möller, A., Mezger, K. and Schenk, V., 2000, U–Pb dating of metamorphic minerals: Pan–African metamorphism and prolonged slow cooling of high pressure granulites in Tanzania, East Africa. Precambrian Research, v. 104(3–4), p. 123–146.

Mruma, A.H., 1989, Stratigraphy, metamorphism and tectonic evolution of the early Proterozoic Usagaran Belt, Tanzania: Research Terrae, 193 p.

Muhongo, S., Kröner, A. and Nemchin, A.A., 2001, Single zircon evaporation and SHRIMP ages for granulite–facies rocks in the Mozambique Belt of Tanzania: The Journal of Geology, v. 109(2), p. 171–189.

Piper, J.D.A., 1972, A Palaeomagnetic Study of the Bukoban System, Tanzania: Geophysical Journal of the Royal Astronomical Society, v. 28, p. 111–127, doi:10.1111/j.1365–246x.1972.tb06116.x.

Prave, A.R., Condon, D.J., Hoffmann, K.H., Tapster, S., and Fallick, A.E., 2016, Duration and nature of the end-Cryogenian (Marinoan) glaciation: Geology, v. 44, p. 631–634, doi:10 .1130/G38089 .1.

Priem, H.N.A., Boelrijk, N.A.I.M., Hebeda, E.H., Verdurmen, E.T., Verschure, R.H., Oen, I.S. and Westra, L., 1979, Isotopic age determinations on granitic and gneissic rocks from the

Ubendian–Usagaran System in southern Tanzania: Precambrian Research, v. 9(3–4), p. 227–239.
Rea, D.K. AND Janecek, T.R., 1981, Late cretaceous history of eolian deposition in the mid–pacific mountains, central North Pacific Ocean: Palaeogeography, Palaeoclimatology, Palaeoecology, v. 36, p. 55–67.
Retallack, G.J., 2011, Neoproterozoic loess and limits to snowball earth: Journal of the Geological Society, v. 168, p. 289–307, doi:10.1144/0016–76492010–051.
Retallack, G.J., 2023, Why was there a Neoproterozoic Snowball Earth?: Precambrian Research, v. 385, doi:10.1016/j.precamres.2022.106952.
Richards, J.P., Cumming, G.L., Krstic, D., Wagner, P.A. and Spooner, E.T.C., 1988, Pb isotope constraints on the age of sulfide ore deposition and U–Pb age of late uraninite veining at the Musoshi stratiform copper deposit, Central Africa copper belt, Zaire: Economic Geology, v. 83(4), p. 724–741.
Roberts, E.M., Stevens, N.J., O'Connor, P.M., Dirks, P.H.G.M., Gottfried, M.D., Clyde, W.C., Armstrong, R.A., Kemp, A.I.S., and Hemming, S., 2012, Initiation of the western branch of the East African Rift coeval with the eastern branch: Nature Geoscience, v. 5, p. 289–294, doi:10.1038/ngeo1432.
Rooney, A.D., Strauss, J.V., Brandon, A.D. and Macdonald, F.A., 2015, A Cryogenian chronology: Two long–lasting synchronous Neoproterozoic glaciations: Geology, v. 43(5), p. 459–462.
Schandelmeier, H., 1983, The geochronology of post–Ubendian granitoids and dolerites from the Mambwe area, northern province, Zambia. Report 83(1): Institute of Geological Sciences, p. 40–46
Schmidt, P.W. and Williams, G.E., 1995, The Neoproterozoic climatic paradox: equatorial palaeolatitude for Marinoan glaciation near sea level in South Australia: Earth and Planetary Science Letters, v. 134(1–2), p. 107–124.
Scotese, C.R., 2021, An atlas of phanerozoic paleogeographic maps: The seas come in and the seas go out: Annual Review of Earth and Planetary Sciences, v. 49, p. 679–728, doi:10.1146/annurev–earth–081320–064052.
Sharman, G.R., Sharman, J.P., and Sylvester, Z., 2018, detritalPy: A Python - based toolset for visualizing and analysing detrital geothermochronologic data, p. 202–215, doi:10.1002/dep2.45.
Stern, R.J., 1994. Arc assembly and continental collision in the Neoproterozoic East African Orogen: implications for the consolidation of Gondwanaland. Annual Review Earth Planetary Science, v. 22, p. 319–351.
Stern, R.J., Avigad, D., Miller, N.R., and Beyth, M., 2006, Evidence for the Snowball Earth hypothesis in the Arabian–Nubian Shield and the East African Orogen: Journal of African Earth Sciences, v. 44, p. 1–20, doi:10.1016/j.jafrearsci.2005.10.003.
Stern, R.J., Avigad, D., Miller, N., and Beyth, M., 2008, From Volcanic Winter to Snowball Earth: An Alternative Explanation for Neoproterozoic Biosphere Stress, in Y. Dilek et al. (eds.), Links Between Geological Processes, Microbial Activities & Evolution of Life: Springer, p. 313 – 337.
Stern, R.J., Johnson, P.R., Ali, K.A., and Mukherjee, S.K., 2011, Evidence for early and mid–Cryogenian glaciation in the Northern Arabian–Nubian Shield (Egypt, Sudan, and western Arabia): Geological Society Memoir, v. 36, p. 277–284, doi:10.1144/m36.22.

Sur, S., Soreghan, M.J., Soreghan, G.S., AND Stagner, A.F., 2010, Extracting the silicate mineral fraction from ancient carbonate: assessing the geologic record of dust: Journal of Sedimentary Research, v. 80, p. 763–769.

Swanson–Hysell, N. L., Maloof, A. C., Weiss, B. P., and Evans, D.A., 2009, No asymmetry in geomagnetic reversals recorded by 1.1–billion–year–old Keweenawan basalts: Nature Geoscience, v. 2 (10), p. 713–717.

Tack, L., Wingate, M.T.D., De Waele, B., Meert, J., Belousova, E., Griffin, B., Tahon, A. and Fernandez–Alonso, M., 2010, The 1375 Ma "Kibaran event" in Central Africa: Prominent emplacement of bimodal magmatism under extensional regime: Precambrian research, v. 180(1–2), p. 63–84.

Trompette, R., 1994, Geology of Western Gondwana (2000–500 Ma), Pan–African–Brasiliano aggregation of South America and Africa: Balkema, 350 p.

Tziperman, E., Halevy, I., Johnston, D.T., Knoll, A.H., and Schrag, D.P., 2011, Biologically induced initiation of Neoproterozoic snowball–Earth events: Proceedings of the National Academy of Sciences, v. 108, p. 15091–15096, doi:10.1073/pnas.1016361108.

Vermeesch, P., 2012, On the visualisation of detrital age distributions: Chemical Geology, v. 312–313, p. 190–194.

Vinyu, M.L., Hanson, R.E., Martin, M.W., Bowring, S.A., Jelsma, H.A., Krol, M.A. and Dirks, P.H., 1999, U–Pb and $^{40}Ar/^{39}Ar$ geochronological constraints on the tectonic evolution of the easternmost part of the Zambezi orogenic belt, northeast Zimbabwe: Precambrian Research, v. 98(1–2), p. 67–82.

Wendt, I., Besang, C., Harre, W., Kreuzer, H., Lenz, H., and Mu¨ller, P., 1972, Age determi– nations of granitic intrusions and metamor– phic events in the Early Precambrian of Tan– zania: International Geological Congress, 24th, Montreal, 1972, Proceedings, p. 295–314.

CHAPTER III

LOESS AND PALEOSOLS RECORDED IN THE NEOPROTEROZOIC MANYOVU REDBEDS OF WESTERN TANZANIA

LOESS AND PALEOSOLS RECORDED IN THE NEOPROTEROZOIC MANYOVU REDBEDS OF WESTERN TANZANIA

ABSTRACT

The Neoproterozoic Manyovu redbeds are exposed along uplifted, normal fault blocks that bound Lake Tanganyika in northwestern Tanzania. These units have been described as thick (up to 400-600 m), red, monotonous, micaceous, fine-grained sandstone and have received minimal study. We logged an ~285-m continuous exposure of this formation west of Mkalinzi, Tanzania and observed massive siltstone with blocky fracturing interbedded with tabular, very fine to fine-grained sandstone overlying a structureless basal sandstone. Results of particle-size analysis indicate that much of the section comprises medium – coarse siltstone (~65%) and the other ~35% of the section consists of very-fine to fine sandstone with grain-size modes <210 μm, with no sedimentary structures, channelization, or erosive contacts consistent with marine, fluvial, lacustrine, or deltaic deposition. Blocky fracturing throughout the siltstone, together with micromorphological features indicative of clay translocation and clay movement record soil-formation mechanisms. Based on these observations, we interpret the Manyovu redbeds to record deposition in an eolian-dominated setting, subject to relatively common pedogenesis. The thick intervals of structureless siltstone are most consistent with an interpretation as paleo-loess, whereas the structureless sandstone likely records eolian sand-sheet deposition. The substantial volume of silt represented by the thick and laterally persistent siltstone facies, together with its mineralogic immaturity and Neoproterozoic age, suggest a possible periglacial origin. Loess has been only rarely documented for the Precambrian, and the Manyovu redbeds records, by far, the most voluminous loess in the Precambrian record.

INTRODUCTION

The Neoproterozoic (541 – 1000 Ma) records a time of global rearrangement of tectonic plates, including rifting of the supercontinent Rodinia (~830 Ma) and the subsequent assembly of Greater Gondwana (~630 Ma; e.g., Li et al., 2008; Stern et al., 2008). In addition to major tectonic events spanning this interval, the Neoproterozoic is known for extreme climatic change during the Cryogenian (720 – 635 Ma) and Ediacaran (635 – 541 Ma) time periods. The Cryogenian records at least two "icehouse" episodes: the Sturtian (~725 – 645 Ma) and Marinoan (~650 – 635 Ma) events (e.g., Hoffman et al., 1998; Hoffman and Schrag, 2002; Halverson et al., 2005; 2020). Many studies have suggested the Marinoan glacial event was pervasive, with glacial deposits located world-wide (e.g., Hoffman et al., 2002, 2017; Stern et al., 2008; Hofmann et al., 2015; Prave et al., 2016), with the end of the Marinoan glaciation marking the start of the Ediacaran period (~635 Ma). The Ediacaran is known for multiple glacial periods, but the most well-studied is the Gaskiers (~580 Ma) which has also been documented globally on at least eight paleocontinents (e.g., Hoffman and Li, 2009). However, studies have documented inferred periglacial deposits within this time range, especially in paleotropical regions (e.g., Edwards 1979; Retallack, 2011, 2023; Benn et al., 2015; Retallack et al., 2015,

2021; Liu et al., 2020), indicating the existence of unglaciated areas and times, especially at the end of the Cryogenian into the Ediacaran.

Here, we provide the first detailed documentation of the Manyovu redbeds— the youngest sedimentary unit within the Neoproterozoic Uha Group, exposed along the eastern margin of Lake Tanganyika in western Tanzania, which was located just south of the equator during the formation of Pannotia (Fig. 1, 2, 3). Previous studies of the unit were entirely reconnaissance in nature as research focused on broad descriptions and paleomagnetism of Precambrian units in Tanzania (e.g., Halligan, 1962; Piper 1972; Cahen and Snelling, 1974). These studies described the Manyovu redbeds as monotonous, massive, fine-grained and micaceous red sandstone and siltstone, locally with "current bedding" and ripple marks (Halligan, 1962; Piper, 1972). No detailed depositional interpretations exist, other than an assertion by Halligan (1962) of a marine origin, and a single sentence in Piper (1972) noting the presence of channel fills, ripple marks, and mud cracks to suggest "rapidly deposited, shallow-water rocks" (Piper, 1972 p. 114). Critically, new age constraints on the Manyovu redbeds indicate maximum depositional ages (MDA) for the mid – upper strata as 613.6 ± 2.0 Ma (Bonar et al., in review), indicating these deposits likely accumulated between the Marinoan Snowball event (~635 Ma) and the Gaskiers event (~580 Ma) in the Ediacaran. Accordingly, these strata present an opportunity to further constrain paleoenvironments in this region during a critical time of severe climate change in Earth history. The goal of this study is to interpret the depositional setting of the Manyovu redbeds and assess the climatic significance of the inferred transport and depositional processes in a neo-tropical setting during this period of profound climatic and paleogeographic change.

GEOLOGIC SETTING

The study area is located approximately 5° south of the equator within northwestern Tanzania, just south of the border with Burundi on the northeastern margin of Lake Tanganyika (Fig. 1). Lake Tanganyika borders western Tanzania and eastern Democratic Republic of the Congo (DRC) in East Africa and is part of a multisegmented rift basin within the Western Branch of the East African Rift System (EARS; Rosendahl et al., 1986; Sander and Rosendahl, 1989). EARS deformation began in the Early Miocene (*ca.* 22 – 25 Ma; e.g., Roberts et al., 2012; Macgregor, 2015), and the Manyovu redbeds crop out in the footwall block of one of the fault segments that border Lake Tanganyika.

During the Neoproterozoic, Tanzania was located between 15 – 30° south of the equator (Fig. 3; e.g., Li et al., 2008, 2013; Scotese, 2021). The early-mid Neoproterozoic marked the formation and subsequent break-up of the supercontinent Rodinia, which resulted in widespread rift-related tectonism and volcanism throughout the Cryogenian period (e.g., Frimmel et al., 2002; Stern et al., 2008). The late Neoproterozoic marked the re-assembly of continental fragments to form Pannotia/Greater Gondwana, resulting in Pan African Orogenesis and the East African Orogen which extends from northeastern Africa to west-central Africa (e.g., Stern et al.,

2008; Scotese, 2009). The formation of Pannotia involved a series of collisions that began around 750 Ma (e.g., Stern, 1994) and Pan-African orogenesis peaked between ~610 – 640 Ma (Fig. 2; e.g., Meert, 2003). Peak orogenesis also coincided with the hypothesized Marinoan Snowball Earth, estimated to extend over ~16 My, lasting from ~651 – 635 Ma, and marking the end of the Cryogenian period (e.g., Zhou et al., 2019; Nelson et al., 2020). Prior to the Cryogenian, multiple glacial episodes occurred, the first being the Bitter Springs glacial event, which is poorly constrained and remains debated, but is hypothesized to have occurred between ~800 – 815 Ma (Fig. 2; Stern et al., 2011; Swanson-Hysell et al., 2015). Following the Bitter Springs, the Mahd (780 – 800 Ma; Stern et al., 2011; Swanson-Hysell et al., 2015), and Kaigas (~750 Ma; Hoffmann et al., 2006) events occurred as separate, non-global glacial episodes. The Sturtian was the first event within the Cryogenian, and while it is identified globally, the timing of glacial events indicates multiple episodes (e.g., Hoffman and Lo, 2009). Finally, the Ediacaran Gaskiers glaciation (~580 Ma) has also been hypothesized to have been global like other Snowball Earth events, considering paleomagnetic data from known deposits suggest paleolatitudes within 30° of the paleoequator (e.g., Pisarevsky et al., 2011; Pu et al., 2016), but data are limited.

The Manyovu redbeds are part of the Uha Group within the Neoproterozoic Bukoban Supergroup in western Tanzania (Fig. 2). The Uha Group consists of three formations: the Gagwe Amygdaloidal Lavas (~ 820 Ma; Briden et al., 1971; Deblond et al., 2001), followed by the Ilagala Dolomitic Limestone (undated; e.g., Halligan, 1962), and finally the Manyovu redbeds, all bounded by unconformities of uncertain durations. New data indicate that the Manyovu redbeds are of Neoproterozoic age, with an oldest reported MDA of 663.8 ± 2.0 Ma in the lower-most strata, and a youngest depositional age of 613.6 ± 1.2 Ma (Bonar et al., in review). These dates imply that the Manyovu redbeds began accumulating either in the late Cryogenian and continued into the Edicaran, or that the Manyovu redbeds are completely Ediacaran in age. Multiple studies on the Gagwe Amygdaloidal Lavas report paleolatitude estimates (29º S – 12º S; Piper et al., 1972; Meert et al., 1995). With the exception of the volcanics, the Uha Group has not been studied in terms of depositional environments or processes.

METHODS

Field Analysis

Generally, dense vegetation obscures the Manyovu redbeds, and has precluded detailed study of these units. We reconnoitered the region and chose a location west of Mkalinzi, Tanzania, where heavy foot-traffic by local villagers created a path, albeit laterally restricted, which reveals a continuous exposure of the Manyovu redbeds in a manner that is perpendicular to dip and easily accessible. The beds exhibit an average strike of 10° N and dips range between 28° – 32° E. This exposure enabled us to log and describe at cm- to meter-scale resolution a total of 285 m of continuous section to provide the first detailed facies descriptions for the Manyovu

redbeds (Fig. 4). Samples were collected from ~20 intervals for thin section petrography, geochemistry, particle-size, and provenance analyses (Bonar et al., in review), but the total rock volume allowable for export was highly regulated, which exerted significant restrictions on sampling. Halligan (1962) estimated a total thickness of up to 900 m for the Manyovu redbeds, but more recent work estimated thicknesses at 400 – 600 m (Deblond et al., 2001), based primarily on map projections, including a basal conglomeratic interval missing in our study region. However, in our section, the base of Manyovu was obscured under valley alluvium and so the total thickness of the Manyovu in this location could be in the range of these previous estimates.

Particle-size Analysis

Particle-size analysis (N=17) was conducted on samples from throughout the logged section. A majority of the Manyovu interval is remarkably friable and easily disaggregated by hand. For more-lithified intervals, a ceramic mortar and pestle was used to crush samples to pea-sized granules (>250 μm) in order to increase surface area for chemical disaggregation techniques (following Sur et al., 2010). After sieving the granules with distilled water to remove any fines generated during crushing, samples were submerged in 2N HCl for 24 hours to remove carbonate minerals and cement, and combusted at 500 ºC for ~15 hours to remove any organic material. Then, samples were treated with citrate-bicarbonate-dithionite (CBD; Rea and Janecek, 1981) to remove iron oxides. All samples were prepped as smear slides and analyzed under a microscope to ensure full disaggregation. Fully disaggregated samples were then sonicated for two minutes with a few drops of sodium hexametaphosphate as a dispersant, immediately prior to analysis using a Malvern Mastersizer 3000 Laser Particle Size Analyzer at the University of Oklahoma. We report particle-size distributions (PSDs) and grain size modes for each interval.

RESULTS

Sedimentologic data and interpretations

Basal Sandstone Facies

Description: The basal sandstone facies forms the first ~70 m of the study section (Fig. 4). This facies is typically light pink to white and occurs in tabular beds that range in thickness from ~20 – 40 cm (Fig. 5). The pink sandstone is less resistant than the white sandstone units, and bedding contacts are nonerosive to gradual. This unit is surprisingly friable, susceptible to disaggregation by hand. The basal sandstone is internally structureless, with no observed grading, laminations, cross-stratification, or ripple marks. In thin section, samples are grain supported, with moderately- to well-rounded grains (Fig. 6). Particle-size analysis reveal modes between 159 – 209 μm (fine sand; Wentworth, 1922) and PSDs are unimodal and generally narrow indicating these samples are well-sorted (Fig. 7). Point counts indicate framework modal compositions of predominantly quartz (76%), with subordinate feldspar (13%), and lithic

fragments (11%), the latter consisting of mostly volcanic lithics with very minor and rare occurrences of metamorphic and sedimentary lithics.

Interpretation: The massive and structureless basal sandstone facies is challenging to interpret given its significant (>70 m) thickness of uniform sandstone, absence of diagnostic structures, limited lateral exposure, and uniformly fine modes (159-209 μm). Given this, we propose multiple working hypotheses for the interpretation of this unit.

This interval could form part of a braided fluvial system, similar to those described by Martin and Turner (1998). Massive and structureless sand bodies in braided fluvial systems result from deposition of highly concentrated sediment/water mixtures associated with hyper-concentrated flooding, and suspension of sandy material (Martin and Turner, 1998; Marren et al., 2002). Hyper-concentrated flows are indicative of extreme flooding with high discharge conditions, and while such high-energy system can produce large volumes of sediment with poor imbrication and structureless character, they also can also produce deposits that show reserve grading, horizontal stratification, and "floating" grains (e.g., Marren et al., 2002), although this depends upon the available sediment caliber. However, massive and structureless sands in braided river systems are typically laterally and vertically associated with cross-stratified sands, basal erosion surfaces and channeling, and/or other features indicative of fluvial deposition (e.g., Jones and Rust, 1983; Khalaf, 2012), which do not occur in the study interval or correlative exposures.

The second hypothesis holds that this facies accumulated in an eolian environment, consistent with its uniformly fine grain size and occurrence of rounded sand grains. Deposition in an eolian sand system classically entails development of diagnostic structures such as large-scale (dune slip-face) cross-stratification, and characteristic small-scale structures such as wind-ripple (translatent), grain-flow and grain-fall stratification (e.g. Hunter, 1977), none of which are observed in this facies. However, massive sandstones similar to those observed in our study area do occur within eolian systems (e.g., Simpson et al., 2002; Parrish and Falcon-Lang, 2007) as mass flow, interdune deposits. The mass flow deposits typically result from extreme precipitation events, and/or seismic activity that disrupts the integrity of dunes and sand sheets, and results in deposition of internally massive, uniformly fine-grained sand (e.g., Loope et al., 1999; Simpson et al., 2002; Parish and Falcon-Lang, 2007). However, mass flows in eolian systems are consistently associated with other eolian-dune sedimentary structures, as described above, which we do not observe at the scale of our outcrops.

An alternative take on the eolian-based hypothesis entails deposition in a large, desert basin such as modern-day Devin Island, Canada (e.g., Lewis et al., 2002). Sparse vegetation in arid settings promotes deflation of fines for down-wind concentration in isolated basins, trapped by microbial mats common in modern cold and arid continental environments (e.g., Sohm et al., 2020), and which result in accumulation of structureless or poorly structured sediment. Such

mats were prevalent during the Neoproterozoic (e.g., Lan and Chen, 2013), although no obvious evidence appears in the study strata.

Massive Red Siltstone Facies

Description: The massive red to red-brown siltstone facies accounts for the predominant fraction of the study section, approximately 65% (180-m) in total. This facies crops out primarily as thick (up to 50 continuous meters lacking perceptible bedding), massive, internally structureless units (Fig. 5). The siltstone facies commonly displays a blocky fracture pattern, with rare occurrences of unfractured, bulbous, thin (~3-30 cm) beds (Fig. 5). Additional occurrences of bedding are rare, but are developed in a few horizons as thin, tabular beds (Fig. 5), between 5 – 30-cm thick. This facies persists laterally, as we located a correlative section ~15 km north of the study area with continuous exposure and comparable attributes – massive siltstone with blocky fractures, and no channelization (see supp. Files for additional field photos).

In thin section, samples are consistently fine albeit poorly sorted with angular – sub-angular grains (Fig. 6). Particle-size analysis indicates modes of 20 – 53 μm (medium – coarse silt; Wentworth, 1922), and PSDs are generally unimodal, but with broad peaks that include both coarse (~200 μm) and very fine (<1 μm) components (Fig. 7). The distributions are fine-skewed with a moderate contribution of grains between 1 – 10 μm, confirming the predominantly poor sorting. Elongated, needle-like (sizes are comparable to other grains within this facies with the largest dimension as ~50 μm, and aspect ratios are ~1:9) white to gray detrital grains occur sporadically (Fig. 6); their morphology together with reported EDS mapping (Supp. Files) indicate these are likely evaporite pseudomorphs replaced by silica. In general, larger grains are supported within a fine-grained matrix typically composed of iron-rich clay minerals, which mimics a porphyroskelic fabric (cf. Retallack, 2008); however, the proportion of clay matrix (both grain-size and mineralogy) varies throughout the facies (Fig. 6). There are also instances of grains coated by bright clays, termed skelsepic plasmic fabrics (Fig. 6; Retallack, 2008). Modal compositions are predominantly quartz (57%) with significant feldspar (23%), and subordinate lithic fragments (11%; predominantly volcanic with rare occurrences of metamorphic and sedimentary lithics), but this facies contains much more mica than the sandstone facies (up to 14%).

Interpretation: The structureless, uniformly fine-grained and positively (fine-) skewed character of the siltstone unit is most consistent with an interpretation as (lithified) loess (e.g., Catt, 1988; Johnson, 1989; Pye, 1995; Assallay et al., 1998; Soreghan et al., 2008; Sweet et al., 2013; Muhs, 2013, 2018; Foster et al., 2014; Pfeifer et al., 2020). Loess consists of deposits of eolian silt, and typically exhibits particle-size modes ranging between ~20 – 50 μm (e.g., Catt, 1988; Smalley, 1995; Assallay et al., 1998; Muhs, 2013), although modal particle size distributions vary because loess fines with transport distance (e.g., Pye, 1987; Muhs and Bettis, 2003; Porter, 2001; Muhs, 2013, 2018). The massive, structureless character precludes sediment

delivery by channelized flow (e.g. fluvial or deltaic systems), or subaqueous deposition, but is consistent with fallout from atmospheric suspension. Furthermore, the occurrence (documented below) of pedogenic features throughout this facies establishes a subaerial environment of deposition, and is common in loess accumulations (see review by Muhs, 2013). These observations and interpretations are consistent with other loess deposits, including modern loess (Catt, 1988; Smalley, 1995; Assallay et al., 1998; Muhs and Bettis, 2003; Muhs, 2013; Li et al., 2020), as well as examples from the late Paleozoic (e.g., Johnson, 1989; Soreghan et al., 2008; Pfeifer et al., 2020), and the rare examples published of Neoproterozoic loess (Edwards, 1979; Retallack, 2011, 2022). The tabular, thin interbeds compose only a small percentage of the siltstone unit (<15%) and other than the range of grain sizes from both silt to fine sand (53 – 199 μm), show no differences from the rest of the facies. We interpret these beds to represent changes in water availability, likely as sand-water flows or intermittent water-pooling. Sand-water flows can have various origins (e.g., melt-water run-off and high precipitation events), various grain to water ratios, and can range in size from cm- to meter-scale and are common in eolian-dominated environments with sparse vegetation (Sweeney and Loope, 2001; Hugenholtz et al., 2007).

The silica pseudomorphs of inferred gypsum are interpreted to have a detrital origin. The pseudomorphs tend to occur as individual grains dispersed throughout the massive siltstone facies, rather than in concentrated horizons. Whereas similar gypsum occurrences in other redbed successions are interpreted as lacustrine deposits (e.g., Valero Garcés and Aguilar, 1992), the dispersed distribution of individual grains in the Manyovu succession suggests a detrital origin, likely sourced from the Katanga Supergroup of the Lufilian Arc west of the study area. Within the Katanga Supergroup, the Roan Group (*ca.* 1050 – 950 Ma; Cahen et al., 1984), contains evaporites, including silica pseudomorphs of both gypsum and anhydrite crystals (Jackson et al., 2003), and the provenance of the Manyovu redbeds reflects both local and regional sources, with transport distances of <50 – 350 km (Bonar et al., in review). These distances are well within the range of transport of silt-sized dust (e.g., Betzer et al., 1988; Ratmeyer et al., 1999; Stuut et al., 2005; Muhs, 2013).

Pedogenesis within the Massive Red Siltstone Facies

Description: Blocky fracturing (Fig 5) occurs throughout the massive siltstone facies, which also contain micromorphologic attributes that include bright clay matrices, which are either highly oriented clay minerals that exhibit a high birefringence under crossed nicols throughout the thin section (Fig. 6; sepic plasmic fabric; Brewer, 1976), or where the highly birefringent clays are more isolated, “wispy,” and randomly oriented (Fig. 6; argillasepic fabric; Retallack, 2008). Concretions of up to ~15-cm diameter occur confined to a few horizons, and tend to occur above thick, continuous sections of this facies, capping the exposures with the blocky fracturing of the siltstone facies (Fig. 4, 5). These concretions are internally massive with no concentric layers and display no obvious changes in mineralogy compared to the overall siltstone facies, but do contain more clay-rich matrix with larger grains more dispersed (Fig. 6).

Interpretation: Several of the macro- and (especially) micromorphological features observed indicate clay translocation and other processes most consistent with pedogenesis, albeit in the absence of rooting or animal activity, given the stratal age. For example, randomly oriented cracks that produce an angular blocky fracture pattern reflect formation of soil aggregates (soil structure) related to processes such as wetting and drying or freezing and thawing at the surface (e.g., Mack et al., 1993; Retallack, 2008; French and Shur; 2010). Soil aggregates can be angular – subangular and range in size from a few centimeters to ~20 cm. Pedogenesis can form by "upbuilding" in loess successions, where paleosol formation competes constantly with dust accumulation as the landscape continues to aggrade, which can cause pedogenesis to pervade the entire loess succession (e.g. Johnson and Watson-Stenger, 1987; Almond and Tonkin, 1999). The random orientations of the fracture patterns, together with the occurrence limited to the loess facies eliminates a tectonic explanation for these fractures.

The identified microfabrics are indicative of soil-forming processes. Bright clay fabrics (e.g., sepic plasmic fabric) obscure original sedimentary textures as a soil develops due to processes such as clay washing into cracks, internal stresses, and surface weathering of soil peds (Brewer, 1976; Fitzpatrick, 1984; Retallack, 2008). The grains coated in bright clays (skelsepic plasmic fabric) can be indicative of pedogenesis as well, but can also be indicative of rip-up clasts or even thin-section preparation (e.g., Retallack, 2008). The bright clay fabric is most distinguishable in the clay concretions (Fig. 6), which also contain the highest percentages of clay-rich matrix; but other thin sections from the siltstone facies show lenses of high-birefringence clay implying pedogenic processes throughout this facies.

The amalgamated concretions are the most enigmatic observation within the Manyovu redbeds, with no modern and ancient analogs currently identified. Other than the concretion-style structure at outcrop scale, little textural or compositional differences occur between the concretions and the siltstone facies. Similar features including micritic nodules of up to 12-cm diameter occur within the Ediacaran Nuccaleena Formation in South Australia, interpreted to record pedogenesis (Retallack, 2011). These nodules do not have concentric layering and contain quartz and other silicate minerals within a micritic matrix, which are considered typical replacement fabrics of caliche nodules (Retallack, 1997, 2011), common in aridisols (e.g., Mack et al., 1993). Given the location of the concretion horizons within the section, they likely record Precambrian soil formation.

DISCUSSION

Recognition of Neoproterozoic Loess

The persistent themes within the study section are: 1) the overall lack of macroscopic sedimentary structures, bedding, and bedding contact features such as erosive or channel features; 2) the mineralogically immature and ubiquitous fine-grained nature of the sediment, 3) the predominance of blocky fracturing within the siltstone unit, and 4) associated occurrences of micromorphological features consistent with pedogenesis. Taken together, these attributes are

most consistent with eolian transport for much of the sediment, and a continental setting conducive at times to pedogenesis. Therefore, we favor an eolian interpretation for the Manyovu redbeds, with the siltstone facies interpreted as Neoproterozoic loess.

Documentation of loess(ite) in the Precambrian is surprisingly rare. Edwards (1979) interpreted siltstone within the Smalfjord Formation of Norway and Svalbard (likely early Ediacaran age but with poor age constraints; Arnaud and Eyles, 2002; Arnaud, 2008) to be loess or loessite, based on observations of the predominance of angular, coarse silt that lacks stratification and sedimentary structures, and its association with inferred glacial deposits. The grain size and shape distributions, as well as the sorting from the Smalfjord Formation are comparable to the siltstone facies within the Manyovu redbeds. Additionally, the Smalfjord Formation has variable thicknesses as well as facies (e.g., Arnaud, 2008), but the fine-grained facies tends to make up a very small fraction (<10%) of the unit (e.g., Arnaud, 2008; Rice et al., 2011), likely only a few 10s of meters. Retallack (2011) re-interpreted cap-carbonates of the Nuccaleena Formation of South Australia (early Ediacaran in age; Knoll et al., 2006) as calcareous loess with evidence of pedogenesis, using criteria similar to that employed by Edwards (1979), such as the occurrence of angular, moderately sorted, coarse and siliciclastic silt, again consistent with the PSDs observed within the Manyovu siltstone. Retallack (2022) also discussed a new interpretation for a cap carbonate in California (Ediacaran Radcliff Member of the Noonday Formation) as a paleosol-loess sequence, with evidence for loess based on the high amounts of siliciclastic silt within the unit (up to 66%). The Nuccaleena Formation (<70 m thick; Plummer, 1978; Rose et al., 2010) and the Radcliff Member of the Noonday Formation (only ~50 m thick; Retallack, 2022) are also substantially thinner than the siltstone unit observed in the Manyovu. Accordingly, the siltstone facies of the Manyovu redbeds appears to record the thickest loess deposit yet documented in Earth's Precambrian record.

Redbed deposition spanning the Cryogenian – Ediacaran has been recognized as a global phenomenon (Kuang et al., 2022), which could be evidence for deposits similar and correlative to the Manyovu redbeds. Kuang and others (2022) noted that occurrences of Precambrian red siltstone are commonly interpreted as recording marine deposition; however, many regional redbeds (within Africa) remain understudied or have vague depositional interpretations, and exhibit attributes analogous to those of the Manyovu siltstone facies (Table 1). For example, the Cryogenian – Ediacaran Nguba and Kundelungu Groups (Katanga Supergroup) exposed in parts of northeastern Zambia and southeastern DRC contain similar attributes to the Manyovu and have been interpreted to represent similar basin histories. In Zambia, both groups contain basal conglomeratic units interpreted as diamictite, followed by carbonate units and upper siliciclastic units comprising shale, siltstone, and sandstone (Caiteux and Putter, 2019). In the DRC, the Katete Formation (middle Nguba Fm) comprises massive, irregularly layered siltstone, up to 230 m thick (Batumike et al., 2007), and the Monwezi member, which overlies the Katate at multiple localities, is described as massive siltstone, up to 500 m thick (Batumike et al., 2007). More distally in West Africa, the Nudas and Urusis Formations (Ediacaran Schwarzrand Subgroup) in

the Nama Basin of southwestern Namibia include siltstone with interbedded, massive, well-sorted sandstone, locally exhibiting wave ripples and desiccation cracks (Saylor et al., 1995; Blanco et al., 2011). None of these strata are currently interpreted as loess or paleosols, or even eolian in general (Table 1), but resemble the previous descriptions of the Manyovu redbeds prior to our reanalysis. Moreover, many of these units have not been dated precisely or studied in detail to better understand their depositional or paleoclimatic significance.

Paleoclimatic Significance

The occurrence of voluminous loess and pedogenically modified loess in the Manyovu redbeds has significant implications for interpretations of late Neoproterozoic climate. The formation of loess deposits implies a ready source of voluminous silt, a dust-emission area with conditions favorable for deflation, and subsequent eolian transport of fine sediment (e.g., Pye, 1995; Muhs, 2013). Abundant loess occurs on today's Earth commonly associated with Quaternary periglacial regions, as glacial grinding is an efficacious means to create large quantities of silt (e.g., Pye, 1995; Smalley, 1990, 1995; Wright et al., 1998; Assallay et al., 1998; Muhs and Bettis, 2003; Soreghan et al., 2008; Muhs, 2013, 2018; Smalley et al., 2019); such silt is commonly entrained in fluvial systems draining glaciated regions, before being deflated from dried floodplains and concentrated downwind. Relatively small accumulations of loess also occur today in warm-desert environments, unassociated with glacial processes (e.g., Pye and Tsoar, 1987; Liu et al., 1994; Porter, 2001; Crouvi et al., 2008), and a few paleo-loess deposits have been interpreted from non-icehouse intervals of Earth history (see Soreghan et al., 2022), but are commonly clay- and/or carbonate-rich. The large volume and mineralogical immaturity of the Manyovu siltstone facies is most consistent with silt generation via predominantly physical-weathering processes, e.g., glacial grinding and frost-weathering, which would indicate a potential correlation between the Manyovu sediments, and glacial periods of the latest Neoproterozoic.

Current work defines the end of the Marinoan Snowball Earth to fall ~635 Ma, based mostly on correlated radiometric ages from ash deposits bounding cap-carbonate and successions of glacial deposits (e.g., Kennedy, 1996; Knoll et al., 2006; Hoffman et al., 2017; Zhou et al., 2019; Nelson et al., 2020). Reported global cap-carbonate ages are all within error of this ~635 Ma age (Table 2). The interpreted loess by Retallack (2011, 2022) and loessite by Edwards (1979) are interpreted as coeval with the end or part of the Marinoan Snowball Earth (e.g., 635 Ma), given that the units discussed by Retallack (2011, 2022) are age-constrained by correlative cap-carbonate sequences, and the Smalfjord Formation discussed by Edwards contains interbeds of tillite and diamictite, yielding broad implications for the Snowball Earth hypothesis given their periglacial origins, indicating at least some nonglaciaited area during this time. The mid-Ediacaran Gaskiers glaciation is far less constrained in terms of age, but the tuffs that bracket diamictites in Newfoundland report U-Pb ages between 580.90 ± 0.40 Ma and 579.24 ± 0.17 Ma (Pu et al., 2016); however, no loess deposits have been documented within this time range. Age constraints for the Manyovu strata are currently reported as MDAs from detrital zircon spectra,

and the siltstone in the Manyovu interval exhibits MDAs as young as 613.6 ± 1.2 Ma (Bonar et al., in review)— indicating the siltstone facies of the Manyovu is at least ~614 Ma. Utilizing MDAs as depositional age-constraints can be laborious, as these ages are typically older than the true depositional age of the sedimentary unit; therefore, it is possible that the Manyovu siltstone is even younger than the reported age of 613.6 ± 1.2 Ma (see Bonar et al., in review for MDA interpretation details).

A depositional age of ~614 Ma (assuming the youngest reported MDA reflects true depositional age) would place Manyovu siltstone deposition within a time between major glaciations: younger than the Marinoan (635 Ma) event, and older than the Gaskiers (580 Ma) event. While much work has recognized paleo-loess associated with icehouse climates, there are examples of ancient loess from non-glaciated times, mostly from the Triassic (e.g., Chan, 1999; Horn and Schultz, 2018; Wilkins et al., 2018; Zhu et al., 2020). Many of these interpreted loess deposits exhibit similar attributes to the Manyovu: lack of macro-sedimentary structures, silt grain-size modes and distributions, and evidence for pedogenesis. However, loess and paleo-loess in modern and ancient non-glacial systems tend to contain substantial clay (~20-55%), in contrast to the quartzo-feldspathic, mineralogically immature composition of the Manyovu, which appears to be more indicative of periglacial loess (e.g., Soreghan et al., 2022). Therefore, it is also possible that the MDAs are much older than the true depositional age, and the Manyovu siltstone records loess deposition associated with periglacial environments during the Gaskiers glaciation around 580 Ma. Regardless, a stronger stratigraphic framework is needed to determine the validity of these working hypothesis, which would have large implications for the climatic context of loess deposition in the Neoproterozoic.

CONCLUSIONS

The Manyovu redbeds record the most extensive accumulation of Neoproterozoic loess yet documented. Our results highlight observations and new data that are consistent with sediment origins from glacial and periglacial environments; therefore, the ultimate depositional timing of the Manyovu redbeds could shed light on the extreme paleoclimatic conditions and fluctuations recorded in the Neoproterozoic. Additionally, the age-equivalent and sedimentologically similar units highlighted in this study could represent extensive dust deposition, fundamentally changing current paleogeographic reconstructions during this time.

ACKNOWLEDGEMENTS

We would like to thank our field assistants, Bren Cable and Mupape Mukuli for help with sample collection and field work. Also, the Tanzanian Fisheries Research Institute (TAFIRI) and the Tanzanian Mining Commission for research and logistics support. Thank you to Declan Martin for assistance with collected LPSA data. This work was completed under Tanzania Commission for Science and Technology Research Permit # 2021-445-NA-2018-169. This work was completed with funding support from the Robberson Research Grant (OU), NSF-EAR-

1424907 (Awarded to M. Soreghan), NSF-OISE-1658614 (Awarded to M. Soreghan and G. Soreghan), and the OU School of Geosciences Eberly Chair.

FIGURES AND TABLES

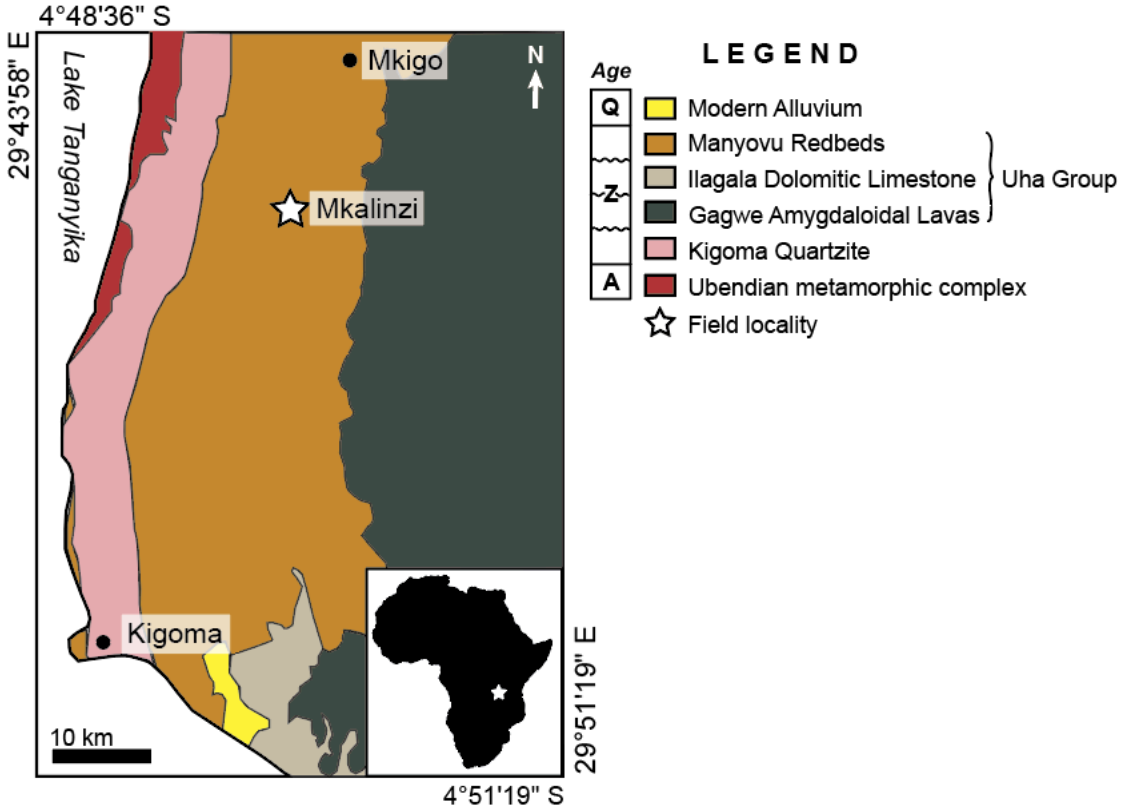


Figure 1. Geologic map showing the northeastern shore of Lake Tanganyika and Northwestern Tanzania just south of Burundi. Study area is marked by the white star. Map modified from Kasanzu and Manya (2020).

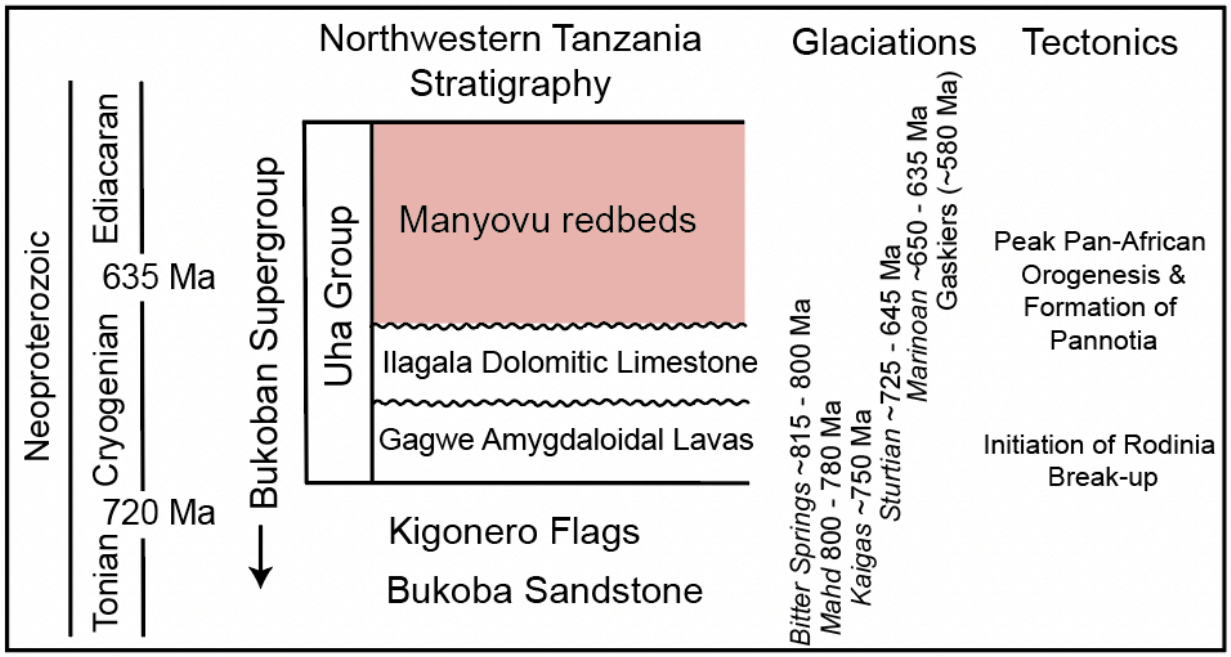


Figure 2. Generalized stratigraphic column showing the relationship among formations in the Neoproterozoic Bukoban Supergroup, Neoproterozoic glaciations, and major tectonic events. Stratigraphic column is modified from Halligan (1962), Cahen and Snelling (1974), and Deblond et al. (2001). Glacial and tectonic events modified from Stern et al. (2008).

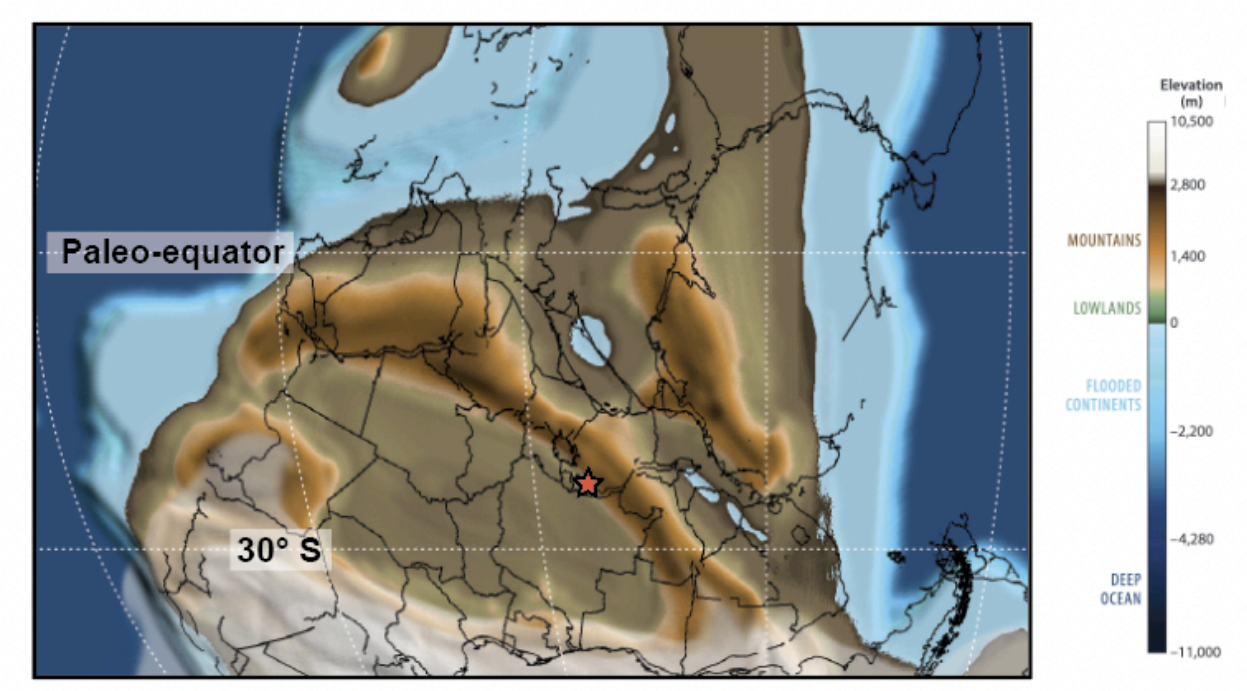


Figure 3. Paleogeographic map depicting continental distributions around 600 Ma (Mid-Ediacaran), representing the end of Manyovu redbed deposition. The study area (marked by the red star) is within 30º S of the paleoequator. Map projection modified from Scotese (2021).

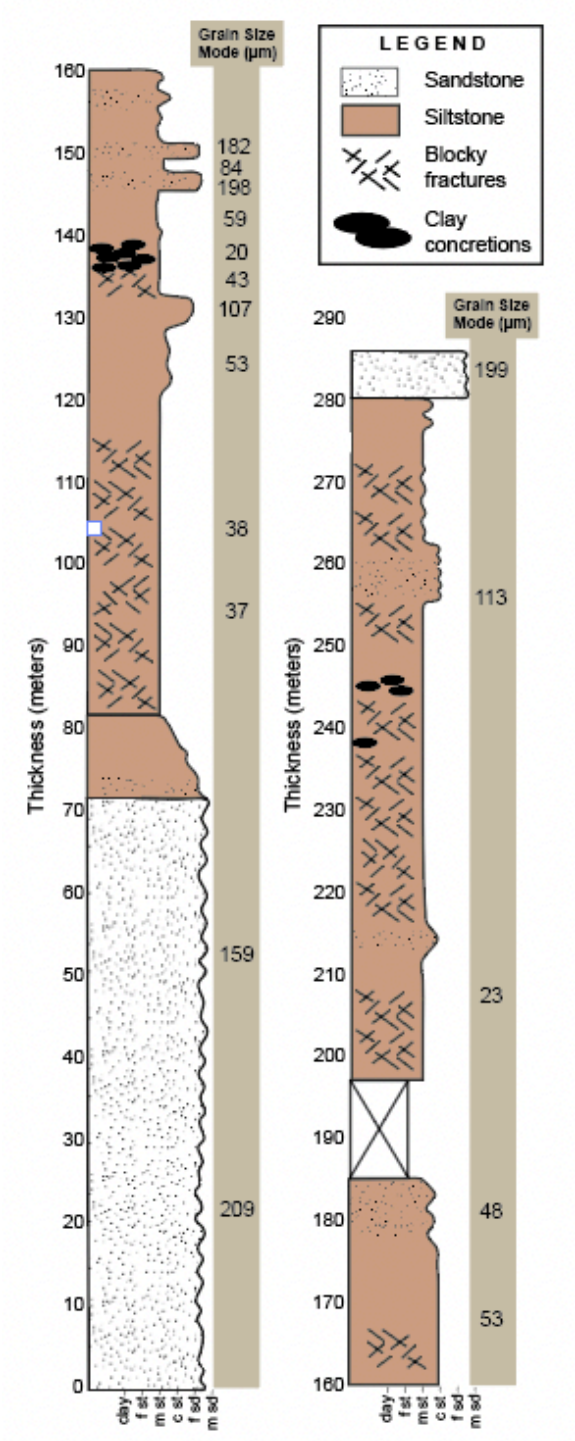


Figure 4. Stratigraphic measured section of the Manyovu redbeds in Mkalinzi, Tanzania. Grain size is represented on the x-axis and cumulative thickness on the y-axis. The tan bar to the right of the columns reports grain size modes for each of the different stratigraphic horizons.

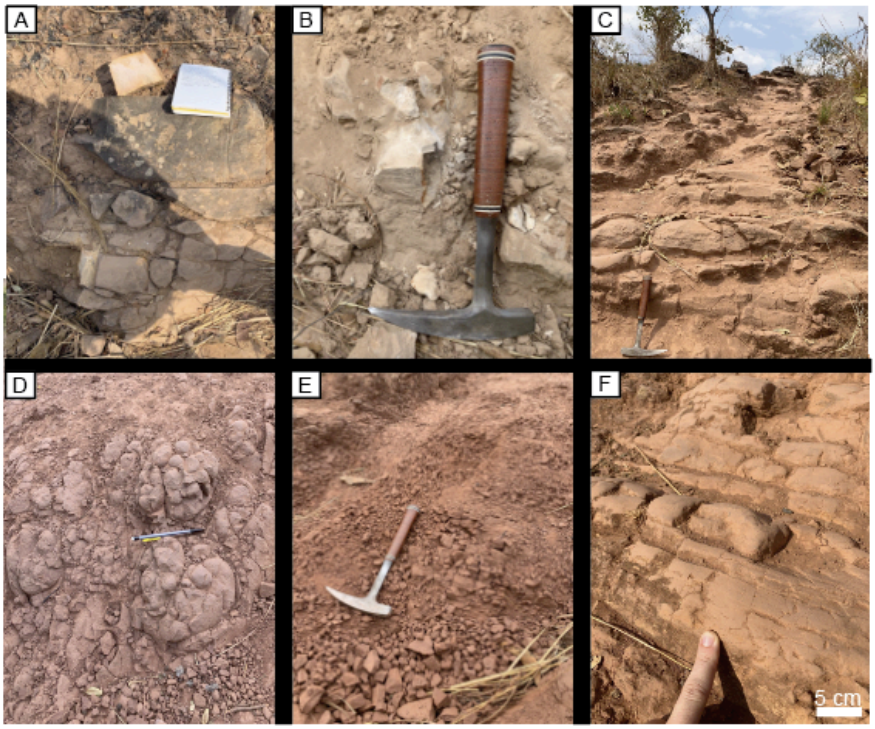


Figure 5. Representative field photos from each facies described within the study area. A) Example of pink sandstone from the basal sandstone facies; field notebook for scale. B) Example of the white sandstone from the basal sandstone facies showing internally structureless character; hammer for scale. C) Photo of the siltstone facies with bulbous bedding; hammer for scale. D) Amalgamated clay concretion horizon with concretions in-place; pencil for scale. E) Blocky fracturing from the siltstone facies; hammer for scale. I) Example of the siltstone facies without blocky fractures, instead as bulbous beds; scale noted.

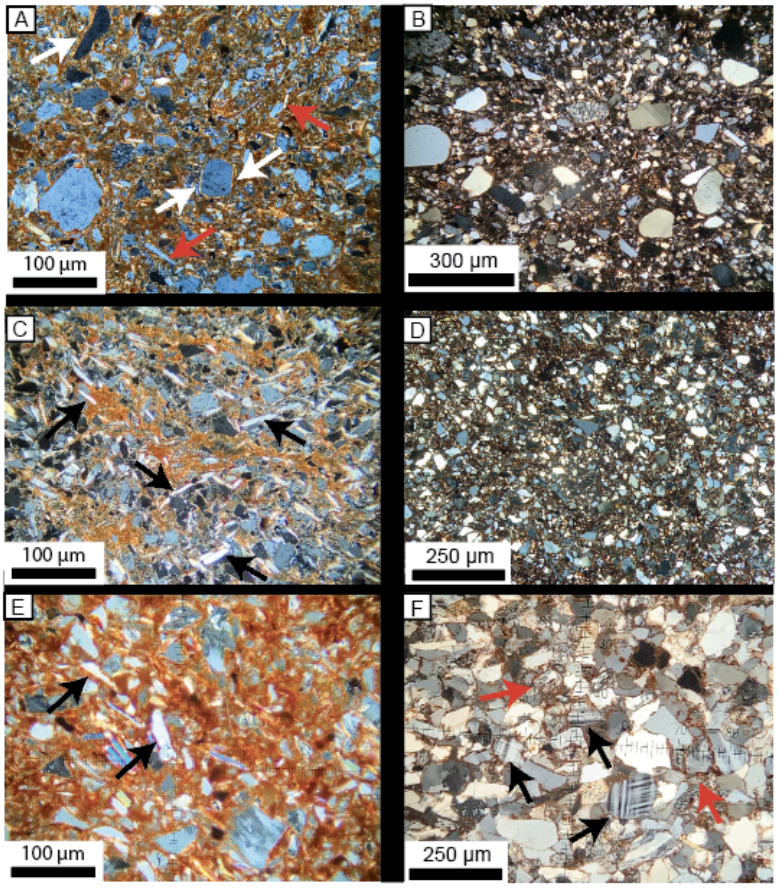


Figure 6. Thin section images (XPL) of diagnostic micromorphologic characteristics, all scales are noted in each image. A) Example of the interbedded siltstone facies. White arrows are highlighting grains with clay-coatings (skelsepic plasmic fabric) and red arrows are highlighting evaporite pseudomorphs. B) Example of sandy interbedded facies showing larger, well-rounded grains floating within a finer-grained matrix. C) Example of the massive siltstone facies. Black arrows are highlighting evaporite pseudomorph grains, and bright clays create wispy alignments (a type of sepic plasmic fabric). D) Example of siltstone unit, with lower percentage of clay-rich matrix. E) Example of a thin section from a clay concretion. Black arrows are indicating evaporite pseudomorph grains, and note the higher percent of bright clay matrix (porphyroskelic fabric). F) Example of the basal sandstone facies. Black arrows highlight pristine potassium and plagioclase feldspar grains, and red arrows indicate some clay coated grains.

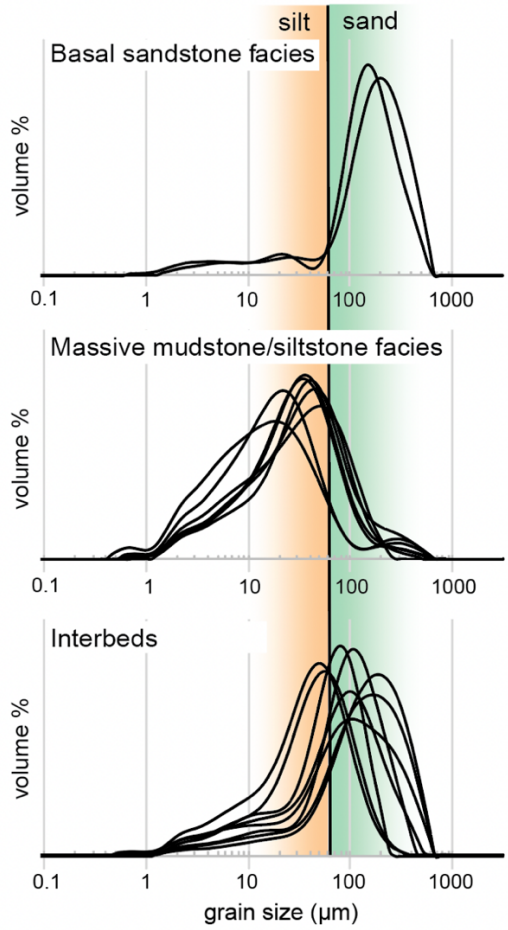


Figure 7. Histograms produced by the LPSA showing grain size distributions for samples from each facies. The silt and sand (63 µm) boundary is highlighted with silt modes highlighted in orange and sand modes highlighted in green.

Unit	Supergroup/Subgroup	Age	Location	Current interpretation	Citations
Nguba & Kundelungu Groups	Katanga Supergroup	Cryogenian - Ediacaran	Lufilian arc / Zambia	basal glacial deposits into shallow marine (?)	Cailteux and Putter, 2019
Katete Fm	Bunkeya Subgroup	Cryogenian - Ediacaran	Democratic Republic of the Congo	shallow marine transgressive sequence	Batumike et al., 2007
Monwezi Fm				shallow marine transgressive sequence	Batumike et al., 2007
Nudas & Urusis Fm	Schwarzrand Subgroup	Ediacaran	Nama Basin / Southwestern Namibia	carbonate ramp deposits	Saylor et al., 1995; Blanco et al., 2011

Table 1. Regionally correlative units (in age and lithologic attributes) to the Manyovu redbeds in Africa.

Cap-carbonate bearing unit	Location	Reported age	Dating Method	Reference
Nantuo Fm	China	636.3 ± 4.9 Ma	U-Pb age from basal tuff	Zhang et al., 2008
Mirassol d'Oeste Fm	Brazil	633 ± 25 Ma	Pb-Pb age isochron age from dolostone	Babinski et al., 2006; Alvarenga et al., 2011
Ghaub Fm	Namibia	635 ± 0.5 Ma	U-Pb age from interbedded ash	Hoffmann et al., 2004
Doushantuo Fm	China	635 ± 0.6 Ma	U-Pb age from interbedded tuff	Condon et al., 2005

Table 2. Summary of geochronologic data for Marinoan cap-carbonates.

REFERENCES CITED

Almond, P.C. and Tonkin, P.J., 1999, Pedogenesis by upbuilding in an extreme leaching and weathering environment, and slow loess accretion, south Westland, New Zealand: Geoderma, v. 92(1–2), p. 1–36.

Alvarenga, C.J., Boggiani, P.C., Babinski, M., Dardenne, M.A., Figueiredo, M.F., Dantas, E.L., Uhlein, A., Santos, R.V., Sial, A.N. and Trompette, R., 2011, Glacially influenced sedimentation of the Puga Formation, Cuiabá Group and Jacadigo Group, and associated carbonates of the Araras and Corumbá groups, Paraguay Belt, Brazil: Geological Society, London, Memoirs, v. 36(1), p. 487–497.

Arnaud, E. and Eyles, C.H., 2002, Glacial influence on Neoproterozoic sedimentation: the Smalfjord Formation, northern Norway: Sedimentology, v. 49(4), p. 765–788.

Arnaud, E., 2008. Deformation in the Neoproterozoic Smalfjord Formation, northern Norway: an indicator of glacial depositional conditions?: Sedimentology, v. 55(2), p. 335–356.

Assallay, A. M., Rogers, C. D. F., Smalley, I. J., and Jefferson, I. F., 1998, Silt: 2-62 μm, 9-4φ: Earth Science Reviews, v. 45, p. 61–88. https://doi.org/10.1016/S0012-8252(98)00035-X

Babinski, M., Trindade, R.I.F.D., Alvarenga, C.J.S., Boggiani, P.C., Liu, D., Santos, R.V. and Brito Neves, B.D., 2006, Chronology of Neoproterozoic ice ages in Central Brazil. In First Symposium on Neoproterozoic-Early Paleozoic Events in SW Gondwana: Extended Abstracts, IGCP Project, v. 478, p. 303–306.

Batumike, M.J., Cailteux, J.L.H. and Kampunzu, A.B., 2007, Lithostratigraphy, basin development, base metal deposits, and regional correlations of the Neoproterozoic Nguba and Kundelungu rock successions, central African Copperbelt: Gondwana Research, v. 11(3), p.432–447.

Betzer, P.R., Carder, K.L., Duce, R.A., Merrill, J.T., Tindale, N.W., Uematsu, M., Costello, D.K., Young, R.W., Feely, R.A., Breland, J.A. and Bernstein, R.E., 1988, Long–range transport of giant mineral aerosol particles: Nature, v. 336(6199), p. 568–571.

Blanco, G., Germs, G.J.B., Rajesh, H.M., Chemale Jr, F., Dussin, I.A. and Justino, D., 2011, Provenance and paleogeography of the Nama Group (Ediacaran to early Palaeozoic, Namibia): petrography, geochemistry and U–Pb detrital zircon geochronology: Precambrian Research, v. 187(1-2), p. 15–32.

Brewer, R., 1976, Fabric and Mineral Analysis of Soils: New York, Krieger, 482 p.

Briden, J. C., Piper, J. D. A., Henthorn, D. I. and Rex, D. C., 1971, New palaeomagnetic results from Africa and related potassium–argon age determinations, University of Leeds, p. 46 – 50.

Cahen, L. and Snelling, N.J., 1974, Potassium–argon ages and additions to the stratigraphy of the Malagarasian (Bukoban system of Tanzania) of SE Burundi: Journal of the Geological Society, v. 130, p. 461–470, doi:10.1144/gsjgs.130.5.0461.

Cahen, L., Snelling, N.J., Delhal, J., Vail, J.R., Bonhomme, M. and Ledent, D., 1984, The geochronology and evolution of Africa: London, Oxford, 512 p.

Cailteux, J.L. and De Putter, T., 2019, The Neoproterozoic Katanga Supergroup (DR Congo): State–of–the–art and revisions of the lithostratigraphy, sedimentary basin and geodynamic evolution: Journal of African Earth Sciences, v. 150, p. 522–531.

Catt, J. A. (1988). Loess—its formation, transport and economic significance, in Physical and chemical weathering in geochemical cycles. Springer, Dordrecht, p. 113–142.

Condon, D., Zhu, M., Bowring, S., Wang, W., Yang, A. and Jin, Y., 2005, U-Pb ages from the Neoproterozoic Doushantuo Formation, China: Science, v. 308(5718), p. 95–98.

Crouvi, O., Amit, R., Enzel, Y., Porat, N. and Sandler, A., 2008, Sand dunes as a major proximal dust source for late Pleistocene loess in the Negev Desert, Israel: Quaternary Research, v. 70(2), p.275–282.

Deblond, A., Punzalan, L.E., Boven, A., and Tack, L., 2001, The Malagarazi supergroup of Southeast Burundi and its correlative Bukoba supergroup of Northwest Tanzania: Neo– and Mesoproterozoic chronostratigraphic constraints from Ar–Ar ages on mafic intrusive rocks: Journal of African Earth Sciences, v. 32, p. 435–449, doi:10.1016/s0899–5362(01)90107–1.

Edwards, M.B., 1979. Late Precambrian glacial loessites from north Norway and Svalbard: Journal of Sedimentary Research, v. 49(1), p.85–91.

Fitzpatrick, E.A. and Fitzpatrick, E.A., 1993, Soil microscopy and micromorphology: New York: John Wiley and Sons, v. 158.

French, H. and Shur, Y., 2010, The principles of cryostratigraphy: Earth-Science Reviews, v. 101(3-4), p. 190–206.

Frimmel, H.E., Fölling, P.G., and Eriksson, P.G., 2002, Neoproterozoic tectonic and climatic evolution recorded in the Gariep belt, Namibia and South Africa: Basin Research, v. 14, p. 55–67, doi:10.1046/j.1365–2117.2002.00166.x.

Foster, T.M., Soreghan, G.S., Soreghan, M.J., Benison, K.C., and Elmore, R.D., 2014, Climatic and paleogeographic significance of eolian sediment in the Middle Permian Dog Creek Shale (midcontinent U.S.): Palaeogeography, Palaeoclimatology, Palaeoecology, v. 402, p. 12–29, https://doi.org/10.1016/j.palaeo.2014.02.031.

Halverson, G.P., Hoffman, P.F., Schrag, D.P., Maloof, A.C., and Rice, A.H.N., 2005, Toward a Neoproterozoic composite carbon–isotope record: Geological Society of America Bulletin, v. 117, p. 1181–1207, doi: 10 .1130 /B25630.1.

Halligan, R., 1963, The Proterozoic rocks of Tanganyika: Geological Survey of Tanzania, 22 p.

Hoffman, P.F., Kaufman, A.J., Halverson, G.P., and Schrag, D.P., 1998, A Neoproterozoic Snowball Earth: Science, v. 281, p. 1342–1346, doi:10.1126/science.281.5381.1342.

Hoffman, P.F. and Schrag, D.P., 2002, The snowball Earth hypothesis: testing the limits of global change: Terra Nova, v. 14, p. 129–155.

Hoffman, P.F. and Li, Z.X., 2009, A paleogeographic context for Neoproterozoic glaciation: Palaeogeography, Palaeoclimatology, Palaeoecology, v. 277(3–4), p. 158–172.

Hoffmann, K.H., Condon, D.J., Bowring, S.A. and Crowley, J.L., 2004, U-Pb zircon date from the Neoproterozoic Ghaub Formation, Namibia: constraints on Marinoan glaciation: Geology, v. 32(9), p.817–820.

Hoffman, P.F., Lamothe, K.G., LoBianco, S.J.C., Hodgskiss, M.S.W., Bellefroid, E.J., Johnson, B.W., Hodgin, E.B., and Halverson, G.P., 2017, Sedimentary depocenters on Snowball Earth: Case studies from the Sturtian Chuos formation in Northern Namibia: Geosphere, v. 13, p. 811–837, doi:10.1130/ges01457.1.

Hofmann, M., Linnemann, U., Hoffmann, K.H., Germs, G., Gerdes, A., Marko, L., Eckelmann, K., Gärtner, A., and Krause, R., 2015, The four Neoproterozoic glaciations of southern Namibia and their detrital zircon record: The fingerprints of four crustal growth events during two supercontinent cycles: Precambrian Research, v. 259, p. 176–188, doi:10.1016/j.precamres.2014.07.021.

Hunter, R.E., 1977, Basic types of stratification in small eolian dunes: Sedimentology, v. 24(3), p. 361–387.

Jackson, M.P.A., Warin, O.N., Woad, G.M. and Hudec, M.R., 2003, Neoproterozoic allochthonous salt tectonics during the Lufilian orogeny in the Katangan Copperbelt, central Africa: Geological Society of America Bulletin, v. 115(3), p. 314–330.

Johnson, S., 1989, The significance of loessite in the Maroon Formation (Middle Pennsylvanian to Lower Permian), Eagle Basin, northwest Colorado: Journal of Sedimentary Petrology, v. 59, p. 789–791.

Johnson, D.L. and Watson-Stegner, D., 1987, Evolution model of pedogenesis. Soil Science, v. 143(5), p. 349–366.

Jones, B.G. and Rust, B.R., 1983, Massive sandstone facies in the Hawkesbury Sandstone, a Triassic fluvial deposit near Sydney, Australia: Journal of Sedimentary Research, v. 53(4), p. 1249–1259.

Kasanzu, C.H., and Manya, S., 2020, Evidence for a Record of Possible Paleo-Tsunami or Storm Deposits in the Fluviatile Neoproterozoic Malagarasi Supergroup of North-Western Tanzania: Tanzania Journal of Science, v. 2, p. 460–474.

Kennedy, M.J., Runnegar, B., Prave, A.R., Hoffmann, K.H. and Arthur, M.A., 1998, Two or four Neoproterozoic glaciations?: Geology, v. 26(12), p. 1059–1063.

Khalaf, E.E.D.A.H., 2012, Mechanisms of volcaniclastic aggradation in fluvial systems influenced by explosive volcanism: An example from Neoproterozoic Hammamat Group, Wadi Queih area, Central Eastern Desert, Egypt: Journal of African Earth Sciences, v. 68, p. 44–66.

Knoll, A., Walter, M., Narbonne, G. and Christie-Blick, N., 2006, The Ediacaran Period: a new addition to the geologic time scale: Lethaia, v. 39(1), p. 13–30.

Kuang, H., Bai, H., Peng, N., Qi, K., Wang, Y., Chen, X. and Liu, Y., 2022. Temporal and spatial distribution of Precambrian red beds and their formation mechanisms: Geosystems and Geoenvironment, v. 1, p. 100098.

Lan, Z.W. and Chen, Z.Q., 2013, Proliferation of MISS-forming microbial mats after the late Neoproterozoic glaciations: evidence from the Kimberley region, NW Australia: Precambrian Research, v. 224, p. 529–550.

Lewis, T., Gilbert, R. and Lamoureux, S.F., 2002, Spatial and temporal changes in sedimentary processes at proglacial Bear Lake, Devon Island, Nunavut, Canada. Arctic, Antarctic, and Alpine Research, v. 34(2), p. 119–129.

Li, Z.X., Bogdanova, S., Collins, A.S., Davidson, A., De Waele, B., Ernst, R.E., Fitzsimons, I.C.W., Fuck, R.A., Gladkochub, D.P., Jacobs, J. and Karlstrom, K.E., 2008, Assembly, configuration, and break-up history of Rodinia: a synthesis: Precambrian research, v. 160(1-2), p.179–210.

Li, Z.X., Evans, D.A. and Halverson, G.P., 2013, Neoproterozoic glaciations in a revised global palaeogeography from the breakup of Rodinia to the assembly of Gondwanaland: Sedimentary Geology, v. 294, p.219–232.

Li, Y., Shi, W., Aydin, A., Beroya-Eitner, M. A., and Gao, G., 2020, Loess genesis and worldwide distribution: Earth Science Reviews, v. 201, p. 102947. https://doi.org/10.1016/j.earscirev.2019.102947

Liu, C., Masuda, A., Okada, A., Yabuki, S., and Zi-Li, F., 1994, Isotope geochemistry of Quaternary deposits from the arid lands in northern China: Earth and Planetary Science Letters, v. 127, p. 25–38, https://doi.org/10.1016/0012-821X(94)90195-3.

Loope, D.B., Mason, J.A. and Dingus, L., 1999, Lethal sandslides from eolian dunes: The Journal of geology, v. 107(6), p. 707–713.

Macgregor, D., 2015, History of the development of the East African Rift System: A series of interpreted maps through time: Journal of African Earth Sciences, v. 101, p. 232–252.
Mack, G.H., James, W.C. and Monger, H.C., 1993, Classification of paleosols: Geological society of America bulletin, v. 105(2), p.129–136.
Marren, P.M., Snorrason, A., Finnsdóttir, H.P. and Moss, M.E., 2002, Criteria for distinguishing high magnitude flood events in the proglacial fluvial sedimentary record: IAHS publication, p. 237–242.
Martin, C.A. and Turner, B.R., 1998, Origins of massive-type sandstones in braided river systems. Earth-Science Reviews, v. 44(1-2), p.15–38.
Meert, J.G., 2003, A synopsis of events related to the assembly of eastern Gondwana: Tectonophysics, v. 362(1–4), p. 1–40.
Meert, J.G., van der Voo, R. and Ayub, S., 1995, Paleomagnetic investigation of the Neoproterozoic Gagwe lavas and Mbozi complex, Tanzania and the assembly of Gondwana. Precambrian Research, v. 74(4), p. 225–244.
Muhs, D.R., 2013, The geologic records of dust in the Quaternary: Aeolian Research, v. 9, p. 3–48.
Muhs, D.R., 2018, The geochemistry of loess: Asian and North American deposits compared: Journal of Asian Earth Sciences, v. 155, p. 81–115, doi:10.1016/j.jseaes.2017.10.032.
Muhs, D. R., and Bettis, E. A., 2003, Quaternary loess-paleosol sequences as examples of climate-driven sedimentary extremes. Special Paper of the Geological Society of America, v. 370(303), p. 53–74. https://doi.org/10.1130/0-8137-2370-1.53
Nelson, L.L., Smith, E.F., Hodgin, E.B., Crowley, J.L., Schmitz, M.D. and Macdonald, F.A., 2020, Geochronological constraints on Neoproterozoic rifting and onset of the Marinoan glaciation from the Kingston Peak Formation in Death Valley, California (USA): Geology, v. 48(11), p. 1083–1087.
Parrish, J.T. and Falcon-Lang, H.J., 2007, Coniferous trees associated with interdune deposits in the Jurassic Navajo Sandstone Formation, Utah, USA: Palaeontology, v. 50(4), p.829–843.
Piper, J.D.A., 1972, A Palaeomagnetic Study of the Bukoban System, Tanzania: Geophysical Journal of the Royal Astronomical Society, v. 28, p. 111–127, doi:10.1111/j.1365–246x.1972.tb06116.x.
Pfeifer, L. S., Soreghan, G. S., Pochat, S., and Van Den Driessche, J., 2020, Loess in eastern equatorial Pangea archives a dusty atmosphere and possible upland glaciation: GSA Bulletin, v. 133(1-2), p. 379–392.
Prave, A.R., Condon, D.J., Hoffmann, K.H., Tapster, S., and Fallick, A.E., 2016, Duration and nature of the end-Cryogenian (Marinoan) glaciation: Geology, v. 44, p. 631–634, doi:10 .1130/G38089 .1.
Plummer, P.S., 1978, Note on the palaeoenvironmental significance of the Nuccaleena Formation (upper Precambrian), central Flinders Ranges, South Australia: Journal of the Geological Society of Australia, v. 25(7-8), p. 395–402.
Porter, S.C., 2001, Chinese loess record of monsoon climate during the last glacial–interglacial cycle: Earth-Science Reviews, v. 54(1-3), p.115–128.
Pye, K., 1995, The nature, origin and accumulation of loess: Quaternary Science Reviews, v. 14(7–8), p. 653–667. https://doi.org/10.1016/0277-3791(95)00047-X
Pye, K. and Tsoar, H., 1987, The mechanics and geological implications of dust transport and deposition in deserts with particular reference to loess formation and dune sand

diagenesis in the northern Negev, Israel: Geological Society, London, Special Publications, v. 35(1), p. 139–156.
Ratmeyer, V., Fischer, G. and Wefer, G., 1999, Lithogenic particle fluxes and grain size distributions in the deep ocean off northwest Africa: Implications for seasonal changes of aeolian dust input and downward transport. Deep Sea Research Part I: Oceanographic Research Papers, v. 46(8), p. 1289–1337.
Rea, D.K. AND Janecek, T.R., 1981, Late cretaceous history of eolian deposition in the mid–pacific mountains, central North Pacific Ocean: Palaeogeography, Palaeoclimatology, Palaeoecology, v. 36, p. 55–67.
Retallack, G.J., 1997, Colour guide to paleosols. John Wiley and Sons Ltd., 175 p.
Retallack, G.J., 2008, Soils of the past: an introduction to paleopedology. John Wiley and Sons. Oxford, UK, Blackwell Science, Ltd, 520 p.
Retallack, G.J., 2011, Neoproterozoic loess and limits to snowball earth: Journal of the Geological Society, v. 168, p. 289–307, doi:10.1144/0016–76492010–051.
Retallack, G.J., 2021, Paleosols and weathering leading up to Snowball Earth in central Australia: Australian Journal of Earth Sciences, v. 68(8), p. 1122–1148.
Retallack, G.J., 2022, Early Ediacaran lichen from Death Valley, California, USA: Journal of Palaeosciences, v. 71(2), p. 187–218.
Retallack, G.J., 2023, Why was there a Neoproterozoic Snowball Earth?: Precambrian Research, v. 385, doi:10.1016/j.precamres.2022.106952.
Retallack, G.J., Gose, B.N., and Osterhout, J.T., 2015, Periglacial paleosols and Cryogenian paleoclimate near Adelaide, South Australia: Precambrian Research, v. 263, p. 1–18, doi:10.1016/j.precamres.2015.03.002.
Rice, A.H.N., Edwards, M.B., Hansen, T.A., Arnaud, E. and Halverson, G.P., 2011, Glaciogenic rocks of the Neoproterozoic Smalfjord and Mortensnes formations, Vestertana Group, E. Finnmark, Norway: Geological Society, London, Memoirs, v. 36(1), p.593–602.
Roberts, E.M., Stevens, N.J., O'Connor, P.M., Dirks, P.H.G.M., Gottfried, M.D., Clyde, W.C., Armstrong, R.A., Kemp, A.I.S. and Hemming, S., 2012, Initiation of the western branch of the East African Rift coeval with the eastern branch: Nature Geoscience, v. 5(4), p.289–294.
Rooney, A.D., Strauss, J.V., Brandon, A.D. and Macdonald, F.A., 2015, A Cryogenian chronology: Two long–lasting synchronous Neoproterozoic glaciations: Geology, v. 43(5), p. 459–462.
Rose, C.V. and Maloof, A.C., 2010, Testing models for post-glacial 'cap dolostone' deposition: Nuccaleena Formation, South Australia: Earth and Planetary Science Letters, v. 296(3-4), p.165–180.
Rosendahl, B.R., Reynolds, D.J., Lorber, P.M., Burgess, C.F., McGill, J., Scott, D., Lambiase, J.J. and Derksen, S.J., 1986, Structural expressions of rifting: lessons from Lake Tanganyika, Africa. Geological Society, London, Special Publications, v. 25(1), p.29–43.
Sander, S. and Rosendahl, B.R., 1989, The geometry of rifting in Lake Tanganyika, east Africa. Journal of African Earth Sciences (and the Middle East), v. 8(2-4), p.323–354.
Saylor, B.Z., Grotzinger, J.P. and Germs, G.J., 1995, Sequence stratigraphy and sedimentology of the Neoproterozoic Kuibis and Schwarzrand subgroups (Nama Group), southwestern Namibia. Precambrian Research, v. 73(1-4), p.153–171.

Schmidt, P.W. and Williams, G.E., 1995, The Neoproterozoic climatic paradox: equatorial palaeolatitude for Marinoan glaciation near sea level in South Australia: Earth and Planetary Science Letters, v. 134(1–2), p. 107–124.

Scotese, C.R., 2009, Late Proterozoic plate tectonics and palaeogeography: A tale of two supercontinents, Rodinia and Pannotia: Geological Society Special Publication, v. 326, p. 67–83, doi:10.1144/sp326.4.

Scotese, C.R., 2021, An atlas of phanerozoic paleogeographic maps: The seas come in and the seas go out: Annual Review of Earth and Planetary Sciences, v. 49, p. 679–728, doi:10.1146/annurev–earth–081320–064052.

Simpson, E.L., Eriksson, K.A., Eriksson, P.A. and Bumby, A.J., 2002, Eolian dune degradation and generation of massive sandstone bodies in the Paleoproterozoic Makgabeng Formation, Waterberg Group, South Africa: Journal of Sedimentary Research, v. 72(1), p.40–45.

Smalley, I.J., 1990, Possible formation mechanisms for the modal coarse silt quartz particles in loess: Quaternary International, v. 7–8, p. 23–27, https://doi.org/10.1016/1040-6182(90)90035-3.

Smalley, I.J., 1995, Making the material: The formation of silt sized primary mineral particles for loess deposits: Quaternary Science Reviews, v. 14(7–8), p. 645–651. https://doi.org/10.1016/0277-3791(95)00046-1

Smalley, I. and Marković, S.B., 2019, Controls on the nature of loess particles and the formation of loess deposits. Quaternary International, v. 502, p. 160–164.

Stern, R.J., 1994. Arc assembly and continental collision in the Neoproterozoic East African Orogen: implications for the consolidation of Gondwanaland: Annual Review Earth Planetary Science, v. 22, p. 319–351.

Stern, R.J., Avigad, D., Miller, N.R., and Beyth, M., 2006, Evidence for the Snowball Earth hypothesis in the Arabian–Nubian Shield and the East African Orogen: Journal of African Earth Sciences, v. 44, p. 1–20, doi:10.1016/j.jafrearsci.2005.10.003.

Stern, R.J., Avigad, D., Miller, N., and Beyth, M., 2008, From Volcanic Winter to Snowball Earth: An Alternative Explanation for Neoproterozoic Biosphere Stress, in Y. Dilek et al. (eds.), Links Between Geological Processes, Microbial Activities and Evolution of Life: Springer, p. 313 – 337.

Stern, R.J., Johnson, P.R., Ali, K.A., and Mukherjee, S.K., 2011, Evidence for early and mid–Cryogenian glaciation in the Northern Arabian–Nubian Shield (Egypt, Sudan, and western Arabia): Geological Society Memoir, v. 36, p. 277–284, doi:10.1144/m36.22.

Stuut, J.B., Zabel, M., Ratmeyer, V., Helmke, P., Schefuß, E., Lavik, G. and Schneider, R., 2005, Provenance of present-day eolian dust collected off NW Africa: Journal of Geophysical Research, Atmospheres, v. 110, p. 1–14.

Sohm, J.A., Niederberger, T.D., Parker, A.E., Tirindelli, J., Gunderson, T., Cary, S.C., Capone, D.G. and Carpenter, E.J., 2020, Microbial mats of the McMurdo Dry Valleys, Antarctica: oases of biological activity in a very cold desert: Frontiers in Microbiology, v. 11, p. 537960.

Soreghan, L. S., Soreghan, M. J., and Hamilton, M. A., 2008, Origin and significance of loess in late Paleozoic western Pangaea: A record of tropical cold?: Palaeogeography, Palaeoclimatology, Palaeoecology, v. 268(3-4), p. 234–259. https://doi.org/10.1016/j.palaeo.2008.03.050

Sur, S., Soreghan, M.J., Soreghan, G.S., AND Stagner, A.F., 2010, Extracting the silicate mineral fraction from ancient carbonate: assessing the geologic record of dust: Journal of Sedimentary Research, v. 80, p. 763–769.

Swanson-Hysell, N.L., Maloof, A.C., Condon, D.J., Jenkin, G.R., Alene, M., Tremblay, M.M., Tesema, T., Rooney, A.D. and Haileab, B., 2015, Stratigraphy and geochronology of the Tambien Group, Ethiopia: Evidence for globally synchronous carbon isotope change in the Neoproterozoic: Geology, v. 43(4), p.323–326.

Sweet, A.C., Soreghan, L.S., Sweet, D.E., Soreghan, M.J., and Madden, A.S., 2013, Permian dust in Oklahoma: Source and origin for middle Permian (Flowerpot-Blaine) redbeds in western tropical Pangaea: Sedimentary Geology, v. 284–285, p. 181–196, https://doi.org/10.1016/j.sedgeo.2012.12.006.

Valero Garcés, B.L. and Aguilar, J.G., 1992, Shallow carbonate lacustrine facies models in the Permian of the Aragon-Bearn basin (Western Spanish-French Pyrenees): Carbonates and Evaporites, v. 7, p.94–107.

Wentworth, C. K., 1922, A scale of grade and class terms for clastic sediments. The journal of geology, v. 30(5), 377-392.

Wright, J., Smith, B. and Whalley, B., 1998, Mechanisms of loess-sized quartz silt production and their relative effectiveness: laboratory simulations. Geomorphology, 23(1), p.15-34.

Zhang, S., Jiang, G. and Han, Y., 2008, The age of the Nantuo Formation and Nantuo glaciation in South China. Terra Nova, v. 20(4), p. 289–294.

Zhou, C., Huyskens, M.H., Lang, X., Xiao, S. and Yin, Q.Z., 2019, Calibrating the terminations of Cryogenian global glaciations: Geology, v. 47(3), p.251–254.

Zhu, Y., Jia, X., and Shao, M., 2018, Loess Thickness Variations Across the Loess Plateau of China. Surveys in Geophysics, v. 39(4), p. 715–727. https://doi.org/10.1007/s10712-018-9462-6

SUPPLEMENTAL MATERIALS
CHAPTER I

All samples used in Chapter I and locations.

Anza Borrego Samples	Location	
Soil		
IGNF-13-SOIL-1	N 32˚51.238' W 116˚17.28	
IGNF-13-SOIL-2	N 32˚51.238' W 116˚17.28	
IGNF-13-SOIL-3	N 32˚51.238' W 116˚17.28	
IGNF-13-SOIL-4	N 32˚51.238' W 116˚17.28	
IGNF-13-SOIL-5	N 32˚51.238' W 116˚17.28	
IGNF-13-SOIL-6	N 32˚51.238' W 116˚17.28	
IGNF-13-SOIL-7	N 32˚51.238' W 116˚17.28	
Bedrock		
IGNF-13-BDRK-1B	32 51.238 N 116 17.282 W	
IGNF-13-FBDRK-1	32 51.214 N 116 17.314 W	
IGNF-13-WBDRK	32 51.214 N 116 17.314 W	
Dust Sample		
T59	N 33° 7' 48" W 116° 31' 48	
T57	N 33° 0' W 116° 8' 24"	
ABD dust sample (s)	N 32˚51.176' W 116˚17.24	
	N 32˚51.486' W 116˚16.39	
	N 32˚51.566' W 116˚15.21	
	N 32˚50.519' W 116˚16.38	
	N 32˚52.441' W 116˚13.12	
	N 32˚52.441' W 116˚13.12	
	N 32˚52.261' W 116˚14.08	
	N 32˚51.958' W 116˚14.55	
	N 32˚50.907' W 116˚15.36	
	N 32˚ 52.434' W 116˚12.06	
	N 32˚ 52.434' W 116˚12.06	
	N 32˚51.176' W 116˚17.24	
Puerto Rico Samples		
Soil		
RG-14-SOIL-1	N 18˚04.876' W 065˚59.05	
RG-14-SOIL-2	N 18˚04.876' W 065˚59.05	
RG-14-SOIL-3	N 18˚04.876' W 065˚59.05	
RG-14-SOIL-4	N 18˚04.876' W 065˚59.05	
RG-14-SOIL-5	N 18˚04.876' W 065˚59.05	
RG-14-SOIL-6	N 18˚04.876' W 065˚59.05	
Bedrock		
RB-14-BDRK-#2A	N 18˚03.076' W 065˚55.79	
RG-14-BDRK-13	N 18˚03.696' W 065˚55.41	
Dust Proxy		
PR-PliBR	17.954971° -66.852811°	

Raw Geochemistry

Puerto Rico									
Soil samples									
	Ba	Ce	Cr	Cs	Dy	Er	Eu	Ga	Gd
<63 microns	ppm	ppm	ppm	ppm	ppm	ppm	ppm	ppm	ppm
RG-14-SOIL-1	338.00	6.70	7.00	2.41	0.94	0.65	0.15	28.70	0.64
RG-14-SOIL-2	283.00	9.00	<10	2.43	0.81	0.66	0.17	27.60	0.71
RG-14-SOIL-3	83.80	9.30	18.00	1.40	0.70	0.44	0.15	34.20	0.51
RG-14-SOIL-4	245.00	15.40	<10	1.50	0.85	0.74	0.17	27.40	0.75
RG-14-SOIL-5	124.00	9.10	11.00	0.94	0.79	0.49	0.11	31.90	0.58
RG-14-SOIL-6	791.00	29.10	<10	2.41	1.34	1.06	0.21	25.90	1.07
Mud fraction subdivisions									
RGSOIL-1-L20	378.00	6.50	20.00	2.51	0.72	0.65	0.16	33.20	0.67
RGSOIL-2-L20	367.00	6.30	20.00	2.68	0.67	0.56	0.18	33.60	0.40
RGSOIL-2-G20	301.00	6.60	10.00	2.38	0.71	0.66	0.17	33.20	0.55
RGSOIL-3-L20	102.00	9.60	30.00	1.35	0.89	0.47	0.15	37.80	0.51
RGSOIL-4-L20	333.00	15.90	20.00	2.03	0.84	0.57	0.12	34.20	0.90
RGSOIL-4-G20	298.00	14.50	10.00	1.76	1.00	0.99	0.18	31.50	0.79
RGSOIL-5-L20	147.00	8.90	20.00	0.95	0.68	0.64	0.16	34.40	0.61
RGSOIL-6-L20	907.00	32.10	10.00	2.92	1.36	0.99	0.27	29.80	1.36
RGSOIL-6-G20	876.00	30.60	10.00	2.66	1.50	1.20	0.26	29.10	1.55
Bedrock									
RB-14-BDRK-#2A		23.50	110.00	0.59	3.96	2.30	0.97	16.30	4.05
RG-14-BDRK-13		11.50	90.00	0.21	4.50	3.12	1.01	14.90	4.29
Dust Proxy									
PR-PliBR	110.00	67.50	360.00	4.80	4.65	3.65	1.11	27.90	4.11
Anza Borrego									
Soil samples									
IGNF-13-SOIL-1	651.00	61.40	30.00	3.14	5.66	3.01	1.21	26.60	6.17
IGNF-13-SOIL-2	666.00	60.50	30.00	3.30	5.67	3.18	1.54	27.00	6.49
IGNF-13-SOIL-3	675.00	54.60	30.00	3.53	5.36	2.53	1.31	27.30	5.28
IGNF-13-SOIL-4	642.00	54.60	30.00	2.83	5.16	3.12	1.29	26.20	6.25
IGNF-13-SOIL-5	655.00	59.80	30.00	2.71	4.93	2.82	1.20	26.10	6.13
IGNF-13-SOIL-6	619.00	55.20	20.00	2.83	5.16	2.75	1.22	25.90	6.07
IGNF-13-SOIL-7	651.00	58.40	30.00	2.67	4.38	2.72	1.31	24.90	5.61
Bedrock									
IGNF-13-BDRK-1B	728.00	5.60	210.00	2.26	1.53	0.80	0.74	19.80	1.94
IGNF-13-FBDRK-1	698.00	7.40	180.00	1.01	1.59	0.78	0.92	19.00	2.05
IGNF-13-WBDRK	1325.00	4.20	180.00	1.93	1.60	0.83	0.88	25.50	2.12
Dust Trap									
ABD dust sample	870.49	47.52	54.14	5.39	3.14	1.74	0.97	21.01	3.57

Puerto Rico									
Soil samples									
	Hf	Ho	La	Lu	Nb	Nd	Pr	Rb	Sm
<63 microns	ppm	ppm	ppm	ppm	ppm	ppm	ppm	ppm	ppm
RG-14-SOIL-1	1.50	0.19	2.00	0.12	3.41	2.30	0.52	34.10	0.58
RG-14-SOIL-2	1.50	0.21	2.20	0.11	4.00	2.90	0.71	27.00	0.75
RG-14-SOIL-3	2.05	0.13	4.00	0.08	5.93	3.00	0.79	13.80	0.62
RG-14-SOIL-4	3.00	0.20	6.20	0.18	4.80	4.40	1.33	23.10	0.89
RG-14-SOIL-5	1.93	0.14	3.10	0.11	5.11	2.30	0.64	12.00	0.54
RG-14-SOIL-6	3.00	0.30	12.50	0.24	3.80	8.70	2.56	47.40	1.53
Mud fraction subdivisions									
RGSOIL-1-L20	1.30	0.15	1.60	0.12	3.80	2.00	0.51	37.40	0.61
RGSOIL-2-L20	1.70	0.17	1.40	0.11	4.60	2.00	0.42	35.10	0.34
RGSOIL-2-G20	1.80	0.18	1.70	0.13	4.40	1.90	0.46	29.70	0.51
RGSOIL-3-L20	2.10	0.18	4.10	0.09	6.60	2.90	0.84	15.30	0.57
RGSOIL-4-L20	2.40	0.22	6.80	0.13	4.90	4.80	1.40	33.10	1.00
RGSOIL-4-G20	3.10	0.24	6.30	0.20	4.80	4.40	1.26	29.80	0.90
RGSOIL-5-L20	1.90	0.15	2.70	0.11	5.50	2.30	0.65	13.80	0.48
RGSOIL-6-L20	2.30	0.34	13.60	0.20	4.20	9.80	2.82	56.20	1.65
RGSOIL-6-G20	3.00	0.34	12.00	0.23	4.20	8.70	2.48	55.90	1.61
Bedrock									
RB-14-BDRK-#2A	3.20	0.77	10.70	0.41	2.50	14.90	3.24	35.90	3.70
RG-14-BDRK-13	2.40	1.06	4.20	0.57	0.40	9.70	1.83	4.50	3.12
Dust Proxy									
PR-PliBR	6.40	0.95	31.40	0.44	17.90	21.70	5.85	56.70	4.21
Anza Borrego									
Soil samples									
IGNF-13-SOIL-1	12.70	1.04	28.00	0.42	10.70	28.90	7.01	70.70	6.43
IGNF-13-SOIL-2	16.50	1.10	28.30	0.48	11.40	29.00	6.94	71.00	6.07
IGNF-13-SOIL-3	12.30	0.88	25.70	0.36	10.90	26.40	6.36	74.90	6.03
IGNF-13-SOIL-4	14.10	0.97	25.60	0.36	10.40	28.40	6.52	65.80	6.48
IGNF-13-SOIL-5	14.50	0.96	29.30	0.42	10.40	29.80	7.45	67.70	6.96
IGNF-13-SOIL-6	11.40	0.93	25.20	0.36	10.50	26.50	6.58	66.10	6.15
IGNF-13-SOIL-7	16.20	0.87	26.40	0.34	9.70	27.10	6.79	64.00	6.14
Bedrock									
IGNF-13-BDRK-1B	4.00	0.27	2.50	0.10	5.60	4.30	0.87	47.00	1.90
IGNF-13-FBDRK-1	4.00	0.28	2.80	0.10	6.00	6.50	1.17	29.00	2.17
IGNF-13-WBDRK	6.10	0.30	2.00	0.11	9.20	4.30	0.69	80.60	1.94
Dust Trap									
ABD dust sample	5.41	0.62	24.33	0.29	11.50	20.98	5.74	90.71	4.31

Puerto Rico									
Soil samples									
	Sr	Ta	Tb	Th	Tm	U	V	W	Y
<63 microns	ppm	ppm	ppm	ppm	ppm	ppm	ppm	ppm	ppm
RG-14-SOIL-1	18.80	0.20	0.11	3.16	0.11	1.43	227.00	1.40	3.90
RG-14-SOIL-2	10.90	0.30	0.13	3.08	0.10	1.46	196.00	1.00	4.10
RG-14-SOIL-3	7.30	0.40	0.06	4.23	0.07	1.54	282.00	1.00	2.70
RG-14-SOIL-4	7.50	0.50	0.12	7.21	0.14	1.73	155.00	1.00	5.50
RG-14-SOIL-5	5.20	0.30	0.12	3.92	0.09	1.58	224.00	1.20	3.30
RG-14-SOIL-6	14.30	0.40	0.19	9.28	0.18	1.74	111.00	1.00	8.60
Mud fraction subdivisions									
RGSOIL-1-L20	22.90	0.30	0.12	2.75	0.10	1.53	217.00	2.00	3.80
RGSOIL-2-L20	14.80	0.30	0.10	3.20	0.11	1.73	218.00	1.00	3.20
RGSOIL-2-G20	13.30	0.30	0.12	3.30	0.12	1.66	223.00	1.00	3.60
RGSOIL-3-L20	8.80	0.50	0.08	4.40	0.08	1.56	316.00	1.00	3.20
RGSOIL-4-L20	8.50	0.40	0.13	8.77	0.13	1.68	167.00	1.00	5.10
RGSOIL-4-G20	8.00	0.40	0.16	8.82	0.14	1.86	159.00	1.00	6.50
RGSOIL-5-L20	4.80	0.40	0.14	3.77	0.10	1.59	218.00	1.00	3.00
RGSOIL-6-L20	21.70	0.40	0.20	9.14	0.15	1.53	136.00	1.00	8.10
RGSOIL-6-G20	19.60	0.40	0.19	9.34	0.16	1.79	143.00	1.00	8.60
Bedrock									
RB-14-BDRK-#2A	464.00	0.20	0.57	2.58	0.36	1.64	201.00	5.00	21.60
RG-14-BDRK-13	179.00	0.10	0.74	0.40	0.49	0.27	162.00	<1	27.40
Dust Proxy									
PR-PliBR	49.10	1.30	0.68	10.85	0.52	2.03	191.00	3.00	28.00
Anza Borrego									
Soil samples									
IGNF-13-SOIL-1	437.00	0.90	0.89	9.15	0.45	2.24	50.00	1.00	28.70
IGNF-13-SOIL-2	446.00	0.90	0.85	9.92	0.48	2.40	53.00	1.00	29.70
IGNF-13-SOIL-3	455.00	0.80	0.84	7.86	0.34	2.01	47.00	1.00	26.00
IGNF-13-SOIL-4	484.00	0.80	0.88	7.92	0.41	2.05	49.00	1.00	28.00
IGNF-13-SOIL-5	493.00	0.80	0.88	9.08	0.43	2.19	49.00	2.00	28.20
IGNF-13-SOIL-6	450.00	0.80	0.91	8.12	0.42	2.11	44.00	1.00	27.90
IGNF-13-SOIL-7	488.00	0.80	0.85	10.30	0.38	2.36	44.00	1.00	24.50
Bedrock									
IGNF-13-BDRK-1B	423.00	0.50	0.23	0.38	0.08	0.47	16.00	2.00	7.20
IGNF-13-FBDRK-1	474.00	0.30	0.25	0.26	0.09	0.72	22.00	2.00	7.40
IGNF-13-WBDRK	517.00	0.50	0.28	0.50	0.11	0.57	34.00	2.00	8.40
Dust Trap									
ABD dust sample	351.73	0.93	0.57	7.35	0.25	1.94	70.31	1.48	20.59

Puerto Rico									
Soil samples									
	Zr	SiO2	Al2O3	Fe2O3	CaO	MgO	Na2O	K2O	Cr2O3
<63 microns	ppm	%	%	%	%	%	%	%	%
RG-14-SOIL-1	38.00	41.50	30.50	10.60	0.02	0.40	0.50	1.46	<0.002
RG-14-SOIL-2	35.00	41.40	29.60	11.20	0.02	0.40	0.92	1.33	<0.002
RG-14-SOIL-3	51.00	38.60	31.00	12.55	0.01	0.29	0.17	0.39	0.00
RG-14-SOIL-4	77.00	44.20	29.80	8.64	0.01	0.34	0.92	1.18	<0.002
RG-14-SOIL-5	54.00	40.60	31.80	10.55	0.03	0.38	0.27	0.49	<0.002
RG-14-SOIL-6	74.00	46.30	29.80	6.24	0.01	0.31	1.38	2.65	<0.002
Mud fraction subdivisions									
RGSOIL-1-L20	31.00	43.70	32.10	9.95	0.02	0.38	0.44	1.61	0.00
RGSOIL-2-L20	34.00	43.00	32.10	10.15	0.01	0.39	0.29	1.59	0.00
RGSOIL-2-G20	37.00	44.60	31.20	11.00	0.01	0.43	0.30	1.31	<0.002
RGSOIL-3-L20	52.00	40.90	32.00	13.15	0.01	0.29	0.12	0.42	0.00
RGSOIL-4-L20	52.00	43.70	32.60	8.09	0.02	0.35	0.25	1.57	0.00
RGSOIL-4-G20	73.00	46.40	31.50	8.32	0.01	0.37	0.25	1.44	<0.002
RGSOIL-5-L20	45.00	42.20	32.90	10.90	0.01	0.36	0.23	0.56	0.00
RGSOIL-6-L20	48.00	45.90	32.80	6.20	0.02	0.33	0.29	2.90	0.00
RGSOIL-6-G20	74.00	48.10	30.90	6.78	0.02	0.36	0.28	2.73	<0.002
Bedrock									
RB-14-BDRK-#2A	115.00	61.20	15.50	7.52	5.96	2.75	3.18	2.06	0.02
RG-14-BDRK-13	73.00	61.00	15.60	8.50	6.50	2.51	4.07	0.35	0.02
Dust Proxy									
PR-PliBR	244.00	28.70	25.90	11.75	9.77	0.75	0.18	0.76	0.05
Anza Borrego									
Soil samples									
IGNF-13-SOIL-1	486.00	61.90	18.50	3.64	3.52	1.28	3.58	1.98	0.00
IGNF-13-SOIL-2	623.00	60.40	18.00	3.60	3.46	1.26	3.47	1.94	0.00
IGNF-13-SOIL-3	454.00	60.90	18.30	3.65	3.41	1.31	3.54	1.99	0.00
IGNF-13-SOIL-4	528.00	61.80	18.70	3.28	3.87	1.12	4.05	1.88	0.00
IGNF-13-SOIL-5	554.00	63.30	18.95	3.23	3.89	1.09	4.11	1.89	0.00
IGNF-13-SOIL-6	436.00	60.50	18.50	3.37	3.79	1.12	3.94	1.93	0.00
IGNF-13-SOIL-7	622.00	64.20	18.55	3.22	3.81	1.13	3.93	1.87	0.00
Bedrock									
IGNF-13-BDRK-1B	138.00	73.20	13.45	2.86	3.30	0.87	3.51	1.54	0.03
IGNF-13-FBDRK-1	146.00	71.90	13.70	2.88	3.94	1.03	3.43	1.10	0.03
IGNF-13-WBDRK	216.00	63.70	16.95	5.15	4.04	1.68	3.99	2.78	0.03
Dust Trap									
ABD dust sample	205.45	62.89	14.07	4.08	4.67	2.08	2.58	2.40	<0.01

Puerto Rico									
Soil samples									
	TiO2	MnO	P2O5	SrO	BaO	LOI	Total	Ag	As
<63 microns	%	%	%	%	%	%	%	ppm	ppm
RG-14-SOIL-1	0.78	0.03	0.08	<0.01	0.04	12.70	98.61	<0.5	6.00
RG-14-SOIL-2	0.90	0.03	0.07	0.01	0.03	14.95	100.86	<0.5	5.00
RG-14-SOIL-3	1.06	0.03	0.07	<0.01	0.01	14.65	98.83	<0.5	<5
RG-14-SOIL-4	0.78	0.03	0.05	<0.01	0.03	15.70	101.68	<0.5	6.00
RG-14-SOIL-5	0.96	0.04	0.07	<0.01	0.01	14.30	99.50	<0.5	<5
RG-14-SOIL-6	0.47	0.06	0.04	<0.01	0.09	14.50	101.85	<0.5	6.00
Mud fraction subdivisions									
RGSOIL-1-L20	0.85	0.03	0.06	<0.01	0.04	12.10	101.28	<0.5	<5
RGSOIL-2-L20	0.96	0.04	0.05	<0.01	0.04	12.70	101.32	<0.5	<5
RGSOIL-2-G20	0.91	0.04	0.07	<0.01	0.03	11.85	101.75	<0.5	<5
RGSOIL-3-L20	1.13	0.03	0.05	<0.01	0.01	13.80	101.91	<0.5	<5
RGSOIL-4-L20	0.73	0.06	0.05	<0.01	0.04	12.65	100.11	<0.5	<5
RGSOIL-4-G20	0.67	0.05	0.04	<0.01	0.03	11.60	100.68	<0.5	<5
RGSOIL-5-L20	1.09	0.04	0.04	<0.01	0.02	13.50	101.85	<0.5	<5
RGSOIL-6-L20	0.52	0.16	0.04	<0.01	0.10	10.95	100.21	<0.5	<5
RGSOIL-6-G20	0.49	0.15	0.04	<0.01	0.09	10.25	100.19	<0.5	<5
Bedrock									
RB-14-BDRK-#2A	0.62	0.16	0.18	0.05	0.10	1.53			
RG-14-BDRK-13	0.68	0.21	0.11	0.03	0.02	1.23			
Dust Proxy									
PR-PliBR	1.29	0.08	0.22	0.01	0.01	18.95	98.42	<0.5	32.00
Anza Borrego									
Soil samples									
IGNF-13-SOIL-1	0.66	0.05	0.26	0.05	0.07	4.92	100.41	<0.5	<5
IGNF-13-SOIL-2	0.67	0.06	0.26	0.05	0.07	4.88	98.12	<0.5	<5
IGNF-13-SOIL-3	0.63	0.06	0.23	0.05	0.07	4.46	98.60	<0.5	<5
IGNF-13-SOIL-4	0.64	0.06	0.25	0.05	0.07	3.90	99.67	<0.5	<5
IGNF-13-SOIL-5	0.63	0.06	0.23	0.05	0.07	3.67	101.17	<0.5	<5
IGNF-13-SOIL-6	0.65	0.06	0.26	0.06	0.07	3.85	98.10	<0.5	<5
IGNF-13-SOIL-7	0.61	0.06	0.23	0.05	0.07	3.50	101.23	<0.5	<5
Bedrock									
IGNF-13-BDRK-1B	0.43	0.04	0.14	0.05	0.08	1.20	100.70	<0.5	<5
IGNF-13-FBDRK-1	0.54	0.04	0.19	0.06	0.07	0.92	99.83	<0.5	<5
IGNF-13-WBDRK	0.87	0.08	0.27	0.06	0.14	1.00	100.74	<0.5	<5
Dust Trap									
ABD dust sample	0.64	0.13	0.19	0.03	0.09	8.15		<0.5	13.31

Puerto Rico									
Soil samples									
	As	Cd	Co	Cu	Li	Ni	Pb	Sc	Zn
<63 microns	ppm	ppm	ppm	ppm	ppm	ppm	ppm	ppm	ppm
RG-14-SOIL-1	6.00	<0.5	8.00	68.00	10.00	9.00	14.00	25.00	46.00
RG-14-SOIL-2	5.00	<0.5	7.00	133.00	10.00	9.00	54.00	29.00	55.00
RG-14-SOIL-3	<5	<0.5	5.00	123.00	10.00	8.00	14.00	21.00	48.00
RG-14-SOIL-4	6.00	<0.5	4.00	109.00	10.00	8.00	19.00	23.00	41.00
RG-14-SOIL-5	<5	<0.5	5.00	99.00	10.00	7.00	11.00	28.00	48.00
RG-14-SOIL-6	6.00	<0.5	5.00	107.00	10.00	8.00	16.00	20.00	40.00
Mud fraction subdivisions									
RGSOIL-1-L20	<5	<0.5	6.00	90.00	10.00	21.00	99.00	24.00	54.00
RGSOIL-2-L20	<5	<0.5	5.00	81.00	10.00	11.00	42.00	26.00	42.00
RGSOIL-2-G20	<5	<0.5	7.00	73.00	10.00	11.00	29.00	26.00	42.00
RGSOIL-3-L20	<5	<0.5	6.00	141.00	10.00	13.00	65.00	20.00	42.00
RGSOIL-4-L20	<5	<0.5	5.00	86.00	10.00	11.00	32.00	24.00	28.00
RGSOIL-4-G20	<5	<0.5	8.00	74.00	10.00	7.00	29.00	23.00	27.00
RGSOIL-5-L20	<5	<0.5	6.00	106.00	10.00	10.00	33.00	29.00	31.00
RGSOIL-6-L20	<5	<0.5	6.00	93.00	10.00	9.00	43.00	21.00	29.00
RGSOIL-6-G20	<5	<0.5	6.00	77.00	10.00	7.00	60.00	21.00	25.00
Bedrock									
RB-14-BDRK-#2A			11.00					24.00	
RG-14-BDRK-13			16.00					18.00	
Dust Proxy									
PR-PliBR	32.00	0.70	14.00	508.00	100.00	93.00	29.00	18.00	189.00
Anza Borrego									
Soil samples									
IGNF-13-SOIL-1	<5	<0.5	4.00	60.00	40.00	8.00	4.00	7.00	102.00
IGNF-13-SOIL-2	<5	<0.5	8.00	44.00	50.00	6.00	3.00	7.00	104.00
IGNF-13-SOIL-3	<5	<0.5	6.00	31.00	40.00	8.00	5.00	7.00	97.00
IGNF-13-SOIL-4	<5	<0.5	4.00	24.00	40.00	6.00	5.00	7.00	82.00
IGNF-13-SOIL-5	<5	<0.5	6.00	19.00	40.00	6.00	2.00	7.00	81.00
IGNF-13-SOIL-6	<5	<0.5	6.00	30.00	40.00	6.00	<2	7.00	96.00
IGNF-13-SOIL-7	<5	<0.5	5.00	41.00	30.00	6.00	5.00	7.00	84.00
Bedrock									
IGNF-13-BDRK-1B	<5	<0.5	4.00	4.00	80.00	4.00	9.00	4.00	77.00
IGNF-13-FBDRK-1	<5	<0.5	4.00	4.00	30.00	4.00	6.00	5.00	72.00
IGNF-13-WBDRK	<5	<0.5	5.00	6.00	60.00	4.00	10.00	7.00	147.00
Dust Trap									
ABD dust sample	13.31	<0.5	9.34	28.55	29.66	21.14	34.41	7.38	1361.15

Tau Values

Sample	Tau values (noramlized to Ti)					
	Th	Ta	Nb	Zr	Fe	Al
Anza Borrego						
Surface	16.33	5.82	0.84	0.00	-0.49	-0.17
0.2 m	17.51	5.72	0.93	0.26	-0.53	-0.20
0.4 m	14.60	5.35	0.97	-0.03	-0.50	-0.14
0.6 m	14.47	5.25	0.85	0.11	-0.53	-0.13
0.8 m	17.02	5.35	0.88	0.19	-0.54	-0.10
1.2 m	14.62	5.15	0.84	-0.09	-0.52	-0.15
1.5 m	20.11	5.56	0.81	0.38	-0.50	-0.09
WBDRK	0.67	1.78	0.58	0.46	-0.33	0.23
FBDRK	0.00	0.00	0.00	0.00	0.00	0.00
Puerto Rico						
0.1 m	0.41	0.53	1.00	-0.75	-0.05	0.58
0.5 m	0.45	0.35	1.15	-0.76	-0.14	0.40
1.0 m	0.70	0.92	1.62	-0.68	-0.06	0.18
1.5 m	4.24	1.37	2.01	-0.51	-0.10	0.87
2.0 m	0.51	0.59	1.26	-0.71	-0.19	0.26
2.5 m	6.67	2.33	2.62	-0.36	-0.03	1.64
FBDRK	0.00	0.00	0.00	0.00	0.00	0.00

CIA Values

	Weathering Index Nebitt and Young 1984						Molar weights	
Puerto RIco	A	CN	K	C	N	CIA with moles	101.96	Al2O3
Soil							61.98	Na2O
RGSOIL-1-L2	0.31	0.01	0.02	0.00	0.00	93.436	94.2	K2O
RGSOIL-2-L2	0.31	0.00	0.02	0.00	0.00	93.989	56.08	CaO
RGSOIL-2-G2	0.31	0.00	0.01	0.00	0.00	94.658		
RG-14-SOIL-2	0.29	0.01	0.01	0.00	0.01	92.293		
RGSOIL-3-L2	0.31	0.00	0.00	0.00	0.00	98.151		
RGSOIL-4-L2	0.32	0.00	0.02	0.00	0.00	94.203		
RGSOIL-4-G2	0.31	0.00	0.02	0.00	0.00	94.460		
RG-14-SOIL-4	0.29	0.01	0.01	0.00	0.01	92.860		
RGSOIL-5-L2	0.32	0.00	0.01	0.00	0.00	97.414		
RGSOIL-6-L2	0.32	0.00	0.03	0.00	0.00	90.385		
RGSOIL-6-G2	0.30	0.00	0.03	0.00	0.00	90.366		
RG-14-SOIL-6	0.29	0.01	0.03	0.00	0.01	87.185		
Bedrock								
RB-14-BDRK	0.15	0.14	0.02	0.11	0.03	48.426		
RG-14-BDRK	0.15	0.16	0.00	0.12	0.04	48.444		
Dust Proxy								
PR-PliBR	0.25	0.00	0.01	0.00	0.00	95.408		
Anza Borrego								
Soil								
IGNF-13-SOI	0.18	0.10	0.02	0.06	0.04	59.836		
IGNF-13-SOI	0.18	0.10	0.02	0.06	0.04	59.709		
IGNF-13-SOI	0.18	0.10	0.02	0.06	0.04	60.029		
IGNF-13-SOI	0.18	0.11	0.02	0.07	0.04	58.157		
IGNF-13-SOI	0.19	0.11	0.02	0.07	0.04	58.278		
IGNF-13-SOI	0.18	0.11	0.02	0.07	0.04	58.278		
IGNF-13-SOI	0.18	0.11	0.02	0.07	0.04	58.416		
Bedrock								
IGNF-13-BDF	0.13	0.10	0.02	0.06	0.04	53.982		
IGNF-13-FBD	0.13	0.11	0.01	0.07	0.04	53.170		
IGNF-13-WB	0.17	0.11	0.03	0.07	0.04	53.600		
Dust Sample								
ABD dust sa	0.14	0.11	0.03	0.08	0.03	50.341		

AB Bedrock Traces



Puerto Rico Bedrock Traces



SUPPLEMENTAL MATERIALS
Chapter II

Metadata for samples in Chapters II and III

Sample	Latitude	Longitude	stike and dip	Thickness (m)
21-MANY-topsands				
21-MANY-15	-4.608768	29.709954		6
21-MANY-14			18 N / 30 E	18
21-MANY-13	-4.609134	29.7096		6
21-MANY-12	-4.689412	29.709163		43.5
21-MANY-11			11 N/32 E	1.5
21-MANY-10				13.5
21-MANY-9				12
21-MANY-8	-4.60991	29.708661		16.5
21-MANY-7				14.25
21-MANY-6			11 N / 32 E	12
21-MANY-5silt	-4.60989	29.707932		6
				10.5
21-MANY-3silt	-4.609822	29.7077	6 N / 26 E	10.5
21-MANY-2silt	-4.609788	29.707547		13.5
21-MANY-1silt	-4.609827	29.707238	9 N / 31 E	16.5
	-4.609929	29.706975		12
	-4.610138	29.706798	354 N / 28 E	16.5
21-MANY-2White	-4.610409	29.706694	332 NW / 31 E	33
21-MANY-1White	-4.610906	29.705868		22.5
			TOTAL	284.25

Raw point count data

Sample	Qm	Qp	chert	Q	P	K	F	Ls	Lm	Lv	L	Lt	Accesso	Total
21-MANY-topsand	263	16	0	279	54	36	90	3	2	22	27	43	4	400
21-MANY-15	203	13	0	216	98	38	136	0	8	40	48	61	0	400
21-MANY-8	178	9	0	187	124	30	154	3	0	42	45	54	14	400
21-MANY-6i	271	17	2	290	54	26	80	8	5	22	35	54	1	404
21-MANY-6F	240	8	0	248	75	12	87	7	1	49	57	65	8	400
21-MANY-5sand	238	15		253	80	37	117	5	1	17	23	38	7	400
21-MANY-4	255	5	0	260	58	38	96	2	5	33	40	45	4	400
21-MANY-3.1	243	13	1	257	37	16	53	3	2	41	46	60	45	400
21-MANY-3	223	7	0	230	34	33	67	1	0	36	37	44	53	387
21-MANY-2white	300	25	0	325	43	1	44	1	2	28	31	56	0	400
21-MANY-2.1white	293	44	0	337	37	2	39	7	2	15	24	68	0	400
21-MANY-1white	199	77	4	280	23	49	72	1	0	37	38	119	1	400
21-MANY-1.1white	253	14	0	267	48	9	57	4	5	66	75	89	1	400

Raw Data for Detrital Zircon Geochronology

Analysis	206Pb	U	U/Th	206Pb*	Â±2s	207Pb*	Â±2s	206Pb*	Â±2s	error	206Pb*	Â±2s	207Pb*	Â±2s	206Pb*	Â±2s	Best age	Â±2s
	204Pb	(ppm)		207Pb*	(%)	235U	(%)	238U	(%)	corr.	238U	(Ma)	235U	(Ma)	207Pb*	(Ma)	(Ma)	(Ma)
21-MANY-1white																		
Spot 276	9069.1	217.1	5.0	15.6	2.2	0.9	3.5	0.1	1.6	0.5	647.3	10.0	661.7	17.0	712.1	65.7	647.3	10.0
Spot 123	10367.0	197.6	1.8	15.6	2.6	0.9	4.3	0.1	1.6	0.4	648.2	10.1	663.5	20.8	716.7	83.6	648.2	10.1
Spot 196	30167.7	340.5	4.3	16.1	2.2	0.9	3.0	0.1	1.2	0.4	654.4	7.5	659.3	14.5	677.0	58.4	654.4	7.5
Spot 112	2707.1	32.9	2.7	14.6	11.0	0.9	18.5	0.1	2.2	0.1	654.5	13.8	672.5	91.2	734.3	390.4	654.5	13.8
Spot 195	32113.8	332.4	2.2	16.0	1.9	0.9	2.4	0.1	1.4	0.6	661.1	8.9	669.0	11.8	696.7	41.5	661.1	8.9
Spot 138	21288.0	195.5	2.7	16.0	2.7	0.9	3.5	0.1	1.4	0.4	665.6	8.6	669.5	17.2	683.7	68.9	665.6	8.6
Spot 110	40429.4	337.1	12.0	16.3	2.1	0.9	2.6	0.1	1.3	0.5	665.7	8.4	663.1	12.5	655.5	46.9	665.7	8.4
Spot 88	13513.5	303.0	3.1	15.6	2.0	0.9	3.9	0.1	1.4	0.4	666.5	9.2	676.4	19.0	710.4	75.9	666.5	9.2
Spot 139	34572.9	305.4	5.4	16.0	2.1	0.9	2.5	0.1	1.3	0.5	667.6	8.2	673.4	12.4	693.6	46.0	667.6	8.2
Spot 107	36575.3	332.2	2.9	16.2	1.7	0.9	2.5	0.1	1.5	0.6	668.0	9.6	665.8	12.2	659.2	42.9	668.0	9.6
Spot 204	47008.3	442.1	1.8	16.1	1.5	0.9	2.1	0.1	1.3	0.6	668.2	8.5	671.9	10.1	685.6	33.6	668.2	8.5
Spot 105	4606.7	330.0	3.0	15.2	2.1	0.9	4.4	0.1	1.4	0.3	668.3	8.6	677.0	21.8	706.8	89.5	668.3	8.6
Spot 277	13077.4	138.7	1.8	15.6	3.6	1.0	4.4	0.1	1.5	0.3	668.7	9.3	682.4	22.1	728.9	88.9	668.7	9.3
Spot 157	19698.0	159.2	4.3	16.0	3.7	0.9	4.3	0.1	1.6	0.4	668.9	10.3	673.1	21.3	687.9	85.7	668.9	10.3
Spot 113	29933.4	267.7	2.1	16.1	2.3	0.9	2.9	0.1	1.5	0.5	670.1	9.6	670.2	14.1	671.2	52.3	670.1	9.6
Spot 133	27586.7	221.7	2.5	16.2	2.4	0.9	3.0	0.1	1.5	0.5	671.4	9.3	669.6	14.8	664.6	56.4	671.4	9.3
Spot 303	22958.0	174.4	1.0	16.5	3.9	0.9	4.1	0.1	1.2	0.3	673.5	7.6	663.5	20.0	630.8	84.6	673.5	7.6
Spot 183	38416.9	370.4	3.8	16.1	2.0	1.0	2.6	0.1	1.5	0.6	674.5	9.4	678.4	12.7	692.1	45.1	674.5	9.4
Spot 280	2764.2	237.4	3.8	14.5	3.0	1.0	4.7	0.1	2.5	0.5	677.5	16.3	693.7	23.6	747.5	83.5	677.5	16.3
Spot 150	26833.7	232.4	4.5	15.8	2.1	1.0	2.9	0.1	1.3	0.4	678.2	8.1	687.9	14.5	720.9	55.3	678.2	8.1
Spot 106	21724.6	212.3	2.8	16.1	2.5	0.9	3.5	0.1	1.3	0.4	679.5	8.3	674.8	17.1	660.1	69.0	679.5	8.3
Spot 27	9484.0	96.2	3.3	15.8	5.5	0.9	6.1	0.1	1.5	0.2	679.9	9.6	677.7	29.9	671.2	125.6	679.9	9.6
Spot 161	14617.4	138.4	3.0	15.8	4.0	1.0	5.3	0.1	1.5	0.3	680.2	9.7	683.3	26.3	694.4	107.8	680.2	9.7
Spot 35	17367.3	172.6	2.7	15.8	2.9	1.0	3.3	0.1	1.5	0.4	682.0	9.5	685.0	16.4	695.8	62.7	682.0	9.5
Spot 149	42617.1	437.9	5.4	16.0	1.6	1.0	2.2	0.1	1.4	0.7	682.4	9.2	686.6	10.8	701.6	34.8	682.4	9.2
Spot 14	21000.0	188.6	3.4	16.2	2.6	1.0	3.5	0.1	1.4	0.4	685.5	9.1	679.5	17.2	660.8	68.0	685.5	9.1
Spot 36	20721.3	211.0	5.1	16.3	2.5	0.9	3.4	0.1	1.4	0.4	686.1	9.2	674.9	16.6	638.7	66.0	686.1	9.2
Spot 176	5310.4	317.0	4.0	15.1	2.2	1.0	3.4	0.1	1.8	0.5	688.4	11.5	701.4	17.0	744.1	60.5	688.4	11.5
Spot 75	10033.3	110.5	1.6	15.3	4.8	1.0	6.0	0.1	1.6	0.3	688.9	10.5	703.4	30.5	750.9	122.3	688.9	10.5
Spot 174	22790.7	222.1	2.9	15.9	2.9	1.0	3.5	0.1	1.4	0.4	689.1	9.0	691.3	17.7	699.6	69.4	689.1	9.0
Spot 234	34374.8	358.8	2.9	16.0	1.6	1.0	2.1	0.1	1.3	0.6	691.6	8.5	689.7	10.6	684.5	36.0	691.6	8.5
Spot 255	37597.1	410.1	44.5	16.4	2.1	1.0	2.8	0.1	1.8	0.6	693.3	11.7	680.7	14.0	640.1	47.3	693.3	11.7
Spot 286	23822.9	281.7	3.0	15.7	1.9	1.0	2.7	0.1	1.4	0.5	693.4	9.5	708.6	13.7	758.0	47.6	693.4	9.5
Spot 126	22373.6	187.2	3.1	16.0	2.7	1.0	3.5	0.1	1.4	0.4	696.4	9.5	693.6	17.5	685.2	67.4	696.4	9.5
Spot 233	5588.3	49.3	2.9	15.5	6.1	1.0	6.8	0.1	1.4	0.2	696.7	9.2	694.8	34.4	689.6	142.6	696.7	9.2
Spot 278	8635.6	79.0	3.6	15.3	7.1	1.0	8.1	0.1	1.9	0.2	697.2	12.5	709.9	41.2	751.1	165.7	697.2	12.5
Spot 297	27446.5	307.6	3.4	16.0	2.4	1.0	2.8	0.1	1.4	0.5	698.0	9.2	701.4	14.2	713.1	51.5	698.0	9.2
Spot 162	21801.3	244.9	4.4	16.0	1.8	1.0	2.6	0.1	1.3	0.5	699.7	8.3	695.1	13.0	681.1	48.2	699.7	8.3
Spot 290	14445.7	188.5	3.3	16.1	2.6	1.0	4.1	0.1	1.5	0.4	700.2	10.2	697.5	20.6	690.0	80.7	700.2	10.2
Spot 93	60681.7	530.9	2.1	15.9	1.5	1.0	2.1	0.1	1.4	0.6	700.5	9.0	699.9	10.8	698.9	35.0	700.5	9.0
Spot 215	15637.5	161.3	2.9	16.0	3.6	1.0	3.9	0.1	1.4	0.4	700.5	9.2	692.6	19.8	667.8	79.2	700.5	9.2
Spot 225	15215.9	150.6	2.7	15.8	3.6	1.0	4.6	0.1	1.3	0.3	701.4	8.4	701.8	23.2	704.0	93.7	701.4	8.4
Spot 284	27350.6	196.9	3.0	16.1	3.1	1.0	3.5	0.1	1.4	0.4	702.0	9.3	701.9	17.5	702.8	67.5	702.0	9.3
Spot 49	15465.6	596.8	2.1	15.9	2.1	1.0	3.7	0.1	1.8	0.5	702.1	12.0	696.9	18.7	680.8	69.0	702.1	12.0
Spot 217	7317.4	68.6	3.1	15.4	5.1	1.0	6.9	0.1	1.5	0.2	702.8	10.2	707.5	35.3	723.2	143.5	702.8	10.2
Spot 18	44334.8	363.0	5.0	16.0	1.9	1.0	2.3	0.1	1.4	0.6	702.9	9.2	701.3	11.9	697.1	40.3	702.9	9.2
Spot 244	21077.7	220.1	3.9	16.2	2.7	1.0	3.1	0.1	1.4	0.4	704.5	9.2	694.3	15.7	662.3	60.1	704.5	9.2
Spot 2	18222.2	218.7	4.5	16.2	2.5	1.0	3.2	0.1	1.5	0.5	707.1	10.0	696.1	16.3	661.7	61.3	707.1	10.0
Spot 279	7888.7	321.7	5.4	14.9	1.8	1.1	3.7	0.1	1.7	0.5	711.8	11.5	733.1	19.3	799.4	68.6	711.8	11.5
Spot 226	30244.1	280.2	2.5	15.9	2.0	1.0	2.8	0.1	1.3	0.5	712.5	8.9	709.8	14.4	702.2	53.1	712.5	8.9
Spot 48	4420.6	87.4	3.0	14.6	4.9	1.1	6.8	0.1	2.4	0.3	722.0	16.1	737.6	35.6	786.2	133.7	722.0	16.1
Spot 221	41763.5	314.8	5.5	15.8	1.8	1.0	2.7	0.1	1.8	0.7	722.0	12.2	722.9	13.7	726.4	41.7	722.0	12.2
Spot 125	33265.2	596.7	4.1	15.6	1.4	1.0	1.9	0.1	1.3	0.7	723.1	8.6	728.6	9.7	746.3	29.3	723.1	8.6
Spot 56	17839.7	298.5	9.4	15.9	2.5	1.0	3.0	0.1	1.4	0.5	726.1	9.9	717.9	15.2	693.2	54.9	726.1	9.9
Spot 188	43080.2	410.9	6.6	16.0	2.1	1.0	2.8	0.1	1.8	0.6	727.3	12.4	721.0	14.4	702.6	45.2	727.3	12.4
Spot 261	20725.7	147.0	3.4	15.5	3.1	1.1	3.6	0.1	1.5	0.4	742.7	10.3	743.0	19.0	744.9	69.6	742.7	10.3

Analysis	206Pb	U	U/Th	206Pb*	Â±2s	207Pb*	Â±2s	206Pb*	Â±2s	error	206Pb*	Â±2s	207Pb*	Â±2s	206Pb*	Â±2s	Best age	Â±2s
Spot 273	23948.8	106.6	1.5	12.7	2.0	2.2	2.7	0.2	1.5	0.6	1171.4	16.4	1168.8	18.4	1164.9	43.1	1164.9	43.1
Spot 41	7136.6	151.0	2.5	12.2	2.0	2.2	2.9	0.2	1.7	0.6	1178.6	18.2	1185.9	20.1	1200.1	45.9	1200.1	45.9
Spot 227	26884.9	140.5	2.0	12.2	1.7	2.4	2.2	0.2	1.2	0.5	1255.7	14.0	1251.6	16.2	1245.4	37.0	1245.4	37.0
Spot 20	13826.2	65.2	1.9	11.9	3.3	2.6	3.6	0.2	1.3	0.4	1308.7	15.5	1298.5	26.3	1282.6	65.2	1282.6	65.2
Spot 22	15613.7	83.3	5.5	11.9	2.7	2.2	3.2	0.2	1.5	0.5	1147.5	16.0	1195.4	22.7	1283.8	55.5	1283.8	55.5
Spot 228	18018.9	78.0	0.9	11.7	2.3	2.6	2.8	0.2	1.4	0.5	1269.4	16.4	1288.5	20.1	1321.4	45.7	1321.4	45.7
Spot 302	44351.0	229.4	2.6	11.5	1.4	2.8	1.9	0.2	1.2	0.6	1348.5	14.1	1360.2	14.1	1379.5	28.5	1379.5	28.5
Spot 209	31217.4	131.1	2.0	11.2	1.6	3.2	2.2	0.3	1.5	0.7	1478.9	19.5	1452.0	16.9	1413.6	30.8	1413.6	30.8
Spot 31	9711.0	41.8	1.1	11.0	4.6	3.1	5.4	0.2	1.6	0.3	1434.3	20.1	1426.2	41.0	1414.9	97.9	1414.9	97.9
Spot 12	11967.9	58.5	2.0	11.1	3.2	3.1	4.0	0.2	1.5	0.4	1437.3	19.6	1428.4	30.6	1416.0	70.7	1416.0	70.7
Spot 224	37417.1	159.4	5.3	11.2	1.3	3.2	1.8	0.3	1.2	0.7	1478.3	16.5	1455.1	14.2	1422.3	25.9	1422.3	25.9
Spot 241	18493.9	95.2	1.9	11.0	2.0	3.2	2.6	0.3	1.3	0.5	1458.1	17.4	1450.8	19.7	1440.9	41.4	1440.9	41.4
Spot 146	94183.0	478.5	2.8	11.0	1.3	3.1	2.0	0.2	1.5	0.8	1427.6	19.7	1437.3	15.6	1452.7	25.1	1452.7	25.1
Spot 205	10498.6	45.1	1.9	10.6	3.2	3.3	3.7	0.3	1.4	0.4	1461.3	17.9	1480.6	28.8	1509.1	64.9	1509.1	64.9
Spot 169	36649.3	256.6	1.9	10.4	1.1	3.6	1.6	0.3	1.1	0.7	1544.7	15.2	1553.2	13.1	1565.5	22.8	1565.5	22.8
Spot 216	64658.1	266.7	1.2	9.8	1.3	4.3	1.9	0.3	1.4	0.7	1708.7	20.6	1689.9	15.5	1667.5	23.8	1667.5	23.8
Spot 252	58752.6	194.4	2.4	9.7	1.2	4.5	1.9	0.3	1.4	0.7	1751.0	21.7	1721.7	15.8	1687.1	23.6	1687.1	23.6
Spot 275	6945.8	26.2	1.2	9.5	4.3	4.4	5.6	0.3	1.6	0.3	1717.4	23.8	1711.4	46.5	1704.9	99.4	1704.9	99.4
Spot 266	29576.1	112.0	2.8	9.5	1.9	4.6	2.5	0.3	1.5	0.6	1765.3	23.6	1744.9	20.4	1721.3	35.2	1721.3	35.2
Spot 186	12548.9	43.7	1.4	9.5	3.3	4.4	4.0	0.3	1.9	0.5	1709.7	28.0	1716.1	33.5	1724.7	65.9	1724.7	65.9
Spot 237	12953.8	128.5	5.0	9.2	1.5	4.5	2.7	0.3	1.6	0.6	1706.4	23.9	1730.9	22.8	1761.4	40.9	1761.4	40.9
Spot 164	65428.7	240.9	1.7	9.3	1.2	4.7	1.7	0.3	1.2	0.7	1759.5	18.4	1760.1	14.2	1761.6	22.1	1761.6	22.1
Spot 3	8421.7	161.8	1.2	9.2	1.2	3.9	3.8	0.3	2.8	0.7	1514.5	37.4	1623.9	30.9	1769.5	47.8	1769.5	47.8
Spot 81	29045.1	91.2	2.2	9.2	1.7	4.7	2.3	0.3	1.4	0.6	1753.4	22.1	1760.8	19.6	1770.3	33.7	1770.3	33.7
Spot 57	38474.6	143.7	2.0	9.2	1.4	4.9	2.2	0.3	1.7	0.8	1813.2	26.2	1794.0	18.2	1772.5	25.5	1772.5	25.5
Spot 6	23512.5	90.0	1.4	9.3	1.4	4.7	2.2	0.3	1.3	0.6	1748.0	20.1	1759.4	18.5	1773.8	32.4	1773.8	32.4
Spot 192	52943.1	404.4	1.4	9.3	1.4	4.8	2.0	0.3	1.4	0.7	1786.2	22.2	1781.5	16.6	1776.8	25.0	1776.8	25.0
Spot 147	20593.7	131.4	1.4	9.2	1.6	4.5	2.4	0.3	1.5	0.6	1679.2	22.6	1728.6	19.8	1789.6	33.2	1789.6	33.2
Spot 118	62771.5	198.6	1.4	9.1	1.4	4.2	2.3	0.3	1.7	0.8	1588.5	24.1	1681.8	18.5	1801.0	26.7	1801.0	26.7
Spot 145	36196.4	174.2	1.2	9.1	1.3	4.7	2.0	0.3	1.5	0.7	1736.2	22.1	1767.3	16.4	1805.1	23.9	1805.1	23.9
Spot 94	7566.3	159.8	2.0	8.9	1.4	4.5	2.2	0.3	1.7	0.8	1672.4	24.8	1733.0	18.3	1807.8	25.8	1807.8	25.8
Spot 170	26718.7	168.2	1.7	9.0	1.2	4.9	1.7	0.3	1.1	0.7	1800.0	18.0	1809.5	14.2	1821.1	22.2	1821.1	22.2
Spot 269	######	524.3	37.7	9.0	0.9	5.2	1.5	0.3	1.2	0.8	1869.4	19.0	1850.0	12.8	1829.1	17.2	1829.1	17.2
Spot 98	35848.9	94.8	1.1	8.9	1.5	5.1	2.1	0.3	1.4	0.7	1839.6	22.8	1837.4	17.9	1835.7	28.1	1835.7	28.1
Spot 80	20551.1	57.8	1.5	8.8	1.9	5.5	2.4	0.4	1.4	0.6	1942.9	23.8	1901.8	20.9	1858.1	35.7	1858.1	35.7
Spot 222	21581.0	67.0	0.6	8.8	1.6	5.4	2.1	0.3	1.2	0.6	1904.1	20.2	1884.0	17.9	1862.7	30.5	1862.7	30.5
Spot 51	26128.8	76.1	1.6	8.8	1.5	5.4	2.1	0.3	1.4	0.6	1914.4	22.4	1889.8	18.0	1863.6	28.8	1863.6	28.8
Spot 257	59221.2	159.3	1.7	8.8	1.6	5.5	2.4	0.3	1.8	0.7	1927.2	29.4	1897.0	20.5	1864.9	28.9	1864.9	28.9
Spot 312	35642.3	106.4	1.3	8.8	1.7	5.1	2.4	0.3	1.6	0.7	1820.1	25.7	1843.2	20.5	1870.2	32.3	1870.2	32.3
Spot 25	23629.5	218.9	2.1	8.7	1.2	5.2	2.1	0.3	1.4	0.7	1836.9	23.0	1853.4	17.9	1872.7	27.7	1872.7	27.7
Spot 199	24296.1	82.4	1.5	8.7	1.6	5.0	2.2	0.3	1.4	0.6	1770.7	22.0	1817.8	19.0	1872.9	31.3	1872.9	31.3
Spot 151	42474.0	95.5	1.4	8.8	1.4	5.3	1.8	0.3	1.2	0.6	1868.9	19.0	1872.8	15.8	1877.8	25.7	1877.8	25.7
Spot 86	28598.8	100.1	1.0	8.7	1.4	5.5	2.2	0.3	1.6	0.7	1929.3	26.3	1905.6	19.0	1880.7	28.0	1880.7	28.0
Spot 47	58379.4	157.7	2.3	8.7	1.5	5.5	2.0	0.3	1.4	0.7	1929.2	23.3	1905.7	17.5	1881.0	26.7	1881.0	26.7
Spot 191	33179.4	331.1	1.6	8.7	1.2	5.2	1.9	0.3	1.4	0.7	1820.5	22.5	1849.3	16.3	1882.6	23.2	1882.6	23.2
Spot 230	42388.4	209.9	1.2	8.7	1.3	4.7	2.0	0.3	1.4	0.7	1673.3	20.6	1768.3	16.7	1883.2	25.7	1883.2	25.7
Spot 294	11897.5	36.8	1.1	8.7	2.8	5.3	3.5	0.3	1.5	0.4	1849.3	24.6	1865.9	29.5	1885.2	55.8	1885.2	55.8
Spot 13	13350.8	58.9	1.2	8.7	1.9	5.4	2.9	0.3	1.5	0.5	1870.9	24.1	1877.7	25.2	1886.1	45.7	1886.1	45.7
Spot 148	58531.6	232.9	2.5	8.7	1.3	5.2	1.9	0.3	1.4	0.7	1830.4	22.4	1856.7	16.3	1887.0	23.5	1887.0	23.5
Spot 10	29018.1	96.9	1.9	8.7	2.0	5.4	3.0	0.3	2.1	0.7	1875.8	34.3	1881.1	25.6	1887.8	38.1	1887.8	38.1
Spot 262	39257.0	103.6	1.2	8.7	1.5	5.5	2.1	0.3	1.5	0.7	1914.9	24.0	1902.2	17.8	1889.2	26.5	1889.2	26.5
Spot 129	52388.6	174.3	1.2	8.7	1.3	5.4	1.9	0.3	1.4	0.7	1868.9	22.6	1878.4	16.6	1889.7	24.2	1889.7	24.2
Spot 1	46515.4	167.0	2.0	8.7	1.2	5.5	1.7	0.3	1.2	0.7	1891.5	20.4	1894.6	15.0	1898.7	22.0	1898.7	22.0
Spot 119	10782.3	300.2	1.0	8.6	1.3	5.2	2.0	0.3	1.5	0.8	1804.8	23.3	1848.7	16.7	1899.3	23.1	1899.3	23.1
Spot 109	69617.2	181.6	1.3	8.6	1.3	5.4	1.9	0.3	1.4	0.7	1868.9	22.8	1883.7	16.3	1900.9	23.1	1900.9	23.1
Spot 76	46796.6	140.5	3.0	8.6	1.5	5.7	2.2	0.4	1.5	0.7	1970.7	26.3	1938.3	18.8	1904.5	27.5	1904.5	27.5
Spot 245	7420.9	23.8	0.7	8.5	3.9	5.5	4.4	0.3	1.4	0.3	1908.6	23.7	1907.1	38.2	1906.2	75.5	1906.2	75.5
Spot 11	64534.0	194.7	1.0	8.5	1.4	5.7	2.0	0.3	1.4	0.7	1933.4	23.9	1930.5	17.3	1928.3	25.0	1928.3	25.0

Analysis	206Pb	U	U/Th	206Pb*	Â±2s	207Pb*	Â±2s	206Pb*	Â±2s	error	206Pb*	Â±2s	207Pb*	Â±2s	206Pb*	Â±2s	Best age	Â±2s
Spot 249	27543.8	215.1	6.9	15.8	2.4	1.1	3.0	0.1	1.5	0.5	748.1	10.3	739.8	15.9	715.7	56.4	748.1	10.3
Spot 210	23323.9	283.3	6.3	15.8	2.5	1.1	2.9	0.1	1.4	0.5	749.5	9.9	740.4	15.4	714.1	54.4	749.5	9.9
Spot 258	39895.6	311.3	4.4	15.7	2.2	1.1	2.9	0.1	1.8	0.6	763.9	12.7	755.2	15.3	730.3	48.2	763.9	12.7
Spot 66	20956.5	175.0	4.5	15.6	3.0	1.1	3.4	0.1	1.3	0.4	767.4	9.1	758.4	17.9	733.0	66.0	767.4	9.1
Spot 307	21883.4	427.5	3.9	15.1	1.8	1.2	2.7	0.1	1.9	0.7	780.6	13.9	790.4	14.9	819.1	40.6	780.6	13.9
Spot 70	6265.8	412.8	3.6	14.6	1.7	1.2	2.4	0.1	1.6	0.7	793.0	12.2	801.1	13.5	824.9	37.4	793.0	12.2
Spot 203	20978.5	139.6	4.3	14.7	2.9	1.3	3.7	0.1	1.2	0.3	849.2	9.7	853.9	21.4	867.0	72.5	849.2	9.7
Spot 83	14931.7	138.8	2.7	14.9	2.7	1.3	3.3	0.1	1.5	0.5	854.8	11.8	843.0	18.7	813.0	60.9	854.8	11.8
Spot 223	41360.1	276.2	2.8	15.0	1.9	1.3	2.3	0.1	1.2	0.5	870.0	9.5	858.4	13.1	829.4	40.3	870.0	9.5
Spot 38	20799.7	112.7	2.2	14.7	2.8	1.4	3.3	0.2	1.5	0.5	901.2	12.7	887.7	19.7	855.2	61.5	901.2	12.7
Spot 248	17657.2	103.1	3.3	14.3	3.1	1.4	3.9	0.1	1.4	0.3	898.9	11.5	903.1	23.4	914.3	75.4	914.3	75.4
Spot 128	14671.1	69.7	0.9	14.2	4.9	1.6	5.5	0.2	1.6	0.3	982.7	14.9	964.1	34.5	922.6	108.7	922.6	108.7
Spot 154	20815.0	530.9	6.3	14.3	1.7	1.4	2.5	0.1	1.7	0.7	886.0	14.1	897.4	14.6	926.8	36.4	926.8	36.4
Spot 172	12227.8	99.4	1.5	14.2	4.0	1.4	4.4	0.1	1.4	0.3	887.7	11.3	900.2	26.1	931.7	85.3	931.7	85.3
Spot 155	8573.9	51.9	2.6	14.0	6.4	1.4	6.9	0.1	1.8	0.3	862.8	14.9	885.0	41.0	941.8	137.1	941.8	137.1
Spot 184	17188.0	177.5	1.0	14.1	2.4	1.5	3.1	0.2	1.5	0.5	915.0	12.9	925.6	19.1	952.1	56.3	952.1	56.3
Spot 189	18702.4	126.3	2.6	14.1	2.3	1.6	2.9	0.2	1.3	0.4	997.0	11.8	983.8	18.5	955.2	54.1	955.2	54.1
Spot 127	31988.6	201.5	2.0	14.1	1.8	1.6	2.4	0.2	1.4	0.6	976.5	12.6	969.9	14.9	955.7	39.7	955.7	39.7
Spot 163	20820.4	161.1	1.4	14.0	2.0	1.6	2.5	0.2	1.2	0.5	981.9	11.0	974.5	15.9	958.9	45.7	958.9	45.7
Spot 130	23261.9	157.8	1.8	14.1	2.4	1.6	3.1	0.2	1.6	0.5	982.1	14.3	974.8	19.1	959.3	53.4	959.3	53.4
Spot 229	3816.1	29.7	1.1	13.4	9.4	1.5	9.9	0.1	2.1	0.2	888.8	17.5	910.0	59.7	962.7	198.2	962.7	198.2
Spot 165	19654.1	127.3	0.9	13.9	2.7	1.6	3.0	0.2	1.2	0.4	995.7	11.3	987.1	19.2	969.0	56.7	969.0	56.7
Spot 194	14718.6	110.1	2.3	13.9	2.7	1.5	3.7	0.2	1.5	0.4	917.8	12.7	932.9	22.9	969.5	70.3	969.5	70.3
Spot 44	28872.0	186.5	1.7	13.9	2.0	1.7	2.6	0.2	1.6	0.6	1027.2	15.4	1012.5	16.9	981.7	42.2	981.7	42.2
Spot 185	27634.2	172.0	1.9	14.0	2.2	1.6	2.8	0.2	1.4	0.5	971.5	12.8	974.7	17.5	982.6	49.1	982.6	49.1
Spot 21	19197.3	148.8	1.1	13.8	2.7	1.7	3.3	0.2	1.5	0.5	1006.1	14.1	1000.3	21.1	988.4	60.2	988.4	60.2
Spot 212	29299.3	162.3	3.1	13.9	2.2	1.7	2.7	0.2	1.4	0.5	1006.4	13.3	1000.5	17.2	988.5	46.7	988.5	46.7
Spot 181	56093.5	356.5	4.5	14.0	1.3	1.6	1.8	0.2	1.2	0.7	969.0	11.2	974.7	11.6	988.6	27.7	988.6	27.7
Spot 15	30240.7	251.0	2.4	13.9	1.8	1.6	2.4	0.2	1.3	0.5	982.0	12.0	984.2	15.3	989.9	41.4	989.9	41.4
Spot 171	4505.3	75.2	1.0	13.4	5.5	1.7	7.4	0.2	1.2	0.2	992.3	11.1	991.4	47.0	990.4	149.1	990.4	149.1
Spot 289	32795.8	233.8	2.4	14.0	1.4	1.7	2.0	0.2	1.3	0.7	991.2	12.2	991.0	12.7	991.5	30.4	991.5	30.4
Spot 315	13454.4	100.9	1.0	13.8	2.6	1.6	3.4	0.2	1.3	0.4	941.6	11.3	956.4	20.8	991.6	63.0	991.6	63.0
Spot 97	29285.2	185.2	3.2	13.8	2.7	1.6	3.3	0.2	1.4	0.4	985.5	13.1	987.1	20.8	991.7	60.3	991.7	60.3
Spot 5	25514.7	187.6	2.5	13.8	2.3	1.6	2.9	0.2	1.5	0.5	971.8	13.8	978.7	17.9	995.2	48.9	995.2	48.9
Spot 52	22447.3	106.8	1.6	13.8	2.6	1.8	3.0	0.2	1.4	0.5	1046.2	13.2	1029.7	19.5	995.6	54.5	995.6	54.5
Spot 58	8469.9	224.4	3.7	13.6	1.8	1.6	2.6	0.2	1.4	0.6	969.0	12.9	977.4	16.3	997.1	43.8	997.1	43.8
Spot 240	6682.1	498.8	3.1	13.5	1.3	1.4	2.2	0.1	1.7	0.8	828.0	13.4	875.3	12.8	997.9	27.0	997.9	27.0
Spot 268	6470.8	46.0	1.1	13.5	7.8	1.7	8.6	0.2	1.7	0.2	1006.3	16.3	1004.5	54.7	1001.5	170.4	1001.5	170.4
Spot 308	5176.1	297.3	0.9	13.4	1.7	1.4	3.2	0.1	1.9	0.6	831.9	14.6	879.5	19.1	1001.9	53.7	1001.9	53.7
Spot 117	8424.6	83.0	3.6	13.6	3.6	1.7	5.2	0.2	2.0	0.4	1031.5	19.0	1021.9	33.5	1002.3	97.5	1002.3	97.5
Spot 298	41657.6	234.6	1.3	13.9	2.0	1.6	2.5	0.2	1.5	0.6	956.3	13.2	970.1	15.8	1002.5	41.5	1002.5	41.5
Spot 231	54554.9	358.8	1.5	13.8	1.4	1.7	1.8	0.2	1.1	0.6	985.3	10.5	990.6	11.6	1003.3	29.2	1003.3	29.2
Spot 136	38230.6	218.8	2.3	13.8	1.8	1.6	2.4	0.2	1.3	0.6	971.2	12.1	981.1	15.0	1004.2	40.0	1004.2	40.0
Spot 260	21723.5	136.0	3.1	13.7	2.7	1.7	3.3	0.2	1.8	0.6	1000.0	17.1	1001.1	21.3	1004.5	56.6	1004.5	56.6
Spot 4	17960.0	145.1	1.2	13.7	2.3	1.6	3.1	0.2	1.5	0.5	975.9	13.5	985.2	19.6	1007.0	55.4	1007.0	55.4
Spot 177	48736.3	332.6	2.2	13.8	1.6	1.7	2.3	0.2	1.5	0.7	998.2	14.3	1001.6	14.5	1010.1	33.9	1010.1	33.9
Spot 175	6147.5	238.4	1.2	13.4	2.0	1.6	2.6	0.2	1.4	0.6	942.5	12.4	963.1	16.0	1011.2	43.5	1011.2	43.5
Spot 8	44285.7	305.8	1.1	13.8	2.0	1.7	3.0	0.2	2.0	0.7	1008.7	19.0	1010.8	19.0	1016.4	43.8	1016.4	43.8
Spot 283	25416.3	126.3	1.7	13.7	2.3	1.7	2.7	0.2	1.4	0.5	1017.9	13.0	1017.3	17.3	1016.7	46.8	1016.7	46.8
Spot 64	32463.3	166.8	3.7	13.6	2.0	1.8	2.4	0.2	1.3	0.5	1076.1	12.8	1057.6	15.7	1020.5	40.8	1020.5	40.8
Spot 153	9837.1	58.3	1.5	13.4	5.4	1.7	6.6	0.2	1.7	0.3	983.8	15.8	999.3	41.9	1034.3	128.3	1034.3	128.3
Spot 132	27905.7	168.7	1.3	13.5	2.2	1.7	2.8	0.2	1.7	0.6	1021.5	16.1	1026.3	18.2	1037.4	45.5	1037.4	45.5
Spot 251	39857.6	219.8	2.5	13.4	1.6	1.9	2.2	0.2	1.3	0.6	1106.4	13.7	1093.0	14.4	1067.1	33.9	1067.1	33.9
Spot 96	11023.4	115.3	1.7	13.1	3.1	1.7	4.1	0.2	1.8	0.4	993.4	16.4	1017.9	26.3	1071.9	74.1	1071.9	74.1
Spot 182	9969.9	66.8	0.5	13.2	4.4	1.9	4.8	0.2	1.6	0.3	1067.0	15.8	1069.9	31.4	1076.7	89.8	1076.7	89.8
Spot 236	3812.8	26.0	0.5	12.6	10.1	1.8	10.8	0.2	2.0	0.2	1017.8	18.5	1041.2	70.7	1091.6	213.8	1091.6	213.8
Spot 142	50868.3	257.9	0.4	13.2	1.5	1.9	2.1	0.2	1.3	0.6	1071.1	13.0	1078.0	13.7	1092.8	31.8	1092.8	31.8
Spot 272	5301.2	368.2	2.8	12.7	1.7	1.9	7.2	0.2	3.1	0.4	1049.2	30.4	1068.6	47.7	1109.4	129.8	1109.4	129.8

Analysis	206Pb	U	U/Th	206Pb*	Â±2s	207Pb*	Â±2s	206Pb*	Â±2s	error	206Pb*	Â±2s	207Pb*	Â±2s	206Pb*	Â±2s	Best age	Â±2s
Spot 100	69249.5	228.1	2.6	8.3	1.9	5.8	2.8	0.4	2.0	0.7	1935.2	33.5	1951.0	24.1	1968.6	34.3	1968.6	34.3
Spot 104	36245.1	116.3	1.1	8.2	1.3	6.0	1.9	0.4	1.3	0.7	1966.6	22.8	1972.9	16.7	1980.2	24.3	1980.2	24.3
Spot 122	######	267.5	3.3	8.3	1.6	5.9	2.3	0.4	1.7	0.7	1953.6	28.4	1966.3	20.1	1980.4	28.2	1980.4	28.2
Spot 267	49973.1	123.2	1.2	8.2	1.3	6.3	2.1	0.4	1.6	0.8	2054.4	28.9	2020.9	18.6	1987.7	23.9	1987.7	23.9
Spot 9	59702.0	209.5	1.4	8.2	1.8	6.1	2.8	0.4	2.1	0.7	2000.0	35.6	1997.2	24.3	1995.0	33.0	1995.0	33.0
Spot 287	75313.6	406.3	1.9	8.3	1.3	6.0	2.0	0.4	1.4	0.7	1958.5	24.3	1977.0	17.1	1997.1	23.8	1997.1	23.8
Spot 55	50511.5	142.8	1.6	8.2	1.2	6.3	1.7	0.4	1.2	0.7	2042.5	21.7	2020.6	15.3	1999.0	21.8	1999.0	21.8
Spot 91	52356.4	129.3	2.2	8.1	1.7	6.3	2.5	0.4	1.7	0.7	2036.3	30.2	2019.1	21.5	2002.4	30.9	2002.4	30.9
Spot 120	13160.6	291.8	2.4	8.0	1.3	5.7	2.3	0.3	1.8	0.8	1832.7	28.8	1928.6	19.7	2034.0	24.6	2034.0	24.6
Spot 314	53680.7	159.3	1.6	8.0	1.6	6.2	2.4	0.4	1.8	0.7	1976.7	30.5	2006.0	21.1	2037.0	28.6	2037.0	28.6
Spot 253	55381.1	154.8	1.5	7.9	1.2	6.7	1.8	0.4	1.3	0.7	2078.4	23.5	2068.8	15.7	2060.0	21.1	2060.0	21.1
Spot 259	14478.3	42.5	1.1	7.9	2.3	6.7	3.3	0.4	1.9	0.6	2079.2	32.9	2069.8	28.9	2061.2	47.6	2061.2	47.6
Spot 140	######	406.8	2.4	7.9	1.2	6.4	1.7	0.4	1.3	0.7	2014.1	22.3	2038.4	15.2	2063.9	20.4	2063.9	20.4
Spot 135	10727.6	388.7	1.7	7.8	1.2	5.9	2.0	0.3	1.5	0.8	1851.4	23.8	1955.9	16.9	2069.2	22.4	2069.2	22.4
Spot 306	24852.8	69.3	1.2	7.8	2.0	6.5	2.7	0.4	1.7	0.7	2020.0	30.1	2050.6	23.4	2082.3	35.4	2082.3	35.4
Spot 152	49801.5	126.3	1.0	7.8	1.2	6.6	1.8	0.4	1.2	0.7	2046.0	21.2	2064.9	15.7	2084.6	22.8	2084.6	22.8
Spot 158	80920.9	219.4	1.1	7.7	1.5	6.8	2.2	0.4	1.6	0.7	2077.6	28.6	2085.6	19.6	2094.3	26.8	2094.3	26.8
Spot 67	17884.8	52.5	1.9	7.6	1.6	7.1	2.2	0.4	1.3	0.6	2147.3	23.8	2127.6	19.6	2109.3	31.2	2109.3	31.2
Spot 300	94710.0	245.7	2.5	7.6	1.4	7.0	2.0	0.4	1.4	0.7	2077.0	25.4	2106.9	17.6	2137.0	23.9	2137.0	23.9
Spot 111	6888.7	17.5	3.0	7.4	4.3	6.7	4.7	0.4	1.6	0.3	1996.6	27.5	2078.1	42.0	2160.5	77.9	2160.5	77.9
Spot 65	88745.3	213.0	3.7	7.4	1.2	7.9	1.7	0.4	1.2	0.7	2265.5	23.6	2217.7	15.2	2174.6	20.1	2174.6	20.1
Spot 82	46325.7	127.8	2.6	7.3	1.4	7.8	2.1	0.4	1.6	0.7	2208.8	29.0	2205.4	19.1	2203.0	25.3	2203.0	25.3
Spot 292	47786.5	104.6	0.9	7.0	1.3	8.4	1.9	0.4	1.3	0.7	2244.8	24.6	2271.0	16.9	2295.4	23.0	2295.4	23.0
Spot 131	######	386.8	1.4	6.7	1.5	8.2	2.2	0.4	1.6	0.7	2166.3	29.4	2255.0	19.7	2337.1	25.3	2337.1	25.3
Spot 263	16881.0	153.0	0.8	6.1	1.2	10.6	2.0	0.5	1.5	0.7	2474.2	31.3	2489.4	18.9	2502.5	22.8	2502.5	22.8
Spot 37	16070.6	458.3	2.5	6.0	1.3	10.1	2.4	0.4	2.0	0.8	2348.7	39.7	2440.3	22.1	2518.2	21.5	2518.2	21.5
Spot 19	27024.2	165.6	2.2	6.0	1.2	9.9	1.7	0.4	1.3	0.7	2316.5	24.7	2428.7	15.9	2524.9	19.7	2524.9	19.7
Spot 313	66330.0	312.5	1.7	5.8	1.5	11.0	2.5	0.5	2.0	0.8	2443.7	41.1	2524.6	23.4	2591.0	25.0	2591.0	25.0
Spot 71	22896.6	133.4	1.2	5.7	1.5	11.9	2.6	0.5	2.1	0.8	2592.7	44.3	2599.8	24.6	2606.1	26.9	2606.1	26.9
Spot 77	######	179.0	1.2	5.7	1.2	12.5	1.9	0.5	1.4	0.8	2667.7	31.4	2639.3	17.7	2618.3	20.3	2618.3	20.3
Spot 50	81069.6	172.1	1.1	5.7	1.3	12.6	1.9	0.5	1.4	0.8	2694.2	31.8	2651.2	18.0	2619.2	20.9	2619.2	20.9
Spot 309	81280.0	232.3	2.0	5.7	1.2	11.9	1.7	0.5	1.2	0.7	2562.8	26.4	2596.0	16.1	2622.7	19.7	2622.7	19.7
Spot 143	######	330.2	2.4	5.7	1.2	12.0	1.9	0.5	1.4	0.8	2574.5	30.3	2604.1	17.7	2628.0	20.5	2628.0	20.5
Spot 87	71006.0	164.7	1.7	5.7	1.2	12.2	1.9	0.5	1.5	0.8	2616.4	31.5	2623.1	17.7	2629.0	19.8	2629.0	19.8
Spot 54	79063.2	154.4	3.3	5.6	1.1	12.8	1.7	0.5	1.2	0.7	2704.5	27.3	2663.7	15.8	2633.5	18.8	2633.5	18.8
Spot 45	70014.7	147.3	3.1	5.6	1.3	13.1	2.0	0.5	1.5	0.7	2745.7	33.6	2688.8	19.1	2646.9	22.5	2646.9	22.5
Spot 211	26385.5	60.5	1.5	5.6	1.4	13.0	2.0	0.5	1.4	0.7	2708.0	31.3	2677.1	18.7	2654.6	22.9	2654.6	22.9
Spot 238	25312.9	280.3	15.7	5.5	1.0	11.6	2.1	0.5	1.8	0.9	2459.1	36.9	2574.1	19.5	2666.6	17.2	2666.6	17.2
Spot 46	6356.9	15.7	3.3	5.4	3.1	13.9	4.0	0.5	1.7	0.4	2794.2	39.0	2740.8	37.6	2702.4	59.1	2702.4	59.1
Spot 7	61516.9	126.6	1.5	5.3	1.2	14.1	1.8	0.5	1.4	0.8	2768.3	31.6	2756.7	17.5	2748.9	19.7	2748.9	19.7
Spot 16	19553.9	53.6	1.0	5.1	1.3	13.3	2.1	0.5	1.6	0.7	2587.8	33.3	2700.9	19.8	2787.3	22.8	2787.3	22.8
Spot 144	######	226.0	2.9	5.1	1.2	14.7	1.8	0.5	1.4	0.7	2772.1	31.2	2795.0	17.6	2812.2	20.1	2812.2	20.1
Spot 250	36588.2	91.2	2.3	5.1	1.2	14.5	1.8	0.5	1.3	0.7	2743.4	28.3	2784.9	16.7	2815.8	20.0	2815.8	20.0
Spot 114	######	540.8	3.7	4.9	1.2	15.3	1.7	0.5	1.3	0.8	2782.4	29.5	2832.0	16.6	2868.1	18.7	2868.1	18.7
Spot 304	78310.4	221.0	0.8	4.1	1.1	18.8	1.9	0.6	1.6	0.8	2858.5	36.2	3031.7	18.5	3149.2	17.5	3149.2	17.5
Spot 74	49094.2	84.3	1.0	4.1	1.4	21.5	2.1	0.6	1.5	0.7	3178.3	38.2	3161.6	19.9	3151.7	21.9	3151.7	21.9
21-MANY-1silt																		
Spot 175	54543.3	505.0	1.7	16.9	1.6	0.7	2.3	0.1	1.6	0.7	559.4	8.4	556.9	9.7	548.0	35.8	559.4	8.4
Spot 309	20090.2	412.7	3.5	15.7	1.9	0.9	3.3	0.1	2.3	0.7	650.7	14.1	662.6	16.3	704.4	51.9	650.7	14.1
Spot 243	36416.1	193.5	5.3	16.0	2.3	0.9	2.8	0.1	1.5	0.5	655.2	9.1	657.9	13.7	667.9	51.9	655.2	9.1
Spot 281	14470.6	111.9	2.0	15.7	3.9	0.9	4.6	0.1	1.3	0.3	662.8	8.5	665.5	22.6	675.5	94.7	662.8	8.5
Spot 75	38359.4	224.7	3.9	16.2	2.0	0.9	2.6	0.1	1.6	0.6	665.0	9.8	662.1	12.6	653.2	44.3	665.0	9.8
Spot 310	26360.0	163.1	2.7	15.9	3.0	0.9	3.6	0.1	1.7	0.5	668.9	11.0	672.2	17.6	684.2	66.9	668.9	11.0
Spot 10	56894.3	378.9	2.6	15.9	1.7	0.9	2.5	0.1	1.8	0.7	674.1	11.2	677.7	12.3	690.6	37.6	674.1	11.2
Spot 30	12851.2	291.9	1.3	15.6	2.0	1.0	3.2	0.1	2.4	0.8	675.6	15.5	679.4	15.7	693.1	43.6	675.6	15.5
Spot 129	42226.1	224.3	2.6	16.0	2.2	1.0	2.7	0.1	1.5	0.5	686.0	9.5	682.5	13.3	672.0	47.8	686.0	9.5
Spot 173	46777.1	305.7	2.1	15.9	1.9	1.0	2.4	0.1	1.5	0.6	687.2	9.9	684.9	12.1	678.3	40.9	687.2	9.9
Spot 14	43902.9	269.5	1.6	15.9	1.8	1.0	2.4	0.1	1.3	0.6	688.1	8.8	686.8	12.2	683.6	43.4	688.1	8.8

Analysis	206Pb	U	U/Th	206Pb*	Â±2s	207Pb*	Â±2s	206Pb*	Â±2s	error	206Pb*	Â±2s	207Pb*	Â±2s	206Pb*	Â±2s	Best age	Â±2s
Spot 285	35116.1	137.7	2.6	15.7	3.0	1.0	3.5	0.1	1.9	0.5	720.9	12.8	716.6	18.2	704.3	63.8	720.9	12.8
Spot 213	67774.0	530.1	4.0	15.8	1.6	1.0	2.1	0.1	1.4	0.7	721.9	9.8	716.0	10.9	698.5	33.2	721.9	9.8
Spot 260	36781.4	201.1	2.4	15.8	1.8	1.0	2.5	0.1	1.3	0.5	723.3	8.9	717.2	12.9	699.2	45.5	723.3	8.9
Spot 242	27967.4	150.0	4.6	15.7	3.1	1.0	3.5	0.1	1.5	0.4	727.6	10.3	724.3	18.2	715.1	67.3	727.6	10.3
Spot 294	24873.2	148.3	2.3	15.6	2.4	1.0	2.8	0.1	1.4	0.5	729.9	9.3	725.2	14.4	711.4	51.6	729.9	9.3
Spot 142	14179.3	159.7	1.8	15.3	2.9	1.1	5.0	0.1	3.8	0.8	732.4	26.2	735.1	25.9	744.2	67.4	732.4	26.2
Spot 237	11631.8	331.5	1.4	15.5	1.8	1.1	4.7	0.1	1.9	0.4	732.5	13.2	729.1	24.4	719.8	91.1	732.5	13.2
Spot 154	50122.9	296.2	4.6	15.6	1.7	1.1	2.2	0.1	1.3	0.6	748.5	9.2	744.9	11.3	734.9	36.3	748.5	9.2
Spot 313	62281.6	337.2	3.0	15.1	1.6	1.1	2.4	0.1	1.8	0.7	763.3	12.7	773.1	12.8	802.3	33.1	763.3	12.7
Spot 222	39704.4	201.4	6.5	15.2	1.9	1.2	2.3	0.1	1.2	0.5	781.7	8.6	780.5	12.6	777.8	42.1	781.7	8.6
Spot 183	14322.9	318.5	1.8	14.9	2.2	1.2	4.0	0.1	1.5	0.4	790.2	11.1	790.9	22.1	793.8	78.3	790.2	11.1
Spot 147	17473.1	73.1	2.6	14.8	4.1	1.2	4.5	0.1	1.4	0.3	796.4	10.2	805.3	25.2	831.1	90.0	796.4	10.2
Spot 150	77247.4	326.8	4.0	15.1	1.3	1.2	1.8	0.1	1.2	0.6	807.0	8.7	805.0	10.1	800.4	29.4	807.0	8.7
Spot 233	75562.9	387.0	1.3	15.2	1.3	1.2	1.9	0.1	1.3	0.7	817.0	9.9	811.3	10.4	796.8	28.3	817.0	9.9
Spot 1	27233.1	135.1	3.1	14.7	3.5	1.3	4.0	0.1	1.6	0.4	817.6	12.5	824.0	22.6	842.2	76.3	817.6	12.5
Spot 98	30660.9	283.7	2.1	14.6	1.4	1.3	2.2	0.1	1.4	0.6	833.6	10.8	841.4	12.6	863.0	35.3	833.6	10.8
Spot 6	53776.6	238.3	1.1	14.4	1.6	1.4	2.3	0.1	1.5	0.7	879.6	12.4	885.2	13.3	899.9	34.5	879.6	12.4
Spot 25	43919.5	232.3	0.9	14.4	1.6	1.4	2.2	0.1	1.4	0.6	881.4	11.9	885.8	13.2	897.7	35.4	881.4	11.9
Spot 289	30141.1	138.4	2.4	14.3	2.8	1.4	3.3	0.1	1.6	0.5	883.7	13.0	886.7	19.3	895.1	59.1	883.7	13.0
Spot 261	73845.1	300.5	4.2	14.3	1.5	1.5	2.0	0.2	1.4	0.7	934.0	12.2	926.5	12.4	909.7	30.5	909.7	30.5
Spot 125	37096.2	114.5	2.0	14.3	2.7	1.5	3.1	0.2	1.4	0.4	930.8	11.9	926.4	18.7	916.8	56.7	916.8	56.7
Spot 198	47498.9	222.1	6.3	14.2	1.7	1.5	2.3	0.2	1.5	0.6	921.2	12.5	922.3	13.8	925.9	36.2	925.9	36.2
Spot 47	18786.5	95.9	2.1	14.0	3.4	1.4	3.9	0.1	1.9	0.5	897.4	15.7	906.7	23.6	930.3	71.2	930.3	71.2
Spot 85	31413.2	127.1	1.7	14.0	2.6	1.6	3.3	0.2	1.9	0.6	963.2	17.4	956.3	20.5	941.4	54.7	941.4	54.7
Spot 61	5332.1	156.6	1.9	13.6	2.6	1.5	4.6	0.2	1.6	0.4	927.7	14.2	931.7	27.8	942.1	87.1	942.1	87.1
Spot 136	22221.5	91.9	3.0	14.0	2.6	1.6	3.0	0.2	1.5	0.5	961.1	13.8	957.4	18.7	949.8	53.0	949.8	53.0
Spot 127	9052.3	50.8	2.6	13.7	4.3	1.6	5.5	0.2	2.2	0.4	998.8	20.6	987.1	34.4	962.0	101.7	962.0	101.7
Spot 68	64975.2	258.1	3.6	13.9	1.4	1.7	2.1	0.2	1.5	0.7	1004.9	13.9	992.6	13.5	966.2	31.2	966.2	31.2
Spot 84	43885.7	202.7	1.8	13.9	1.7	1.6	2.5	0.2	1.8	0.7	1000.0	16.7	989.3	16.1	966.6	36.4	966.6	36.4
Spot 187	76968.0	342.7	2.0	13.9	1.5	1.6	2.6	0.2	2.0	0.8	959.1	18.2	962.8	15.9	972.1	31.3	972.1	31.3
Spot 108	19428.9	78.7	0.6	13.8	2.9	1.6	3.5	0.2	1.5	0.4	994.8	13.6	987.9	22.2	973.6	65.0	973.6	65.0
Spot 197	60281.6	279.8	2.3	13.8	1.5	1.6	2.2	0.2	1.5	0.7	975.8	13.6	975.8	13.7	976.9	32.1	976.9	32.1
Spot 35	14442.3	490.1	1.7	13.7	1.5	1.5	2.3	0.2	1.8	0.8	902.4	15.0	924.5	14.2	978.4	31.2	978.4	31.2
Spot 92	63889.8	289.7	2.1	13.8	1.3	1.6	1.9	0.2	1.4	0.7	968.7	12.5	972.0	12.1	980.3	27.3	980.3	27.3
Spot 180	76403.5	300.7	2.3	13.8	1.2	1.6	1.8	0.2	1.2	0.7	969.4	10.6	972.8	11.0	981.2	26.5	981.2	26.5
Spot 270	18607.1	497.6	0.0	13.7	1.6	1.5	2.8	0.1	2.3	0.8	898.7	19.0	923.6	16.8	984.3	32.2	984.3	32.2
Spot 259	40079.0	277.5	1.6	13.8	1.6	1.5	2.7	0.2	2.0	0.7	917.7	16.9	937.4	16.3	984.7	36.6	984.7	36.6
Spot 244	36323.5	145.9	3.4	13.8	2.2	1.7	2.7	0.2	1.6	0.6	1017.1	14.6	1006.6	17.0	984.9	44.0	984.9	44.0
Spot 256	26343.5	146.0	1.3	13.8	2.2	1.6	3.1	0.2	1.8	0.6	985.5	16.8	986.0	19.4	988.2	50.2	988.2	50.2
Spot 266	45016.1	210.1	2.8	13.7	1.6	1.7	2.3	0.2	1.6	0.7	1008.7	14.5	1003.1	14.6	991.8	34.1	991.8	34.1
Spot 290	65653.0	386.3	3.3	13.7	1.6	1.6	2.3	0.2	1.6	0.7	982.0	14.7	985.2	14.2	993.3	31.9	993.3	31.9
Spot 72	35719.1	119.5	0.3	13.8	2.2	1.7	2.7	0.2	1.4	0.5	1036.4	13.6	1022.7	17.2	994.4	46.0	994.4	46.0
Spot 286	38475.1	152.4	2.0	13.7	1.6	1.7	2.3	0.2	1.6	0.7	994.0	14.4	994.7	14.5	997.0	33.9	997.0	33.9
Spot 293	61771.3	202.4	3.4	13.7	1.3	1.7	1.9	0.2	1.4	0.7	993.9	12.7	996.2	12.4	1002.2	28.0	1002.2	28.0
Spot 174	44162.8	265.5	3.8	13.6	1.4	1.6	2.2	0.2	1.5	0.7	982.6	13.4	988.5	13.6	1002.3	31.9	1002.3	31.9
Spot 229	38249.5	134.7	3.2	13.7	2.1	1.7	2.7	0.2	1.7	0.6	1021.7	15.6	1015.9	17.4	1004.2	43.4	1004.2	43.4
Spot 79	13633.5	80.0	1.3	13.5	3.0	1.6	4.2	0.2	1.7	0.4	982.7	15.6	989.4	26.2	1005.2	76.7	1005.2	76.7
Spot 91	18186.4	111.0	1.6	13.6	2.2	1.8	2.7	0.2	1.4	0.5	1047.7	13.8	1034.0	17.4	1006.0	46.1	1006.0	46.1
Spot 96	97343.5	400.6	2.1	13.7	1.2	1.8	1.9	0.2	1.5	0.8	1042.4	14.3	1031.3	12.5	1008.8	25.0	1008.8	25.0
Spot 221	54928.9	231.9	3.4	13.6	1.4	1.7	1.9	0.2	1.2	0.7	1019.6	11.6	1016.0	12.1	1009.2	28.9	1009.2	28.9
Spot 144	36718.8	124.0	1.3	13.6	2.3	1.7	3.0	0.2	1.7	0.6	1034.0	15.9	1026.0	19.1	1009.8	49.4	1009.8	49.4
Spot 101	45914.0	244.7	3.5	13.6	1.4	1.7	2.3	0.2	1.7	0.7	1003.8	15.8	1005.5	14.6	1010.0	30.8	1010.0	30.8
Spot 234	18823.2	76.7	3.3	13.5	3.3	1.9	3.7	0.2	1.4	0.4	1087.2	14.2	1067.0	24.6	1026.8	69.6	1026.8	69.6
Spot 225	81310.2	271.2	7.8	13.5	1.4	1.8	2.2	0.2	1.6	0.7	1073.7	16.0	1058.1	14.4	1027.1	30.0	1027.1	30.0
Spot 171	76662.3	245.6	1.8	13.5	1.7	1.7	2.2	0.2	1.4	0.6	1001.5	13.0	1009.4	14.2	1027.5	35.0	1027.5	35.0
Spot 210	57114.0	234.4	2.2	13.5	1.4	1.7	2.4	0.2	1.9	0.8	1019.0	18.1	1022.5	15.5	1030.8	29.4	1030.8	29.4
Spot 278	28680.1	109.3	1.4	13.4	2.3	1.8	2.9	0.2	1.4	0.5	1039.9	13.8	1036.9	18.8	1031.4	50.8	1031.4	50.8
Spot 303	49642.3	267.9	2.3	13.5	1.5	1.7	2.1	0.2	1.5	0.7	1001.2	13.7	1010.4	13.5	1031.4	30.5	1031.4	30.5

Analysis	206Pb	U	U/Th	206Pb*	Â±2s	207Pb*	Â±2s	206Pb*	Â±2s	error	206Pb*	Â±2s	207Pb*	Â±2s	206Pb*	Â±2s	Best age	Â±2s
Spot 276	38119.0	143.7	1.5	13.3	2.0	1.9	2.5	0.2	1.4	0.6	1076.9	14.0	1069.2	16.3	1054.4	40.8	1054.4	40.8
Spot 111	15364.1	63.1	1.3	13.2	4.2	1.8	5.0	0.2	1.9	0.4	1016.3	17.8	1028.9	32.2	1056.6	92.7	1056.6	92.7
Spot 78	11130.7	237.6	2.8	13.2	1.7	1.8	3.2	0.2	1.9	0.6	1052.9	18.0	1055.2	21.1	1060.7	52.9	1060.7	52.9
Spot 287	7509.1	28.4	1.2	13.0	7.9	1.7	9.0	0.2	1.9	0.2	969.2	16.7	998.5	57.2	1064.2	177.1	1064.2	177.1
Spot 204	48154.7	173.1	5.6	13.1	1.9	2.0	2.4	0.2	1.4	0.6	1115.6	14.5	1107.0	16.4	1090.9	39.7	1090.9	39.7
Spot 94	2885.4	12.2	0.9	12.3	10.8	1.8	15.5	0.2	3.4	0.2	1028.3	32.1	1053.3	101.9	1106.5	303.3	1106.5	303.3
Spot 161	54617.8	343.9	7.5	13.0	1.9	1.9	2.9	0.2	2.2	0.8	1076.0	22.2	1086.2	19.6	1107.6	38.0	1107.6	38.0
Spot 291	61733.0	499.8	4.0	12.9	1.1	2.0	1.7	0.2	1.3	0.8	1091.0	13.4	1100.2	11.7	1119.4	22.5	1119.4	22.5
Spot 162	8042.1	180.3	2.8	12.5	1.5	2.0	2.1	0.2	1.4	0.7	1077.2	13.6	1101.1	14.1	1149.5	31.7	1149.5	31.7
Spot 54	19462.7	59.2	0.5	12.3	2.9	2.4	3.5	0.2	1.5	0.4	1246.2	17.3	1229.9	24.8	1202.2	61.5	1202.2	61.5
Spot 18	94208.6	241.5	2.9	12.2	1.3	2.4	1.8	0.2	1.3	0.7	1236.7	14.5	1236.0	13.2	1235.5	25.8	1235.5	25.8
Spot 202	48348.0	161.2	1.1	12.1	1.7	2.4	2.2	0.2	1.4	0.6	1249.0	15.4	1244.6	15.7	1238.0	33.6	1238.0	33.6
Spot 48	84637.3	277.3	2.5	12.1	1.7	2.4	2.6	0.2	1.9	0.7	1236.8	21.9	1237.3	18.6	1239.0	33.8	1239.0	33.8
Spot 235	15947.4	193.7	1.2	12.1	1.5	2.5	2.3	0.2	1.4	0.6	1314.0	16.8	1285.9	16.5	1240.1	34.5	1240.1	34.5
Spot 295	60601.0	175.8	1.6	12.1	1.5	2.4	2.1	0.2	1.4	0.7	1238.2	15.6	1238.9	14.8	1241.1	30.0	1241.1	30.0
Spot 257	60540.4	187.4	0.6	12.1	1.9	2.5	2.6	0.2	1.8	0.7	1276.8	21.3	1267.5	19.2	1252.6	37.3	1252.6	37.3
Spot 112	15338.0	270.8	0.9	11.9	1.6	2.3	2.2	0.2	1.5	0.7	1167.8	16.0	1203.3	15.5	1268.5	31.4	1268.5	31.4
Spot 2	8258.1	25.8	61.7	11.7	7.8	2.4	8.5	0.2	2.4	0.3	1240.7	27.1	1252.5	61.1	1273.8	158.7	1273.8	158.7
Spot 274	24577.6	73.5	1.3	11.8	2.7	2.5	3.2	0.2	1.4	0.4	1276.4	16.3	1276.8	23.5	1278.3	56.6	1278.3	56.6
Spot 263	2994.0	10.6	0.3	11.3	12.5	2.5	16.1	0.2	2.5	0.2	1248.4	28.4	1259.5	116.1	1279.3	309.9	1279.3	309.9
Spot 71	25980.8	72.7	1.7	11.8	2.5	2.7	3.0	0.2	1.3	0.4	1360.0	16.3	1334.9	22.1	1295.7	51.9	1295.7	51.9
Spot 138	68979.7	211.3	2.2	11.5	1.3	2.8	2.0	0.2	1.4	0.7	1345.7	17.3	1346.5	14.6	1348.4	26.1	1348.4	26.1
Spot 17	54810.1	169.2	2.4	11.4	1.3	2.9	1.9	0.2	1.4	0.7	1393.8	17.3	1382.7	14.7	1366.4	26.5	1366.4	26.5
Spot 226	29250.6	173.8	5.0	11.4	1.5	3.0	2.2	0.3	1.4	0.6	1451.7	18.2	1418.0	17.1	1368.5	33.5	1368.5	33.5
Spot 201	45245.7	219.8	2.8	11.3	1.3	2.9	2.1	0.2	1.6	0.8	1402.2	19.9	1393.0	15.9	1379.8	26.6	1379.8	26.6
Spot 186	84000.9	210.5	1.0	11.3	1.5	2.9	2.1	0.2	1.5	0.7	1390.7	18.4	1386.6	15.7	1381.3	28.1	1381.3	28.1
Spot 181	16029.6	323.6	1.6	11.1	1.1	2.8	1.6	0.2	1.1	0.7	1329.1	13.7	1351.2	11.7	1387.3	20.8	1387.3	20.8
Spot 228	34815.9	96.5	2.0	11.2	1.9	3.0	2.6	0.2	1.6	0.6	1415.8	20.9	1407.3	19.8	1395.2	38.5	1395.2	38.5
Spot 5	28332.0	68.6	2.0	11.0	1.8	3.1	2.5	0.2	1.7	0.7	1422.0	21.9	1424.4	19.2	1428.8	34.8	1428.8	34.8
Spot 146	48921.1	426.7	4.3	11.0	1.1	3.1	1.7	0.2	1.3	0.8	1423.2	16.8	1426.2	13.2	1431.5	21.3	1431.5	21.3
Spot 43	60590.7	306.9	1.6	10.9	1.1	2.9	1.8	0.2	1.4	0.8	1348.4	17.1	1385.8	13.6	1444.6	21.4	1444.6	21.4
Spot 107	22438.7	85.5	3.1	10.8	1.8	3.2	2.3	0.3	1.3	0.6	1474.6	16.9	1465.7	17.6	1453.5	35.5	1453.5	35.5
Spot 49	26579.0	62.5	1.6	10.8	2.4	3.4	3.0	0.3	1.7	0.6	1542.8	23.5	1507.2	23.7	1458.4	47.1	1458.4	47.1
Spot 311	16656.2	42.8	0.9	10.6	2.8	3.3	3.2	0.3	1.5	0.5	1469.9	20.1	1477.2	25.1	1488.4	53.7	1488.4	53.7
Spot 269	33535.3	107.5	2.6	10.5	1.8	3.5	2.5	0.3	1.7	0.7	1558.1	23.5	1537.9	19.6	1511.2	34.1	1511.2	34.1
Spot 280	######	258.8	4.2	10.5	1.4	3.4	2.0	0.3	1.5	0.7	1504.9	19.6	1511.2	15.8	1520.7	25.8	1520.7	25.8
Spot 264	######	388.0	3.2	10.5	1.2	3.6	1.9	0.3	1.4	0.8	1560.8	19.5	1546.1	14.9	1526.8	23.4	1526.8	23.4
Spot 167	93390.5	514.3	7.0	9.9	1.2	3.3	2.1	0.2	1.8	0.8	1373.0	22.0	1482.9	16.7	1644.7	21.9	1644.7	21.9
Spot 64	47178.8	85.7	2.1	9.8	1.7	4.3	2.3	0.3	1.5	0.7	1728.8	22.6	1692.2	18.8	1647.9	32.1	1647.9	32.1
Spot 219	88947.5	196.4	1.8	9.6	1.4	4.3	2.2	0.3	1.7	0.8	1710.3	24.9	1701.9	18.2	1692.4	26.8	1692.4	26.8
Spot 306	38198.9	87.7	0.7	9.5	1.5	4.4	2.4	0.3	1.8	0.7	1710.2	26.8	1710.6	19.8	1711.9	29.4	1711.9	29.4
Spot 165	38236.5	138.8	1.3	9.5	1.5	4.2	2.0	0.3	1.3	0.7	1630.7	19.2	1667.6	16.3	1715.1	27.3	1715.1	27.3
Spot 212	94229.1	206.7	3.9	9.3	1.3	4.8	2.1	0.3	1.6	0.8	1807.4	24.7	1779.8	17.3	1748.3	24.5	1748.3	24.5
Spot 275	9501.7	23.2	1.5	9.1	3.4	4.4	3.9	0.3	1.6	0.4	1689.1	24.4	1719.5	32.1	1757.5	64.3	1757.5	64.3
Spot 214	######	172.2	1.0	9.2	1.3	4.8	2.0	0.3	1.4	0.7	1802.1	22.7	1785.5	16.6	1767.0	24.7	1767.0	24.7
Spot 168	46535.4	90.3	1.3	9.1	1.5	4.6	2.0	0.3	1.3	0.6	1733.4	20.0	1750.4	16.9	1771.5	28.2	1771.5	28.2
Spot 45	39230.1	93.1	0.9	9.1	1.2	5.0	2.0	0.3	1.4	0.7	1868.4	22.9	1822.8	16.7	1771.9	25.1	1771.9	25.1
Spot 211	63935.0	137.8	2.5	9.1	1.4	4.9	2.0	0.3	1.4	0.7	1820.3	22.5	1800.0	16.7	1777.4	25.3	1777.4	25.3
Spot 23	55012.1	137.0	1.4	9.1	1.6	4.8	2.3	0.3	1.7	0.7	1781.7	26.3	1781.3	19.7	1781.6	29.8	1781.6	29.8
Spot 63	41553.3	119.8	2.1	9.1	1.4	4.8	2.0	0.3	1.4	0.7	1770.8	21.4	1776.4	16.9	1783.7	26.8	1783.7	26.8
Spot 20	28563.9	130.4	1.0	9.1	3.2	3.9	8.7	0.3	8.1	0.9	1487.8	107.8	1615.8	70.6	1787.5	58.3	1787.5	58.3
Spot 19	18454.3	112.5	0.9	9.0	1.3	4.8	2.3	0.3	1.7	0.7	1767.7	26.8	1776.8	19.6	1788.3	28.6	1788.3	28.6
Spot 253	43584.2	77.3	1.6	9.1	1.7	5.0	2.4	0.3	1.7	0.7	1834.7	26.4	1814.6	20.3	1792.4	31.9	1792.4	31.9
Spot 33	54726.4	124.7	1.6	9.0	1.6	5.1	2.4	0.3	1.8	0.7	1871.8	29.4	1843.7	20.6	1812.8	29.2	1812.8	29.2
Spot 53	######	182.6	1.6	8.9	1.2	5.2	1.9	0.3	1.4	0.7	1884.6	22.7	1851.6	15.9	1815.5	22.7	1815.5	22.7
Spot 163	77341.6	148.1	1.3	9.0	1.3	4.9	2.0	0.3	1.6	0.8	1790.7	24.3	1802.6	17.2	1817.1	24.1	1817.1	24.1
Spot 57	40656.1	243.6	3.9	8.9	1.2	4.8	1.9	0.3	1.5	0.8	1756.1	23.1	1790.4	16.3	1831.3	22.1	1831.3	22.1
Spot 118	49608.3	205.9	1.4	8.9	1.1	5.0	1.7	0.3	1.2	0.7	1804.3	19.6	1817.1	14.3	1832.7	20.9	1832.7	20.9

Analysis	206Pb	U	U/Th	206Pb*	Â±2s	207Pb*	Â±2s	206Pb*	Â±2s	error	206Pb*	Â±2s	207Pb*	Â±2s	206Pb*	Â±2s	Best age	Â±2s
Spot 50	57826.2	108.7	2.3	8.7	1.2	5.3	2.4	0.3	2.0	0.8	1881.8	33.0	1869.7	20.5	1857.0	23.2	1857.0	23.2
Spot 21	39279.6	85.2	1.4	8.7	1.7	5.1	2.5	0.3	1.8	0.7	1827.2	29.3	1842.8	21.4	1861.2	31.0	1861.2	31.0
Spot 100	19923.9	35.1	0.6	8.7	2.4	5.4	3.1	0.3	1.8	0.6	1914.3	29.6	1890.5	26.3	1865.2	45.1	1865.2	45.1
Spot 156	45856.9	158.2	1.6	8.7	1.1	4.9	1.8	0.3	1.4	0.8	1752.3	22.1	1804.2	15.4	1865.6	20.3	1865.6	20.3
Spot 97	39931.6	95.3	0.6	8.7	1.2	5.5	1.9	0.3	1.4	0.7	1933.8	23.1	1901.1	16.0	1866.3	22.4	1866.3	22.4
Spot 4	70008.3	137.4	1.6	8.7	1.5	5.4	2.3	0.3	1.7	0.8	1915.0	28.4	1891.9	19.3	1867.4	26.4	1867.4	26.4
Spot 216	31385.8	108.1	2.2	8.7	1.2	5.8	2.0	0.4	1.4	0.7	2012.2	24.9	1941.9	17.0	1868.5	24.0	1868.5	24.0
Spot 312	66044.7	132.9	1.2	8.7	1.3	5.3	1.9	0.3	1.4	0.7	1865.6	23.3	1868.1	16.5	1871.6	23.2	1871.6	23.2
Spot 159	21931.9	47.0	0.9	8.7	2.4	5.2	3.1	0.3	1.9	0.6	1828.9	30.0	1848.8	26.6	1871.9	44.9	1871.9	44.9
Spot 176	######	248.6	3.0	8.7	1.3	5.3	2.1	0.3	1.6	0.8	1867.5	26.2	1869.4	17.6	1872.3	23.1	1872.3	23.1
Spot 191	34904.2	78.1	0.9	8.7	1.3	5.3	1.8	0.3	1.2	0.7	1875.0	19.9	1874.2	15.8	1874.1	24.9	1874.1	24.9
Spot 224	96443.7	165.8	2.2	8.7	1.1	5.5	1.7	0.3	1.3	0.7	1925.4	21.4	1900.5	14.7	1874.3	20.5	1874.3	20.5
Spot 9	######	186.1	0.8	8.7	1.5	5.3	2.3	0.3	1.8	0.8	1864.3	29.0	1868.9	20.0	1874.8	27.2	1874.8	27.2
Spot 28	67392.2	168.7	0.8	8.7	1.3	5.4	2.0	0.3	1.5	0.8	1903.0	25.5	1890.0	17.2	1876.5	23.0	1876.5	23.0
Spot 258	83673.5	175.5	1.6	8.7	1.2	5.6	1.9	0.4	1.4	0.7	1938.5	22.9	1908.5	16.0	1876.7	22.6	1876.7	22.6
Spot 90	85900.8	181.1	0.9	8.7	1.1	5.5	1.6	0.3	1.2	0.7	1929.2	20.0	1903.7	13.9	1876.7	19.7	1876.7	19.7
Spot 52	31024.4	61.1	1.3	8.6	1.5	5.3	2.3	0.3	1.6	0.7	1849.8	26.0	1862.5	19.2	1877.6	28.3	1877.6	28.3
Spot 105	43491.0	82.2	1.0	8.6	1.5	5.3	2.1	0.3	1.5	0.7	1869.8	24.0	1874.5	18.0	1880.5	27.0	1880.5	27.0
Spot 131	85754.3	208.6	0.9	8.6	1.2	5.3	1.7	0.3	1.2	0.7	1864.7	20.1	1871.9	14.7	1880.6	21.4	1880.6	21.4
Spot 200	13996.4	152.4	1.5	8.6	1.4	5.4	2.3	0.3	1.5	0.6	1879.5	24.4	1880.6	20.0	1882.6	32.3	1882.6	32.3
Spot 59	43184.6	75.4	1.0	8.6	2.0	5.5	2.8	0.3	1.9	0.7	1930.7	32.0	1907.3	24.0	1882.8	36.5	1882.8	36.5
Spot 254	57048.7	164.0	1.3	8.7	1.5	5.4	2.1	0.3	1.5	0.7	1899.3	24.8	1891.2	18.4	1883.1	27.5	1883.1	27.5
Spot 86	21080.1	48.6	1.3	8.6	1.9	5.6	2.8	0.4	1.8	0.6	1948.0	29.7	1916.5	23.8	1883.3	38.2	1883.3	38.2
Spot 140	######	217.5	1.0	8.7	1.2	5.5	1.9	0.3	1.4	0.8	1906.0	23.4	1894.9	16.2	1883.5	22.4	1883.5	22.4
Spot 143	17198.6	42.7	0.5	8.6	2.2	5.6	3.1	0.4	1.8	0.6	1937.8	30.0	1912.2	27.1	1885.4	46.6	1885.4	46.6
Spot 297	44845.2	87.7	1.7	8.6	1.5	5.4	2.2	0.3	1.6	0.7	1891.9	25.8	1889.2	19.3	1887.1	28.9	1887.1	28.9
Spot 172	99165.6	863.1	103.5	8.6	1.3	5.2	2.0	0.3	1.5	0.8	1808.7	24.1	1845.4	16.9	1887.7	22.9	1887.7	22.9
Spot 83	14853.2	348.1	1.8	8.5	1.2	5.1	2.6	0.3	2.2	0.9	1795.4	35.1	1838.8	21.8	1889.1	22.7	1889.1	22.7
Spot 139	######	433.2	4.8	8.6	1.2	5.4	1.9	0.3	1.5	0.8	1890.3	24.5	1890.5	16.3	1891.4	21.2	1891.4	21.2
Spot 251	60915.9	102.2	0.7	8.6	1.7	5.6	2.3	0.4	1.5	0.7	1945.3	25.8	1919.7	19.6	1893.0	30.1	1893.0	30.1
Spot 148	11376.7	187.6	0.9	8.5	1.2	4.5	2.5	0.3	2.2	0.9	1603.6	30.7	1732.8	20.5	1893.4	21.3	1893.4	21.3
Spot 232	47124.6	108.7	1.6	8.6	1.3	5.6	1.8	0.3	1.3	0.7	1922.3	21.0	1909.0	15.6	1895.3	23.4	1895.3	23.4
Spot 304	42299.4	347.0	1.1	8.5	1.2	5.2	2.0	0.3	1.5	0.8	1819.3	24.2	1858.2	16.8	1902.8	22.3	1902.8	22.3
Spot 117	######	437.9	2.7	8.5	1.1	5.7	1.7	0.4	1.3	0.8	1941.9	21.9	1929.8	14.9	1917.6	20.1	1917.6	20.1
Spot 12	52209.6	102.4	1.2	8.3	1.1	5.8	1.9	0.4	1.5	0.8	1940.9	24.3	1942.2	16.2	1944.4	21.2	1944.4	21.2
Spot 296	######	254.9	2.3	8.3	1.1	5.8	1.8	0.3	1.4	0.8	1932.7	23.0	1939.1	15.5	1946.6	20.5	1946.6	20.5
Spot 55	14997.5	169.9	1.8	8.3	1.2	6.0	2.4	0.4	1.7	0.7	2009.2	30.1	1978.4	20.8	1947.1	29.3	1947.1	29.3
Spot 155	65067.1	469.8	1.7	8.3	1.2	6.0	1.9	0.4	1.4	0.8	2002.9	24.0	1980.7	16.1	1958.4	21.8	1958.4	21.8
Spot 26	77881.1	143.8	2.2	8.2	1.3	5.9	1.9	0.4	1.4	0.7	1945.5	23.2	1953.9	16.4	1963.6	23.1	1963.6	23.1
Spot 11	######	236.5	2.6	8.2	1.0	6.1	1.9	0.4	1.6	0.8	2002.5	27.6	1984.5	16.6	1966.5	18.5	1966.5	18.5
Spot 115	18234.4	30.3	0.8	8.2	2.3	6.0	2.8	0.4	1.6	0.6	1987.3	26.9	1976.9	24.1	1966.9	40.7	1966.9	40.7
Spot 178	68413.2	125.2	0.9	8.2	1.4	6.0	2.0	0.4	1.5	0.7	1969.0	25.4	1969.5	17.6	1970.7	24.4	1970.7	24.4
Spot 8	61920.2	127.0	1.1	8.2	1.5	6.1	2.5	0.4	2.0	0.8	2023.0	34.0	1997.3	21.7	1971.6	27.3	1971.6	27.3
Spot 149	58535.8	92.1	1.4	8.2	1.3	6.0	1.9	0.4	1.4	0.7	1974.2	24.1	1973.6	16.6	1973.8	22.8	1973.8	22.8
Spot 314	48989.0	90.1	0.8	8.2	1.4	5.9	2.1	0.4	1.5	0.7	1942.2	25.2	1957.5	18.1	1974.5	25.7	1974.5	25.7
Spot 106	######	347.2	1.4	8.2	1.1	6.1	1.8	0.4	1.4	0.8	2002.3	24.0	1988.5	15.7	1975.0	20.2	1975.0	20.2
Spot 65	73440.8	148.7	1.7	8.2	1.3	6.4	2.0	0.4	1.5	0.8	2075.8	26.7	2026.9	17.3	1978.4	22.8	1978.4	22.8
Spot 262	77935.0	178.0	1.2	8.2	1.2	6.4	1.8	0.4	1.3	0.7	2076.5	23.7	2027.5	15.9	1978.7	21.9	1978.7	21.9
Spot 95	81900.0	158.7	1.9	8.2	1.1	6.0	1.6	0.4	1.2	0.7	1976.7	20.0	1977.7	14.3	1979.5	20.5	1979.5	20.5
Spot 205	71943.1	128.3	2.6	8.2	1.3	6.2	1.8	0.4	1.3	0.7	2017.0	22.1	1999.1	15.9	1981.5	23.0	1981.5	23.0
Spot 192	62686.3	143.0	0.9	8.2	1.3	6.1	2.2	0.4	1.7	0.8	1986.5	29.3	1984.0	19.0	1982.1	23.8	1982.1	23.8
Spot 110	90670.6	155.2	1.1	8.2	1.2	6.0	1.8	0.4	1.2	0.7	1979.5	21.1	1982.4	15.4	1986.3	22.3	1986.3	22.3
Spot 132	14594.6	146.3	1.5	8.1	1.6	6.1	2.5	0.4	1.4	0.6	1985.7	24.7	1985.7	21.8	1986.4	36.2	1986.4	36.2
Spot 230	96422.6	177.1	1.8	8.2	1.6	6.0	2.4	0.4	1.8	0.8	1964.5	30.5	1975.5	20.7	1987.9	27.7	1987.9	27.7
Spot 70	######	252.0	1.0	8.2	1.2	6.3	1.9	0.4	1.4	0.8	2035.2	25.2	2012.1	16.7	1989.2	22.2	1989.2	22.2
Spot 166	######	172.9	1.8	8.2	1.2	6.1	1.8	0.4	1.4	0.8	2001.8	24.2	1995.5	15.9	1989.7	20.6	1989.7	20.6
Spot 15	52527.5	363.7	2.2	8.1	1.9	6.0	2.4	0.4	1.5	0.6	1959.5	25.0	1975.6	21.0	1993.2	33.8	1993.2	33.8
Spot 308	73659.6	151.2	2.4	8.1	1.4	6.0	2.2	0.4	1.7	0.8	1950.5	28.8	1971.7	19.1	1994.7	24.4	1994.7	24.4

Analysis	206Pb	U	U/Th	206Pb*	Â±2s	207Pb*	Â±2s	206Pb*	Â±2s	error	206Pb*	Â±2s	207Pb*	Â±2s	206Pb*	Â±2s	Best age	Â±2s
Spot 66	######	441.4	2.0	7.9	1.2	6.8	1.8	0.4	1.3	0.7	2112.2	23.5	2081.6	15.5	2052.2	20.7	2052.2	20.7
Spot 283	38111.1	67.4	2.0	7.7	1.5	6.9	2.2	0.4	1.6	0.7	2127.1	29.0	2101.3	19.5	2076.8	26.6	2076.8	26.6
Spot 209	64875.8	109.4	1.8	7.7	1.1	7.0	1.8	0.4	1.3	0.8	2146.2	24.4	2110.7	15.6	2077.0	20.0	2077.0	20.0
Spot 267	90612.4	166.7	2.9	7.7	1.3	7.2	1.9	0.4	1.5	0.7	2183.4	26.9	2139.0	17.4	2097.4	22.8	2097.4	22.8
Spot 194	######	170.1	1.8	7.5	1.3	7.2	2.0	0.4	1.6	0.8	2144.4	28.3	2137.6	18.1	2131.9	22.8	2131.9	22.8
Spot 188	######	180.5	1.8	7.5	1.4	7.1	2.1	0.4	1.6	0.8	2121.0	29.0	2129.0	18.7	2137.5	23.8	2137.5	23.8
Spot 81	######	333.2	3.0	7.3	1.2	7.7	1.8	0.4	1.4	0.7	2224.8	25.9	2198.5	16.6	2174.8	21.4	2174.8	21.4
Spot 16	######	243.9	1.0	7.3	1.0	7.7	1.7	0.4	1.4	0.8	2198.6	25.6	2192.1	15.3	2186.8	17.6	2186.8	17.6
Spot 248	76955.8	124.4	1.3	7.2	1.2	8.1	1.8	0.4	1.4	0.7	2261.0	26.0	2237.0	16.6	2215.8	21.4	2215.8	21.4
Spot 208	71412.1	109.6	3.6	6.1	1.0	10.9	1.9	0.5	1.6	0.8	2568.5	33.2	2516.1	17.4	2474.7	17.1	2474.7	17.1
Spot 113	######	320.4	1.3	5.8	1.4	11.1	2.5	0.5	2.0	0.8	2455.6	41.3	2528.4	23.2	2588.1	24.2	2588.1	24.2
Spot 116	######	158.4	1.6	5.7	1.2	12.1	1.9	0.5	1.5	0.8	2610.8	31.9	2610.7	18.2	2611.3	20.8	2611.3	20.8
Spot 184	89569.4	271.0	2.2	5.6	1.2	12.0	1.9	0.5	1.5	0.8	2587.8	32.7	2602.0	18.1	2613.9	19.6	2613.9	19.6
Spot 123	80899.5	153.0	1.3	5.6	1.1	12.2	1.7	0.5	1.3	0.8	2616.1	28.0	2618.0	16.1	2620.2	18.5	2620.2	18.5
Spot 199	56917.2	72.2	1.4	5.6	1.3	12.7	1.9	0.5	1.3	0.7	2707.0	29.3	2660.7	17.7	2626.4	22.2	2626.4	22.2
Spot 246	17809.7	262.8	1.8	5.6	1.7	11.6	2.8	0.5	2.2	0.8	2502.9	45.5	2571.3	25.9	2626.5	28.1	2626.5	28.1
Spot 40	88215.9	122.6	1.5	5.6	1.1	12.3	1.7	0.5	1.3	0.8	2630.6	27.5	2628.0	15.6	2626.7	17.8	2626.7	17.8
Spot 152	7889.6	146.9	1.3	5.6	1.2	12.0	2.2	0.5	1.2	0.5	2569.9	25.6	2605.5	21.0	2634.0	31.4	2634.0	31.4
Spot 238	19461.5	285.1	1.1	5.6	1.2	10.1	2.4	0.4	2.1	0.9	2213.9	39.0	2439.7	22.3	2634.3	20.5	2634.3	20.5
Spot 207	33689.6	127.5	1.0	5.6	1.2	12.5	1.8	0.5	1.4	0.8	2646.8	30.9	2640.6	17.3	2636.6	19.3	2636.6	19.3
Spot 153	######	164.4	0.7	5.6	1.2	11.4	2.1	0.5	1.7	0.8	2462.0	35.7	2558.7	20.0	2637.0	20.4	2637.0	20.4
Spot 76	72135.2	268.3	1.3	5.6	1.1	12.7	2.0	0.5	1.6	0.8	2683.1	35.1	2659.6	18.6	2642.4	19.2	2642.4	19.2
Spot 34	95176.9	124.2	0.7	5.5	1.5	12.7	2.2	0.5	1.7	0.7	2666.9	36.4	2656.5	21.1	2649.3	24.9	2649.3	24.9
Spot 41	######	115.3	2.3	5.5	1.1	13.0	1.7	0.5	1.3	0.8	2718.6	29.9	2678.9	16.2	2649.8	17.5	2649.8	17.5
Spot 13	40267.7	400.4	2.6	5.5	1.0	11.5	2.3	0.5	2.1	0.9	2459.7	42.8	2567.0	21.8	2653.5	17.0	2653.5	17.0
Spot 315	######	300.0	0.7	5.5	1.1	12.1	1.7	0.5	1.3	0.8	2545.6	27.3	2609.5	16.1	2660.2	18.7	2660.2	18.7
Spot 190	98176.5	138.4	3.2	5.4	1.1	12.7	1.6	0.5	1.3	0.8	2627.6	27.2	2654.6	15.5	2676.0	17.5	2676.0	17.5
Spot 69	75527.2	99.8	1.3	5.4	1.2	13.5	1.9	0.5	1.4	0.8	2753.7	31.8	2713.0	17.9	2683.5	20.6	2683.5	20.6
Spot 7	60666.8	75.9	1.9	5.4	1.2	13.4	1.9	0.5	1.5	0.8	2745.7	33.6	2709.8	18.4	2683.8	20.5	2683.8	20.5
Spot 133	67616.1	73.1	1.0	5.4	1.1	13.2	1.8	0.5	1.4	0.8	2686.6	31.8	2694.4	17.0	2700.9	17.7	2700.9	17.7
Spot 58	######	188.8	4.2	5.4	1.1	13.8	1.8	0.5	1.4	0.8	2786.3	31.4	2738.9	16.9	2704.9	18.6	2704.9	18.6
Spot 102	62023.7	73.5	1.4	5.3	1.1	13.5	1.7	0.5	1.3	0.8	2732.1	28.1	2718.5	15.8	2709.2	18.1	2709.2	18.1
Spot 128	66183.5	70.0	1.9	5.3	1.3	13.7	2.0	0.5	1.5	0.8	2741.8	34.0	2725.8	19.0	2714.7	21.6	2714.7	21.6
Spot 177	72264.5	91.5	1.3	5.3	1.3	13.5	2.0	0.5	1.5	0.8	2715.3	34.0	2714.8	19.1	2715.1	21.6	2715.1	21.6
Spot 189	12022.5	16.1	1.7	5.3	2.1	13.4	2.7	0.5	1.6	0.6	2694.3	34.6	2706.5	25.1	2716.3	35.4	2716.3	35.4
Spot 217	68542.0	98.7	1.7	5.3	1.1	14.1	1.7	0.5	1.3	0.8	2805.5	29.8	2758.5	16.5	2724.9	18.9	2724.9	18.9
Spot 250	10333.5	17.7	1.6	5.1	2.4	12.7	3.0	0.5	1.7	0.6	2504.6	35.9	2660.0	28.4	2781.1	40.6	2781.1	40.6
Spot 74	18161.9	301.6	4.0	5.1	1.2	13.2	2.8	0.5	2.5	0.9	2564.3	53.4	2695.8	26.2	2796.7	19.1	2796.7	19.1
Spot 268	27967.2	75.3	1.2	4.9	1.5	15.8	2.2	0.6	1.6	0.7	2904.5	38.0	2864.6	20.9	2837.4	23.9	2837.4	23.9
Spot 301	56927.3	78.3	2.0	4.9	1.2	15.3	2.0	0.5	1.5	0.8	2800.2	35.1	2831.5	18.8	2854.6	19.9	2854.6	19.9
Spot 284	######	299.9	1.7	4.8	1.1	16.4	1.6	0.6	1.3	0.8	2934.3	29.7	2898.8	15.8	2874.8	17.3	2874.8	17.3
Spot 51	48274.7	72.6	1.8	4.6	1.1	17.0	1.9	0.6	1.6	0.8	2938.9	38.3	2936.9	18.6	2936.3	17.0	2936.3	17.0
Spot 158	######	193.7	3.0	4.5	1.0	17.5	1.7	0.6	1.4	0.8	2917.9	33.1	2965.3	16.8	2998.3	16.6	2998.3	16.6
21-MANY-7silt																		
Spot 193	16764.5	142.1	2.0	16.4	2.1	0.8	2.3	0.1	0.9	0.4	598.5	5.3	597.2	10.6	593.3	46.6	598.5	5.3
Spot 301	24127.3	215.2	1.0	16.1	1.0	0.8	1.3	0.1	0.8	0.6	608.9	4.5	617.8	6.1	651.5	23.1	608.9	4.5
Spot 177	14304.6	188.6	3.6	15.9	1.3	0.8	2.0	0.1	0.8	0.4	614.3	4.6	623.6	9.1	658.6	38.3	614.3	4.6
Spot 187	19526.2	134.9	5.0	16.4	1.6	0.8	1.9	0.1	1.0	0.5	615.7	5.7	613.1	8.9	604.0	36.0	615.7	5.7
Spot 307	20677.1	160.0	4.0	16.2	1.3	0.8	1.6	0.1	0.9	0.5	617.0	5.0	619.2	7.5	628.2	29.9	617.0	5.0
Spot 30	1197.5	79.4	2.9	13.6	2.7	0.9	8.5	0.1	0.9	0.1	624.8	5.1	627.8	39.6	639.9	181.2	624.8	5.1
Spot 194	22034.0	251.5	2.7	16.2	0.9	0.9	1.5	0.1	1.1	0.7	625.6	6.3	625.8	6.9	627.6	21.8	625.6	6.3
Spot 161	27650.7	172.1	1.9	16.6	1.6	0.8	2.0	0.1	1.0	0.5	625.9	6.2	621.2	9.3	605.1	36.7	625.9	6.2
Spot 303	40644.3	318.9	3.4	16.2	0.9	0.9	1.3	0.1	0.9	0.7	627.3	5.4	630.1	6.2	641.1	20.5	627.3	5.4
Spot 302	32809.8	197.1	2.5	16.2	1.1	0.9	1.4	0.1	0.8	0.6	627.4	5.0	629.0	6.4	635.7	23.3	627.4	5.0
Spot 243	14895.8	121.7	4.7	16.4	1.6	0.8	2.1	0.1	0.7	0.3	627.4	4.3	620.1	9.8	594.3	42.9	627.4	4.3
Spot 182	28910.9	214.4	4.3	16.1	1.2	0.9	1.6	0.1	1.0	0.6	627.5	5.8	632.9	7.7	653.3	28.1	627.5	5.8
Spot 17	21793.5	159.7	5.2	16.4	1.4	0.8	1.8	0.1	0.8	0.5	627.6	5.1	623.9	8.4	611.5	34.2	627.6	5.1
Spot 248	15081.9	118.8	6.4	16.0	1.5	0.9	1.7	0.1	0.7	0.4	627.7	4.3	632.4	8.2	650.1	34.1	627.7	4.3

Analysis	206Pb	U	U/Th	206Pb*	Â±2s	207Pb*	Â±2s	206Pb*	Â±2s	error	206Pb*	Â±2s	207Pb*	Â±2s	206Pb*	Â±2s	Best age	Â±2s
Spot 83	18352.2	147.4	4.9	16.1	1.4	0.9	1.8	0.1	0.8	0.4	638.1	5.0	638.0	8.8	638.5	35.6	638.1	5.0
Spot 157	24065.9	181.0	5.0	16.4	1.4	0.9	1.7	0.1	0.9	0.5	639.5	5.4	631.6	7.8	604.0	30.3	639.5	5.4
Spot 279	15184.2	116.4	3.1	16.1	1.8	0.9	2.4	0.1	0.9	0.4	639.7	5.7	638.5	11.3	635.3	46.9	639.7	5.7
Spot 285	29711.3	182.0	5.2	16.1	1.3	0.9	1.7	0.1	0.9	0.5	639.9	5.7	642.2	8.3	651.1	31.6	639.9	5.7
Spot 98	20916.4	153.2	5.4	16.2	1.5	0.9	1.9	0.1	1.0	0.5	641.0	6.3	638.8	9.0	632.2	34.1	641.0	6.3
Spot 260	20063.3	139.2	4.7	16.1	1.7	0.9	1.9	0.1	0.7	0.4	641.1	4.4	641.1	9.0	642.1	37.4	641.1	4.4
Spot 174	17119.8	126.8	4.1	16.3	1.7	0.9	2.2	0.1	0.9	0.4	641.2	5.4	635.3	10.2	615.6	42.6	641.2	5.4
Spot 283	851.2	83.8	4.1	12.5	2.7	0.9	4.5	0.1	0.9	0.2	642.2	5.4	653.3	21.9	692.5	95.1	642.2	5.4
Spot 70	12434.2	85.8	1.5	16.1	2.0	0.9	2.4	0.1	1.1	0.4	642.7	6.5	637.4	11.6	619.7	47.7	642.7	6.5
Spot 3	25170.8	164.7	5.2	16.2	1.1	0.9	1.4	0.1	0.7	0.5	642.9	4.3	641.8	6.7	639.1	26.4	642.9	4.3
Spot 7	45143.0	287.2	4.6	16.3	1.0	0.9	1.3	0.1	0.7	0.5	644.4	4.3	639.8	6.2	624.3	23.9	644.4	4.3
Spot 29	23733.6	153.5	2.6	16.2	1.7	0.9	2.1	0.1	0.9	0.4	648.6	5.3	645.8	9.9	636.9	40.3	648.6	5.3
Spot 71	11697.5	78.1	3.6	16.1	2.9	0.9	3.1	0.1	0.9	0.3	648.9	5.3	644.4	14.9	629.4	64.7	648.9	5.3
Spot 102	47676.6	398.6	1.7	16.3	0.7	0.9	1.2	0.1	0.9	0.7	650.5	5.4	646.0	5.8	631.4	18.3	650.5	5.4
Spot 166	28762.3	233.5	2.0	16.1	0.9	0.9	1.4	0.1	0.8	0.6	652.0	4.9	657.1	6.8	675.6	25.0	652.0	4.9
Spot 80	42380.6	234.2	4.6	16.2	1.1	0.9	1.4	0.1	0.7	0.5	652.7	4.4	650.0	6.5	641.5	24.9	652.7	4.4
Spot 245	5007.5	270.8	6.3	15.7	1.4	0.9	4.7	0.1	0.7	0.2	653.5	4.4	645.3	22.2	617.7	99.4	653.5	4.4
Spot 68	51908.8	341.4	4.2	16.2	1.0	0.9	1.4	0.1	0.9	0.7	656.3	5.8	652.3	6.6	639.7	22.0	656.3	5.8
Spot 235	88296.8	468.9	4.9	16.3	0.7	0.9	1.0	0.1	0.7	0.7	660.2	4.5	654.2	4.8	634.3	15.0	660.2	4.5
Spot 192	330.5	22.6	1.6	9.2	5.8	1.0	28.7	0.1	1.4	0.0	663.7	8.7	687.2	144.0	765.8	614.9	663.7	8.7
Spot 226	52666.6	381.3	6.2	16.4	0.8	0.9	1.1	0.1	0.8	0.7	663.8	4.9	655.4	5.6	627.2	18.3	663.8	4.9
Spot 313	19276.6	163.8	1.2	15.7	1.3	0.9	1.7	0.1	0.7	0.4	668.3	4.6	673.8	8.3	693.1	32.5	668.3	4.6
Spot 34	20752.0	373.8	1.5	15.7	0.7	0.9	1.4	0.1	0.6	0.4	671.5	3.7	676.5	7.1	693.8	28.2	671.5	3.7
Spot 103	20119.8	137.0	13.2	16.0	1.5	0.9	1.9	0.1	0.9	0.5	672.7	5.7	667.8	9.1	652.2	35.2	672.7	5.7
Spot 234	13777.5	81.1	4.5	15.6	1.7	1.0	2.1	0.1	0.8	0.4	674.2	4.9	679.7	10.6	698.9	42.6	674.2	4.9
Spot 278	4673.8	265.3	1.1	15.3	1.1	0.9	4.7	0.1	0.8	0.2	675.7	5.2	674.4	23.1	670.8	98.9	675.7	5.2
Spot 294	10999.2	76.4	4.5	15.3	2.1	1.0	2.5	0.1	0.9	0.3	676.8	5.5	690.7	12.7	737.3	50.7	676.8	5.5
Spot 11	6816.2	39.5	2.1	15.1	3.1	1.0	4.2	0.1	1.1	0.3	680.4	7.4	695.6	21.2	745.8	85.7	680.4	7.4
Spot 18	19140.3	92.1	1080.6	15.8	2.1	1.0	2.5	0.1	1.1	0.5	682.3	7.4	682.6	12.5	684.3	47.7	682.3	7.4
Spot 147	32757.4	211.0	6.9	16.1	1.1	0.9	1.4	0.1	0.8	0.6	685.2	5.3	676.7	7.0	649.5	25.0	685.2	5.3
Spot 100	26450.2	338.4	1.6	15.8	0.7	1.0	1.1	0.1	0.8	0.7	689.3	5.1	690.6	5.4	695.9	16.0	689.3	5.1
Spot 255	76526.0	448.5	0.8	15.9	0.7	1.0	1.1	0.1	0.8	0.8	690.5	5.4	690.9	5.6	693.1	15.6	690.5	5.4
Spot 236	16928.0	198.9	4.3	16.0	1.0	1.0	1.4	0.1	0.7	0.5	691.9	4.5	683.6	7.2	657.4	27.3	691.9	4.5
Spot 9	28371.6	213.6	2.3	15.7	1.1	1.0	1.5	0.1	1.0	0.6	694.3	6.3	699.6	7.6	717.5	24.3	694.3	6.3
Spot 55	20789.1	159.6	4.0	15.9	1.4	1.0	1.9	0.1	0.8	0.4	696.9	5.0	692.5	9.3	679.1	36.3	696.9	5.0
Spot 129	50041.7	263.5	2.0	15.9	0.8	1.0	1.2	0.1	0.9	0.7	697.3	6.0	695.4	6.2	690.1	17.7	697.3	6.0
Spot 169	11614.5	76.7	2.4	15.2	2.5	1.0	2.9	0.1	1.2	0.4	699.2	8.1	713.0	14.7	757.7	54.9	699.2	8.1
Spot 250	15545.4	97.1	2.7	15.6	2.0	1.0	2.3	0.1	1.0	0.4	699.8	6.8	701.3	11.8	707.1	44.4	699.8	6.8
Spot 296	20717.6	130.0	1.8	16.0	1.5	1.0	1.8	0.1	0.7	0.4	702.3	4.9	690.5	8.9	653.2	34.8	702.3	4.9
Spot 85	45980.3	282.3	1.9	15.7	0.9	1.0	1.5	0.1	1.1	0.8	703.8	7.3	703.1	7.4	702.1	20.2	703.8	7.3
Spot 125	63813.7	299.8	3.3	16.0	0.8	1.0	1.1	0.1	0.8	0.7	705.4	5.4	697.6	5.8	673.5	17.1	705.4	5.4
Spot 86	30348.2	202.9	2.9	15.9	1.1	1.0	1.5	0.1	0.9	0.6	706.7	5.8	699.1	7.4	675.9	24.9	706.7	5.8
Spot 164	46280.7	311.1	2.2	15.8	0.8	1.0	1.2	0.1	0.8	0.7	707.2	5.4	708.6	6.2	713.8	19.3	707.2	5.4
Spot 202	3688.9	43.0	3.3	14.5	3.6	1.0	6.8	0.1	0.9	0.1	707.7	5.9	723.0	34.9	771.6	141.1	707.7	5.9
Spot 257	33568.8	359.9	13.6	15.4	0.9	1.0	1.6	0.1	1.3	0.8	708.7	8.6	721.1	8.5	761.0	21.5	708.7	8.6
Spot 160	30345.0	177.0	3.8	15.8	1.3	1.0	2.7	0.1	2.4	0.9	712.6	16.0	710.6	14.0	705.0	29.3	712.6	16.0
Spot 276	17360.2	134.3	3.0	15.8	1.3	1.0	1.6	0.1	0.8	0.5	714.3	5.7	706.2	8.1	681.3	28.7	714.3	5.7
Spot 82	19346.5	112.2	2.0	15.6	1.7	1.0	2.1	0.1	0.8	0.4	721.2	5.6	719.4	10.8	714.9	41.1	721.2	5.6
Spot 65	5976.6	45.6	2.7	14.7	3.2	1.1	4.7	0.1	0.9	0.2	721.9	6.2	737.0	24.7	784.2	97.2	721.9	6.2
Spot 106	23284.4	143.6	1.3	16.0	1.5	1.0	1.9	0.1	0.9	0.5	726.1	6.3	710.3	9.8	661.8	35.9	726.1	6.3
Spot 37	15180.7	128.9	3.1	15.5	1.7	1.0	2.3	0.1	0.9	0.4	729.7	6.2	726.8	11.9	718.9	44.6	729.7	6.2
Spot 150	21804.2	147.4	1.9	15.8	1.4	1.0	1.7	0.1	0.8	0.5	730.2	5.8	719.1	9.0	685.6	32.4	730.2	5.8
Spot 114	16382.4	92.4	8.3	15.3	1.8	1.1	2.2	0.1	0.8	0.4	735.1	5.7	738.4	11.6	749.2	43.2	735.1	5.7
Spot 67	10500.2	107.4	1.8	15.4	1.7	1.1	2.8	0.1	0.8	0.3	736.5	5.4	730.6	14.5	713.4	56.9	736.5	5.4
Spot 51	18768.2	180.7	4.6	15.5	1.2	1.1	1.6	0.1	0.7	0.5	749.9	5.1	741.9	8.4	718.6	30.0	749.9	5.1
Spot 315	25567.9	130.8	3.7	15.6	1.6	1.1	1.8	0.1	0.7	0.4	754.5	4.7	744.3	9.6	714.8	35.8	754.5	4.7
Spot 90	77208.2	410.3	11.3	15.5	0.7	1.1	1.1	0.1	0.8	0.8	760.9	5.8	755.2	5.6	739.3	14.2	760.9	5.8
Spot 272	21545.9	110.9	7.4	15.1	1.6	1.1	2.0	0.1	1.1	0.5	762.3	8.0	766.4	10.9	779.3	35.8	762.3	8.0

Analysis	206Pb	U	U/Th	206Pb*	Â±2s	207Pb*	Â±2s	206Pb*	Â±2s	error	206Pb*	Â±2s	207Pb*	Â±2s	206Pb*	Â±2s	Best age	Â±2s
Spot 10	52642.0	305.8	3.2	15.3	0.8	1.1	1.2	0.1	0.8	0.7	771.6	6.2	772.0	6.5	773.8	17.9	771.6	6.2
Spot 141	45752.3	277.9	1.7	15.6	0.8	1.1	1.1	0.1	0.7	0.7	772.3	5.3	760.7	5.9	727.7	17.4	772.3	5.3
Spot 24	30787.8	173.7	4.2	15.2	1.3	1.1	1.7	0.1	1.1	0.6	778.6	7.8	776.8	9.3	772.6	28.2	778.6	7.8
Spot 156	44253.4	319.3	6.1	15.3	0.8	1.1	1.4	0.1	1.0	0.8	778.8	7.7	774.7	7.3	763.8	18.0	778.8	7.7
Spot 217	28226.4	429.9	3.1	15.5	0.6	1.1	1.0	0.1	0.7	0.7	778.8	5.4	768.6	5.7	739.9	15.9	778.8	5.4
Spot 112	47111.5	252.6	3.3	15.3	0.9	1.2	1.4	0.1	1.1	0.8	779.4	7.7	778.5	7.5	776.9	19.0	779.4	7.7
Spot 180	7650.1	35.4	1.5	15.1	3.3	1.1	3.6	0.1	1.1	0.3	782.1	8.0	773.0	19.4	747.8	72.1	782.1	8.0
Spot 167	43279.3	237.8	5.0	15.0	0.9	1.2	1.2	0.1	0.8	0.7	785.6	5.8	797.2	6.5	830.6	18.2	785.6	5.8
Spot 216	10498.0	59.6	3.0	14.8	2.7	1.2	3.3	0.1	0.7	0.2	786.0	5.0	791.3	18.0	807.2	66.9	786.0	5.0
Spot 42	34724.8	172.7	1.3	15.4	0.9	1.2	1.2	0.1	0.7	0.6	788.5	5.1	778.5	6.7	750.7	21.4	788.5	5.1
Spot 282	3108.8	275.8	0.9	13.8	1.0	1.2	1.7	0.1	1.0	0.6	791.0	7.7	806.9	9.3	852.2	27.2	791.0	7.7
Spot 158	38917.6	187.5	4.1	15.3	1.1	1.2	1.4	0.1	0.8	0.6	794.2	6.2	790.6	7.6	781.4	23.3	794.2	6.2
Spot 72	13287.3	83.1	5.7	15.2	2.1	1.2	2.5	0.1	0.8	0.3	795.5	6.1	785.5	13.7	758.2	50.0	795.5	6.1
Spot 2	54045.2	263.3	2.8	15.3	0.7	1.2	1.1	0.1	0.8	0.7	796.2	5.7	788.0	6.1	765.8	17.1	796.2	5.7
Spot 240	24487.4	159.3	2.3	14.9	1.0	1.2	1.4	0.1	0.8	0.5	799.1	5.8	803.1	7.9	815.1	24.9	799.1	5.8
Spot 73	4961.2	147.0	1.8	14.2	1.1	1.2	1.6	0.1	1.1	0.7	806.2	8.3	815.0	9.1	840.0	24.9	806.2	8.3
Spot 101	7287.9	41.0	1.1	14.7	3.1	1.2	3.8	0.1	0.9	0.2	820.0	7.0	815.1	21.5	802.6	77.9	820.0	7.0
Spot 314	7292.2	42.7	1.9	14.6	3.0	1.2	3.7	0.1	1.0	0.3	825.2	7.8	820.6	20.7	809.2	74.0	825.2	7.8
Spot 241	33327.2	253.5	2.2	14.7	0.9	1.3	1.3	0.1	0.8	0.7	825.5	6.5	830.9	7.3	846.4	20.2	825.5	6.5
Spot 290	26613.7	196.1	3.1	14.7	0.8	1.3	1.4	0.1	0.9	0.7	837.4	7.2	839.2	7.8	844.9	20.9	837.4	7.2
Spot 204	35281.4	191.5	2.8	15.1	0.8	1.3	1.3	0.1	0.8	0.6	848.3	6.4	834.0	7.1	796.7	20.2	848.3	6.4
Spot 69	13544.4	72.5	1.7	14.8	2.0	1.3	2.4	0.1	1.0	0.4	852.1	8.2	842.7	13.5	818.9	44.4	852.1	8.2
Spot 49	16228.7	66.3	3.1	14.7	1.9	1.3	2.2	0.1	1.0	0.5	866.5	8.5	857.4	12.7	834.9	40.0	866.5	8.5
Spot 142	21308.1	99.5	3.4	14.6	1.2	1.4	1.7	0.1	0.7	0.4	885.9	6.0	874.3	10.2	846.0	32.8	885.9	6.0
Spot 209	48218.6	213.7	3.0	14.6	0.8	1.4	1.1	0.1	0.7	0.6	897.7	5.9	887.4	6.5	862.5	17.6	897.7	5.9
Spot 254	13592.0	82.7	1.5	14.2	1.4	1.4	1.7	0.2	0.8	0.5	905.1	6.5	905.1	10.2	905.8	31.4	905.8	31.4
Spot 6	8742.1	55.6	1.6	14.0	1.9	1.5	2.7	0.2	0.7	0.3	927.7	6.4	921.2	16.3	906.6	53.2	906.6	53.2
Spot 119	32395.5	170.4	3.4	14.2	1.2	1.5	2.1	0.2	1.7	0.8	938.9	15.1	932.3	13.1	917.7	25.8	917.7	25.8
Spot 191	16529.6	85.2	2.0	14.1	1.2	1.5	1.6	0.2	0.9	0.5	940.5	7.5	935.8	10.0	925.6	28.7	925.6	28.7
Spot 287	8286.9	203.2	2.6	13.8	1.1	1.6	2.2	0.2	1.1	0.5	972.7	10.3	963.6	14.0	944.0	39.7	944.0	39.7
Spot 289	38090.2	164.1	2.5	13.9	0.8	1.6	1.2	0.2	0.9	0.7	984.6	7.9	976.9	7.6	960.5	17.5	960.5	17.5
Spot 153	15949.2	186.9	1.8	13.8	0.9	1.7	1.3	0.2	0.7	0.5	1014.6	6.3	999.6	8.3	967.7	22.9	967.7	22.9
Spot 186	38034.8	139.8	1.9	13.9	1.0	1.6	1.4	0.2	1.0	0.7	962.0	9.0	963.6	9.0	968.0	21.2	968.0	21.2
Spot 227	37979.1	139.7	2.8	13.9	0.9	1.7	1.2	0.2	0.7	0.6	1011.8	6.6	997.8	7.6	968.1	19.9	968.1	19.9
Spot 120	30780.7	122.6	1.6	13.9	1.0	1.7	1.3	0.2	0.8	0.6	1021.9	7.7	1005.1	8.6	969.4	21.8	969.4	21.8
Spot 266	20683.3	242.1	3.2	13.8	0.9	1.6	1.3	0.2	0.9	0.7	979.4	7.9	976.8	8.4	971.9	20.6	971.9	20.6
Spot 123	9217.0	137.2	2.0	13.6	1.1	1.6	2.0	0.2	0.9	0.4	982.0	8.1	979.2	12.6	973.8	36.7	973.8	36.7
Spot 151	37203.7	148.6	2.1	13.8	0.8	1.7	1.1	0.2	0.7	0.7	1009.0	6.8	997.7	7.0	974.0	16.9	974.0	16.9
Spot 183	47455.9	197.6	1.8	13.8	0.9	1.6	1.3	0.2	0.9	0.7	963.1	8.4	967.2	8.1	977.3	18.5	977.3	18.5
Spot 179	18556.6	66.8	1.2	13.7	1.7	1.6	2.1	0.2	0.8	0.4	985.6	7.2	983.0	13.2	978.0	39.6	978.0	39.6
Spot 190	12853.1	45.0	1.2	13.7	1.9	1.7	2.3	0.2	1.0	0.5	1034.3	10.0	1016.4	14.5	979.0	40.7	979.0	40.7
Spot 116	32132.7	123.1	1.8	13.8	1.5	1.6	1.9	0.2	1.1	0.6	972.5	10.1	974.3	12.1	979.2	32.0	979.2	32.0
Spot 56	40796.9	155.6	1.2	13.8	0.9	1.7	1.2	0.2	0.7	0.5	1017.7	6.2	1005.3	7.9	979.2	21.3	979.2	21.3
Spot 105	17067.2	130.6	0.8	13.7	1.2	1.6	1.5	0.2	0.8	0.5	942.3	6.9	954.1	9.1	982.2	25.4	982.2	25.4
Spot 62	42098.9	164.8	2.5	13.8	0.9	1.7	1.3	0.2	0.8	0.7	1012.2	7.8	1002.9	8.1	983.5	19.6	983.5	19.6
Spot 4	15292.8	208.9	1.5	13.7	0.9	1.6	1.8	0.2	1.0	0.6	947.2	9.1	958.1	11.3	984.2	30.4	984.2	30.4
Spot 16	35140.2	154.4	1.0	13.8	0.9	1.7	1.2	0.2	0.8	0.7	999.8	7.6	995.0	7.8	985.5	18.4	985.5	18.4
Spot 40	18474.3	193.8	1.1	13.7	0.9	1.6	1.4	0.2	1.0	0.7	979.9	8.7	981.8	8.5	986.8	19.6	986.8	19.6
Spot 26	45968.4	149.4	8.3	13.8	0.8	1.7	1.1	0.2	0.7	0.6	1007.2	6.6	1000.7	7.2	987.3	17.8	987.3	17.8
Spot 154	28118.0	128.7	2.3	13.7	1.1	1.7	1.4	0.2	0.8	0.6	1030.0	8.0	1016.6	8.7	988.9	21.8	988.9	21.8
Spot 176	20672.8	103.7	2.0	13.6	1.2	1.5	1.7	0.2	0.9	0.5	922.9	7.5	943.7	10.4	993.4	29.7	993.4	29.7
Spot 304	38172.4	153.0	2.4	13.7	1.0	1.7	1.6	0.2	1.2	0.8	997.8	11.1	996.2	10.1	993.6	21.4	993.6	21.4
Spot 237	19281.3	86.8	1.0	13.6	1.0	1.7	1.3	0.2	0.8	0.6	989.3	6.9	990.7	8.4	994.7	22.4	994.7	22.4
Spot 14	23074.3	85.2	0.9	13.7	1.3	1.6	1.7	0.2	0.9	0.5	985.5	8.2	988.8	11.0	997.0	30.3	997.0	30.3
Spot 23	25500.4	117.9	3.8	13.6	1.2	1.8	1.5	0.2	0.8	0.6	1042.8	8.2	1030.0	9.6	1003.9	24.6	1003.9	24.6
Spot 136	42337.5	180.5	2.7	13.6	1.0	1.7	1.4	0.2	0.9	0.6	1026.5	8.1	1019.3	8.8	1004.6	21.5	1004.6	21.5
Spot 88	32584.9	149.0	5.1	13.6	0.9	1.8	1.3	0.2	0.7	0.6	1063.0	7.2	1044.5	8.2	1007.0	20.8	1007.0	20.8
Spot 5	47804.9	236.3	5.0	13.6	0.7	1.7	1.1	0.2	0.9	0.8	1024.8	8.2	1018.9	7.2	1007.0	14.3	1007.0	14.3

Analysis	206Pb	U	U/Th	206Pb*	Â±2s	207Pb*	Â±2s	206Pb*	Â±2s	error	206Pb*	Â±2s	207Pb*	Â±2s	206Pb*	Â±2s	Best age	Â±2s
Spot 155	31306.8	166.2	1.7	13.5	0.9	1.7	1.4	0.2	0.9	0.6	1016.3	8.1	1015.0	9.0	1013.1	22.3	1013.1	22.3
Spot 163	8580.1	60.5	1.4	13.4	1.5	1.7	2.1	0.2	0.8	0.4	986.2	7.1	994.9	13.5	1015.1	40.2	1015.1	40.2
Spot 259	44293.8	182.3	12.3	13.6	0.8	1.8	1.2	0.2	0.8	0.7	1047.8	7.8	1037.5	7.7	1016.5	17.7	1016.5	17.7
Spot 246	42047.1	208.5	10.0	13.5	0.8	1.7	1.2	0.2	0.9	0.7	1021.4	8.3	1022.2	7.9	1024.8	17.4	1024.8	17.4
Spot 77	18448.0	69.7	3.3	13.4	1.7	1.9	2.0	0.2	0.8	0.4	1084.7	8.3	1064.9	13.3	1025.4	37.0	1025.4	37.0
Spot 54	16127.0	78.8	1.5	13.4	1.3	1.8	1.6	0.2	0.7	0.4	1058.1	6.6	1047.6	10.5	1026.6	29.6	1026.6	29.6
Spot 184	17334.3	75.1	1.5	13.4	1.4	1.7	1.9	0.2	0.9	0.5	983.5	8.6	996.9	12.2	1027.4	34.0	1027.4	34.0
Spot 25	39913.9	316.5	2.9	13.5	0.9	1.7	1.4	0.2	1.0	0.7	1020.0	9.8	1022.3	9.0	1028.0	18.8	1028.0	18.8
Spot 22	49219.0	399.7	5.0	13.5	0.8	1.7	1.1	0.2	0.8	0.7	1024.0	7.9	1025.5	7.4	1029.6	15.9	1029.6	15.9
Spot 44	18745.0	77.9	4.1	13.4	1.5	1.7	1.8	0.2	0.7	0.4	1021.4	6.3	1023.9	11.4	1029.9	33.0	1029.9	33.0
Spot 203	62219.5	219.7	3.9	13.5	0.6	1.8	0.9	0.2	0.7	0.7	1044.6	6.3	1039.8	5.9	1030.5	12.6	1030.5	12.6
Spot 206	13286.1	52.4	3.4	13.3	1.4	1.8	1.9	0.2	0.7	0.4	1067.6	7.4	1055.8	12.7	1032.3	36.0	1032.3	36.0
Spot 113	46094.5	183.4	1.9	13.5	0.9	1.8	1.4	0.2	1.0	0.7	1045.4	9.5	1041.2	8.9	1033.4	18.9	1033.4	18.9
Spot 239	31236.8	146.5	2.7	13.4	0.8	1.8	1.2	0.2	0.8	0.7	1055.2	7.8	1048.4	7.8	1035.0	17.8	1035.0	17.8
Spot 127	20614.8	87.9	1.1	13.4	1.3	1.7	1.7	0.2	0.9	0.5	1016.7	8.4	1022.4	11.3	1035.6	30.3	1035.6	30.3
Spot 13	11143.8	91.5	1.4	13.3	1.3	1.8	2.0	0.2	1.0	0.5	1028.2	9.1	1031.1	12.8	1038.1	34.9	1038.1	34.9
Spot 39	81514.2	347.8	2.8	13.4	0.7	1.8	1.2	0.2	0.9	0.8	1052.9	8.4	1048.5	7.6	1040.0	15.4	1040.0	15.4
Spot 111	57276.6	238.2	6.0	13.4	0.9	1.8	1.4	0.2	1.1	0.8	1047.3	10.5	1045.2	9.3	1041.8	18.5	1041.8	18.5
Spot 168	48323.6	193.8	2.4	13.5	0.8	1.8	1.1	0.2	0.8	0.7	1037.4	7.3	1039.5	7.2	1045.0	16.1	1045.0	16.1
Spot 107	47007.9	198.3	1.3	13.4	0.8	1.8	1.1	0.2	0.8	0.7	1051.5	7.6	1049.2	7.5	1045.5	16.9	1045.5	16.9
Spot 201	24635.0	99.6	6.0	13.3	0.8	1.9	1.3	0.2	0.7	0.5	1089.1	7.3	1074.8	8.8	1046.7	22.4	1046.7	22.4
Spot 198	18471.6	242.9	1.5	13.3	0.9	1.8	1.5	0.2	1.0	0.6	1020.4	9.1	1029.2	9.8	1048.7	23.7	1048.7	23.7
Spot 36	64114.4	292.9	3.1	13.3	0.8	1.9	1.3	0.2	1.0	0.8	1077.5	9.5	1068.2	8.3	1050.3	16.6	1050.3	16.6
Spot 19	27165.6	118.5	1.9	13.3	1.3	1.8	1.6	0.2	0.9	0.6	1060.6	8.7	1057.4	10.4	1051.6	26.2	1051.6	26.2
Spot 221	7002.2	23.9	0.6	13.0	4.1	1.9	4.9	0.2	1.1	0.2	1107.3	11.5	1088.7	32.9	1052.5	96.6	1052.5	96.6
Spot 288	16437.8	62.9	2.6	13.2	1.6	1.8	2.0	0.2	1.0	0.5	1047.6	9.9	1049.5	13.2	1054.6	35.2	1054.6	35.2
Spot 178	26701.5	104.9	1.3	13.3	0.9	1.8	1.4	0.2	0.9	0.6	1018.6	8.2	1030.4	9.2	1056.6	22.6	1056.6	22.6
Spot 64	32827.7	143.0	1.8	13.2	0.9	1.9	1.3	0.2	0.9	0.7	1069.2	8.5	1066.2	8.7	1061.0	20.2	1061.0	20.2
Spot 132	39290.9	164.3	0.6	13.2	0.8	1.9	1.8	0.2	1.5	0.9	1077.1	15.4	1071.5	11.8	1061.2	17.9	1061.2	17.9
Spot 32	13644.3	237.3	2.4	13.1	0.7	1.9	1.8	0.2	0.9	0.5	1085.2	9.3	1077.5	12.1	1063.1	31.4	1063.1	31.4
Spot 200	14480.5	58.8	1.9	13.1	2.5	1.9	2.8	0.2	1.2	0.4	1089.7	12.3	1082.4	18.5	1068.7	50.2	1068.7	50.2
Spot 61	28153.6	111.4	3.0	13.2	0.9	1.9	1.4	0.2	0.8	0.6	1111.1	7.8	1096.6	9.1	1068.8	22.3	1068.8	22.3
Spot 128	23018.5	82.1	3.2	13.2	1.3	1.9	1.6	0.2	0.8	0.5	1082.3	8.2	1077.9	10.8	1069.9	28.3	1069.9	28.3
Spot 15	24245.7	79.1	3.1	13.2	1.6	1.9	1.9	0.2	0.8	0.4	1078.3	7.7	1075.7	12.5	1071.5	34.4	1071.5	34.4
Spot 205	27235.8	106.3	2.8	13.2	1.4	1.8	1.7	0.2	1.0	0.6	1059.4	9.4	1063.3	11.3	1072.1	28.6	1072.1	28.6
Spot 162	47255.9	171.7	3.6	13.3	0.8	1.9	1.2	0.2	0.8	0.7	1071.3	8.1	1071.3	7.9	1072.3	17.3	1072.3	17.3
Spot 172	24721.2	78.1	4.7	13.2	1.5	1.9	1.9	0.2	1.1	0.6	1063.4	10.6	1066.3	12.6	1073.3	31.7	1073.3	31.7
Spot 308	30512.1	130.6	2.6	13.2	0.9	1.9	1.4	0.2	1.0	0.7	1082.9	9.7	1080.0	9.0	1075.1	19.1	1075.1	19.1
Spot 148	92061.2	284.7	3.2	13.2	0.7	2.0	1.2	0.2	0.9	0.8	1111.4	9.5	1099.8	8.0	1077.8	15.1	1077.8	15.1
Spot 118	39496.3	135.8	2.4	13.2	1.0	1.9	1.5	0.2	1.2	0.8	1077.1	11.5	1077.0	10.3	1077.8	20.5	1077.8	20.5
Spot 291	18282.2	89.2	0.8	13.1	0.9	1.9	1.6	0.2	1.1	0.7	1061.0	10.5	1066.6	10.7	1079.0	24.3	1079.0	24.3
Spot 143	39443.6	124.3	1.6	13.1	0.9	2.0	1.2	0.2	0.8	0.6	1116.9	7.8	1104.5	8.1	1081.0	18.7	1081.0	18.7
Spot 265	9855.1	40.2	0.7	12.9	2.6	2.0	3.2	0.2	1.2	0.4	1121.0	12.0	1108.3	21.5	1084.2	59.6	1084.2	59.6
Spot 293	17979.8	65.7	1.5	13.0	1.4	1.9	1.7	0.2	0.8	0.5	1061.9	8.3	1069.5	11.2	1086.0	29.4	1086.0	29.4
Spot 213	59522.0	303.6	4.0	13.1	0.6	2.0	0.9	0.2	0.7	0.7	1129.4	7.2	1115.1	6.4	1088.2	12.7	1088.2	12.7
Spot 262	66863.7	246.3	2.8	13.1	0.7	1.9	1.0	0.2	0.8	0.8	1093.3	7.9	1091.7	6.9	1089.3	13.3	1089.3	13.3
Spot 220	41353.4	149.2	3.5	13.1	0.9	2.1	1.2	0.2	0.8	0.7	1157.6	8.6	1135.0	8.2	1092.9	17.8	1092.9	17.8
Spot 108	30503.6	112.7	0.9	13.0	1.1	2.0	1.4	0.2	0.8	0.6	1126.1	8.2	1118.3	9.2	1104.0	21.9	1104.0	21.9
Spot 48	3178.5	14.1	3.0	12.3	4.5	1.9	7.1	0.2	1.3	0.2	1046.0	12.5	1067.5	47.2	1112.5	140.6	1112.5	140.6
Spot 263	32617.5	111.4	5.4	12.8	0.9	2.1	1.2	0.2	0.7	0.6	1155.2	7.4	1147.7	8.2	1134.5	19.2	1134.5	19.2
Spot 275	20889.9	96.8	3.0	12.6	1.0	2.1	1.5	0.2	0.9	0.6	1142.5	9.3	1147.7	10.1	1158.3	23.3	1158.3	23.3
Spot 261	68550.7	254.2	4.0	12.7	0.6	2.1	1.1	0.2	0.9	0.8	1163.9	9.7	1162.1	7.6	1159.6	12.3	1159.6	12.3
Spot 189	4568.4	18.7	3.1	12.1	4.7	2.0	5.5	0.2	1.6	0.3	1063.8	15.6	1100.1	37.0	1173.6	104.2	1173.6	104.2
Spot 126	36560.7	121.0	1.2	12.3	1.0	2.4	1.3	0.2	0.7	0.6	1252.5	8.4	1236.8	8.9	1210.3	19.9	1210.3	19.9
Spot 280	50813.6	227.5	6.4	12.1	0.7	2.5	1.2	0.2	0.9	0.8	1301.2	10.7	1276.7	8.4	1236.7	14.0	1236.7	14.0
Spot 231	8241.4	23.6	1.9	12.0	2.6	2.3	3.2	0.2	0.9	0.3	1204.3	10.4	1216.1	22.8	1238.0	60.1	1238.0	60.1
Spot 238	13028.1	271.4	0.9	11.7	0.6	2.4	1.4	0.2	1.0	0.8	1235.7	11.5	1253.1	9.8	1283.9	17.3	1283.9	17.3
Spot 242	19075.3	69.1	2.2	11.3	1.3	2.5	2.1	0.2	1.7	0.8	1212.3	18.8	1270.3	15.5	1370.6	25.0	1370.6	25.0

Analysis	206Pb	U	U/Th	206Pb*	Â±2s	207Pb*	Â±2s	206Pb*	Â±2s	error	206Pb*	Â±2s	207Pb*	Â±2s	206Pb*	Â±2s	Best age	Â±2s
Spot 84	24228.2	57.1	0.6	10.8	1.1	3.2	1.4	0.3	0.9	0.6	1477.9	11.6	1468.5	11.1	1455.9	21.6	1455.9	21.6
Spot 124	14836.2	61.6	1.2	10.7	1.0	3.3	1.5	0.3	0.8	0.5	1501.9	10.6	1488.1	11.3	1469.2	23.1	1469.2	23.1
Spot 309	73090.9	151.8	1.0	9.2	0.6	4.4	1.2	0.3	1.0	0.9	1667.3	15.0	1709.0	9.9	1761.2	11.3	1761.2	11.3
Spot 230	49779.4	113.1	1.9	9.2	0.7	4.8	1.0	0.3	0.7	0.7	1798.8	10.9	1781.9	8.3	1762.9	12.8	1762.9	12.8
Spot 188	49224.0	128.6	2.5	9.2	0.7	4.6	0.9	0.3	0.6	0.7	1733.8	9.5	1747.4	7.6	1764.4	12.0	1764.4	12.0
Spot 170	55121.7	138.5	1.4	9.1	0.6	4.7	1.2	0.3	1.0	0.8	1765.8	14.9	1774.0	9.7	1784.4	11.7	1784.4	11.7
Spot 286	7153.9	18.9	0.8	8.8	1.9	5.2	2.5	0.3	1.0	0.4	1878.1	16.2	1847.3	20.9	1813.7	40.8	1813.7	40.8
Spot 281	28857.7	79.4	0.8	8.9	0.8	5.1	1.2	0.3	0.8	0.7	1856.8	13.3	1842.2	9.8	1826.5	14.6	1826.5	14.6
Spot 92	67358.8	126.7	1.5	8.8	0.7	5.3	1.1	0.3	0.8	0.8	1885.5	13.8	1869.4	9.5	1852.3	12.9	1852.3	12.9
Spot 196	26535.5	53.3	1.2	8.7	1.0	5.3	1.4	0.3	0.9	0.6	1874.6	15.1	1864.4	12.2	1853.8	19.7	1853.8	19.7
Spot 299	######	267.1	1.9	8.7	2.3	5.1	7.6	0.3	7.2	1.0	1828.2	115.0	1841.5	64.5	1857.2	41.8	1857.2	41.8
Spot 117	62476.7	152.4	0.8	8.7	0.9	5.3	1.3	0.3	1.0	0.7	1863.1	15.4	1862.8	11.1	1863.2	16.1	1863.2	16.1
Spot 300	50575.8	95.4	1.3	8.7	2.3	5.2	7.6	0.3	7.2	1.0	1841.9	115.6	1851.6	64.6	1863.3	42.2	1863.3	42.2
Spot 252	26030.4	70.2	1.1	8.7	0.7	5.3	1.0	0.3	0.7	0.7	1862.1	11.9	1863.2	8.9	1865.3	13.3	1865.3	13.3
Spot 274	38144.3	98.3	1.1	8.7	0.8	5.6	1.2	0.4	0.9	0.7	1962.2	14.4	1916.4	10.2	1867.9	14.8	1867.9	14.8
Spot 173	32046.7	73.6	0.9	8.7	0.9	5.1	1.3	0.3	0.8	0.7	1813.5	13.4	1839.5	10.7	1869.8	16.7	1869.8	16.7
Spot 58	86385.5	176.5	1.7	8.7	0.6	5.5	0.9	0.4	0.7	0.7	1937.2	11.0	1904.7	7.5	1870.3	10.5	1870.3	10.5
Spot 152	37018.7	76.3	0.8	8.6	0.6	5.5	0.9	0.4	0.7	0.7	1939.9	11.1	1908.2	8.1	1874.6	12.1	1874.6	12.1
Spot 229	12580.4	111.9	1.4	8.6	0.6	5.4	1.3	0.3	1.1	0.8	1891.0	17.6	1883.2	11.1	1875.3	13.1	1875.3	13.1
Spot 181	49120.8	111.4	0.8	8.6	0.7	5.4	1.0	0.3	0.7	0.7	1896.9	12.1	1887.5	9.0	1877.9	13.4	1877.9	13.4
Spot 63	42143.9	82.0	2.2	8.6	0.8	5.5	1.2	0.4	0.9	0.7	1934.8	14.2	1907.5	10.2	1878.7	14.8	1878.7	14.8
Spot 244	87718.5	140.9	1.7	8.6	0.6	5.5	0.9	0.3	0.6	0.7	1930.8	10.7	1906.0	7.7	1879.8	11.2	1879.8	11.2
Spot 122	######	266.1	0.8	8.6	0.7	5.6	1.0	0.3	0.8	0.8	1933.7	13.5	1909.0	9.0	1883.0	11.9	1883.0	11.9
Spot 311	49359.5	134.8	0.9	8.6	0.7	5.3	1.2	0.3	0.9	0.8	1858.5	15.2	1870.2	10.0	1884.0	12.3	1884.0	12.3
Spot 284	15078.0	43.8	1.6	8.6	0.9	5.5	1.4	0.3	1.0	0.7	1921.6	16.8	1903.4	12.4	1884.4	18.5	1884.4	18.5
Spot 271	27469.6	149.9	0.8	8.6	1.0	5.5	1.6	0.3	1.1	0.7	1923.1	18.9	1904.9	13.3	1885.8	19.0	1885.8	19.0
Spot 268	30904.9	65.3	1.4	8.6	0.8	5.7	1.2	0.4	0.9	0.7	1980.3	15.2	1934.5	10.7	1886.5	15.5	1886.5	15.5
Spot 146	59714.6	123.8	2.1	8.5	0.7	5.7	1.1	0.4	0.9	0.8	1974.4	14.6	1936.5	9.9	1897.0	13.5	1897.0	13.5
Spot 218	87465.5	197.4	3.1	8.5	0.7	5.9	1.1	0.4	0.8	0.7	2002.2	13.4	1962.5	9.3	1921.6	13.3	1921.6	13.3
Spot 225	37805.6	114.9	2.7	8.3	0.7	5.9	1.1	0.4	0.8	0.7	1968.4	13.7	1961.8	9.4	1955.5	13.0	1955.5	13.0
Spot 115	46990.2	90.0	1.2	8.3	0.7	5.9	1.1	0.4	0.9	0.8	1951.0	14.6	1955.9	9.8	1961.8	12.9	1961.8	12.9
Spot 224	45053.5	200.4	1.5	8.3	0.6	6.1	1.1	0.4	0.9	0.8	2001.2	16.2	1983.3	9.8	1965.5	10.9	1965.5	10.9
Spot 50	28445.9	50.2	1.1	8.2	1.1	6.3	1.5	0.4	1.0	0.7	2062.5	17.8	2014.7	13.3	1966.9	20.3	1966.9	20.3
Spot 104	16917.6	49.0	1.0	8.2	0.8	6.0	1.1	0.4	0.8	0.7	1990.0	13.7	1979.4	9.9	1969.0	14.5	1969.0	14.5
Spot 305	34772.3	70.2	1.4	8.2	0.9	6.0	1.2	0.4	0.8	0.7	1970.8	13.9	1969.8	10.3	1969.5	15.3	1969.5	15.3
Spot 134	######	250.9	2.2	8.2	0.7	5.9	1.0	0.4	0.8	0.8	1942.6	12.8	1956.4	8.8	1971.8	12.0	1971.8	12.0
Spot 95	52561.6	116.1	2.2	8.2	0.6	6.3	1.0	0.4	0.8	0.8	2055.6	14.4	2014.4	8.8	1973.3	10.3	1973.3	10.3
Spot 310	60185.3	177.3	2.2	8.2	0.6	5.9	1.0	0.4	0.8	0.8	1937.1	12.7	1954.4	8.4	1973.5	10.9	1973.5	10.9
Spot 264	######	164.3	2.8	8.2	0.5	6.1	0.9	0.4	0.7	0.8	2002.7	12.2	1988.2	7.7	1973.9	9.4	1973.9	9.4
Spot 131	24815.9	45.4	1.5	8.1	0.9	6.0	1.3	0.4	0.8	0.6	1967.4	13.6	1975.4	10.9	1984.5	17.1	1984.5	17.1
Spot 110	65160.3	138.4	1.5	8.1	0.6	6.3	1.0	0.4	0.8	0.8	2033.5	13.8	2011.7	8.7	1990.3	10.7	1990.3	10.7
Spot 207	85633.7	129.5	8.9	8.1	0.6	6.3	1.0	0.4	0.8	0.8	2032.7	13.3	2017.3	8.8	2002.3	11.5	2002.3	11.5
Spot 295	96660.3	150.8	1.8	8.0	0.6	6.4	1.1	0.4	0.9	0.8	2036.2	16.4	2032.5	10.0	2029.6	11.3	2029.6	11.3
Spot 81	98217.4	207.0	5.4	7.9	0.6	6.6	1.1	0.4	0.9	0.8	2077.5	15.8	2056.3	9.7	2035.9	11.5	2035.9	11.5
Spot 57	22313.2	62.1	1.2	7.9	0.7	6.6	1.0	0.4	0.7	0.7	2088.1	11.9	2062.1	9.0	2036.9	13.5	2036.9	13.5
Spot 251	######	200.6	3.5	7.7	0.6	6.7	1.1	0.4	0.9	0.8	2052.5	15.6	2067.8	9.5	2083.9	10.8	2083.9	10.8
Spot 8	34827.3	66.8	4.2	7.6	0.8	7.3	1.2	0.4	0.8	0.7	2180.8	15.6	2143.9	10.7	2109.6	14.9	2109.6	14.9
Spot 247	32816.2	73.2	3.5	7.4	0.6	7.5	1.0	0.4	0.7	0.7	2177.8	13.7	2169.1	9.0	2161.7	11.9	2161.7	11.9
Spot 38	87083.2	174.9	6.9	6.8	1.2	8.3	2.1	0.4	1.6	0.8	2219.6	31.0	2263.9	18.7	2304.9	21.3	2304.9	21.3
Spot 175	38120.5	62.8	1.0	6.1	0.7	10.1	1.1	0.5	0.8	0.7	2400.8	16.8	2440.3	10.4	2474.0	12.8	2474.0	12.8
Spot 270	37239.1	39.8	1.8	4.9	0.7	16.4	1.1	0.6	0.8	0.7	2962.9	18.6	2901.0	10.1	2859.0	11.4	2859.0	11.4
Spot 74	40362.0	191.1	3.1	4.3	0.6	20.2	1.0	0.6	0.8	0.8	3151.3	19.0	3098.6	9.5	3065.4	9.8	3065.4	9.8
21-MANY-8																		
Spot 245	21737.2	252.9	4.4	16.3	1.9	0.8	2.4	0.1	1.4	0.6	610.7	7.9	611.9	11.3	617.1	44.1	610.7	7.9
Spot 220	41607.3	237.3	4.4	16.4	2.4	0.8	2.9	0.1	1.4	0.5	617.7	8.0	616.4	13.3	612.5	54.9	617.7	8.0
Spot 113	46061.9	314.9	1.6	16.3	1.9	0.8	2.7	0.1	1.7	0.6	620.3	10.0	623.8	12.6	637.8	45.2	620.3	10.0
Spot 209	27095.9	155.6	5.1	16.0	2.6	0.9	3.1	0.1	1.4	0.4	620.4	8.0	627.6	14.4	654.6	59.2	620.4	8.0
Spot 37	40522.1	275.2	4.2	16.1	1.9	0.9	2.6	0.1	1.5	0.6	629.1	8.9	634.7	12.3	655.4	46.1	629.1	8.9

Analysis	206Pb	U	U/Th	206Pb*	Â±2s	207Pb*	Â±2s	206Pb*	Â±2s	error	206Pb*	Â±2s	207Pb*	Â±2s	206Pb*	Â±2s	Best age	Â±2s
Spot 139	14663.0	82.8	2.5	15.6	4.3	0.9	5.3	0.1	1.6	0.3	670.6	10.4	677.3	26.0	700.3	106.5	670.6	10.4
Spot 280	28341.0	175.0	2.5	16.0	2.6	0.9	3.2	0.1	1.5	0.5	671.3	9.4	667.7	15.4	656.4	59.9	671.3	9.4
Spot 229	11173.2	194.6	2.0	15.5	2.0	1.0	3.1	0.1	1.2	0.4	671.4	7.8	678.4	15.3	702.7	60.6	671.4	7.8
Spot 40	13655.3	131.9	2.2	15.9	3.2	0.9	3.7	0.1	1.4	0.4	672.0	8.9	669.5	18.0	662.2	72.7	672.0	8.9
Spot 269	53125.1	308.7	1.8	15.7	1.5	1.0	2.1	0.1	1.4	0.7	672.0	9.1	682.0	10.6	716.0	33.8	672.0	9.1
Spot 198	14644.5	68.9	2.9	15.3	4.2	1.0	4.6	0.1	1.6	0.4	672.5	10.4	687.9	23.2	739.6	92.0	672.5	10.4
Spot 250	30009.1	170.5	1.8	16.1	3.0	0.9	3.7	0.1	2.1	0.6	674.9	13.4	671.0	18.1	658.8	65.1	674.9	13.4
Spot 224	60925.5	416.5	3.6	16.0	1.4	0.9	2.0	0.1	1.4	0.7	675.2	9.3	673.7	10.0	669.4	30.3	675.2	9.3
Spot 102	12635.6	128.0	2.5	15.8	2.8	1.0	4.1	0.1	1.2	0.3	675.4	7.7	678.1	20.1	688.1	82.8	675.4	7.7
Spot 119	27870.4	163.8	1.6	15.8	2.5	1.0	3.1	0.1	1.5	0.5	677.9	9.4	682.9	15.2	700.4	57.2	677.9	9.4
Spot 215	43485.9	260.3	3.8	15.9	1.8	0.9	2.7	0.1	1.8	0.7	678.5	11.9	677.6	13.5	675.3	42.8	678.5	11.9
Spot 223	30904.9	152.6	1.4	15.8	2.9	1.0	3.2	0.1	1.3	0.4	679.7	8.5	680.9	15.8	685.9	61.7	679.7	8.5
Spot 137	40732.7	221.3	2.3	16.0	2.4	1.0	3.0	0.1	1.7	0.6	680.3	10.7	679.2	14.7	676.3	52.9	680.3	10.7
Spot 166	8969.0	53.1	1.7	15.7	6.6	1.0	7.2	0.1	1.5	0.2	681.1	9.9	679.9	35.7	677.0	150.4	681.1	9.9
Spot 116	44589.9	256.0	1.6	16.0	1.8	1.0	2.5	0.1	1.7	0.7	681.9	10.7	679.9	12.3	674.3	39.3	681.9	10.7
Spot 282	45165.7	300.8	1.9	15.8	1.9	1.0	2.4	0.1	1.4	0.6	682.3	9.3	685.3	12.1	695.9	41.9	682.3	9.3
Spot 162	9889.3	54.9	3.0	14.9	5.9	1.0	7.0	0.1	1.6	0.2	683.5	10.7	707.6	35.7	785.9	143.0	683.5	10.7
Spot 295	39938.3	224.1	2.3	16.0	2.3	1.0	2.9	0.1	1.5	0.5	686.1	10.0	682.7	14.5	672.4	53.0	686.1	10.0
Spot 55	47738.6	270.4	2.2	15.8	1.7	1.0	2.2	0.1	1.2	0.6	686.4	8.0	689.7	10.9	701.5	38.3	686.4	8.0
Spot 308	15836.8	240.8	2.5	15.6	2.0	1.0	3.1	0.1	1.7	0.6	687.2	11.2	692.3	15.6	709.8	55.1	687.2	11.2
Spot 293	31704.3	175.8	6.5	16.0	2.8	1.0	3.6	0.1	1.9	0.5	687.8	12.4	682.2	17.8	664.7	64.9	687.8	12.4
Spot 5	56432.1	241.5	2.0	16.0	2.0	1.0	2.7	0.1	1.7	0.6	689.3	11.2	687.5	13.4	682.5	44.3	689.3	11.2
Spot 183	31412.4	196.2	2.1	15.9	2.1	1.0	2.7	0.1	1.5	0.5	691.7	9.6	690.6	13.5	687.8	48.3	691.7	9.6
Spot 108	22558.2	207.2	3.1	15.8	2.5	1.0	3.2	0.1	2.0	0.6	692.4	13.1	693.9	16.2	699.9	53.8	692.4	13.1
Spot 87	21760.2	165.6	2.1	15.9	3.0	1.0	3.6	0.1	1.4	0.4	694.0	9.5	690.3	18.2	679.1	71.5	694.0	9.5
Spot 99	9499.6	393.4	1.7	15.8	1.5	1.0	2.0	0.1	1.4	0.7	695.9	8.9	690.4	10.2	673.7	32.7	695.9	8.9
Spot 287	6571.4	352.5	2.3	15.2	1.9	1.0	6.1	0.1	1.2	0.2	700.7	7.7	702.8	31.0	710.5	127.4	700.7	7.7
Spot 185	38674.0	199.5	2.2	15.8	2.1	1.0	2.5	0.1	1.4	0.5	701.0	9.1	700.1	12.8	698.4	45.3	701.0	9.1
Spot 262	22604.2	121.4	10.5	15.5	2.8	1.0	3.5	0.1	1.5	0.4	705.5	10.2	710.0	17.9	725.0	66.8	705.5	10.2
Spot 199	27063.5	144.0	4.0	15.9	2.2	1.0	2.7	0.1	1.5	0.5	706.4	9.8	698.2	13.9	673.0	49.8	706.4	9.8
Spot 136	19907.0	90.2	3.4	15.7	4.4	1.0	4.9	0.1	1.7	0.3	710.8	11.3	709.0	25.2	704.4	98.6	710.8	11.3
Spot 76	59521.5	287.7	8.2	15.9	1.9	1.0	2.5	0.1	1.6	0.6	716.1	10.8	713.4	13.0	705.9	41.7	716.1	10.8
Spot 131	15151.5	218.0	2.7	15.1	1.8	1.1	2.6	0.1	1.5	0.6	737.5	10.3	745.5	13.6	770.7	44.3	737.5	10.3
Spot 230	89008.8	381.5	1.9	15.4	1.5	1.1	2.1	0.1	1.4	0.7	737.6	9.5	743.8	10.9	763.3	32.7	737.6	9.5
Spot 172	13737.5	72.6	3.7	15.4	4.9	1.1	5.5	0.1	1.7	0.3	738.7	11.5	735.6	28.7	727.0	111.0	738.7	11.5
Spot 111	3527.2	66.8	1.2	13.9	4.2	1.1	9.5	0.1	2.3	0.2	741.5	16.0	771.7	51.2	861.0	190.8	741.5	16.0
Spot 246	4188.5	155.5	3.8	14.7	2.9	1.1	4.1	0.1	2.1	0.5	746.0	14.6	748.1	21.8	755.4	74.9	746.0	14.6
Spot 84	45649.5	255.1	2.8	15.5	1.9	1.1	2.5	0.1	1.6	0.6	746.6	11.0	746.5	13.0	747.2	40.4	746.6	11.0
Spot 309	9119.8	137.5	1.7	15.1	2.7	1.1	3.2	0.1	1.5	0.5	749.5	10.4	749.8	16.8	751.8	59.2	749.5	10.4
Spot 187	17789.7	90.7	2.4	15.2	5.3	1.1	5.8	0.1	1.6	0.3	752.2	11.1	756.6	31.1	770.4	118.4	752.2	11.1
Spot 263	29744.3	189.1	3.4	15.2	1.9	1.1	2.4	0.1	1.3	0.5	758.7	9.2	763.4	13.0	778.3	43.2	758.7	9.2
Spot 67	73096.1	423.1	4.1	15.4	1.6	1.1	2.4	0.1	1.7	0.7	759.7	11.8	759.1	12.6	758.1	35.7	759.7	11.8
Spot 251	22225.5	122.7	2.8	15.0	2.8	1.2	3.2	0.1	1.4	0.4	773.6	10.6	778.5	17.7	793.4	61.0	773.6	10.6
Spot 13	11485.9	309.1	7.8	15.0	1.6	1.2	2.3	0.1	1.5	0.7	775.2	11.3	777.3	12.4	784.3	35.1	775.2	11.3
Spot 284	23705.1	123.9	3.1	15.3	3.3	1.1	3.7	0.1	1.5	0.4	779.6	10.7	773.7	20.1	757.8	72.0	779.6	10.7
Spot 174	16975.9	74.2	1.9	14.7	4.6	1.2	5.0	0.1	1.8	0.4	796.9	13.5	805.5	27.8	830.5	97.4	796.9	13.5
Spot 157	11249.8	56.1	3.4	14.5	5.1	1.3	6.3	0.1	1.5	0.2	814.9	11.7	825.9	35.4	856.6	126.3	814.9	11.7
Spot 188	22885.8	86.6	2.3	14.3	4.1	1.4	4.5	0.2	1.6	0.4	912.8	13.6	906.9	27.2	893.5	87.7	893.5	87.7
Spot 18	55131.2	271.2	2.5	14.4	1.4	1.4	2.1	0.2	1.5	0.7	901.3	12.4	902.2	12.6	905.3	30.9	905.3	30.9
Spot 17	25555.7	99.8	1.8	14.3	2.5	1.5	3.3	0.2	1.6	0.5	913.3	13.4	912.0	19.8	909.6	59.3	909.6	59.3
Spot 16	11727.6	42.1	1.5	14.1	4.4	1.6	4.8	0.2	1.4	0.3	982.3	13.2	962.9	30.1	919.8	95.0	919.8	95.0
Spot 218	21376.5	101.1	3.9	14.0	2.5	1.6	2.9	0.2	1.3	0.5	965.2	11.8	953.9	17.9	929.0	52.8	929.0	52.8
Spot 148	22312.7	97.8	1.9	14.1	2.6	1.6	3.3	0.2	1.4	0.4	967.9	12.2	956.0	20.4	929.7	61.7	929.7	61.7
Spot 124	16219.6	69.5	1.2	14.0	4.6	1.6	4.9	0.2	1.4	0.3	984.9	12.9	968.5	30.3	932.4	95.4	932.4	95.4
Spot 159	5871.7	30.1	0.8	13.7	8.0	1.4	9.4	0.1	2.5	0.3	889.0	21.0	903.3	56.2	939.2	185.6	939.2	185.6
Spot 48	25765.6	115.0	1.2	14.0	2.5	1.6	3.0	0.2	1.6	0.5	970.3	14.7	962.7	19.0	946.2	52.6	946.2	52.6
Spot 2	12103.5	234.7	2.3	13.9	1.8	1.5	3.7	0.2	3.2	0.9	921.3	27.5	930.1	22.7	952.0	38.5	952.0	38.5
Spot 145	8900.2	38.7	1.6	13.7	4.4	1.6	5.2	0.2	1.8	0.3	966.4	15.8	964.3	32.6	960.5	100.8	960.5	100.8

Analysis	206Pb	U	U/Th	206Pb*	Â±2s	207Pb*	Â±2s	206Pb*	Â±2s	error	206Pb*	Â±2s	207Pb*	Â±2s	206Pb*	Â±2s	Best age	Â±2s
Spot 125	75307.4	281.4	3.2	13.9	1.4	1.6	2.2	0.2	1.6	0.8	946.7	14.5	954.1	13.4	972.1	28.7	972.1	28.7
Spot 138	54807.2	257.9	2.8	13.9	1.7	1.6	2.4	0.2	1.7	0.7	961.1	14.7	964.2	15.1	972.2	36.2	972.2	36.2
Spot 237	70256.0	246.8	1.8	13.9	1.7	1.6	2.4	0.2	1.6	0.7	958.0	14.7	963.1	15.1	975.7	36.2	975.7	36.2
Spot 313	43510.1	118.4	1.7	13.9	1.8	1.6	2.3	0.2	1.4	0.6	986.0	12.8	982.6	14.4	975.7	37.1	975.7	37.1
Spot 173	15004.4	202.4	2.7	13.7	1.8	1.5	4.3	0.2	3.6	0.8	925.8	30.8	941.2	26.3	978.0	48.2	978.0	48.2
Spot 271	7879.0	31.1	0.7	13.5	6.2	1.7	6.7	0.2	1.9	0.3	1013.3	17.5	1002.1	42.8	978.6	131.4	978.6	131.4
Spot 153	40598.9	165.1	2.3	13.8	1.7	1.7	2.5	0.2	1.8	0.7	995.8	16.3	990.5	15.7	979.7	35.4	979.7	35.4
Spot 47	31248.6	151.4	1.6	13.8	2.0	1.6	2.7	0.2	1.6	0.6	969.4	14.7	973.3	17.1	983.0	44.4	983.0	44.4
Spot 192	46217.8	193.7	2.3	13.8	1.4	1.6	2.0	0.2	1.2	0.6	961.4	10.8	969.0	12.2	986.9	31.3	986.9	31.3
Spot 240	63235.3	239.4	2.1	13.8	1.5	1.6	2.1	0.2	1.4	0.7	977.1	12.4	981.2	13.2	991.3	32.1	991.3	32.1
Spot 85	12150.9	174.2	1.5	13.6	1.8	1.6	3.8	0.2	1.4	0.4	955.2	12.8	969.5	24.0	1003.0	72.2	1003.0	72.2
Spot 307	2239.2	84.3	0.6	12.6	4.4	1.5	8.5	0.1	2.1	0.2	891.7	17.3	924.1	51.3	1003.3	166.5	1003.3	166.5
Spot 150	8748.0	195.4	1.0	13.4	1.5	1.6	1.9	0.2	1.1	0.6	938.6	9.8	959.4	11.8	1008.3	31.0	1008.3	31.0
Spot 194	8030.5	31.9	0.9	13.4	5.6	1.6	6.3	0.2	1.3	0.2	960.5	12.0	975.1	39.6	1009.1	125.3	1009.1	125.3
Spot 266	31042.5	112.7	6.7	13.5	2.2	1.7	2.9	0.2	1.6	0.5	1022.6	15.1	1019.7	19.0	1014.3	50.2	1014.3	50.2
Spot 242	9351.9	34.2	2.0	13.3	5.0	1.8	5.4	0.2	1.5	0.3	1032.7	14.3	1028.1	34.8	1019.3	104.8	1019.3	104.8
Spot 210	15451.5	175.4	0.9	13.4	2.2	1.7	3.6	0.2	1.5	0.4	992.3	13.5	1001.9	23.0	1023.7	66.6	1023.7	66.6
Spot 238	23455.8	89.8	1.3	13.5	2.7	1.8	3.1	0.2	1.3	0.4	1036.2	12.5	1032.8	20.0	1026.5	56.5	1026.5	56.5
Spot 134	3068.6	167.4	1.6	12.8	3.5	1.6	9.7	0.2	2.6	0.3	957.5	23.3	978.9	61.0	1028.1	189.0	1028.1	189.0
Spot 191	33289.6	154.3	1.0	13.5	1.8	1.8	2.5	0.2	1.6	0.6	1034.6	14.8	1032.4	16.0	1028.4	38.7	1028.4	38.7
Spot 110	6571.1	406.6	0.7	13.2	1.9	1.7	2.8	0.2	2.0	0.7	976.9	17.8	993.4	17.6	1030.7	39.8	1030.7	39.8
Spot 214	28860.7	321.3	1.8	13.4	1.8	1.5	2.6	0.1	1.7	0.6	875.9	14.0	921.3	16.0	1032.6	40.8	1032.6	40.8
Spot 169	48200.7	173.5	0.6	13.4	1.8	1.7	2.4	0.2	1.4	0.6	1022.2	13.5	1026.5	15.4	1036.4	38.6	1036.4	38.6
Spot 202	19059.5	90.5	1.0	13.2	2.9	1.8	3.7	0.2	1.7	0.5	1063.2	17.1	1058.6	24.4	1050.2	66.2	1050.2	66.2
Spot 205	28374.6	77.5	1.3	13.3	2.9	1.8	3.6	0.2	1.7	0.5	1057.2	16.7	1054.9	23.4	1051.1	63.1	1051.1	63.1
Spot 52	30369.1	141.8	3.4	13.3	1.7	1.8	2.2	0.2	1.2	0.6	1032.3	11.5	1038.4	14.2	1052.1	36.7	1052.1	36.7
Spot 189	31000.5	94.6	1.5	13.3	2.8	1.8	3.4	0.2	1.8	0.5	1067.8	18.0	1062.5	22.6	1052.5	58.5	1052.5	58.5
Spot 1	12300.2	46.9	1.6	13.2	3.7	1.8	4.2	0.2	1.8	0.4	1046.3	17.4	1048.7	27.2	1054.4	75.7	1054.4	75.7
Spot 272	26234.1	192.8	2.3	13.2	1.7	1.8	2.5	0.2	1.6	0.6	1031.0	15.0	1038.7	16.4	1055.9	39.8	1055.9	39.8
Spot 306	27892.1	160.6	0.8	13.3	1.8	1.8	2.6	0.2	1.6	0.6	1052.1	15.1	1053.9	17.2	1058.5	42.4	1058.5	42.4
Spot 147	3850.7	91.7	0.9	12.7	2.3	1.8	2.8	0.2	1.5	0.5	1019.2	14.4	1032.4	18.5	1061.4	48.4	1061.4	48.4
Spot 255	32374.2	117.0	2.0	13.2	2.0	1.8	2.7	0.2	1.6	0.6	1025.6	15.6	1037.6	17.3	1063.9	42.2	1063.9	42.2
Spot 222	4818.6	192.4	1.0	12.7	2.0	1.7	3.0	0.2	1.6	0.6	1002.2	15.2	1022.9	19.1	1068.4	49.6	1068.4	49.6
Spot 248	15219.8	189.0	1.2	13.1	2.2	1.8	3.2	0.2	2.0	0.6	1008.7	18.4	1029.9	20.6	1075.9	50.1	1075.9	50.1
Spot 81	5468.4	85.8	0.5	12.9	2.7	1.8	6.8	0.2	1.2	0.2	1042.3	11.7	1053.4	44.5	1077.4	134.2	1077.4	134.2
Spot 256	23921.4	81.8	1.9	13.1	2.6	1.8	2.9	0.2	1.2	0.4	1022.0	11.7	1039.8	18.9	1078.4	52.8	1078.4	52.8
Spot 294	9379.4	178.0	1.4	12.9	1.8	1.9	4.0	0.2	1.9	0.5	1078.9	18.6	1078.5	26.5	1078.5	70.6	1078.5	70.6
Spot 62	51590.3	265.9	3.4	13.1	1.7	1.9	3.9	0.2	3.4	0.9	1056.9	33.6	1065.5	25.6	1083.9	35.6	1083.9	35.6
Spot 297	8016.6	34.0	1.2	12.8	5.4	1.8	6.0	0.2	1.6	0.3	1048.6	15.4	1060.8	39.2	1086.7	115.1	1086.7	115.1
Spot 34	53213.3	189.3	1.1	13.1	2.1	1.8	2.7	0.2	1.8	0.6	1050.5	17.3	1062.6	18.1	1088.3	41.9	1088.3	41.9
Spot 141	57410.0	184.1	1.6	13.1	1.5	1.9	2.1	0.2	1.4	0.7	1068.1	14.2	1076.1	13.9	1093.1	30.4	1093.1	30.4
Spot 298	31903.3	84.0	1.2	13.0	2.3	2.0	2.9	0.2	1.6	0.6	1104.4	16.2	1100.9	19.4	1094.7	48.1	1094.7	48.1
Spot 36	42652.7	168.5	2.7	13.0	1.5	2.0	2.2	0.2	1.6	0.7	1109.3	15.9	1106.8	14.9	1102.8	31.3	1102.8	31.3
Spot 164	28471.5	100.4	2.2	13.0	1.9	2.0	2.7	0.2	1.4	0.5	1107.6	14.4	1106.1	18.2	1103.9	46.0	1103.9	46.0
Spot 118	67063.3	270.8	3.4	13.0	1.3	2.0	2.2	0.2	1.8	0.8	1104.6	17.9	1105.4	15.0	1108.0	27.2	1108.0	27.2
Spot 80	4612.0	234.8	1.0	12.6	1.8	1.9	5.9	0.2	1.6	0.3	1052.9	15.9	1072.2	38.9	1112.4	112.5	1112.4	112.5
Spot 268	80775.0	334.7	5.5	12.6	1.3	2.1	1.9	0.2	1.3	0.7	1138.2	13.6	1145.4	12.8	1160.0	26.4	1160.0	26.4
Spot 161	63245.0	216.3	1.9	12.4	1.6	2.2	2.4	0.2	1.8	0.7	1188.1	19.0	1191.7	16.6	1199.1	31.3	1199.1	31.3
Spot 279	40111.5	418.3	1.4	12.3	1.2	2.2	1.9	0.2	1.5	0.8	1177.3	15.9	1187.3	13.4	1206.5	24.2	1206.5	24.2
Spot 232	55785.0	188.1	962.0	12.1	1.6	2.3	2.3	0.2	1.5	0.7	1200.4	16.8	1217.9	16.3	1250.0	33.4	1250.0	33.4
Spot 249	4808.0	38.7	3.4	11.6	3.9	2.3	6.2	0.2	2.2	0.4	1189.6	23.9	1219.7	43.9	1274.3	112.7	1274.3	112.7
Spot 39	38194.1	116.2	2.5	11.4	1.6	2.8	2.2	0.2	1.4	0.7	1343.7	17.4	1349.8	16.3	1360.2	31.7	1360.2	31.7
Spot 95	15107.3	191.4	1.9	11.4	1.5	2.9	2.3	0.2	1.6	0.7	1379.1	19.6	1373.1	17.4	1364.6	32.5	1364.6	32.5
Spot 296	97012.8	215.8	8.2	11.3	1.2	2.9	2.0	0.2	1.5	0.8	1370.9	19.1	1375.0	14.8	1382.3	23.2	1382.3	23.2
Spot 56	45172.5	131.9	1.8	11.3	1.6	3.0	2.0	0.2	1.2	0.6	1404.6	14.7	1397.2	15.5	1386.9	32.2	1386.9	32.2
Spot 177	10652.0	36.0	1.3	10.9	4.6	3.0	5.2	0.2	1.6	0.3	1415.9	20.7	1418.5	39.7	1423.1	94.2	1423.1	94.2
Spot 121	79177.8	213.0	1.4	11.0	1.3	3.1	1.8	0.2	1.3	0.7	1405.9	16.9	1420.5	14.1	1443.2	24.3	1443.2	24.3
Spot 278	14594.1	45.6	1.2	10.8	3.2	3.1	4.1	0.2	1.6	0.4	1401.3	19.6	1420.6	31.4	1450.4	72.3	1450.4	72.3

Analysis	206Pb	U	U/Th	206Pb*	Â±2s	207Pb*	Â±2s	206Pb*	Â±2s	error	206Pb*	Â±2s	207Pb*	Â±2s	206Pb*	Â±2s	Best age	Â±2s
Spot 296	97012.8	215.8	8.2	11.3	1.2	2.9	2.0	0.2	1.5	0.8	1370.9	19.1	1375.0	14.8	1382.3	23.2	1382.3	23.2
Spot 56	45172.5	131.9	1.8	11.3	1.6	3.0	2.0	0.2	1.2	0.6	1404.6	14.7	1397.2	15.5	1386.9	32.2	1386.9	32.2
Spot 177	10652.0	36.0	1.3	10.9	4.6	3.0	5.2	0.2	1.6	0.3	1415.9	20.7	1418.5	39.7	1423.1	94.2	1423.1	94.2
Spot 121	79177.8	213.0	1.4	11.0	1.3	3.1	1.8	0.2	1.3	0.7	1405.9	16.9	1420.5	14.1	1443.2	24.3	1443.2	24.3
Spot 278	14594.1	45.6	1.2	10.8	3.2	3.1	4.1	0.2	1.6	0.4	1401.3	19.6	1420.6	31.4	1450.4	72.3	1450.4	72.3
Spot 182	9470.1	30.1	0.9	10.7	4.1	3.0	5.4	0.2	1.5	0.3	1389.0	19.2	1414.2	41.1	1453.3	98.2	1453.3	98.2
Spot 91	19183.5	72.9	4.6	10.5	1.6	3.5	2.4	0.3	1.3	0.6	1513.6	18.0	1518.8	18.8	1526.9	37.3	1526.9	37.3
Spot 103	13099.5	49.7	1.4	9.2	1.9	4.7	2.5	0.3	1.3	0.5	1770.7	20.7	1764.9	20.7	1758.8	38.1	1758.8	38.1
Spot 126	83955.4	166.2	2.1	9.2	1.2	4.6	1.8	0.3	1.3	0.7	1736.1	20.2	1747.0	14.8	1760.9	21.6	1760.9	21.6
Spot 275	62656.0	130.8	0.7	9.2	1.5	4.6	2.1	0.3	1.5	0.7	1750.9	23.2	1756.5	17.7	1763.9	27.1	1763.9	27.1
Spot 90	74626.8	337.0	3.9	8.9	1.0	4.8	1.6	0.3	1.2	0.8	1733.0	17.9	1781.5	13.1	1839.5	18.5	1839.5	18.5
Spot 73	23326.4	42.3	1.1	8.9	5.4	5.1	9.6	0.3	7.9	0.8	1841.2	126.9	1840.8	82.0	1841.1	99.6	1841.1	99.6
Spot 24	4706.4	41.1	1.3	8.6	2.1	5.1	5.2	0.3	4.8	0.9	1838.9	76.4	1843.8	44.6	1850.0	39.3	1850.0	39.3
Spot 33	24993.2	332.9	3.0	8.8	1.7	4.8	2.5	0.3	1.8	0.7	1714.0	27.3	1777.4	20.8	1853.5	30.6	1853.5	30.6
Spot 32	20400.8	43.5	1.3	8.7	2.2	5.2	3.0	0.3	1.7	0.6	1856.7	28.2	1856.6	25.7	1857.3	44.5	1857.3	44.5
Spot 51	46087.1	71.4	1.6	8.8	1.5	5.2	2.0	0.3	1.3	0.6	1848.5	21.1	1852.8	17.2	1858.4	27.7	1858.4	27.7
Spot 258	######	223.7	1.9	8.7	1.1	5.1	1.8	0.3	1.4	0.8	1827.7	22.8	1842.2	15.4	1859.5	20.1	1859.5	20.1
Spot 69	######	165.5	1.4	8.8	1.1	5.2	1.7	0.3	1.3	0.8	1857.5	21.3	1860.1	14.8	1863.9	20.3	1863.9	20.3
Spot 115	40164.9	114.1	0.9	8.7	1.3	5.2	1.9	0.3	1.3	0.7	1830.4	21.1	1848.1	16.3	1868.7	24.8	1868.7	24.8
Spot 83	24122.3	49.2	1.3	8.7	2.0	5.2	2.5	0.3	1.5	0.6	1844.7	23.3	1857.1	21.1	1871.8	36.3	1871.8	36.3
Spot 257	39670.5	82.4	1.1	8.7	1.3	5.2	1.9	0.3	1.3	0.7	1850.4	21.5	1860.5	16.5	1872.6	25.4	1872.6	25.4
Spot 19	89832.1	129.7	1.6	8.7	1.4	5.4	2.0	0.3	1.4	0.7	1889.0	22.9	1881.1	16.7	1873.2	24.6	1873.2	24.6
Spot 3	33549.3	61.5	0.6	8.7	1.8	5.4	2.5	0.3	1.7	0.7	1891.0	27.7	1882.2	21.4	1873.3	33.3	1873.3	33.3
Spot 58	22146.9	63.0	1.2	8.6	1.4	5.2	2.0	0.3	1.3	0.6	1825.7	20.5	1848.5	16.9	1875.1	27.4	1875.1	27.4
Spot 244	######	179.2	1.3	8.7	1.2	5.3	1.8	0.3	1.4	0.8	1871.8	22.2	1873.5	15.5	1876.3	21.5	1876.3	21.5
Spot 243	59464.3	113.2	1.2	8.7	1.3	5.3	1.9	0.3	1.4	0.7	1851.7	22.4	1863.5	16.3	1877.5	23.5	1877.5	23.5
Spot 82	38951.5	83.5	1.0	8.7	1.4	5.4	2.1	0.3	1.4	0.7	1892.7	23.8	1885.2	17.6	1877.7	26.1	1877.7	26.1
Spot 241	######	364.5	1.5	8.7	1.1	5.2	1.7	0.3	1.2	0.7	1829.7	19.4	1852.1	14.1	1878.1	20.1	1878.1	20.1
Spot 226	29840.4	62.8	1.5	8.6	1.5	5.3	2.1	0.3	1.3	0.7	1847.5	21.6	1862.1	17.5	1879.3	27.9	1879.3	27.9
Spot 35	36243.7	218.9	0.9	8.6	1.7	5.2	2.7	0.3	2.0	0.8	1840.0	32.0	1858.7	22.7	1880.4	31.8	1880.4	31.8
Spot 160	48455.6	95.7	1.3	8.7	1.6	5.3	2.4	0.3	1.7	0.7	1851.0	27.1	1864.6	20.1	1880.6	29.6	1880.6	29.6
Spot 120	28757.2	55.4	14.5	8.6	1.7	5.4	2.3	0.3	1.6	0.7	1891.4	25.6	1886.9	19.9	1882.7	30.9	1882.7	30.9
Spot 156	5126.7	109.3	1.1	8.5	1.4	4.9	2.3	0.3	1.8	0.8	1723.6	26.8	1797.6	19.7	1885.4	27.5	1885.4	27.5
Spot 11	15369.7	127.5	1.2	8.6	1.4	5.5	2.4	0.3	1.8	0.7	1909.8	29.7	1898.2	20.8	1886.4	29.2	1886.4	29.2
Spot 142	7075.7	135.5	0.7	8.5	1.4	5.1	2.9	0.3	1.3	0.4	1795.2	20.5	1837.8	24.9	1887.1	47.3	1887.1	47.3
Spot 129	79850.2	165.7	0.7	8.6	1.1	5.3	2.0	0.3	1.7	0.8	1862.0	27.3	1874.5	17.3	1889.2	20.1	1889.2	20.1
Spot 65	26907.2	143.3	1.1	8.6	1.5	5.3	2.4	0.3	1.8	0.8	1850.5	28.9	1868.7	20.2	1889.8	27.8	1889.8	27.8
Spot 235	34763.7	65.7	1.1	8.6	1.9	5.5	2.6	0.3	1.7	0.7	1896.2	27.6	1895.3	21.9	1895.0	34.6	1895.0	34.6
Spot 104	25573.1	146.8	1.5	8.6	1.1	5.3	1.9	0.3	1.5	0.8	1838.2	24.0	1866.4	16.4	1898.8	21.7	1898.8	21.7
Spot 74	85253.4	164.4	2.2	8.6	1.5	5.3	2.2	0.3	1.6	0.7	1843.6	26.1	1870.8	19.1	1902.0	27.5	1902.0	27.5
Spot 86	7618.8	93.8	1.1	8.5	1.4	4.7	3.4	0.3	2.9	0.8	1667.1	42.1	1773.8	28.5	1902.6	33.1	1902.6	33.1
Spot 149	39540.3	86.5	1.0	8.5	1.4	5.4	1.9	0.3	1.3	0.7	1880.4	20.9	1890.8	16.2	1903.1	24.9	1903.1	24.9
Spot 79	######	430.4	5.4	8.6	1.3	5.6	1.9	0.3	1.4	0.7	1931.2	22.7	1918.9	16.0	1906.4	22.8	1906.4	22.8
Spot 225	25857.2	185.2	1.2	8.3	1.1	5.6	1.7	0.3	1.3	0.7	1896.1	20.6	1914.8	14.8	1935.8	21.1	1935.8	21.1
Spot 227	36134.8	193.6	3.1	8.3	1.2	5.6	2.8	0.3	2.5	0.9	1902.3	40.7	1923.1	24.0	1946.4	23.1	1946.4	23.1
Spot 299	25969.9	139.8	1.9	8.3	1.4	5.5	2.2	0.3	1.6	0.8	1869.8	26.6	1906.7	18.6	1947.8	25.4	1947.8	25.4
Spot 261	34866.5	222.8	1.8	8.3	1.0	5.7	1.8	0.3	1.5	0.8	1922.0	24.4	1934.6	15.5	1948.9	18.5	1948.9	18.5
Spot 163	######	294.0	1.8	8.3	1.1	5.4	1.7	0.3	1.3	0.8	1831.2	21.3	1886.6	14.7	1949.0	19.4	1949.0	19.4
Spot 59	17263.1	185.5	1.8	8.3	1.2	5.6	2.1	0.3	1.2	0.6	1891.5	20.2	1921.7	17.8	1955.2	29.5	1955.2	29.5
Spot 291	45033.5	68.7	2.2	8.3	1.9	5.8	2.7	0.3	1.9	0.7	1932.0	31.7	1943.0	23.3	1955.6	34.1	1955.6	34.1
Spot 14	90475.4	198.6	1.7	8.3	1.1	5.7	1.7	0.3	1.2	0.7	1898.8	20.3	1927.3	14.4	1959.0	20.2	1959.0	20.2
Spot 143	######	223.9	2.6	8.3	1.2	5.6	1.8	0.3	1.4	0.7	1878.3	22.2	1918.2	15.7	1962.4	21.6	1962.4	21.6
Spot 234	61556.6	208.0	1.8	8.2	1.4	5.6	2.0	0.3	1.4	0.7	1867.0	23.0	1914.2	17.1	1966.6	24.8	1966.6	24.8
Spot 206	55917.5	82.9	2.5	8.2	1.5	6.0	2.0	0.4	1.4	0.7	1974.1	23.4	1970.9	17.6	1968.4	26.4	1968.4	26.4
Spot 181	######	218.5	2.6	8.2	1.3	5.9	2.1	0.4	1.6	0.8	1945.9	27.3	1957.3	17.9	1970.2	22.7	1970.2	22.7
Spot 286	######	198.2	1.4	8.2	1.0	5.8	1.5	0.3	1.2	0.8	1930.1	19.6	1950.2	13.4	1972.4	17.9	1972.4	17.9
Spot 193	######	194.5	1.9	8.2	1.0	5.9	1.6	0.4	1.2	0.8	1945.6	20.2	1959.1	13.5	1974.2	17.5	1974.2	17.5
Spot 233	79763.8	156.9	2.2	8.2	1.4	5.8	2.0	0.3	1.5	0.7	1933.9	24.4	1953.8	17.4	1975.7	24.4	1975.7	24.4

Analysis	206Pb	U	U/Th	206Pb*	Â±2s	207Pb*	Â±2s	206Pb*	Â±2s	error	206Pb*	Â±2s	207Pb*	Â±2s	206Pb*	Â±2s	Best age	Â±2s
Spot 6	31896.6	58.7	2.2	8.2	1.7	5.9	2.4	0.4	1.7	0.7	1958.8	29.0	1967.2	21.2	1976.9	30.9	1976.9	30.9
Spot 175	######	189.0	1.6	8.2	1.4	5.9	2.1	0.4	1.6	0.8	1950.2	27.0	1962.9	18.3	1977.1	24.2	1977.1	24.2
Spot 130	######	167.7	1.2	8.2	1.2	5.9	1.8	0.4	1.3	0.8	1942.7	22.6	1959.6	15.5	1978.3	20.9	1978.3	20.9
Spot 93	17888.5	161.5	1.7	8.2	1.4	5.9	2.5	0.4	1.8	0.7	1936.5	29.3	1956.9	21.3	1979.2	30.7	1979.2	30.7
Spot 71	84759.8	160.2	2.6	8.2	5.0	6.0	9.4	0.4	7.9	0.8	1982.7	135.1	1980.8	81.7	1979.5	89.6	1979.5	89.6
Spot 140	63713.7	106.0	2.1	8.2	1.2	5.8	1.9	0.3	1.4	0.7	1920.4	23.3	1949.2	16.3	1980.7	22.3	1980.7	22.3
Spot 98	15945.3	237.9	2.3	8.2	1.4	6.1	2.1	0.4	1.6	0.8	1998.0	27.6	1989.5	18.6	1981.4	25.0	1981.4	25.0
Spot 186	38053.8	86.8	1.3	8.2	1.3	5.9	2.1	0.4	1.6	0.8	1948.8	27.3	1965.0	18.1	1982.8	23.2	1982.8	23.2
Spot 154	56048.1	98.6	2.0	8.2	1.1	5.9	1.7	0.4	1.3	0.8	1947.9	22.0	1964.6	15.1	1982.9	20.4	1982.9	20.4
Spot 28	29142.4	419.0	19.8	8.1	1.2	6.0	2.2	0.4	1.8	0.8	1968.3	30.1	1980.7	18.9	1994.5	22.3	1994.5	22.3
Spot 78	11459.4	270.9	3.6	8.1	1.4	6.1	2.2	0.4	1.5	0.7	1977.2	24.8	1985.7	19.5	1995.3	30.2	1995.3	30.2
Spot 315	38912.0	132.5	1.4	8.1	1.3	6.1	2.3	0.4	1.9	0.8	1973.4	32.2	1986.3	20.4	2000.6	24.4	2000.6	24.4
Spot 276	20426.2	369.5	1.0	8.0	1.2	6.0	2.1	0.4	1.7	0.8	1938.1	27.7	1972.3	18.1	2009.0	22.3	2009.0	22.3
Spot 61	######	218.2	0.7	8.0	1.1	6.1	1.7	0.4	1.3	0.8	1969.9	21.6	1989.4	14.6	2010.4	19.3	2010.4	19.3
Spot 292	85941.4	147.5	3.3	7.9	1.5	6.4	2.3	0.4	1.7	0.7	2046.1	29.7	2038.9	19.9	2032.3	26.4	2032.3	26.4
Spot 289	######	185.0	0.5	7.8	1.2	6.5	1.8	0.4	1.4	0.8	2040.5	24.0	2046.8	16.1	2053.9	21.4	2053.9	21.4
Spot 128	######	204.6	3.0	7.8	1.1	6.5	1.9	0.4	1.6	0.8	2025.0	27.7	2039.5	16.9	2054.9	18.9	2054.9	18.9
Spot 146	18022.5	335.9	5.2	7.7	1.1	6.5	1.7	0.4	1.2	0.7	1999.0	21.3	2040.3	14.8	2083.2	20.0	2083.2	20.0
Spot 211	23201.8	77.3	1.4	7.6	1.7	6.9	2.7	0.4	1.9	0.7	2107.0	33.6	2099.2	23.7	2092.3	33.5	2092.3	33.5
Spot 105	41862.4	111.2	2.1	7.4	1.1	7.5	1.9	0.4	1.5	0.8	2170.3	27.5	2167.1	16.8	2164.7	19.8	2164.7	19.8
Spot 50	23954.0	59.4	1.4	5.7	1.3	12.0	1.9	0.5	1.3	0.7	2601.4	28.8	2605.7	17.4	2609.8	21.3	2609.8	21.3
Spot 44	52055.0	293.1	3.3	5.7	1.1	12.0	1.7	0.5	1.3	0.8	2601.7	28.4	2606.8	16.3	2611.6	18.6	2611.6	18.6
Spot 288	38812.2	216.7	2.0	5.6	1.1	11.6	1.6	0.5	1.2	0.7	2523.9	24.6	2575.8	15.0	2617.6	18.3	2617.6	18.3
Spot 43	74761.9	104.0	1.3	5.6	1.2	12.3	1.7	0.5	1.2	0.7	2630.1	26.6	2627.0	15.9	2625.4	19.3	2625.4	19.3
Spot 219	32314.0	51.3	2.0	5.6	1.4	11.9	1.9	0.5	1.4	0.7	2553.3	28.7	2595.0	18.1	2628.4	22.7	2628.4	22.7
Spot 290	88197.9	113.8	1.2	5.6	1.1	12.3	1.9	0.5	1.5	0.8	2620.1	32.3	2628.7	17.5	2636.0	18.5	2636.0	18.5
Spot 171	55048.3	79.3	2.3	5.6	1.1	12.4	1.9	0.5	1.5	0.8	2628.4	32.7	2634.8	17.8	2640.5	18.9	2640.5	18.9
Spot 106	99210.6	126.1	0.5	5.6	1.1	11.9	1.7	0.5	1.3	0.8	2539.3	27.7	2597.6	16.1	2644.1	18.2	2644.1	18.2
Spot 254	######	441.3	0.6	5.5	1.1	11.9	1.7	0.5	1.2	0.7	2527.6	25.9	2597.8	15.8	2653.6	19.1	2653.6	19.1
Spot 42	60321.8	257.2	3.0	5.5	1.2	12.5	1.8	0.5	1.3	0.7	2619.4	28.4	2641.9	16.8	2659.9	19.9	2659.9	19.9
Spot 29	43566.7	84.3	2.4	5.5	1.3	12.6	1.9	0.5	1.3	0.7	2629.3	29.0	2647.2	17.6	2661.6	21.5	2661.6	21.5
Spot 107	######	167.8	2.2	5.5	1.1	12.9	1.7	0.5	1.4	0.8	2678.4	29.9	2671.3	16.3	2666.6	17.7	2666.6	17.7
Spot 239	87043.7	257.7	1.9	5.5	1.2	12.4	1.9	0.5	1.5	0.8	2579.5	31.3	2632.0	17.7	2673.3	19.4	2673.3	19.4
Spot 196	93596.4	200.8	1.1	5.4	1.3	13.1	2.1	0.5	1.7	0.8	2680.8	36.4	2683.9	19.7	2686.9	20.9	2686.9	20.9
Spot 123	######	130.6	2.2	5.4	1.2	13.2	1.8	0.5	1.3	0.8	2685.7	29.6	2691.3	16.8	2696.2	19.3	2696.2	19.3
Spot 264	54061.0	44.5	1.6	3.5	1.1	26.7	1.7	0.7	1.3	0.8	3350.9	33.4	3371.5	16.6	3384.5	17.4	3384.5	17.4
21-MANY-12																		
Spot 163	34169.8	259.5	5.1	16.2	2.6	0.9	3.3	0.1	1.5	0.5	633.2	9.2	634.0	15.4	637.8	62.2	633.2	9.2
Spot 206	15439.2	115.0	3.2	15.9	5.1	0.9	5.8	0.1	1.5	0.3	633.8	9.1	640.5	27.7	665.0	120.5	633.8	9.1
Spot 135	31542.9	303.8	4.2	16.2	2.2	0.9	3.0	0.1	2.0	0.7	634.7	12.1	635.0	14.2	637.0	48.1	634.7	12.1
Spot 34	26612.6	294.1	4.7	16.3	2.7	0.9	3.3	0.1	1.4	0.4	637.6	8.5	633.4	15.6	619.1	64.6	637.6	8.5
Spot 190	40827.9	292.6	6.1	16.1	2.5	0.9	3.0	0.1	1.6	0.5	638.2	9.9	640.3	14.2	648.7	54.0	638.2	9.9
Spot 2	15115.8	415.3	4.3	16.0	1.9	0.9	3.4	0.1	1.7	0.5	639.3	10.4	641.4	16.3	650.0	63.9	639.3	10.4
Spot 23	57327.8	373.4	3.3	16.1	1.9	0.9	2.4	0.1	1.5	0.6	639.7	9.4	643.2	11.6	656.3	40.8	639.7	9.4
Spot 200	45294.4	284.7	5.7	16.3	2.8	0.9	3.1	0.1	1.4	0.5	641.9	8.8	638.0	14.9	625.2	60.4	641.9	8.8
Spot 51	15474.0	140.0	2.3	15.9	4.1	0.9	4.7	0.1	1.8	0.4	646.1	11.0	648.4	22.4	657.3	92.5	646.1	11.0
Spot 61	32492.0	263.0	1.9	16.5	2.2	0.9	2.7	0.1	1.5	0.5	648.8	9.2	638.5	13.0	603.2	49.5	648.8	9.2
Spot 220	41810.8	359.9	4.7	16.3	1.8	0.9	2.4	0.1	1.3	0.6	650.4	8.2	645.2	11.2	628.2	42.0	650.4	8.2
Spot 214	46749.9	333.6	5.3	16.4	1.9	0.9	2.5	0.1	1.5	0.6	654.0	9.6	647.1	12.0	624.2	42.8	654.0	9.6
Spot 240	55596.5	323.7	5.6	16.3	2.2	0.9	2.7	0.1	1.6	0.6	654.4	9.9	652.4	13.2	646.3	47.8	654.4	9.9
Spot 257	95337.4	665.8	4.4	16.3	1.4	0.9	2.0	0.1	1.5	0.7	655.3	9.0	652.7	9.7	644.5	30.0	655.3	9.0
Spot 66	10186.0	210.8	2.8	15.7	3.0	0.9	4.1	0.1	1.6	0.4	659.6	10.1	663.6	20.2	678.1	81.4	659.6	10.1
Spot 196	18241.6	145.4	4.2	15.6	3.8	0.9	4.1	0.1	1.4	0.3	660.1	8.5	670.0	20.4	704.3	83.4	660.1	8.5
Spot 29	19302.4	129.0	4.7	16.0	3.7	0.9	4.6	0.1	1.7	0.4	660.6	10.6	657.2	22.2	646.5	91.8	660.6	10.6
Spot 13	27981.1	200.5	3.4	16.3	2.8	0.9	3.3	0.1	1.2	0.4	661.7	7.7	653.2	16.1	625.1	66.9	661.7	7.7
Spot 292	61074.4	621.0	1.6	16.0	1.3	0.9	1.9	0.1	1.3	0.7	669.1	8.4	670.4	9.3	675.5	28.7	669.1	8.4
Spot 64	68411.3	451.9	19.7	16.1	1.6	0.9	2.4	0.1	1.7	0.7	671.8	10.9	669.9	11.6	664.7	35.0	671.8	10.9
Spot 161	40398.3	338.8	10.5	15.8	2.1	0.9	2.6	0.1	1.5	0.6	673.7	9.6	677.4	12.9	690.7	45.3	673.7	9.6

Analysis	206Pb	U	U/Th	206Pb*	Â±2s	207Pb*	Â±2s	206Pb*	Â±2s	error	206Pb*	Â±2s	207Pb*	Â±2s	206Pb*	Â±2s	Best age	Â±2s
Spot 167	55474.1	498.4	4.5	16.0	1.5	1.0	2.1	0.1	1.3	0.7	682.6	8.7	679.0	10.2	668.0	33.3	682.6	8.7
Spot 176	25525.0	431.2	2.8	15.9	2.5	1.0	3.4	0.1	1.7	0.5	682.7	10.7	679.6	16.7	670.1	63.0	682.7	10.7
Spot 114	60987.6	410.6	1.9	15.9	1.8	1.0	2.5	0.1	1.6	0.6	683.4	10.3	685.0	12.3	691.2	40.3	683.4	10.3
Spot 74	65656.3	467.0	16.5	16.0	1.8	1.0	2.6	0.1	1.7	0.7	683.5	11.1	682.7	12.7	681.0	40.6	683.5	11.1
Spot 254	6185.9	604.6	1.8	15.2	1.6	1.0	2.6	0.1	1.8	0.7	686.7	12.0	694.5	13.1	720.8	39.3	686.7	12.0
Spot 104	28133.1	1373.1	4.1	15.7	1.3	1.0	2.7	0.1	2.2	0.8	687.5	14.4	690.3	13.3	700.2	31.2	687.5	14.4
Spot 309	60075.4	568.7	1.7	15.8	1.4	1.0	2.2	0.1	1.6	0.7	688.9	10.3	692.3	11.2	704.4	33.6	688.9	10.3
Spot 68	35987.4	257.6	1.5	15.7	2.6	1.0	3.2	0.1	1.4	0.4	690.3	9.0	696.1	16.0	715.7	60.9	690.3	9.0
Spot 146	91347.7	575.8	3.9	15.8	1.6	1.0	2.3	0.1	1.6	0.7	690.4	10.5	691.6	11.3	696.4	33.6	690.4	10.5
Spot 267	5790.5	631.4	3.4	15.2	1.3	1.0	3.7	0.1	1.2	0.3	691.5	8.0	698.3	18.7	721.2	74.1	691.5	8.0
Spot 116	69306.9	440.4	2.6	15.9	1.6	1.0	2.2	0.1	1.4	0.7	692.4	9.3	692.1	10.9	692.1	34.8	692.4	9.3
Spot 132	45167.0	336.9	1.4	15.8	1.9	1.0	2.6	0.1	1.8	0.7	693.4	11.7	694.5	13.3	699.0	41.4	693.4	11.7
Spot 180	9733.6	72.2	2.8	15.2	6.0	1.0	6.8	0.1	2.0	0.3	694.0	13.1	704.2	34.7	737.5	138.4	694.0	13.1
Spot 184	34340.6	281.6	2.4	15.8	1.9	1.0	2.4	0.1	1.4	0.6	695.1	9.4	694.3	12.1	692.6	41.4	695.1	9.4
Spot 28	7668.3	317.1	2.2	15.2	2.2	1.0	2.8	0.1	1.6	0.6	695.3	10.8	703.7	14.1	731.5	47.6	695.3	10.8
Spot 259	24047.8	411.5	2.3	15.9	1.7	1.0	2.8	0.1	1.4	0.5	695.3	9.4	692.3	14.3	683.4	52.6	695.3	9.4
Spot 35	61670.4	397.5	3.5	16.1	1.9	1.0	2.6	0.1	1.6	0.6	695.9	10.8	685.9	12.7	654.1	42.1	695.9	10.8
Spot 83	5946.0	55.9	2.9	14.3	8.4	1.1	8.9	0.1	2.0	0.2	697.4	13.0	736.5	46.8	858.3	181.0	697.4	13.0
Spot 10	######	621.1	1.9	15.9	2.2	1.0	3.1	0.1	2.2	0.7	698.1	14.8	696.7	15.7	693.1	46.3	698.1	14.8
Spot 16	29031.5	412.3	1.5	15.7	1.7	1.0	2.4	0.1	1.6	0.7	700.3	10.4	700.3	12.0	701.1	37.8	700.3	10.4
Spot 315	22003.9	362.1	1.2	15.7	1.6	1.0	2.5	0.1	1.3	0.5	700.6	8.5	701.0	12.7	703.4	45.8	700.6	8.5
Spot 90	88296.7	489.7	2.8	16.0	1.4	1.0	2.0	0.1	1.4	0.7	702.0	9.4	698.4	10.2	687.9	30.9	702.0	9.4
Spot 102	23613.3	175.4	2.6	15.4	3.1	1.0	3.6	0.1	1.6	0.4	703.0	10.4	710.9	18.6	737.0	69.5	703.0	10.4
Spot 140	32372.8	212.7	1.7	15.7	2.6	1.0	3.0	0.1	1.4	0.5	703.1	9.5	704.4	15.5	709.3	57.1	703.1	9.5
Spot 9	33986.1	258.3	3.0	15.8	2.8	1.0	3.6	0.1	2.2	0.6	704.0	14.5	701.0	18.3	692.5	61.4	704.0	14.5
Spot 141	12592.5	291.1	2.2	15.3	2.3	1.0	3.5	0.1	1.3	0.4	704.1	8.8	713.2	17.8	742.9	67.7	704.1	8.8
Spot 271	25019.1	762.7	2.3	15.7	1.7	1.0	2.4	0.1	1.7	0.7	706.0	11.2	704.9	12.1	702.6	35.9	706.0	11.2
Spot 79	90337.4	581.0	3.2	16.1	1.3	1.0	1.7	0.1	1.1	0.7	709.5	7.7	701.9	8.7	678.4	27.1	709.5	7.7
Spot 32	11462.8	104.4	2.3	15.7	4.4	1.0	5.4	0.1	1.8	0.3	711.1	12.4	703.4	27.3	680.0	108.1	711.1	12.4
Spot 283	28216.3	231.2	2.6	15.7	2.3	1.0	2.8	0.1	1.4	0.5	712.0	9.7	709.0	14.5	700.4	52.3	712.0	9.7
Spot 93	37019.9	266.3	2.3	15.9	2.5	1.0	3.1	0.1	1.5	0.5	712.4	9.8	706.8	15.9	690.1	59.1	712.4	9.8
Spot 105	48396.3	312.5	1.5	15.9	2.1	1.0	2.6	0.1	1.5	0.6	713.0	10.1	706.8	13.2	688.0	45.2	713.0	10.1
Spot 81	20112.2	504.9	2.6	15.6	1.3	1.0	2.6	0.1	1.2	0.5	721.0	8.3	721.5	13.6	723.8	49.2	721.0	8.3
Spot 134	82466.5	514.0	1.5	15.7	1.8	1.0	2.5	0.1	1.7	0.7	722.6	11.6	720.3	12.8	714.2	38.6	722.6	11.6
Spot 26	53212.6	331.8	0.9	15.7	1.9	1.0	2.5	0.1	1.6	0.6	723.6	10.8	720.3	12.7	711.0	40.2	723.6	10.8
Spot 52	41597.5	302.9	4.2	15.7	2.1	1.0	2.7	0.1	1.4	0.5	723.8	9.6	719.5	14.1	706.9	50.0	723.8	9.6
Spot 99	28755.8	208.9	2.8	15.9	2.8	1.0	3.3	0.1	1.2	0.4	724.6	8.5	714.5	16.9	683.8	65.2	724.6	8.5
Spot 210	44515.2	582.1	2.7	15.7	1.6	1.0	2.3	0.1	1.6	0.7	725.2	10.8	722.7	12.0	715.7	36.2	725.2	10.8
Spot 209	74305.5	476.1	2.7	15.9	1.7	1.0	2.3	0.1	1.5	0.6	725.3	10.0	715.6	12.0	686.4	38.9	725.3	10.0
Spot 275	40046.9	240.2	2.2	15.8	2.2	1.0	2.7	0.1	1.5	0.5	727.1	10.3	721.3	14.2	704.3	49.0	727.1	10.3
Spot 238	32582.6	340.3	2.5	15.8	1.8	1.0	2.4	0.1	1.5	0.6	728.8	10.3	723.8	12.3	709.2	39.0	728.8	10.3
Spot 203	######	882.1	1.9	15.7	1.4	1.0	3.2	0.1	2.9	0.9	730.3	19.9	725.5	16.8	711.7	31.6	730.3	19.9
Spot 260	60009.2	337.7	4.8	15.8	1.8	1.0	2.4	0.1	1.5	0.6	732.1	10.4	724.9	12.5	703.8	40.0	732.1	10.4
Spot 151	21541.5	158.8	3.3	15.4	3.2	1.1	3.7	0.1	1.7	0.5	732.8	11.6	736.3	19.3	747.7	69.2	732.8	11.6
Spot 188	29051.7	181.4	4.6	15.4	3.6	1.1	4.0	0.1	1.7	0.4	736.3	11.8	736.9	21.1	739.5	77.4	736.3	11.8
Spot 258	66976.3	594.2	3.9	15.6	1.5	1.1	2.2	0.1	1.4	0.7	738.1	10.0	739.1	11.4	742.8	34.7	738.1	10.0
Spot 25	85431.3	580.4	8.8	15.5	1.6	1.1	2.3	0.1	1.6	0.7	743.8	11.0	741.7	11.9	736.5	34.7	743.8	11.0
Spot 297	53143.7	317.8	3.0	15.6	2.1	1.1	2.8	0.1	1.8	0.6	747.7	12.7	740.7	14.8	720.5	46.1	747.7	12.7
Spot 177	20454.2	155.8	1.3	15.3	3.0	1.1	3.5	0.1	1.7	0.5	750.4	11.8	748.7	18.5	744.7	65.0	750.4	11.8
Spot 118	15008.7	79.0	3.0	15.4	6.0	1.1	6.3	0.1	1.6	0.3	753.7	11.4	747.6	33.4	730.4	129.5	753.7	11.4
Spot 266	7156.6	334.1	4.2	15.0	4.1	1.1	7.2	0.1	1.6	0.2	755.1	11.1	755.3	38.2	756.8	147.7	755.1	11.1
Spot 89	69468.8	407.5	5.7	15.4	1.9	1.1	2.5	0.1	1.5	0.6	755.4	10.4	756.5	13.2	760.7	42.1	755.4	10.4
Spot 48	21315.6	1250.1	24.9	15.4	1.3	1.1	2.1	0.1	1.4	0.7	759.9	10.4	754.3	11.0	738.9	31.5	759.9	10.4
Spot 164	48697.2	281.9	3.4	15.4	2.1	1.1	2.5	0.1	1.2	0.5	766.3	8.9	762.3	13.3	751.5	45.4	766.3	8.9
Spot 204	51357.0	300.4	3.0	15.6	1.9	1.1	2.5	0.1	1.6	0.6	768.0	11.7	756.7	13.5	724.3	41.1	768.0	11.7
Spot 75	33774.0	241.1	3.0	15.3	2.5	1.1	3.2	0.1	1.7	0.6	771.7	12.7	769.9	17.0	765.5	55.2	771.7	12.7
Spot 158	79468.0	596.1	2.6	15.2	1.4	1.1	2.1	0.1	1.5	0.7	775.0	10.6	775.9	11.2	779.4	30.7	775.0	10.6
Spot 250	######	757.4	4.3	15.5	1.3	1.1	1.8	0.1	1.3	0.7	775.3	9.3	769.3	9.8	752.9	27.2	775.3	9.3

Analysis	206Pb	U	U/Th	206Pb*	Â±2s	207Pb*	Â±2s	206Pb*	Â±2s	error	206Pb*	Â±2s	207Pb*	Â±2s	206Pb*	Â±2s	Best age	Â±2s
Spot 50	42185.2	345.4	1.7	15.3	1.6	1.2	2.2	0.1	1.4	0.6	787.7	10.3	779.9	11.7	758.5	34.8	787.7	10.3
Spot 252	8978.7	56.3	2.1	15.4	7.0	1.1	7.8	0.1	1.8	0.2	788.5	13.4	770.6	42.1	719.9	161.2	788.5	13.4
Spot 44	17432.9	403.7	2.7	14.9	2.0	1.2	2.7	0.1	1.7	0.6	792.8	13.0	796.2	14.8	806.4	42.9	792.8	13.0
Spot 137	37736.0	216.0	4.7	15.1	1.9	1.2	2.4	0.1	1.4	0.6	809.5	11.0	802.8	13.6	785.3	41.3	809.5	11.0
Spot 124	17347.0	129.1	1.9	14.9	3.7	1.2	4.2	0.1	1.6	0.4	813.6	12.4	811.5	23.3	806.8	80.5	813.6	12.4
Spot 231	19735.8	110.1	3.9	15.3	4.6	1.2	5.1	0.1	1.8	0.3	819.4	13.5	802.4	28.4	756.6	101.5	819.4	13.5
Spot 123	11210.3	83.8	2.1	14.9	5.3	1.3	5.7	0.1	1.7	0.3	844.0	13.2	830.4	32.3	795.1	114.1	844.0	13.2
Spot 205	80101.0	523.7	2.5	14.9	1.5	1.3	2.2	0.1	1.6	0.7	852.5	12.7	843.8	12.5	822.0	31.1	852.5	12.7
Spot 160	19510.0	108.0	1.6	14.4	3.9	1.4	4.7	0.1	2.2	0.5	870.8	18.2	874.6	27.7	884.9	86.0	870.8	18.2
Spot 284	11813.6	58.9	1.5	14.0	6.3	1.4	6.7	0.1	1.7	0.3	872.9	14.1	886.1	39.4	920.1	132.3	872.9	14.1
Spot 156	16696.2	94.1	1.9	14.6	3.9	1.4	4.5	0.1	1.6	0.4	878.0	13.2	868.6	26.0	845.8	86.4	878.0	13.2
Spot 178	21384.7	118.0	6.1	14.3	3.6	1.4	4.1	0.1	1.7	0.4	883.2	14.0	887.8	24.3	900.2	77.1	883.2	14.0
Spot 84	21496.1	104.1	0.4	14.3	3.6	1.5	4.2	0.2	1.5	0.4	933.3	12.8	923.8	25.4	902.0	80.7	902.0	80.7
Spot 59	13940.3	738.7	4.1	14.1	1.2	1.5	1.8	0.2	1.4	0.7	944.3	12.1	937.4	11.3	922.0	25.3	922.0	25.3
Spot 302	8817.0	43.5	3.4	13.9	8.1	1.6	8.3	0.2	1.5	0.2	980.3	13.4	962.2	51.9	922.2	169.0	922.2	169.0
Spot 229	44926.9	206.5	4.3	14.2	1.7	1.5	2.1	0.2	1.3	0.6	944.2	11.6	937.8	13.1	923.6	34.6	923.6	34.6
Spot 55	79500.1	562.5	3.2	14.2	1.2	1.5	1.9	0.2	1.5	0.8	956.3	13.2	946.9	11.9	926.0	25.7	926.0	25.7
Spot 143	54619.5	244.5	1.6	14.1	1.8	1.5	2.4	0.2	1.5	0.6	901.5	12.9	910.5	14.3	933.4	37.5	933.4	37.5
Spot 57	9708.9	180.7	2.7	13.9	1.9	1.5	2.5	0.2	1.3	0.5	925.1	10.8	928.1	15.2	936.0	44.4	936.0	44.4
Spot 303	45988.8	279.7	2.8	14.1	1.3	1.6	1.8	0.2	1.2	0.7	963.0	11.1	955.5	11.4	939.3	27.9	939.3	27.9
Spot 237	35820.8	184.3	1.6	14.1	1.9	1.6	2.5	0.2	1.4	0.6	968.5	12.8	960.0	15.5	941.4	42.2	941.4	42.2
Spot 43	37625.1	183.6	3.2	14.0	2.1	1.6	2.5	0.2	1.3	0.5	966.9	11.6	959.1	15.3	942.2	43.2	942.2	43.2
Spot 12	32713.7	132.6	1.0	14.0	2.7	1.6	3.2	0.2	1.4	0.4	980.2	12.7	969.6	20.1	946.5	59.5	946.5	59.5
Spot 311	5594.9	188.8	2.2	13.6	2.5	1.6	5.8	0.2	1.8	0.3	1006.3	16.8	988.5	36.5	950.0	112.3	950.0	112.3
Spot 36	25794.6	159.1	1.9	13.9	2.3	1.6	3.0	0.2	1.7	0.6	1002.9	15.7	986.3	18.6	950.3	49.6	950.3	49.6
Spot 111	56565.5	264.9	2.1	14.0	1.7	1.6	2.3	0.2	1.5	0.6	968.2	13.3	963.1	14.5	952.4	36.7	952.4	36.7
Spot 276	19552.5	90.2	2.6	13.9	3.6	1.7	4.1	0.2	1.6	0.4	1006.7	14.9	990.3	26.0	954.8	77.6	954.8	77.6
Spot 223	52896.5	274.9	3.2	14.0	2.2	1.6	2.7	0.2	1.5	0.5	953.2	12.9	953.6	16.5	955.4	45.8	955.4	45.8
Spot 313	71760.7	354.2	1.3	14.0	1.9	1.6	2.6	0.2	1.8	0.7	977.2	16.0	970.6	16.2	956.5	38.8	956.5	38.8
Spot 150	20740.2	93.9	1.2	13.9	3.4	1.6	4.1	0.2	1.9	0.5	988.0	17.2	978.1	26.0	956.8	75.2	956.8	75.2
Spot 183	35537.8	202.6	1.1	13.9	1.9	1.6	2.4	0.2	1.4	0.6	979.8	12.5	972.6	14.8	957.2	39.3	957.2	39.3
Spot 207	32764.3	179.9	2.4	13.9	1.9	1.6	2.6	0.2	1.4	0.5	996.8	12.9	984.5	16.3	958.1	44.4	958.1	44.4
Spot 298	11715.4	57.4	2.0	13.7	5.3	1.5	6.0	0.1	1.7	0.3	898.5	14.1	915.8	36.1	958.7	117.3	958.7	117.3
Spot 86	22971.4	108.1	1.4	13.9	2.7	1.6	3.4	0.2	1.4	0.4	990.6	12.9	981.8	21.4	963.1	63.4	963.1	63.4
Spot 1	39045.6	208.9	2.0	13.9	1.7	1.6	2.3	0.2	1.4	0.6	986.3	12.4	978.9	14.2	963.1	37.1	963.1	37.1
Spot 110	36649.4	159.6	1.3	13.9	2.3	1.6	2.8	0.2	1.6	0.5	985.6	14.2	978.7	17.8	964.1	48.4	964.1	48.4
Spot 130	23974.6	109.8	1.4	13.8	3.0	1.6	3.4	0.2	1.5	0.4	982.7	13.4	977.1	21.6	965.3	63.5	965.3	63.5
Spot 91	48423.5	260.7	1.3	13.9	1.6	1.7	2.1	0.2	1.3	0.6	1012.3	12.6	997.4	13.7	965.7	34.2	965.7	34.2
Spot 129	22385.1	107.4	1.4	13.8	3.3	1.6	3.8	0.2	1.6	0.4	971.9	14.5	969.8	23.7	965.9	70.2	965.9	70.2
Spot 6	84171.4	400.6	2.2	13.9	1.4	1.6	2.1	0.2	1.5	0.7	981.4	13.7	976.8	13.0	967.2	29.1	967.2	29.1
Spot 202	68358.2	365.2	2.0	13.9	1.5	1.6	2.2	0.2	1.6	0.7	977.6	14.2	974.4	14.1	968.3	32.8	968.3	32.8
Spot 296	80411.9	311.2	3.8	13.9	1.5	1.6	2.0	0.2	1.3	0.6	982.6	11.5	978.0	12.5	968.7	31.2	968.7	31.2
Spot 117	20632.7	94.0	1.0	13.8	3.6	1.6	4.1	0.2	1.7	0.4	957.3	15.4	961.1	25.7	970.5	76.6	970.5	76.6
Spot 194	48782.5	268.6	2.0	13.9	1.5	1.6	2.3	0.2	1.6	0.7	988.7	14.4	982.9	14.3	970.9	33.3	970.9	33.3
Spot 262	52842.5	228.8	2.1	13.9	2.0	1.7	2.5	0.2	1.3	0.5	1011.1	12.5	998.9	16.0	973.1	43.6	973.1	43.6
Spot 170	32261.1	170.3	2.0	13.8	2.1	1.6	2.7	0.2	1.5	0.6	993.8	13.7	987.4	16.9	974.0	45.4	974.0	45.4
Spot 108	51328.2	307.6	1.5	13.9	1.3	1.6	1.8	0.2	1.1	0.6	974.1	10.3	974.2	11.4	975.3	28.9	975.3	28.9
Spot 278	57772.5	261.4	1.4	13.9	1.5	1.7	2.2	0.2	1.5	0.7	1016.6	14.2	1003.8	14.3	976.8	33.9	976.8	33.9
Spot 269	80519.9	311.5	1.5	13.9	1.4	1.6	1.9	0.2	1.3	0.7	986.8	11.8	983.7	11.9	977.7	28.1	977.7	28.1
Spot 67	37074.3	367.9	2.7	13.8	1.5	1.6	2.3	0.2	1.4	0.6	972.7	13.1	974.2	14.5	978.4	36.9	978.4	36.9
Spot 100	37461.6	541.7	2.4	13.8	1.2	1.6	1.9	0.2	1.4	0.8	974.6	12.7	975.5	11.6	978.5	24.7	978.5	24.7
Spot 125	55976.2	355.2	3.5	13.8	1.6	1.6	2.4	0.2	1.8	0.7	980.9	16.3	979.9	15.3	978.6	33.8	978.6	33.8
Spot 282	10816.6	41.7	2.0	13.6	6.2	1.7	6.7	0.2	1.7	0.3	1002.4	16.1	994.7	42.7	978.8	132.7	978.8	132.7
Spot 47	50450.0	603.5	1.5	13.8	1.3	1.7	2.0	0.2	1.4	0.7	1005.1	13.4	996.6	12.7	978.9	28.2	978.9	28.2
Spot 42	70655.4	373.1	2.2	13.8	1.3	1.7	1.9	0.2	1.4	0.7	1000.4	12.6	993.8	12.0	979.9	27.0	979.9	27.0
Spot 211	58097.3	526.2	2.2	13.8	1.5	1.6	2.2	0.2	1.6	0.7	991.4	14.6	987.6	13.9	980.1	30.8	980.1	30.8
Spot 21	58225.1	380.2	1.8	13.8	1.3	1.6	2.0	0.2	1.4	0.7	979.0	13.1	979.2	12.5	980.5	27.7	980.5	27.7

Analysis	206Pb	U	U/Th	206Pb*	Â±2s	207Pb*	Â±2s	206Pb*	Â±2s	error	206Pb*	Â±2s	207Pb*	Â±2s	206Pb*	Â±2s	Best age	Â±2s
Spot 300	27954.0	185.7	1.9	13.7	2.2	1.6	2.8	0.2	1.6	0.6	967.6	14.5	971.8	17.7	982.3	47.4	982.3	47.4
Spot 246	25119.2	147.9	1.7	13.8	2.3	1.7	3.1	0.2	1.6	0.5	1001.5	14.5	995.5	19.7	983.3	54.6	983.3	54.6
Spot 112	33146.5	200.5	0.3	13.8	2.0	1.6	2.6	0.2	1.5	0.6	961.4	13.5	968.4	15.9	985.3	41.9	985.3	41.9
Spot 149	22314.7	193.5	0.6	13.7	2.0	1.5	2.8	0.2	1.8	0.6	930.9	15.3	946.9	17.0	985.3	43.3	985.3	43.3
Spot 208	39368.4	452.8	2.6	13.8	1.3	1.6	2.0	0.2	1.4	0.7	985.7	13.1	985.4	12.7	985.7	28.8	985.7	28.8
Spot 287	29726.8	161.2	2.4	13.7	2.1	1.6	2.5	0.2	1.3	0.5	963.6	11.8	970.3	15.4	986.2	42.5	986.2	42.5
Spot 233	38215.4	187.7	1.2	13.8	2.4	1.8	2.9	0.2	1.7	0.6	1048.4	16.4	1028.4	19.0	986.9	48.8	986.9	48.8
Spot 45	72455.1	376.5	2.8	13.8	1.8	1.7	2.6	0.2	1.7	0.7	1016.8	16.4	1007.2	16.3	987.4	37.9	987.4	37.9
Spot 179	69177.6	281.7	2.5	13.8	1.9	1.6	2.5	0.2	1.5	0.6	978.4	14.0	981.0	15.5	987.8	39.0	987.8	39.0
Spot 18	12928.4	73.6	1.5	13.6	4.7	1.6	5.3	0.2	1.4	0.3	976.4	12.7	979.8	33.2	988.3	103.5	988.3	103.5
Spot 142	43555.3	258.7	1.7	13.7	1.7	1.6	2.2	0.2	1.3	0.6	965.7	11.8	972.3	13.6	988.3	35.3	988.3	35.3
Spot 307	66325.3	324.4	3.2	13.7	1.3	1.7	2.1	0.2	1.6	0.7	991.9	14.3	990.6	13.4	988.8	29.3	988.8	29.3
Spot 175	7872.0	206.5	0.5	13.4	1.7	1.6	2.4	0.2	1.5	0.6	934.5	13.1	950.6	14.6	989.1	36.9	989.1	36.9
Spot 56	49522.7	228.3	1.2	13.8	1.9	1.7	2.4	0.2	1.4	0.6	993.4	12.6	992.0	15.2	989.8	40.3	989.8	40.3
Spot 293	49274.7	261.3	2.0	13.7	1.5	1.7	2.1	0.2	1.3	0.6	1005.9	12.3	1001.5	13.2	992.7	32.4	992.7	32.4
Spot 295	######	613.5	2.8	13.7	1.2	1.7	1.8	0.2	1.3	0.7	1006.5	12.2	1002.0	11.4	993.1	25.1	993.1	25.1
Spot 235	9494.6	666.4	1.2	13.5	1.1	1.7	1.7	0.2	1.2	0.7	990.3	11.2	991.7	10.9	995.7	24.9	995.7	24.9
Spot 98	23894.7	101.1	2.8	13.7	3.3	1.7	3.7	0.2	1.4	0.4	1008.5	13.2	1004.7	23.6	997.2	69.5	997.2	69.5
Spot 107	14734.9	217.2	1.2	13.6	1.7	1.6	2.1	0.2	1.2	0.6	965.0	10.9	974.8	13.4	997.8	35.7	997.8	35.7
Spot 249	52857.0	325.7	3.6	13.7	1.3	1.8	1.9	0.2	1.2	0.7	1053.5	12.0	1035.4	12.2	998.1	28.7	998.1	28.7
Spot 245	28715.4	123.2	2.5	13.7	2.5	1.7	3.1	0.2	1.4	0.5	1026.5	13.7	1018.0	20.0	1000.8	56.0	1000.8	56.0
Spot 17	29593.0	182.2	2.1	13.6	1.8	1.7	2.4	0.2	1.4	0.6	988.6	12.9	993.0	15.0	1003.6	38.7	1003.6	38.7
Spot 172	1125.0	88.9	2.2	11.6	7.2	1.4	23.7	0.1	1.9	0.1	858.6	15.5	901.3	141.8	1008.3	480.7	1008.3	480.7
Spot 174	66507.1	382.4	2.7	13.6	1.3	1.7	2.0	0.2	1.5	0.8	996.3	13.9	1000.0	12.7	1009.1	26.5	1009.1	26.5
Spot 182	15238.4	201.3	0.9	13.5	2.6	1.7	3.2	0.2	1.8	0.6	1012.6	16.5	1011.7	20.4	1010.6	53.9	1010.6	53.9
Spot 162	92371.6	471.9	1.9	13.6	1.4	1.7	2.1	0.2	1.5	0.7	1012.3	14.5	1012.4	13.5	1013.4	28.9	1013.4	28.9
Spot 219	28377.4	104.6	3.7	13.5	3.0	1.8	3.4	0.2	1.5	0.4	1052.2	14.4	1041.4	22.3	1019.7	62.5	1019.7	62.5
Spot 312	28788.6	139.4	1.9	13.5	2.7	1.8	3.3	0.2	1.9	0.6	1033.1	17.9	1030.0	21.5	1024.3	55.7	1024.3	55.7
Spot 22	41481.8	223.2	1.5	13.5	1.7	1.7	2.2	0.2	1.3	0.6	1024.1	12.4	1025.0	14.0	1027.6	34.9	1027.6	34.9
Spot 103	65208.2	295.1	1.9	13.5	1.6	1.8	2.2	0.2	1.4	0.7	1034.7	13.4	1033.6	14.0	1031.9	33.1	1031.9	33.1
Spot 256	8160.7	39.5	2.4	13.3	9.1	1.5	9.5	0.1	1.8	0.2	892.1	15.0	933.0	58.1	1031.9	189.0	1031.9	189.0
Spot 4	60977.0	296.7	1.3	13.5	1.4	1.8	2.1	0.2	1.5	0.7	1064.6	14.2	1053.9	13.7	1032.6	30.5	1032.6	30.5
Spot 153	23143.5	92.4	0.7	13.4	4.0	1.8	4.7	0.2	2.0	0.4	1052.6	19.8	1046.2	30.9	1033.8	86.2	1033.8	86.2
Spot 87	26303.7	130.3	2.8	13.4	2.8	1.7	3.3	0.2	1.6	0.5	986.4	14.2	1001.4	20.9	1035.3	58.5	1035.3	58.5
Spot 65	9433.6	42.6	2.1	13.2	6.6	1.6	7.2	0.2	1.8	0.2	947.9	15.6	977.0	44.9	1044.0	139.9	1044.0	139.9
Spot 217	17606.9	119.5	1.5	13.3	2.9	1.8	4.2	0.2	2.6	0.6	1046.7	25.0	1046.9	27.4	1048.1	66.6	1048.1	66.6
Spot 120	51320.7	245.1	3.0	13.3	1.5	1.8	2.1	0.2	1.4	0.7	1034.9	13.8	1039.6	13.5	1050.5	30.2	1050.5	30.2
Spot 308	23190.9	303.3	0.7	13.3	1.6	1.8	2.6	0.2	1.8	0.7	1045.2	17.0	1047.3	17.3	1052.5	39.9	1052.5	39.9
Spot 216	2370.0	85.2	3.4	12.4	2.8	1.8	3.4	0.2	1.4	0.4	1047.4	13.3	1049.1	22.0	1053.7	61.7	1053.7	61.7
Spot 148	56913.2	206.9	1.8	13.3	1.9	1.8	2.4	0.2	1.5	0.6	1041.3	14.4	1045.7	15.9	1055.8	38.8	1055.8	38.8
Spot 247	55800.0	287.3	1.8	13.4	1.7	1.9	2.4	0.2	1.6	0.7	1093.2	16.5	1080.5	16.0	1055.9	35.7	1055.9	35.7
Spot 281	21673.5	105.4	2.0	13.2	2.9	1.9	3.5	0.2	1.6	0.5	1073.4	16.1	1068.3	23.3	1058.9	62.9	1058.9	62.9
Spot 192	9513.4	348.7	1.0	13.1	1.4	1.7	4.7	0.2	2.3	0.5	987.9	21.2	1010.0	29.8	1059.1	81.5	1059.1	81.5
Spot 101	9911.1	339.1	1.3	13.1	1.5	1.7	2.2	0.2	1.4	0.6	1011.4	13.0	1027.0	14.3	1061.4	34.6	1061.4	34.6
Spot 39	39428.5	176.1	1.5	13.2	2.6	2.0	3.6	0.2	2.4	0.7	1124.7	24.9	1103.0	24.2	1061.4	53.5	1061.4	53.5
Spot 85	22640.1	111.3	2.5	13.3	2.7	1.9	3.5	0.2	1.6	0.5	1068.9	15.6	1066.8	22.9	1063.3	62.1	1063.3	62.1
Spot 305	18704.5	96.7	1.1	13.2	2.8	1.8	3.6	0.2	1.5	0.4	1039.1	14.5	1046.9	23.8	1064.2	66.8	1064.2	66.8
Spot 15	24479.4	115.6	0.9	13.2	1.9	2.0	2.6	0.2	1.2	0.5	1116.7	12.7	1099.3	17.6	1065.8	46.4	1065.8	46.4
Spot 78	34122.0	124.0	4.0	13.2	2.2	2.0	2.8	0.2	1.5	0.5	1153.1	15.4	1124.3	19.0	1070.0	47.9	1070.0	47.9
Spot 310	8414.5	47.4	1.8	12.9	4.8	1.9	5.5	0.2	1.7	0.3	1069.7	17.0	1070.6	36.5	1073.2	105.4	1073.2	105.4
Spot 46	16110.5	84.2	0.6	13.0	3.3	2.0	4.1	0.2	1.5	0.4	1114.9	14.9	1101.6	27.9	1076.4	77.9	1076.4	77.9
Spot 268	37844.3	369.3	10.5	13.2	1.2	2.0	1.8	0.2	1.2	0.7	1135.0	12.3	1116.1	12.0	1080.2	26.6	1080.2	26.6
Spot 154	11305.4	227.3	1.4	13.0	2.0	1.8	3.4	0.2	1.5	0.4	1047.1	14.3	1057.7	22.2	1080.4	60.8	1080.4	60.8
Spot 274	######	361.2	2.5	13.2	1.5	2.0	2.2	0.2	1.6	0.7	1107.7	16.5	1101.0	15.1	1088.7	31.1	1088.7	31.1
Spot 82	32471.1	150.4	4.0	13.1	2.0	2.0	2.7	0.2	1.7	0.6	1105.0	17.2	1101.3	18.1	1094.7	41.8	1094.7	41.8
Spot 171	38904.0	164.6	1.5	13.0	2.1	1.9	2.8	0.2	1.7	0.6	1064.8	16.2	1076.1	18.5	1099.8	45.1	1099.8	45.1
Spot 127	22229.7	117.4	1.6	12.9	2.2	2.0	3.0	0.2	1.6	0.5	1122.4	16.7	1114.9	20.2	1101.1	50.2	1101.1	50.2
Spot 95	42970.6	322.5	2.0	13.0	1.3	2.0	1.8	0.2	1.1	0.6	1106.0	11.6	1107.6	12.0	1111.6	27.2	1111.6	27.2

Analysis	206Pb	U	U/Th	206Pb*	Â±2s	207Pb*	Â±2s	206Pb*	Â±2s	error	206Pb*	Â±2s	207Pb*	Â±2s	206Pb*	Â±2s	Best age	Â±2s
Spot 248	22121.6	81.0	3.3	12.3	2.9	2.3	3.3	0.2	1.5	0.4	1201.5	16.0	1202.0	23.0	1203.6	57.7	1203.6	57.7
Spot 187	55374.9	207.3	62.4	12.2	1.9	2.4	2.5	0.2	1.6	0.6	1236.9	18.3	1233.3	18.0	1228.0	37.9	1228.0	37.9
Spot 30	35561.8	165.6	2.3	12.2	1.9	2.3	2.4	0.2	1.6	0.6	1200.8	17.1	1210.9	17.2	1229.8	36.7	1229.8	36.7
Spot 289	55333.7	224.9	0.4	12.1	1.4	2.4	2.1	0.2	1.5	0.7	1258.1	17.2	1252.6	15.1	1244.1	28.6	1244.1	28.6
Spot 290	79869.6	333.4	10.1	12.1	1.5	2.4	2.3	0.2	1.7	0.8	1247.2	19.6	1247.3	16.3	1248.3	29.0	1248.3	29.0
Spot 72	18912.1	227.4	1.8	11.9	1.7	2.7	3.3	0.2	2.4	0.7	1353.3	29.8	1325.9	24.1	1282.6	42.1	1282.6	42.1
Spot 139	52819.1	258.7	1.5	11.8	1.5	2.5	2.1	0.2	1.4	0.7	1283.5	16.7	1283.7	15.4	1284.8	30.1	1284.8	30.1
Spot 185	58446.1	265.3	2.8	11.5	1.4	2.7	2.1	0.2	1.6	0.8	1338.3	18.9	1336.9	15.4	1335.4	26.4	1335.4	26.4
Spot 20	34107.2	107.2	1.7	11.4	2.0	2.9	2.5	0.2	1.4	0.6	1376.2	17.2	1369.4	18.7	1359.6	39.9	1359.6	39.9
Spot 138	61982.6	228.4	3.3	11.3	1.5	2.9	2.3	0.2	1.8	0.8	1370.8	22.1	1369.9	17.6	1369.3	29.1	1369.3	29.1
Spot 232	######	440.4	2.1	11.3	1.6	3.0	2.4	0.2	1.7	0.7	1418.2	22.3	1407.4	18.2	1391.8	31.4	1391.8	31.4
Spot 221	33274.3	102.5	2.0	11.2	2.2	3.0	2.7	0.2	1.5	0.6	1426.6	19.0	1413.4	20.4	1394.4	42.7	1394.4	42.7
Spot 58	22220.6	51.0	1.3	11.1	2.8	3.2	3.3	0.3	1.7	0.5	1488.7	22.2	1455.4	25.6	1407.8	54.9	1407.8	54.9
Spot 270	6594.8	22.5	0.4	10.9	6.6	3.2	7.1	0.3	1.7	0.2	1467.9	22.5	1448.3	54.7	1420.5	131.4	1420.5	131.4
Spot 314	35655.8	103.2	0.8	10.9	1.8	3.2	2.3	0.3	1.4	0.6	1460.5	18.5	1454.0	17.6	1445.4	34.1	1445.4	34.1
Spot 241	15382.6	48.5	3.5	10.9	3.1	3.1	3.5	0.3	1.7	0.5	1443.9	21.6	1444.7	27.2	1446.5	59.2	1446.5	59.2
Spot 54	20687.9	69.5	1.7	10.6	2.2	3.3	2.6	0.3	1.3	0.5	1482.1	16.8	1484.8	20.6	1489.6	43.8	1489.6	43.8
Spot 198	######	350.8	95.1	10.3	1.2	3.7	1.9	0.3	1.5	0.8	1579.2	20.5	1570.8	15.3	1560.4	23.0	1560.4	23.0
Spot 285	68283.3	202.2	3.5	10.1	1.4	3.9	2.0	0.3	1.4	0.7	1610.4	20.5	1603.7	16.3	1595.7	26.6	1595.7	26.6
Spot 261	1979.5	8.7	3.3	9.2	15.2	3.3	17.3	0.2	4.6	0.3	1352.1	56.6	1472.2	134.6	1650.8	309.3	1650.8	309.3
Spot 288	54168.5	153.8	1.7	9.3	1.4	4.7	2.0	0.3	1.5	0.7	1770.1	23.2	1759.7	17.0	1748.0	25.3	1748.0	25.3
Spot 33	######	359.8	3.3	9.2	1.3	4.7	2.2	0.3	1.7	0.8	1779.5	27.0	1769.9	18.3	1759.3	24.1	1759.3	24.1
Spot 242	43102.0	131.7	1.3	9.2	1.3	4.9	1.9	0.3	1.3	0.7	1818.7	21.3	1800.6	16.1	1780.5	24.8	1780.5	24.8
Spot 152	######	294.0	1.9	9.1	1.3	4.9	2.0	0.3	1.4	0.7	1813.6	22.9	1805.7	16.7	1797.3	24.5	1797.3	24.5
Spot 280	52179.9	147.6	1.7	9.0	1.5	5.0	2.1	0.3	1.5	0.7	1826.4	23.4	1814.8	17.9	1802.3	27.6	1802.3	27.6
Spot 71	52871.0	152.0	0.5	9.0	1.3	5.1	1.9	0.3	1.4	0.7	1840.3	21.9	1828.0	16.3	1814.8	24.4	1814.8	24.4
Spot 62	21171.2	145.1	0.8	8.9	1.3	4.9	2.2	0.3	1.7	0.8	1777.8	25.7	1799.1	18.3	1824.6	25.4	1824.6	25.4
Spot 49	34240.6	70.4	1.0	8.8	1.9	5.3	2.5	0.3	1.5	0.6	1899.7	25.0	1874.7	21.0	1848.0	34.8	1848.0	34.8
Spot 31	######	330.1	1.2	8.8	1.3	5.1	1.9	0.3	1.4	0.7	1836.1	22.2	1841.9	16.3	1849.3	23.8	1849.3	23.8
Spot 109	10912.6	90.7	1.2	8.7	1.4	5.1	2.3	0.3	1.4	0.6	1824.7	22.3	1837.3	19.6	1852.5	33.2	1852.5	33.2
Spot 14	90164.5	260.9	0.8	8.8	1.1	5.2	1.7	0.3	1.3	0.8	1855.3	20.8	1856.1	14.3	1857.8	19.2	1857.8	19.2
Spot 193	29430.9	82.2	1.3	8.7	1.7	5.2	2.5	0.3	1.6	0.7	1848.8	26.5	1852.9	21.0	1858.4	33.1	1858.4	33.1
Spot 169	60357.8	278.8	0.8	8.7	1.1	5.4	1.8	0.3	1.4	0.8	1917.3	23.8	1891.7	15.8	1864.5	21.0	1864.5	21.0
Spot 5	65387.6	171.2	1.1	8.7	1.3	5.4	2.0	0.3	1.5	0.7	1909.2	24.6	1888.3	17.2	1866.3	24.3	1866.3	24.3
Spot 225	14770.6	41.6	1.4	8.7	2.6	5.5	3.3	0.3	1.5	0.5	1927.9	25.6	1898.4	28.2	1867.0	52.2	1867.0	52.2
Spot 201	27077.2	64.2	1.1	8.7	2.0	5.5	2.5	0.3	1.4	0.6	1927.1	23.8	1898.1	21.4	1867.3	36.9	1867.3	36.9
Spot 24	91530.0	203.7	0.8	8.7	1.4	5.3	2.0	0.3	1.5	0.7	1874.1	23.9	1871.0	17.4	1868.3	25.3	1868.3	25.3
Spot 181	66917.4	169.0	1.2	8.7	1.5	5.3	2.2	0.3	1.7	0.7	1865.7	26.9	1867.3	19.0	1869.8	26.7	1869.8	26.7
Spot 186	10832.5	87.5	0.6	8.6	1.8	5.2	2.7	0.3	1.6	0.6	1831.9	25.8	1850.3	23.4	1871.7	40.0	1871.7	40.0
Spot 286	62433.6	164.3	1.0	8.7	1.2	5.4	1.7	0.3	1.2	0.7	1892.4	20.0	1883.2	14.5	1873.9	21.3	1873.9	21.3
Spot 273	41664.0	91.8	1.0	8.7	1.9	5.4	2.6	0.3	1.7	0.7	1886.4	28.3	1882.1	22.3	1878.2	35.1	1878.2	35.1
Spot 96	80015.7	181.7	1.2	8.7	1.3	5.4	1.8	0.3	1.3	0.7	1883.1	20.5	1880.6	15.5	1878.7	23.5	1878.7	23.5
Spot 239	######	359.2	1.5	8.7	1.2	5.5	1.8	0.3	1.3	0.7	1931.6	21.6	1906.4	15.4	1879.9	22.3	1879.9	22.3
Spot 155	######	345.5	2.1	8.6	1.3	5.3	1.9	0.3	1.5	0.8	1865.6	23.8	1872.3	16.6	1880.5	22.8	1880.5	22.8
Spot 121	20263.0	55.4	0.7	8.6	1.6	5.5	2.4	0.3	1.6	0.6	1925.2	26.2	1903.7	20.9	1881.1	33.3	1881.1	33.3
Spot 7	######	500.7	1.9	8.6	1.2	5.3	2.0	0.3	1.6	0.8	1860.9	25.5	1871.1	17.1	1883.2	22.2	1883.2	22.2
Spot 230	10295.8	293.3	1.5	8.6	1.3	5.2	2.9	0.3	2.5	0.9	1835.1	39.9	1857.9	24.8	1884.3	26.9	1884.3	26.9
Spot 136	19041.0	208.9	0.8	8.6	1.3	5.2	2.0	0.3	1.5	0.7	1811.2	23.2	1845.4	16.9	1885.0	24.2	1885.0	24.2
Spot 279	60388.3	153.3	1.2	8.6	1.4	5.4	2.0	0.3	1.4	0.7	1877.2	23.5	1881.3	17.3	1886.6	25.4	1886.6	25.4
Spot 122	15112.7	36.4	1.1	8.6	2.6	5.5	3.4	0.3	1.6	0.5	1909.0	26.2	1898.1	28.8	1887.0	53.3	1887.0	53.3
Spot 70	63546.5	152.5	1.3	8.6	1.4	5.6	2.0	0.3	1.5	0.7	1925.4	24.5	1908.4	17.3	1890.7	24.5	1890.7	24.5
Spot 243	######	359.7	2.6	8.6	1.1	5.6	1.7	0.3	1.3	0.8	1928.7	21.8	1910.2	15.0	1890.9	20.6	1890.9	20.6
Spot 157	97374.4	291.1	2.4	8.6	1.3	5.4	1.9	0.3	1.4	0.7	1888.4	23.5	1889.9	16.7	1892.3	23.5	1892.3	23.5
Spot 226	33020.0	88.8	0.9	8.6	1.6	5.6	2.3	0.4	1.5	0.7	1940.6	25.7	1918.5	19.4	1895.4	29.7	1895.4	29.7
Spot 19	86914.1	415.5	2.6	8.6	1.2	5.5	1.9	0.3	1.4	0.8	1906.3	23.5	1900.7	16.2	1895.4	22.2	1895.4	22.2
Spot 244	71221.3	200.2	2.1	8.6	1.2	5.7	1.7	0.4	1.2	0.7	1966.6	20.5	1932.5	14.6	1896.8	21.3	1896.8	21.3
Spot 264	20254.4	47.2	1.5	8.6	2.0	5.6	2.6	0.3	1.6	0.6	1934.3	26.0	1916.1	22.2	1897.3	36.8	1897.3	36.8
Spot 8	70899.4	152.8	1.9	8.6	2.1	5.6	3.0	0.4	2.2	0.7	1944.5	36.2	1921.9	25.8	1898.4	37.4	1898.4	37.4

Analysis	206Pb	U	U/Th	206Pb*	Â±2s	207Pb*	Â±2s	206Pb*	Â±2s	error	206Pb*	Â±2s	207Pb*	Â±2s	206Pb*	Â±2s	Best age	Â±2s
Spot 119	67659.6	169.0	1.8	8.2	1.1	6.1	1.7	0.4	1.3	0.7	2005.5	21.7	1988.0	14.8	1970.6	20.2	1970.6	20.2
Spot 213	77163.1	131.5	2.7	8.2	1.4	6.1	2.0	0.4	1.5	0.7	2013.6	25.9	1992.2	17.9	1970.8	24.9	1970.8	24.9
Spot 40	######	353.1	2.4	8.2	2.2	6.0	3.2	0.4	2.3	0.7	1992.6	39.8	1982.3	27.8	1972.3	38.9	1972.3	38.9
Spot 306	71857.4	196.7	1.1	8.2	1.2	6.0	1.9	0.4	1.5	0.8	1975.4	26.1	1974.3	16.8	1973.9	20.9	1973.9	20.9
Spot 294	51554.3	105.8	1.4	8.2	1.5	6.1	2.1	0.4	1.5	0.7	2002.8	25.1	1988.3	18.5	1974.0	27.4	1974.0	27.4
Spot 147	75733.4	172.2	2.2	8.2	1.3	5.9	1.9	0.4	1.4	0.7	1954.5	23.0	1963.9	16.7	1974.6	24.0	1974.6	24.0
Spot 27	85653.1	179.6	1.2	8.2	1.4	6.0	2.2	0.4	1.7	0.8	1970.5	29.2	1973.1	19.3	1976.5	24.9	1976.5	24.9
Spot 37	######	387.4	5.5	8.2	2.2	6.1	3.2	0.4	2.4	0.7	1993.0	41.3	1985.1	28.3	1977.6	38.8	1977.6	38.8
Spot 236	79159.8	196.9	2.4	8.2	1.3	6.1	1.9	0.4	1.5	0.8	2005.6	25.3	1991.6	17.0	1977.8	22.8	1977.8	22.8
Spot 165	76818.3	151.0	2.0	8.2	1.2	6.0	1.8	0.4	1.3	0.7	1981.0	22.3	1979.1	15.4	1977.9	21.3	1977.9	21.3
Spot 199	######	382.1	3.0	8.2	1.2	6.0	1.8	0.4	1.4	0.8	1986.1	23.7	1982.1	15.9	1978.6	21.1	1978.6	21.1
Spot 53	86238.2	256.4	2.2	8.2	1.2	6.2	1.8	0.4	1.3	0.7	2020.4	23.0	1999.6	15.5	1979.0	21.1	1979.0	21.1
Spot 159	53569.1	145.3	2.0	8.2	1.4	6.1	2.0	0.4	1.5	0.7	1986.2	24.9	1983.5	17.6	1981.4	24.9	1981.4	24.9
Spot 224	######	276.7	3.3	8.2	1.2	6.1	1.9	0.4	1.5	0.8	1997.7	25.4	1990.2	16.9	1983.1	22.2	1983.1	22.2
Spot 88	55351.7	99.1	1.2	8.1	1.4	6.1	2.2	0.4	1.6	0.8	1997.5	28.1	1995.7	19.0	1994.6	25.3	1994.6	25.3
Spot 299	######	584.5	1.1	8.1	1.4	6.0	2.1	0.4	1.6	0.8	1955.5	27.1	1975.3	18.5	1996.9	24.9	1996.9	24.9
Spot 291	27359.7	114.7	1.6	8.1	1.5	6.1	2.3	0.4	1.6	0.7	1978.8	28.1	1988.0	19.9	1998.3	27.9	1998.3	27.9
Spot 222	13357.8	323.7	1.6	7.9	1.4	6.2	2.0	0.4	1.4	0.7	1982.4	24.0	2009.2	17.3	2037.6	24.5	2037.6	24.5
Spot 263	######	335.8	10.1	7.9	1.2	6.8	1.8	0.4	1.3	0.7	2109.9	23.0	2080.3	15.5	2051.9	21.3	2051.9	21.3
Spot 113	70583.7	215.6	2.8	7.8	1.4	6.5	2.2	0.4	1.7	0.8	2016.5	29.8	2042.0	19.5	2068.5	24.5	2068.5	24.5
Spot 128	81712.4	149.6	2.4	7.7	1.3	6.7	2.3	0.4	1.9	0.8	2063.1	33.6	2067.6	20.6	2072.9	23.7	2072.9	23.7
Spot 73	74109.5	147.0	1.5	7.8	1.5	7.0	2.4	0.4	1.8	0.8	2133.9	32.2	2106.6	20.9	2080.7	27.3	2080.7	27.3
Spot 251	89216.7	192.9	0.5	7.7	1.2	7.0	1.9	0.4	1.4	0.8	2132.9	25.9	2108.5	16.5	2085.6	20.9	2085.6	20.9
Spot 41	######	304.4	8.6	7.6	1.2	7.0	2.1	0.4	1.7	0.8	2135.2	31.6	2117.6	18.8	2101.3	21.1	2101.3	21.1
Spot 191	80965.1	116.1	2.3	7.6	1.3	7.0	2.0	0.4	1.5	0.7	2107.2	26.4	2111.2	17.5	2115.8	23.0	2115.8	23.0
Spot 106	20883.5	456.9	3.9	6.8	1.3	8.2	2.8	0.4	2.4	0.9	2213.0	45.4	2255.7	25.1	2295.3	23.0	2295.3	23.0
Spot 173	29257.7	175.2	1.3	5.8	1.2	10.3	3.1	0.4	2.8	0.9	2354.5	55.0	2463.7	28.3	2555.7	20.7	2555.7	20.7
Spot 92	88151.2	332.2	2.2	5.7	1.2	11.0	2.5	0.5	2.2	0.9	2440.2	44.9	2525.2	23.4	2594.9	20.1	2594.9	20.1
Spot 215	83036.0	134.7	1.5	5.3	1.3	13.9	1.9	0.5	1.4	0.7	2756.0	31.9	2743.9	18.3	2735.8	21.6	2735.8	21.6
Spot 115	57201.4	217.0	1.6	5.1	1.3	14.5	2.1	0.5	1.6	0.8	2771.4	35.3	2782.7	19.6	2791.6	22.0	2791.6	22.0
Spot 197	73000.6	119.7	1.4	5.0	1.2	15.0	1.9	0.5	1.4	0.8	2804.3	32.2	2816.1	17.8	2825.2	20.0	2825.2	20.0
Spot 97	73410.0	115.9	2.4	5.0	1.2	14.6	1.7	0.5	1.3	0.7	2735.0	28.2	2788.9	16.6	2828.9	19.7	2828.9	19.7
Spot 304	16281.3	27.6	2.7	4.9	1.5	15.1	2.3	0.5	1.8	0.8	2801.2	40.3	2823.3	22.3	2839.8	24.9	2839.8	24.9
Spot 227	######	158.7	1.2	4.6	1.4	16.3	2.2	0.6	1.7	0.8	2827.8	39.6	2896.5	21.4	2945.4	23.0	2945.4	23.0
21-MANY-15																		
Spot 81	15064.7	370.5	2.9	16.1	2.2	0.8	3.9	0.1	1.6	0.4	616.7	9.2	621.0	18.1	637.4	76.7	616.7	9.2
Spot 5	28189.1	282.6	4.0	16.2	2.5	0.8	3.4	0.1	2.0	0.6	617.2	11.9	621.0	15.8	635.7	58.9	617.2	11.9
Spot 161	21386.3	188.0	1.7	15.8	2.9	0.9	4.0	0.1	2.2	0.6	635.6	13.3	647.0	19.1	687.9	70.8	635.6	13.3
Spot 177	36777.0	297.8	3.0	16.1	2.2	0.9	3.0	0.1	2.1	0.7	642.4	12.7	643.8	14.4	649.5	46.8	642.4	12.7
Spot 245	19404.6	145.1	2.7	15.9	3.9	0.9	5.0	0.1	2.1	0.4	651.7	13.1	655.2	24.2	668.3	97.2	651.7	13.1
Spot 203	46624.0	265.6	1.9	16.3	2.3	0.9	3.4	0.1	2.3	0.7	652.0	14.5	646.4	16.0	628.1	51.6	652.0	14.5
Spot 170	6263.2	132.4	1.8	15.0	3.8	0.9	4.7	0.1	1.9	0.4	652.9	11.9	672.5	23.2	739.8	91.4	652.9	11.9
Spot 3	3931.3	204.2	3.9	14.8	2.5	0.9	3.3	0.1	2.1	0.6	655.1	13.3	671.6	16.3	728.5	53.7	655.1	13.3
Spot 254	10603.6	383.6	4.7	15.4	2.2	0.9	3.5	0.1	2.6	0.7	659.0	16.0	670.8	17.1	711.5	50.0	659.0	16.0
Spot 236	28993.0	253.6	2.9	16.2	2.1	0.9	3.0	0.1	1.9	0.6	660.2	11.8	656.7	14.7	645.4	51.7	660.2	11.8
Spot 237	19185.8	142.5	9.8	15.7	4.0	0.9	4.6	0.1	1.8	0.4	664.5	11.1	673.3	22.4	703.9	89.5	664.5	11.1
Spot 31	20317.1	166.0	9.3	16.0	3.8	0.9	4.5	0.1	1.8	0.4	664.6	11.5	664.0	21.7	663.0	87.2	664.6	11.5
Spot 50	10795.4	87.2	3.5	15.7	4.8	0.9	5.9	0.1	2.0	0.3	665.0	12.4	668.6	29.0	681.5	119.5	665.0	12.4
Spot 122	18979.9	154.8	1.7	15.9	3.5	0.9	4.6	0.1	2.2	0.5	666.4	13.8	666.6	22.3	668.0	85.9	666.4	13.8
Spot 82	46914.7	431.8	3.2	16.0	1.7	0.9	2.3	0.1	1.5	0.7	666.8	9.8	666.1	11.4	664.4	37.7	666.8	9.8
Spot 69	14569.1	112.7	2.2	16.3	4.6	0.9	5.2	0.1	2.0	0.4	667.1	12.8	654.2	25.0	611.0	103.4	667.1	12.8
Spot 125	48879.2	394.8	4.9	15.8	2.1	0.9	3.0	0.1	2.0	0.7	667.7	13.0	674.3	14.6	697.6	45.7	667.7	13.0
Spot 213	12536.7	657.1	2.5	15.5	1.3	1.0	2.4	0.1	2.0	0.8	669.7	12.9	679.4	12.1	712.8	28.6	669.7	12.9
Spot 32	20496.9	123.9	3.2	16.2	4.6	0.9	5.2	0.1	2.2	0.4	669.7	13.8	660.3	25.2	629.2	101.8	669.7	13.8
Spot 240	44122.8	353.8	2.7	15.9	1.4	0.9	2.3	0.1	1.8	0.8	669.8	11.4	672.3	11.3	681.3	30.7	669.8	11.4
Spot 24	7586.1	65.4	1.6	15.2	6.7	1.0	7.5	0.1	2.2	0.3	670.0	14.1	684.7	37.4	734.0	152.0	670.0	14.1
Spot 173	27880.1	237.3	8.6	15.8	2.5	0.9	3.0	0.1	1.7	0.6	670.1	10.9	675.0	15.0	692.2	53.7	670.1	10.9
Spot 227	20276.4	182.5	4.1	15.7	3.0	0.9	3.9	0.1	2.2	0.6	670.1	13.8	675.5	19.3	694.5	69.3	670.1	13.8

Analysis	206Pb	U	U/Th	206Pb*	Â±2s	207Pb*	Â±2s	206Pb*	Â±2s	error	206Pb*	Â±2s	207Pb*	Â±2s	206Pb*	Â±2s	Best age	Â±2s
Spot 139	7578.9	199.5	1.9	15.4	2.5	1.0	4.6	0.1	1.9	0.4	673.7	12.2	680.9	22.9	705.5	89.6	673.7	12.2
Spot 273	8406.7	55.3	2.1	15.3	7.5	1.0	8.1	0.1	2.0	0.2	674.3	12.8	685.2	40.6	722.0	167.6	674.3	12.8
Spot 216	6438.8	254.1	2.4	15.3	2.2	1.0	5.9	0.1	2.0	0.3	675.1	13.0	682.5	29.6	707.7	119.0	675.1	13.0
Spot 271	25200.3	170.3	3.0	16.0	3.1	0.9	3.7	0.1	1.9	0.5	675.4	12.3	672.9	18.2	665.5	67.9	675.4	12.3
Spot 283	15817.4	144.6	1.5	15.7	3.7	1.0	5.1	0.1	2.0	0.4	675.6	12.8	683.0	25.5	708.1	100.4	675.6	12.8
Spot 147	32624.8	262.2	2.6	16.0	2.2	0.9	2.9	0.1	1.8	0.6	675.9	11.4	672.8	14.1	663.2	48.2	675.9	11.4
Spot 189	20992.9	172.2	1.7	15.9	2.8	0.9	4.2	0.1	2.2	0.5	677.9	14.0	675.8	20.6	669.5	76.4	677.9	14.0
Spot 242	37860.4	230.2	3.8	16.1	2.3	0.9	3.1	0.1	1.8	0.6	678.2	11.5	673.8	15.3	659.8	54.5	678.2	11.5
Spot 124	60367.9	520.0	2.2	15.8	1.8	1.0	2.8	0.1	2.2	0.8	679.4	14.1	686.3	14.1	710.0	37.9	679.4	14.1
Spot 140	18261.4	146.1	1.7	15.5	3.4	1.0	4.0	0.1	1.9	0.5	679.5	12.5	688.9	19.9	720.7	73.6	679.5	12.5
Spot 11	36540.4	272.8	3.5	15.9	2.1	1.0	2.9	0.1	1.9	0.7	681.0	12.3	681.0	14.4	681.8	46.7	681.0	12.3
Spot 134	41774.4	335.9	3.0	15.9	2.1	1.0	2.6	0.1	1.5	0.6	681.1	9.9	681.6	13.0	684.5	45.5	681.1	9.9
Spot 25	39755.7	317.0	2.7	15.8	2.1	1.0	2.9	0.1	1.9	0.7	681.2	12.3	686.1	14.6	703.1	47.2	681.2	12.3
Spot 225	56429.2	678.6	3.0	15.8	1.5	1.0	2.7	0.1	2.2	0.8	681.7	14.2	685.1	13.6	697.2	34.7	681.7	14.2
Spot 52	38430.0	370.5	2.1	15.9	1.9	1.0	2.9	0.1	2.2	0.8	682.3	14.3	681.1	14.5	677.9	40.9	682.3	14.3
Spot 135	19541.6	154.4	3.6	15.8	3.6	1.0	4.1	0.1	1.8	0.4	682.3	11.9	683.4	20.5	688.0	78.8	682.3	11.9
Spot 276	13449.5	80.1	2.0	15.7	5.5	1.0	6.5	0.1	1.9	0.3	682.9	12.5	685.9	32.6	696.5	133.2	682.9	12.5
Spot 232	48026.5	307.7	3.1	15.8	2.0	1.0	2.7	0.1	1.8	0.7	683.4	11.8	686.7	13.5	698.1	42.6	683.4	11.8
Spot 46	7651.7	103.1	3.7	14.9	4.2	1.0	7.1	0.1	2.0	0.3	683.5	12.7	705.1	36.1	775.5	143.5	683.5	12.7
Spot 160	9741.0	62.7	2.0	15.6	6.4	1.0	7.4	0.1	1.9	0.3	683.9	12.4	685.1	37.0	690.1	152.9	683.9	12.4
Spot 13	31746.4	259.4	1.7	16.0	2.5	1.0	3.1	0.1	1.8	0.6	684.0	11.8	679.9	15.5	667.0	54.4	684.0	11.8
Spot 94	30886.9	191.0	3.2	15.9	2.8	1.0	3.6	0.1	2.1	0.6	684.1	13.3	682.6	18.0	678.3	63.9	684.1	13.3
Spot 243	16877.2	125.6	6.7	16.1	4.2	0.9	5.3	0.1	2.3	0.4	685.2	15.0	675.0	26.0	642.0	101.9	685.2	15.0
Spot 218	16503.3	136.8	2.9	15.8	4.0	1.0	4.5	0.1	1.9	0.4	685.2	12.6	682.3	22.3	673.8	86.5	685.2	12.6
Spot 73	29564.3	268.7	2.6	15.9	2.1	1.0	2.8	0.1	1.8	0.6	685.7	11.8	684.9	14.0	683.1	45.7	685.7	11.8
Spot 48	17321.2	563.4	2.6	15.6	1.6	1.0	2.7	0.1	2.2	0.8	686.5	14.0	693.2	13.5	715.7	34.4	686.5	14.0
Spot 57	22126.7	176.6	2.8	15.5	3.1	1.0	4.2	0.1	2.6	0.6	687.2	17.1	695.4	21.1	723.0	69.5	687.2	17.1
Spot 40	21430.6	410.2	2.5	15.6	1.4	1.0	2.7	0.1	1.8	0.7	687.8	11.6	694.8	13.5	718.7	42.8	687.8	11.6
Spot 289	7832.8	64.9	1.9	15.5	6.1	1.0	6.9	0.1	2.2	0.3	687.9	14.5	685.2	34.3	677.3	139.4	687.9	14.5
Spot 63	28999.3	210.9	2.8	15.9	2.3	1.0	3.0	0.1	1.8	0.6	689.1	11.8	686.0	14.8	676.5	50.2	689.1	11.8
Spot 36	75580.6	482.1	2.9	15.9	1.7	1.0	2.5	0.1	1.8	0.7	689.4	11.5	690.3	12.4	694.0	36.8	689.4	11.5
Spot 279	26960.3	215.1	3.8	15.9	2.3	1.0	3.2	0.1	1.8	0.6	689.8	12.0	689.0	16.3	687.3	57.3	689.8	12.0
Spot 75	50890.3	309.0	1.0	15.7	1.6	1.0	2.5	0.1	1.8	0.7	690.2	11.5	693.8	12.4	706.6	37.2	690.2	11.5
Spot 60	19025.7	145.0	3.9	15.8	3.2	1.0	4.2	0.1	2.5	0.6	690.3	16.2	689.3	21.0	687.0	72.3	690.3	16.2
Spot 86	43829.7	250.4	3.9	15.9	2.1	1.0	3.1	0.1	2.0	0.7	690.5	13.3	688.3	15.2	682.2	48.5	690.5	13.3
Spot 85	99088.4	589.3	2.9	15.8	1.3	1.0	2.3	0.1	1.9	0.8	691.4	12.2	693.1	11.7	699.4	29.4	691.4	12.2
Spot 306	16031.4	124.3	3.4	16.0	4.9	1.0	5.4	0.1	2.1	0.4	693.8	13.8	684.8	26.8	656.2	106.3	693.8	13.8
Spot 269	55979.3	378.5	2.3	16.0	1.5	1.0	2.9	0.1	2.3	0.8	694.2	15.4	687.8	14.3	668.1	34.8	694.2	15.4
Spot 71	13598.1	105.8	1.5	15.4	5.4	1.0	6.3	0.1	2.6	0.4	695.2	17.1	700.8	31.7	719.5	121.1	695.2	17.1
Spot 78	66754.4	380.6	2.5	15.9	1.7	1.0	2.7	0.1	2.1	0.8	695.4	13.6	691.6	13.5	680.1	36.9	695.4	13.6
Spot 20	32823.8	308.1	3.3	15.7	2.2	1.0	3.0	0.1	2.1	0.7	699.9	13.6	703.8	15.4	717.0	47.6	699.9	13.6
Spot 301	28181.2	179.7	2.3	15.7	3.0	1.0	3.7	0.1	2.0	0.5	700.8	13.1	701.2	18.6	703.3	65.9	700.8	13.1
Spot 187	62816.4	536.7	7.1	15.9	1.5	1.0	2.4	0.1	1.8	0.8	701.1	12.2	698.5	12.0	691.1	32.4	701.1	12.2
Spot 222	37921.5	256.4	3.6	15.9	2.1	1.0	3.2	0.1	2.2	0.7	702.8	14.5	697.1	15.9	679.9	48.9	702.8	14.5
Spot 197	33230.7	227.8	3.0	15.9	3.0	1.0	3.5	0.1	1.8	0.5	709.3	11.8	699.8	17.9	670.6	65.5	709.3	11.8
Spot 196	34309.7	231.3	2.7	15.7	2.3	1.0	3.6	0.1	2.7	0.8	712.3	18.1	710.2	18.2	704.2	50.0	712.3	18.1
Spot 287	35240.7	197.5	3.2	15.8	2.6	1.0	3.6	0.1	2.4	0.7	712.8	15.9	706.4	18.3	687.0	57.7	712.8	15.9
Spot 74	46869.8	376.0	1.3	15.7	1.8	1.0	2.7	0.1	1.9	0.7	718.2	12.8	716.1	13.6	710.5	39.6	718.2	12.8
Spot 118	13978.5	80.5	3.1	14.5	18.5	1.2	25.8	0.1	17.9	0.7	751.3	127.2	779.0	140.4	860.3	384.9	751.3	127.2
Spot 166	42062.6	285.5	3.8	15.5	1.7	1.1	2.4	0.1	1.6	0.7	753.9	11.5	751.5	13.0	745.4	38.8	753.9	11.5
Spot 219	13906.8	96.0	3.5	15.0	4.5	1.1	5.1	0.1	2.1	0.4	755.4	15.0	762.4	27.4	783.9	97.8	755.4	15.0
Spot 204	13662.4	90.4	2.1	15.2	4.7	1.1	5.3	0.1	2.3	0.4	760.2	16.5	758.7	28.6	755.2	101.8	760.2	16.5
Spot 112	6538.5	145.4	4.2	14.9	3.1	1.1	5.4	0.1	1.7	0.3	764.1	12.6	764.1	29.1	765.3	108.2	764.1	12.6
Spot 15	######	669.6	4.3	15.3	1.3	1.1	2.4	0.1	2.0	0.8	767.5	14.4	770.2	13.0	778.8	28.5	767.5	14.4
Spot 201	38985.6	249.6	2.7	15.1	1.8	1.1	3.1	0.1	2.3	0.8	769.0	16.8	773.3	16.6	786.3	41.9	769.0	16.8
Spot 244	39448.1	193.4	2.6	15.1	2.5	1.1	3.3	0.1	2.0	0.6	769.6	14.8	775.5	17.6	793.6	53.2	769.6	14.8
Spot 194	60331.1	442.6	3.5	15.0	1.6	1.2	2.7	0.1	2.2	0.8	772.2	15.9	781.4	14.8	808.7	33.9	772.2	15.9
Spot 126	97228.1	576.9	3.6	15.2	1.4	1.1	2.3	0.1	1.8	0.8	774.5	13.1	776.7	12.4	783.8	29.8	774.5	13.1

Analysis	206Pb	U	U/Th	206Pb*	Â±2s	207Pb*	Â±2s	206Pb*	Â±2s	error	206Pb*	Â±2s	207Pb*	Â±2s	206Pb*	Â±2s	Best age	Â±2s
Spot 191	16932.0	96.1	3.2	15.5	5.3	1.1	5.9	0.1	1.8	0.3	777.8	13.4	761.4	31.8	714.4	120.0	777.8	13.4
Spot 121	57183.7	489.8	1.9	15.1	1.5	1.2	2.3	0.1	1.7	0.8	778.0	12.8	782.6	12.6	796.5	32.0	778.0	12.8
Spot 248	20702.9	158.4	1.6	15.1	3.3	1.2	4.3	0.1	2.0	0.5	778.9	14.8	780.7	23.3	786.6	79.0	778.9	14.8
Spot 235	15650.7	98.5	4.2	15.5	4.9	1.1	5.8	0.1	2.0	0.3	779.9	14.7	765.2	31.0	723.7	114.8	779.9	14.7
Spot 114	12340.3	73.3	3.5	14.7	5.7	1.2	6.7	0.1	2.0	0.3	783.5	14.6	793.1	37.1	821.2	134.6	783.5	14.6
Spot 215	10862.0	71.5	2.0	15.0	4.9	1.2	5.7	0.1	2.1	0.4	783.5	15.2	780.0	30.8	770.9	110.9	783.5	15.2
Spot 152	18126.2	111.4	3.4	15.3	3.2	1.2	4.6	0.1	2.3	0.5	785.6	16.9	779.0	25.1	761.0	84.4	785.6	16.9
Spot 284	19666.0	500.2	3.5	15.0	1.4	1.2	3.1	0.1	2.1	0.7	787.8	15.3	787.3	16.8	787.0	47.7	787.8	15.3
Spot 163	28453.3	609.6	2.4	15.0	1.3	1.2	2.5	0.1	1.9	0.8	793.8	14.2	796.6	13.6	805.2	32.7	793.8	14.2
Spot 188	9180.8	135.4	2.2	14.6	2.7	1.2	3.6	0.1	2.2	0.6	794.6	16.5	800.5	19.7	817.8	58.4	794.6	16.5
Spot 246	22399.4	151.1	4.5	15.2	2.7	1.2	3.6	0.1	2.4	0.7	798.0	18.0	790.7	19.9	771.0	57.3	798.0	18.0
Spot 278	29007.0	171.1	3.9	14.7	3.1	1.3	3.8	0.1	2.1	0.5	844.2	16.3	846.9	21.6	854.9	65.3	844.2	16.3
Spot 62	15197.9	68.8	1.3	14.1	6.0	1.4	6.6	0.1	2.0	0.3	888.4	16.9	896.1	39.3	915.9	129.3	915.9	129.3
Spot 30	10305.7	72.5	1.5	14.0	4.8	1.5	5.5	0.2	2.2	0.4	936.4	19.2	931.5	33.4	921.0	103.2	921.0	103.2
Spot 157	12248.5	72.0	2.5	14.0	4.2	1.4	5.2	0.1	2.5	0.5	899.5	20.8	907.7	31.4	928.7	94.6	928.7	94.6
Spot 45	83277.9	469.0	2.6	14.2	1.4	1.5	2.7	0.2	2.3	0.9	919.3	19.8	923.8	16.3	935.6	27.9	935.6	27.9
Spot 28	13049.7	76.7	1.2	14.0	4.0	1.5	5.0	0.2	2.2	0.4	956.9	19.6	950.4	30.6	936.2	91.1	936.2	91.1
Spot 108	14711.8	81.8	3.0	13.9	4.3	1.6	5.3	0.2	2.1	0.4	969.5	19.1	961.2	32.9	943.1	99.4	943.1	99.4
Spot 110	30609.0	130.0	2.1	14.0	2.7	1.5	3.6	0.2	2.2	0.6	948.8	19.5	947.5	21.9	945.5	56.9	945.5	56.9
Spot 61	4034.2	86.3	1.7	13.4	3.9	1.6	10.6	0.2	1.9	0.2	960.5	17.4	959.2	65.8	957.0	213.2	957.0	213.2
Spot 282	7644.2	140.2	1.3	13.7	2.5	1.6	6.1	0.2	1.8	0.3	971.4	16.1	967.7	38.1	960.1	119.3	960.1	119.3
Spot 181	19124.5	114.4	0.8	13.8	2.7	1.7	3.8	0.2	2.0	0.5	1003.0	18.6	989.7	23.8	961.4	65.0	961.4	65.0
Spot 91	18082.7	98.3	2.1	13.8	3.5	1.6	4.3	0.2	2.1	0.5	962.8	18.7	963.0	26.9	964.4	77.2	964.4	77.2
Spot 119	46293.0	241.6	3.3	13.9	17.9	1.5	25.3	0.2	17.9	0.7	933.0	155.6	942.3	155.9	965.0	366.9	965.0	366.9
Spot 202	35085.3	165.7	2.4	13.9	2.3	1.6	3.4	0.2	2.3	0.7	967.3	20.3	967.2	20.9	968.0	50.7	968.0	50.7
Spot 264	43067.1	196.8	3.0	13.9	2.0	1.6	3.1	0.2	2.3	0.7	967.8	20.9	967.7	19.4	968.5	42.3	968.5	42.3
Spot 190	56345.6	260.3	1.8	13.9	1.5	1.6	2.5	0.2	2.0	0.8	968.7	18.0	969.4	15.7	971.8	31.2	971.8	31.2
Spot 312	50889.5	258.0	1.9	13.9	1.7	1.6	3.5	0.2	3.0	0.9	986.3	27.4	981.5	22.0	971.8	36.9	971.8	36.9
Spot 198	62688.2	298.2	2.9	13.8	1.6	1.7	2.6	0.2	2.0	0.8	1003.9	18.5	994.1	16.6	973.5	34.5	973.5	34.5
Spot 77	78521.8	343.1	1.1	13.9	1.3	1.6	2.2	0.2	1.8	0.8	964.0	15.7	966.7	13.7	973.7	26.8	973.7	26.8
Spot 100	42407.0	320.9	2.4	13.8	1.4	1.6	2.4	0.2	2.0	0.8	988.1	17.9	983.6	15.2	974.6	29.0	974.6	29.0
Spot 294	29883.0	157.5	1.1	13.8	2.2	1.6	2.8	0.2	1.7	0.6	991.5	16.0	986.0	17.8	974.6	45.4	974.6	45.4
Spot 67	70745.6	247.7	1.5	13.8	1.7	1.6	2.6	0.2	2.0	0.8	970.2	17.9	971.7	16.5	975.8	35.4	975.8	35.4
Spot 72	33922.3	190.2	3.3	13.8	1.8	1.6	2.8	0.2	1.9	0.7	969.2	16.9	971.7	17.2	978.0	41.1	978.0	41.1
Spot 199	68905.6	369.8	2.4	13.8	1.3	1.6	2.4	0.2	2.0	0.8	941.1	17.1	952.3	14.7	979.1	27.8	979.1	27.8
Spot 105	24977.0	281.6	2.2	13.8	1.6	1.6	2.5	0.2	1.8	0.7	963.7	15.8	968.4	15.4	979.9	34.9	979.9	34.9
Spot 253	66300.5	361.2	2.3	13.8	1.8	1.6	2.7	0.2	2.0	0.7	970.5	17.7	973.3	16.8	980.3	37.1	980.3	37.1
Spot 55	19582.3	381.6	2.3	13.7	1.2	1.6	2.7	0.2	1.9	0.7	975.6	17.3	976.8	17.1	980.5	39.6	980.5	39.6
Spot 146	66075.8	320.6	2.0	13.8	1.3	1.6	2.3	0.2	1.8	0.8	969.6	15.9	973.7	14.2	983.9	29.0	983.9	29.0
Spot 178	7613.7	542.0	1.7	13.5	1.7	1.5	2.7	0.2	2.1	0.8	934.4	18.2	950.0	16.7	987.4	34.7	987.4	34.7
Spot 22	75649.4	637.1	1.8	13.8	1.4	1.6	2.3	0.2	1.8	0.8	959.6	15.9	968.6	14.2	990.1	28.5	990.1	28.5
Spot 92	######	406.6	0.6	13.7	1.4	1.7	2.4	0.2	1.9	0.8	996.6	17.1	995.9	14.9	995.5	29.5	995.5	29.5
Spot 4	20909.3	152.7	2.0	13.7	2.2	1.6	3.0	0.2	2.0	0.7	970.7	17.8	978.1	18.8	995.7	45.5	995.7	45.5
Spot 33	41190.7	367.8	1.0	13.7	1.4	1.5	2.3	0.2	1.7	0.8	926.9	15.0	947.8	13.9	997.6	29.4	997.6	29.4
Spot 292	28061.7	151.2	2.6	13.6	2.1	1.7	2.9	0.2	1.8	0.6	1030.7	16.9	1019.9	18.6	997.7	46.4	997.7	46.4
Spot 29	36794.3	180.0	2.4	13.7	1.8	1.7	3.0	0.2	2.4	0.8	1007.1	22.3	1004.0	19.3	998.2	37.6	998.2	37.6
Spot 229	60019.0	320.5	2.9	13.7	1.4	1.7	2.4	0.2	2.0	0.8	998.3	18.4	999.7	15.6	1003.8	28.9	1003.8	28.9
Spot 288	19157.3	82.7	1.2	13.5	3.5	1.8	4.2	0.2	1.9	0.4	1042.6	18.2	1030.5	27.3	1005.8	76.3	1005.8	76.3
Spot 106	6228.0	313.8	2.4	13.3	1.5	1.6	3.2	0.2	2.8	0.9	941.0	24.5	960.7	20.0	1006.8	32.0	1006.8	32.0
Spot 19	55623.1	361.4	1.8	13.7	1.5	1.7	2.8	0.2	2.3	0.8	984.0	21.3	990.8	17.6	1006.8	30.5	1006.8	30.5
Spot 208	41593.4	177.4	1.8	13.6	1.9	1.7	2.7	0.2	1.9	0.7	1028.0	18.3	1022.2	17.7	1010.5	39.6	1010.5	39.6
Spot 168	3286.6	283.3	1.5	12.8	2.3	1.5	4.1	0.2	1.5	0.4	905.2	12.8	938.1	25.4	1017.0	78.1	1017.0	78.1
Spot 241	66647.2	282.3	4.8	13.6	1.4	1.7	2.3	0.2	1.8	0.8	994.3	16.8	1001.4	14.7	1017.6	28.5	1017.6	28.5
Spot 298	8891.0	46.3	4.3	13.3	6.5	1.6	7.0	0.2	2.3	0.3	967.8	20.7	983.8	44.1	1020.4	134.0	1020.4	134.0
Spot 297	3568.6	53.7	1.7	12.8	5.2	1.7	9.8	0.2	2.2	0.2	986.8	19.7	999.3	62.2	1027.7	192.9	1027.7	192.9
Spot 265	48705.6	207.0	0.8	13.5	1.7	1.7	2.7	0.2	2.0	0.7	1024.6	19.2	1025.4	17.6	1027.7	36.7	1027.7	36.7
Spot 16	29481.7	147.1	1.7	13.4	1.9	1.8	3.0	0.2	1.9	0.6	1032.5	18.4	1031.7	19.2	1030.6	45.6	1030.6	45.6
Spot 12	20808.2	94.4	1.8	13.4	3.1	1.7	4.1	0.2	2.0	0.5	1020.3	19.2	1024.2	26.6	1033.3	72.5	1033.3	72.5

Analysis	206Pb	U	U/Th	206Pb*	Â±2s	207Pb*	Â±2s	206Pb*	Â±2s	error	206Pb*	Â±2s	207Pb*	Â±2s	206Pb*	Â±2s	Best age	Â±2s
Spot 209	19651.6	96.1	1.9	13.2	3.0	1.8	3.9	0.2	1.8	0.5	1054.9	17.4	1054.8	25.9	1055.4	70.9	1055.4	70.9
Spot 58	20350.6	101.6	1.9	13.2	3.3	1.8	4.1	0.2	2.3	0.6	1058.0	22.2	1059.5	27.2	1063.4	69.4	1063.4	69.4
Spot 70	21879.4	124.9	1.7	13.2	2.4	1.8	3.1	0.2	1.8	0.6	1044.8	17.5	1050.6	20.4	1063.5	50.8	1063.5	50.8
Spot 47	15205.7	69.1	1.4	13.1	3.1	1.7	4.2	0.2	2.0	0.5	1002.5	18.8	1023.1	27.2	1068.4	74.4	1068.4	74.4
Spot 266	35753.4	157.0	1.0	13.2	1.9	1.8	2.9	0.2	2.1	0.7	1041.1	19.9	1049.8	18.8	1069.0	39.9	1069.0	39.9
Spot 228	17191.8	69.6	1.2	13.2	4.1	1.8	4.9	0.2	1.9	0.4	1051.5	18.9	1057.3	32.4	1070.1	91.1	1070.1	91.1
Spot 39	12425.3	62.4	1.2	13.1	3.3	1.8	4.8	0.2	2.0	0.4	1044.5	19.6	1053.5	31.6	1073.1	87.9	1073.1	87.9
Spot 49	33186.7	220.0	1.7	13.2	1.7	1.9	2.7	0.2	1.9	0.7	1073.5	18.4	1073.5	17.7	1074.3	38.5	1074.3	38.5
Spot 195	13800.6	68.1	1.4	13.0	4.6	1.9	5.3	0.2	2.1	0.4	1062.2	20.9	1066.4	34.9	1075.8	97.2	1075.8	97.2
Spot 255	27129.3	106.3	0.9	13.1	2.5	1.8	3.4	0.2	1.9	0.6	1045.7	18.4	1058.8	22.0	1086.6	55.3	1086.6	55.3
Spot 79	45586.6	185.8	1.4	13.0	1.7	1.9	2.5	0.2	1.8	0.7	1096.7	18.1	1096.2	16.7	1096.2	34.6	1096.2	34.6
Spot 184	30615.9	112.6	3.3	12.9	2.5	2.0	3.6	0.2	2.6	0.7	1119.3	26.4	1114.0	24.6	1104.3	51.5	1104.3	51.5
Spot 193	35362.2	128.2	1.4	12.9	2.0	2.0	3.0	0.2	2.0	0.7	1107.2	20.6	1109.3	20.2	1114.2	44.1	1114.2	44.1
Spot 87	23475.0	99.7	1.9	12.8	2.5	2.0	3.5	0.2	2.1	0.6	1098.4	21.0	1104.9	23.7	1118.7	56.7	1118.7	56.7
Spot 226	42749.5	202.7	1.7	12.9	1.8	1.9	2.8	0.2	2.1	0.7	1074.0	20.5	1088.7	18.5	1119.2	36.8	1119.2	36.8
Spot 183	6700.0	29.5	1.2	12.6	9.8	2.0	10.3	0.2	3.0	0.3	1088.7	30.2	1100.2	69.4	1123.8	197.0	1123.8	197.0
Spot 59	63673.5	251.2	2.2	12.1	1.8	2.4	2.8	0.2	2.1	0.7	1234.1	23.8	1236.4	20.2	1241.2	36.8	1241.2	36.8
Spot 133	49686.4	190.7	2.4	12.1	1.4	2.4	2.5	0.2	2.0	0.8	1227.4	22.2	1234.4	17.7	1247.5	29.2	1247.5	29.2
Spot 99	30341.8	134.1	0.8	12.0	1.8	2.4	2.9	0.2	2.2	0.8	1242.6	25.2	1250.3	20.7	1264.3	35.3	1264.3	35.3
Spot 89	55601.8	188.6	4.2	11.3	1.4	2.9	2.3	0.2	1.8	0.8	1393.2	22.9	1384.5	17.6	1371.9	27.8	1371.9	27.8
Spot 286	40829.7	100.6	2.0	11.2	2.3	2.9	3.4	0.2	2.4	0.7	1391.5	30.0	1391.3	25.6	1391.8	45.7	1391.8	45.7
Spot 43	6982.6	20.6	0.5	10.7	8.0	3.1	8.9	0.2	2.2	0.3	1431.6	28.7	1437.2	68.5	1446.4	164.3	1446.4	164.3
Spot 127	21371.2	66.3	1.2	10.9	2.7	3.1	3.4	0.2	2.0	0.6	1416.4	25.0	1430.1	26.3	1451.3	53.5	1451.3	53.5
Spot 65	82907.8	257.0	9.4	10.4	1.4	3.5	2.7	0.3	2.3	0.8	1543.3	31.4	1536.9	21.4	1528.9	27.0	1528.9	27.0
Spot 76	74827.4	216.4	1.0	9.9	1.6	3.8	3.8	0.3	3.5	0.9	1561.9	48.3	1589.4	30.9	1626.9	30.6	1626.9	30.6
Spot 101	27514.6	74.9	1.7	9.2	2.1	3.9	3.5	0.3	2.8	0.8	1524.5	38.2	1623.7	28.5	1755.7	38.6	1755.7	38.6
Spot 26	60110.4	153.9	1.8	9.2	1.5	4.5	2.6	0.3	2.1	0.8	1712.8	31.9	1736.2	21.7	1765.2	27.8	1765.2	27.8
Spot 300	11269.0	63.9	1.6	9.1	2.0	4.8	3.5	0.3	2.1	0.6	1804.3	32.6	1789.7	29.8	1773.6	52.6	1773.6	52.6
Spot 35	94974.8	341.3	1.6	9.2	1.2	4.5	2.1	0.3	1.8	0.8	1706.3	26.4	1737.1	17.8	1775.0	22.4	1775.0	22.4
Spot 53	16228.9	35.3	0.6	8.7	2.1	5.3	3.0	0.3	2.0	0.7	1874.1	32.4	1869.2	25.8	1864.6	40.9	1864.6	40.9
Spot 295	96110.5	206.2	1.1	8.7	1.2	5.3	2.5	0.3	2.2	0.9	1886.6	35.9	1876.3	21.3	1865.7	21.2	1865.7	21.2
Spot 270	######	311.5	1.5	8.7	1.1	5.2	2.3	0.3	2.0	0.9	1844.7	31.4	1854.6	19.3	1866.4	20.7	1866.4	20.7
Spot 192	59987.0	183.3	1.7	8.7	1.3	5.0	3.4	0.3	3.1	0.9	1770.7	48.4	1815.1	28.8	1867.3	24.3	1867.3	24.3
Spot 172	73239.0	192.1	1.2	8.7	1.3	5.3	2.4	0.3	2.0	0.8	1859.1	32.2	1864.4	20.4	1871.1	23.7	1871.1	23.7
Spot 296	7114.1	132.7	0.8	8.5	1.2	5.3	2.2	0.3	1.4	0.6	1855.4	21.9	1862.9	18.6	1872.0	30.7	1872.0	30.7
Spot 171	41563.2	87.2	3.4	8.7	1.7	5.3	2.7	0.3	2.1	0.8	1857.7	34.2	1864.3	23.4	1872.5	31.3	1872.5	31.3
Spot 291	9579.8	121.8	2.6	8.6	1.4	5.0	2.7	0.3	2.0	0.8	1767.3	31.0	1817.8	22.6	1876.9	31.9	1876.9	31.9
Spot 290	29943.6	74.4	1.0	8.6	1.5	5.4	2.6	0.3	2.0	0.8	1897.2	33.1	1888.9	22.4	1880.6	29.9	1880.6	29.9
Spot 138	51981.8	109.3	1.5	8.6	1.4	5.3	2.6	0.3	2.1	0.8	1865.8	33.4	1873.9	21.8	1883.6	27.1	1883.6	27.1
Spot 274	37127.4	96.1	1.0	8.7	1.6	5.3	2.4	0.3	1.7	0.7	1853.6	28.1	1867.6	20.3	1884.1	29.3	1884.1	29.3
Spot 66	12617.8	323.4	0.9	8.5	1.4	5.5	2.9	0.3	2.2	0.7	1922.8	36.3	1904.3	25.1	1884.9	35.0	1884.9	35.0
Spot 132	20004.1	60.5	0.9	8.6	2.4	5.2	3.7	0.3	2.5	0.7	1838.6	39.7	1860.1	31.2	1885.0	48.5	1885.0	48.5
Spot 210	62150.5	149.0	1.8	8.6	1.3	5.4	2.6	0.3	2.2	0.8	1874.2	36.2	1879.3	22.5	1885.6	25.0	1885.6	25.0
Spot 23	98241.2	205.5	1.7	8.7	1.3	5.3	2.3	0.3	1.9	0.8	1851.3	30.3	1867.2	19.5	1885.8	23.1	1885.8	23.1
Spot 185	54165.4	131.5	0.9	8.6	1.4	5.6	2.2	0.4	1.7	0.8	1940.2	28.4	1914.2	18.8	1886.8	24.7	1886.8	24.7
Spot 206	61981.0	133.7	1.9	8.6	1.4	5.0	2.6	0.3	2.3	0.9	1758.9	34.9	1818.3	22.4	1887.8	24.5	1887.8	24.5
Spot 97	40712.9	109.2	2.1	8.6	1.8	5.0	2.8	0.3	2.1	0.7	1772.3	32.0	1826.4	23.6	1889.5	33.8	1889.5	33.8
Spot 217	31980.9	84.2	0.8	8.6	1.4	5.2	2.4	0.3	1.9	0.8	1827.8	29.7	1857.4	20.3	1891.6	26.5	1891.6	26.5
Spot 120	42508.5	86.5	1.2	8.6	17.9	5.3	25.3	0.3	17.9	0.7	1845.5	287.6	1867.7	217.2	1893.3	322.9	1893.3	322.9
Spot 56	######	219.0	1.9	8.6	1.9	5.5	3.1	0.3	2.5	0.8	1894.7	40.4	1894.2	26.5	1894.5	33.5	1894.5	33.5
Spot 275	9124.8	149.7	0.6	8.5	1.4	5.3	2.1	0.3	1.5	0.7	1847.9	24.8	1875.2	18.2	1906.2	26.3	1906.2	26.3
Spot 281	5005.7	111.0	2.5	8.4	2.5	4.9	5.2	0.3	2.4	0.5	1706.5	36.6	1800.2	43.5	1911.2	81.5	1911.2	81.5
Spot 200	88479.3	235.8	1.6	8.4	1.2	5.5	2.5	0.3	2.2	0.9	1881.5	36.5	1907.4	21.8	1936.4	21.2	1936.4	21.2
Spot 256	######	234.5	2.5	8.3	1.1	5.8	2.2	0.3	1.8	0.9	1933.0	30.9	1939.7	18.7	1947.6	20.0	1947.6	20.0
Spot 247	83239.3	222.1	2.1	8.3	1.1	5.7	2.3	0.3	2.0	0.9	1909.4	32.7	1930.5	19.7	1953.9	20.5	1953.9	20.5
Spot 261	86100.9	182.7	1.6	8.3	1.6	5.7	2.8	0.3	2.3	0.8	1912.2	38.5	1932.8	24.6	1955.7	29.2	1955.7	29.2
Spot 129	57446.7	116.9	2.3	8.3	1.4	6.0	2.5	0.4	2.1	0.8	1980.0	35.5	1970.0	22.0	1960.2	25.7	1960.2	25.7
Spot 186	######	292.4	1.4	8.2	1.3	5.6	2.2	0.3	1.7	0.8	1883.0	27.8	1921.9	18.6	1965.0	23.5	1965.0	23.5

Analysis	206Pb	U	U/Th	206Pb*	Â±2s	207Pb*	Â±2s	206Pb*	Â±2s	error	206Pb*	Â±2s	207Pb*	Â±2s	206Pb*	Â±2s	Best age	Â±2s
Spot 277	62465.0	229.9	2.3	8.3	1.3	5.7	2.3	0.3	1.9	0.8	1900.8	31.3	1931.9	20.3	1966.2	24.6	1966.2	24.6
Spot 303	54211.0	110.7	2.4	8.2	1.4	6.0	2.4	0.4	1.9	0.8	1988.2	32.5	1977.3	20.5	1966.6	24.9	1966.6	24.9
Spot 176	######	306.4	2.7	8.2	1.6	6.0	2.7	0.4	2.2	0.8	1986.7	38.3	1976.7	23.8	1967.0	27.8	1967.0	27.8
Spot 220	55141.4	144.8	1.5	8.2	1.4	5.8	2.8	0.4	2.4	0.9	1936.3	39.8	1951.9	24.1	1969.3	25.5	1969.3	25.5
Spot 83	######	318.9	2.0	8.2	1.2	5.6	2.1	0.3	1.8	0.8	1877.2	28.6	1921.2	18.1	1969.8	20.6	1969.8	20.6
Spot 158	73104.7	140.6	2.0	8.2	1.4	5.9	2.5	0.4	2.1	0.8	1944.0	34.7	1956.6	21.7	1970.6	24.9	1970.6	24.9
Spot 313	41875.8	211.8	1.3	8.2	1.3	5.7	3.0	0.3	2.7	0.9	1903.1	43.9	1936.0	25.7	1972.2	23.3	1972.2	23.3
Spot 68	######	311.0	2.5	8.2	1.5	6.1	2.7	0.4	2.2	0.8	1998.4	38.6	1985.4	23.3	1972.7	26.0	1972.7	26.0
Spot 257	48437.5	98.3	2.0	8.2	1.3	5.9	2.6	0.4	2.2	0.9	1959.4	37.5	1966.4	22.5	1974.4	23.9	1974.4	23.9
Spot 310	######	250.8	2.6	8.2	1.4	6.1	2.8	0.4	2.5	0.9	1993.5	42.4	1983.9	24.7	1974.7	24.8	1974.7	24.8
Spot 156	71118.0	144.1	2.5	8.2	1.3	5.9	2.4	0.4	2.1	0.9	1943.8	34.4	1958.5	20.9	1974.8	22.6	1974.8	22.6
Spot 239	######	295.3	2.6	8.2	0.9	6.0	2.2	0.4	2.0	0.9	1965.2	33.5	1969.6	19.1	1975.0	16.9	1975.0	16.9
Spot 109	82874.8	180.0	1.4	8.2	1.3	6.0	2.1	0.4	1.6	0.8	1962.7	27.1	1968.6	17.9	1975.5	22.9	1975.5	22.9
Spot 250	79429.0	183.0	2.1	8.2	1.4	5.9	2.5	0.4	2.0	0.8	1955.1	34.4	1964.8	21.4	1975.8	24.5	1975.8	24.5
Spot 98	######	351.4	2.6	8.2	1.7	6.1	2.9	0.4	2.3	0.8	2002.3	40.0	1989.3	24.9	1976.5	29.7	1976.5	29.7
Spot 223	70853.7	179.5	2.8	8.2	1.3	5.9	2.5	0.4	2.1	0.8	1949.2	35.7	1962.4	21.8	1977.1	24.0	1977.1	24.0
Spot 137	68621.3	111.6	1.5	8.2	1.5	5.9	2.6	0.4	2.1	0.8	1945.7	35.8	1960.8	22.7	1977.6	26.9	1977.6	26.9
Spot 249	######	343.1	2.0	8.2	1.3	6.0	2.2	0.4	1.8	0.8	1962.1	30.8	1970.1	19.3	1979.3	22.6	1979.3	22.6
Spot 93	######	399.7	2.2	8.2	1.1	5.9	2.2	0.4	1.9	0.9	1950.7	32.2	1964.4	19.2	1979.7	20.0	1979.7	20.0
Spot 159	30324.0	179.4	2.4	8.2	1.4	5.9	2.4	0.4	1.8	0.8	1941.0	30.8	1959.5	20.5	1980.0	26.4	1980.0	26.4
Spot 234	######	194.3	3.1	8.2	1.2	5.9	2.1	0.4	1.8	0.8	1937.1	29.3	1958.3	18.4	1981.6	21.3	1981.6	21.3
Spot 84	53370.8	118.4	2.4	8.2	1.2	6.1	2.3	0.4	2.0	0.9	1994.4	34.3	1988.0	20.4	1982.2	21.7	1982.2	21.7
Spot 230	87798.4	188.0	2.2	8.2	1.1	6.0	2.3	0.4	2.0	0.9	1959.2	32.9	1970.6	19.6	1983.4	20.1	1983.4	20.1
Spot 107	63093.4	119.3	1.4	8.2	1.3	5.8	2.3	0.3	1.9	0.8	1920.1	31.2	1951.2	20.0	1985.2	23.9	1985.2	23.9
Spot 174	93561.7	157.1	1.7	8.1	1.4	6.4	2.5	0.4	2.0	0.8	2087.8	36.2	2037.1	21.6	1986.8	24.4	1986.8	24.4
Spot 149	21054.5	177.5	1.5	8.1	1.1	5.7	2.2	0.3	1.9	0.8	1878.5	30.6	1930.7	19.1	1987.9	21.0	1987.9	21.0
Spot 309	13715.3	134.4	0.9	8.1	1.3	5.8	2.5	0.3	2.1	0.8	1898.4	34.3	1943.0	21.8	1991.6	25.1	1991.6	25.1
Spot 44	56100.5	165.0	0.8	8.1	1.2	6.0	2.1	0.4	1.7	0.8	1957.7	29.4	1974.5	18.7	1992.9	22.3	1992.9	22.3
Spot 268	10552.3	444.3	4.9	8.0	1.1	5.3	2.3	0.3	2.1	0.9	1733.8	31.2	1862.1	20.0	2009.2	20.0	2009.2	20.0
Spot 145	86318.3	152.9	0.9	7.9	1.8	6.1	3.0	0.4	2.4	0.8	1950.1	41.2	1990.0	26.4	2032.3	31.5	2032.3	31.5
Spot 21	40861.0	154.4	1.5	7.9	1.3	5.9	1.9	0.3	1.4	0.7	1892.2	23.2	1964.5	16.8	2042.4	23.2	2042.4	23.2
Spot 51	17419.3	219.6	1.9	7.8	1.4	6.3	2.4	0.4	1.8	0.8	1986.7	31.1	2015.7	21.2	2046.2	28.2	2046.2	28.2
Spot 315	51547.5	119.6	2.1	7.9	1.7	6.4	2.9	0.4	2.3	0.8	2025.3	40.6	2036.0	25.8	2047.6	31.4	2047.6	31.4
Spot 2	62317.0	168.6	6.2	7.8	1.4	6.6	2.4	0.4	2.0	0.8	2054.8	34.4	2055.6	21.2	2057.2	24.8	2057.2	24.8
Spot 88	50739.4	113.8	2.0	7.8	1.4	6.6	2.5	0.4	2.0	0.8	2050.0	35.5	2058.3	21.9	2067.3	25.3	2067.3	25.3
Spot 305	96719.4	245.8	2.9	7.7	1.4	6.9	2.7	0.4	2.4	0.9	2111.3	42.5	2095.1	24.3	2080.0	24.8	2080.0	24.8
Spot 111	14299.0	37.3	1.2	7.0	1.9	7.6	2.5	0.4	1.6	0.6	2139.7	28.5	2190.5	22.9	2239.0	34.7	2239.0	34.7
Spot 96	819.3	5.3	2.3	5.7	42.4	2.0	46.2	0.1	17.6	0.4	576.3	97.3	1128.0	317.3	2434.8	732.9	2434.8	732.9
Spot 307	63848.6	126.7	1.8	6.0	1.4	11.2	2.8	0.5	2.4	0.9	2554.5	50.6	2540.3	25.9	2529.6	23.7	2529.6	23.7
Spot 10	######	277.0	1.8	5.9	1.1	11.2	2.2	0.5	2.0	0.9	2524.9	41.3	2536.1	21.0	2545.7	18.1	2545.7	18.1
Spot 162	90994.9	361.6	15.6	5.9	1.0	10.0	2.0	0.4	1.7	0.9	2278.8	32.5	2430.9	18.3	2561.6	17.5	2561.6	17.5
Spot 80	######	267.2	1.1	5.8	1.0	11.6	2.2	0.5	2.0	0.9	2579.9	42.2	2575.8	20.7	2573.3	16.6	2573.3	16.6
Spot 95	48041.7	332.1	3.8	5.6	1.1	10.8	1.9	0.4	1.5	0.8	2374.0	30.1	2508.5	17.4	2619.9	18.4	2619.9	18.4
Spot 144	######	554.9	7.1	5.6	1.3	12.0	2.2	0.5	1.8	0.8	2578.6	38.3	2607.4	20.9	2630.5	21.7	2630.5	21.7
Spot 224	74011.7	125.8	1.7	5.6	1.3	11.5	2.3	0.5	2.0	0.8	2477.0	40.3	2563.1	21.8	2632.6	21.1	2632.6	21.1
Spot 262	######	185.4	0.6	5.6	1.6	12.3	2.7	0.5	2.2	0.8	2612.1	46.5	2628.5	25.1	2641.9	25.9	2641.9	25.9
Spot 1	33525.1	65.5	1.1	5.5	1.4	12.2	2.5	0.5	2.0	0.8	2583.7	43.6	2621.4	23.7	2651.4	24.4	2651.4	24.4
Spot 14	89092.0	261.3	1.6	5.5	1.2	12.1	2.5	0.5	2.2	0.9	2556.5	47.3	2610.2	23.9	2652.9	19.9	2652.9	19.9
Spot 280	36536.7	228.5	1.2	5.5	1.2	12.1	2.1	0.5	1.8	0.8	2563.3	37.7	2614.1	20.2	2654.3	19.9	2654.3	19.9
Spot 148	26994.2	50.1	3.2	5.5	1.4	12.5	2.3	0.5	1.8	0.8	2619.3	39.0	2643.1	21.7	2662.1	23.6	2662.1	23.6
Spot 179	######	425.1	3.4	5.5	1.0	12.2	2.1	0.5	1.8	0.9	2562.8	37.6	2620.0	19.3	2665.2	17.2	2665.2	17.2
Spot 259	######	218.5	2.7	5.5	2.7	12.8	4.1	0.5	3.0	0.7	2658.4	65.8	2664.5	38.4	2669.8	45.3	2669.8	45.3
Spot 304	42737.5	84.3	2.1	5.4	1.3	13.4	2.5	0.5	2.1	0.9	2741.7	48.0	2705.4	23.6	2679.2	21.3	2679.2	21.3
Spot 207	61634.4	117.9	1.1	5.3	1.1	13.1	2.2	0.5	1.9	0.9	2644.8	41.2	2683.9	20.7	2714.1	18.1	2714.1	18.1
Spot 311	9739.8	86.3	1.4	5.3	1.5	13.4	2.7	0.5	2.0	0.7	2688.2	44.1	2707.9	25.5	2723.3	29.7	2723.3	29.7
Spot 34	28164.4	41.2	1.9	5.3	1.5	13.5	2.3	0.5	1.8	0.8	2697.5	38.6	2713.0	21.6	2725.2	24.3	2725.2	24.3
Spot 18	######	244.1	0.9	5.0	1.3	14.9	2.5	0.5	2.1	0.9	2792.7	48.4	2806.9	23.7	2817.8	21.0	2817.8	21.0
Spot 272	40061.9	404.9	1.4	5.0	1.2	14.4	2.2	0.5	1.9	0.9	2728.2	42.5	2779.7	21.3	2818.0	19.1	2818.0	19.1

SUPPLEMENTAL MATERIALS
Chapter III

Metadata for samples in Chapters II and III

Sample	Latitude	Longitude	strike and dip	Thickness (m)
21-MANY-topsands				
21-MANY-15	-4.608768	29.709954		6
21-MANY-14			18 N / 30 E	18
21-MANY-13	-4.609134	29.7096		6
21-MANY-12	-4.689412	29.709163		43.5
21-MANY-11			11 N/32 E	1.5
21-MANY-10				13.5
21-MANY-9				12
21-MANY-8	-4.60991	29.708661		16.5
21-MANY-7				14.25
21-MANY-6			11 N / 32 E	12
21-MANY-5silt	-4.60989	29.707932		6
				10.5
21-MANY-3silt	-4.609822	29.7077	6 N / 26 E	10.5
21-MANY-2silt	-4.609788	29.707547		13.5
21-MANY-1silt	-4.609827	29.707238	9 N / 31 E	16.5
	-4.609929	29.706975		12
	-4.610138	29.706798	354 N / 28 E	16.5
21-MANY-2White	-4.610409	29.706694	332 NW / 31 E	33
21-MANY-1White	-4.610906	29.705868		22.5
			TOTAL	284.25

Raw point count data

Sample	Qm	Qp	chert	Q	P	K	F	Ls	Lm	Lv	L	Lt	Access	Total
21-MANY-topsand	263	16	0	279	54	36	90	3	2	22	27	43	4	400
21-MANY-15	203	13	0	216	98	38	136	0	8	40	48	61	0	400
21-MANY-8	178	9	0	187	124	30	154	3	0	42	45	54	14	400
21-MANY-6i	271	17	2	290	54	26	80	8	5	22	35	54	1	404
21-MANY-6F	240	8	0	248	75	12	87	7	1	49	57	65	8	400
21-MANY-5sand	238	15		253	80	37	117	5	1	17	23	38	7	400
21-MANY-4	255	5	0	260	58	38	96	2	5	33	40	45	4	400
21-MANY-3.1	243	13	1	257	37	16	53	3	2	41	46	60	45	400
21-MANY-3	223	7	0	230	34	33	67	1	0	36	37	44	53	387
21-MANY-2white	300	25	0	325	43	1	44	1	2	28	31	56	0	400
21-MANY-2.1white	293	44	0	337	37	2	39	7	2	15	24	68	0	400
21-MANY-1white	199	77	4	280	23	49	72	1	0	37	38	119	1	400
21-MANY-1.1white	253	14	0	267	48	9	57	4	5	66	75	89	1	400

Supp. Figure 1. Field Photos from Mkigo showing 1) extensive, internally massive siltstone and 2) concretion horizons.



Supp. Figure 2. SEM images and EDS mapping results from all four facies. EDS mapping did not identify sulfur (indicative of evaporite minerals) in any of the facies within the Manyovu.

